INFORMATION TO USERS

This manuscript has been reproduced from the microfilm master. UMI films the text directly from the original or copy submitted. Thus, some thesis and dissertation copies are in typewriter face, while others may be from any type of computer printer.

The quality of this reproduction is dependent upon the quality of the copy submitted. Broken or indistinct print, colored or poor quality illustrations and photographs, print bleedthrough, substandard margins, and improper alignment can adversely affect reproduction.

In the unlikely event that the author did not send UMI a complete manuscript and there are missing pages, these will be noted. Also, if unauthorized copyright material had to be removed, a note will indicate the deletion.

Oversize materials (e.g., maps, drawings, charts) are reproduced by sectioning the original, beginning at the upper left-hand corner and continuing from left to right in equal sections with small overlaps.

Photographs included in the original manuscript have been reproduced xerographically in this copy. Higher quality 6" x 9" black and white photographic prints are available for any photographs or illustrations appearing in this copy for an additional charge. Contact UMI directly to order.

Bell & Howell Information and Learning
300 North Zeeb Road, Ann Arbor, MI 48106-1346 USA
800-521-0600

Université d'Ottawa · University of Ottawa

بسم أله أ لرحمن ألرحيم

ACKNOWLEDGMENTS

Infinite thanks go to Allah (God) for giving me health, blessing, guidance, help, trust and strength to finish my Ph. D. and for everything in my whole life.

I dedicate this thesis to my father Mohamed, my sister Thirya, my brother Mohamed, my niece Samah, and my sister in-law Rhawda who passed away to Heaven during my Ph. D. study.

I would like to express my sincere love and appreciation of support to my mother, all my brothers, sisters and especially my brothers Ali and Naji who had no chance to go to school and did all their best to allow me to pursue advanced studies.

Much love and thanks go to my wife, Aziza Naif, whose contributions to my life and during the course of this work are immeasurable. To my two lovely children, Samah and Ahmed, I thank you for being so wonderful and kind. Your unconditional love inspires my positive outlook on my life and work.

I would like to express my gratitude and thanks to my supervisor Dr. Mario Morin for his support, encouragement, enthusiasm and infinite patience whose understanding made my stay at the University of Ottawa both educational and enjoyable.

I would like to express my appreciation to all my colleagues in the Morin group during my four and half years here, for many discussions and creating an atmosphere which was always exciting and friendly. Thanks go to glass-blower John Hopkins and everybody else who made my studies successful and smooth. Finally, I would like to thank the University of Ottawa for a scholarship and the University of Sana'a for a leave of absence.

ABSTRACT

Organic thiols adsorb on metallic surfaces and form so-called self-assembled monolayers (SAMs). These interfacial systems have attracted a lot of attention because of their possible use in various technologies such as electrochemical sensors, organic conductors or corrosion inhibitors. These applications make use of the ability of thiols to prevent charge transfer between the metal surface and the electrolyte solution. However, organic materials can undergo phase transitions in the range of temperature where modified electrodes are used. Few studies have been done on the thermal stability of molecular films. This thesis is a study of the electrochemical properties of alkanethiols chemisorbed on Au(111) between 5°C and 60°C.

We used an electrochemical sample preparation technique which allows us to have a clean gold substrate on which the thiols are then adsorbed. We obtained, using this method, an excellent reproducibility which was lacking in earlier electrochemical studies. This method makes it possible to use the reduction current to calculate a surface concentration of alkanethiols with a good accuracy. We measured a surface concentration of alkanethiols of $7.3(\pm 0.5) \times 10^{-10}$ mol cm^{-2}, in agreement with the literature value of 7.6×10^{-10} mol cm^{-2}. Our method of preparation was also checked by vibrational spectroscopy. Ex-situ vibrational Fourier transform infrared spectroscopy shows that long chain alkanethiols form crystalline-like monolayers (ordered) while short ones form more disordered overlayer structures on metallic surfaces, in agreement with the literature.

We found that soluble alkanethiols are reduced in a single step. This is shown by the single reductive current peak observed in the voltammograms. We found that insoluble alkanethiols are reduced in two steps. The reduced products (thiolates) are insoluble and thus remain physisorbed at the electrode surface. They can be oxidatively redeposited when the potential is scanned in the positive direction. The development of a fine structure in the voltammogram of insoluble thiols is shown to be caused by the low solubility of the thiols. We

propose a model in which the reductive desorption and the oxidative redeposition processes proceed through the same two-step mechanism. The first step of the reductive desorption is assigned to the reduction of the chemisorbed alkanethiols. This leads to the formation of a monolayer of physisorbed thiolates. This gives rise to a faradaic charge which account for approximately 70 % of the integrated total charge. The second step of the reduction occurs at more negative potentials and is assigned to the formation of micelles of thiolates. This results in an important capacitive current which integrates for the remaining 30 % of the total charge. The physisorbed micelles of thiolates are oxidatively readsorbed on the positive going potential scan of a cyclic voltammogram by the same two step process, but in the reverse order.

We have studied the effect of temperature on insoluble thiols that can be induced, by the application of an electric field, to reversibly go from a chemisorbed state to a physisorbed state. We found that the physisorbed thiolates remain at the electrode surface at temperatures as high as 70°C. A complex variation with the temperature is observed in the voltammograms. Our results reveal a change in the reductive desorption/oxidative redeposition at 23° C. We assign this change to an order-disorder transition.

The ion blocking properties of insoluble thiols were studied with differential capacitance and with cyclic voltammetry using ferricyanide as a redox probe. We found that monolayers with low numbers of defects are formed after a single incubation in a solution of thiols. Multiple incubations in a solution of thiols give a monolayer with such an extremely low number of defects that electron transfer occurs via tunneling. The same phase transition at 23°C was observed for the monolayers obtained after a single incubation. In this case, the increased disorder causes a collapse of the thiols at the edge of defects. This decreases the electroactive area of the electrode and a decrease of the electron transfer current.

Finally, we determined the oxidation mechanism of adsorbed butanethiol in neutral and alkaline aqueous solutions. Under neutral conditions, the butanethiols are oxidized via a

nine electrons process, whereas in alkaline solutions, the oxidation is greater and requires thirteen electrons. These results are found to be related to the greater electrocatalytic activity of gold in alkaline solutions.

TABLE OF CONTENTS

Chapter 2

Experimental

Chapter 3

The Role of the Solubility of Alkanethiols on the Reductive and Oxidative Electrochemistry of Alkanethiols

Chapter 4

Electron Transfer Kinetics

Chapter 5

Temperature and Scan Rate Dependence of the reductive desorption and oxidative redeposition of hexadecanethiol Adsorbed on a Crystal Gold (111) Electrode

Chapter 9
Overall Conclusions

بسم الله الرحمن الرحيم

Chapter 1

Self-Assembled Monolayers of Alkanethiols on Metallic Substrates

1. Introduction

Self-assembled monolayers (SAMs) of alkanethiols are easy to form. The method simply consists of making a millimolar solution of thiols in an organic solvent, such as methanol, ethanol or heptane, and dipping a clean metallic substrate into this solution. This results in the formation of an ordered monolayer strongly attached to the substrate surface.

The formation of self-assembled monolayers has been examined on many substrates. A variety of compounds that form self-assembled monolayers have been adsorbed on Au [1-5], Ag [6], Cu [6], Hg [7], GaAs [8], Al_2O_3 [9], SiO_2 [10], Si [11] and superconducting materials [12,13]. In 1983 Nuzzo and Allara [14] were the first to study the adsorption of organic disulfides on gold. Since then, SAMs of alkanethiols of different chain length on gold (111) substrates [15-18] have been thoroughly studied [1-4]. Gold has several attractive characteristics that makes it the substrate of choice. It is not very sensitive to contaminations and can thus be easily cleaned. The thiols strongly adsorb on gold and form densely packed monolayers [1,16,17,19-23]. Alkanethiols also passivate other metallic surfaces very effectively [1,24,25].

The order and coverage of SAMs are strongly dependent on the nature of the substrate, its morphology [1] and structure of the adsorbate. Functionalized alkanethiols on gold form well ordered monolayers whose composition, chemical and physical structures and thickness can be manipulated [23,26-31]. Short-chain alkanethiols form less stable and more

disordered monolayers [1,15,16,26,32-35]. The structures of short-chains (less than nine carbons) and long-chains (more than nine carbons) show some differences. Generally, as the chain length decreases, the structure becomes increasingly disordered with lower packing on gold. However, careful STM studies by Poirier et al. [18,36] and STM and IR-RAS studies by Rowntree et al. [20] show that even with short-chain systems, in which the chain-chain interactions are relatively weak, a comparable degree of surface ordering to those of the long chain systems can be achieved.

Adsorption from solution is believed to be governed by three processes. Firstly, alkanethiols adsorb rapidly. The chemisorption is exothermic (~ 160-190 kJ/mole) [1,37]. The sulfur binds more strongly to gold than other groups such as NH_2, OH, COOH, COOEt, $CONH_2$, Br, CN [1,6,16,38]. Secondly, the alkanethiol chains arrange themselves to maximize the van der Waals interactions between them. This is a slow exothermic ($\leq$ 40 kJ/mole) process which depends on the adsorbate [1,16]. Finally, there is a weak endothermic (approximately 3 kJ/mole) process due to the interactions between the terminal methyl groups (non-polar) and the air or a liquid interface.

Numerous techniques (see the characterization techniques in a later section) have been used to characterize SAMs. Most of them indicated the formation of well-defined, highly oriented, densely packed and very stable monolayers [1,39]. These interesting surface properties demonstrate the potential of applications in several important technological fields such as corrosion inhibitors [1,15,26,40,41], chemical sensors [42,43], optical imaging [1,15,26,40,41] and many others [1,15,26,40,41]. These model systems were also used in the study of fundamental electrochemical processes. Their potential applications in various areas such as corrosion control [25,44-46], electron-transfer processes [38,47-50], biological membranes [51-55], sensing devices [25,56-59] and many others [1,26,60-65] have been studied.

Examples of applications of these monolayers include: (1) Work on patterned substrates in which thiols selectively adsorb on photolithographically etched gold

microelectrodes [66,67] ; (2) Chemical sensors [42] ; (3) Protein adsorption. For example, Prime and Whitesides [52] used the molecular selectivity of the surface to study protein adsorption via co-adsorption of hydrophilic {hydroxy-, maltose-, and hexa(ethylene glycol)-} and hydrophobic {methyl-} terminated alkane thiols, in which the surfaces could be tailored to either reject or accept protein adsorption.

Corrosion is an important problem worldwide. There are several strategies for corrosion passivation, including deposition of thin passivating metal, metal oxide and organic coatings [68,69]. It has been shown that a densely packed monolayer of thiols can block electrochemical reactions and effectively reduce (passivate) the rate of corrosion [1,15,25,44,70]. Crooks and co-workers [71-73] have reported a series of studies on corrosion protection of thiols monolayer using spectroscopic, electrochemical, and STM methods. In the first report, they compared the CN–induced corrosion of bare gold and gold modified with a hexadecyl mercaptan monolayer. In the second report, they found that corrosion passivation is improved when underpotential deposition, UPD, of Cu on the gold surface before the adsorption of the thiols. In their most recent report, they examined the influence of changing the chain length and terminal function group on corrosion passivation of gold in acidic Br^- solutions. They concluded that monolayers are reoriented parallel to the surface during corrosion. They also found that thiols terminated with either OH or COOH passivate the gold surface more effectively than CH_3-terminated monolayers. They suggest that this effect is due to the fact that these thiols are more stable, mobile, and they form hydrogen bonds among themselves.

2. Comparison of Langmuir-Blodgett (LB) and Self-Assembled Monolayers

Langmuir-Blodgett monolayers are made by forming a monolayer film of surfactant molecules in a Langmuir trough. The molecules are forced to order on a liquid subphase by gradually increasing the surface pressure. The resulting film is then transferred to a solid substrate [1,61,74]. The Langmuir-Blodgett monolayers are well-ordered. However, the

procedure is difficult and restricted to certain molecules. Another limitation of such monolayers is their stability. The monolayer-substrate interaction is weak since the molecules are only physisorbed, and thus they are not very stable. In contrast thiols are strongly bound to the surface and should be more stable. However, the number of structures formed by SAMs of thiols is limited by the substrate since it determine the distance between the adsorbed thiols.

3. Characterization of SAMs

A variety of techniques have been used in the characterization of SAMs on gold (111) substrates. Optical ellipsometry [6,14-16,75,76], contact angle measurements [16,77], various electrochemical techniques [2-4,15,50,78-85], He-diffraction [86], atomic diffraction [87], low energy electron diffraction [88,89], high energy electron diffraction [77], X-ray electron and He-atom diffraction [35,41,90-94], reflection-absorption IR spectroscopy [15,76], FTIR-RAS/EQCM [95], Raman spectroscopy [96], XPS [33,88], FT-mass spectrometry [97], FTIR [14,15,45,77,96,98-100], AFM [76,101,102], STM [76,78,101-106], MDS [41,107-108], sum-frequency generation [109] and other more specialized methods [1,26,61,62].

As mentioned above three processes are involved in the formation of a self-assembled monolayer of thiols. They are shown in Fig. 1.1. We will now discuss each of these processes.

3.1 Gold-Sulfur bond :

X-ray photoelectron spectroscopy (XPS) measurements reported that the gold substrate-sulfur head group is strongly bound (~ 180 kJ/mol) and the monolayers formed are quite stable [110]. The gold-sulfur bond is believed to be covalent. Theoretical calculations suggest that thiols adsorb on three-fold hollow sites. Low- (LEED) and high (HEED) energy electron diffraction, scanning tunneling microscopy (STM) studies [38,41,78,111-113], atomic

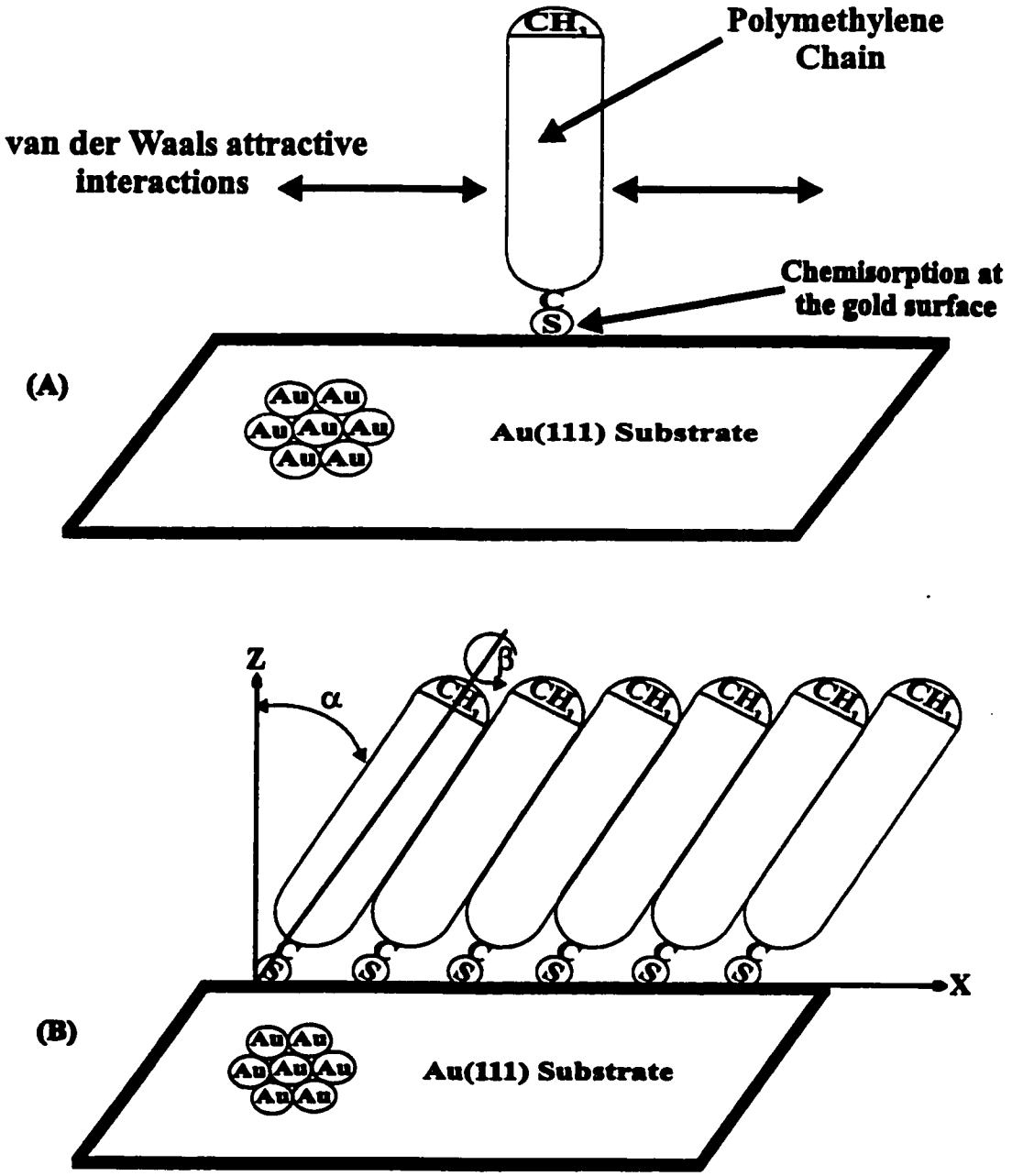

Figure 1.1 : Diagram of (a) a single alkane thiol molecule adsorbed onto a Au(111) single crystal electrode with the forces involved in the formation of a self-assembled monolayer ; (b) the tilt angle α and the twist angle β of all trans n-alkanethiolate molecules adsorbed onto a Au(111) surface.

force microscopy (AFM) studies [112] and He-atom diffraction [92] revealed that the monolayer forms a ($\sqrt{3}$ x $\sqrt{3}$)R30°overlayer structure on the underlying gold (111) surfaces. This structure is shown in Figure 1.2. The sulfur-sulfur distance is 4.99 Å between adjacent sulfur atoms. The sulfur atom diameter is 1.85 Å, meaning the spacing between adjacent sulfur atoms is approximately 3-times larger. The formation of a strong covalent bond between sulfur and gold causes the displacement of more weakly bound contaminants from the gold surface. The spontaneous formation of a 2-dimensional assembly is the result of the strong bonding of the sulfur to the gold surface and of the intermolecular interactions (mainly weak van der Waals interactions) [114].

3.2 Polymethylene structure :

Results from ellipsometry and differential capacitance [15,98], IR and Raman spectroscopy [77,88,115], molecular mechanics calculations [34], second harmonic generation [109], X-ray diffraction [91], near-edge X-ray absorption fine structure [116], molecular dynamics simulations [107], and surface potential [117] all reported that the chains are mostly in an all-trans configuration and tilted with respect to the surface normal. This arrangement gives rise to a linear correlation between the thickness of the monolayer and the chain length.

IR spectroscopy provides insight into the structure (i.e. orientation) of the polymethylene chains [118]. The position and width of the asymmetric CH_2 stretching vibration at 2918 cm^{-1} suggest that the chains are in a crystalline-like environment [96]. Deviations from this value (usually shifts to a higher frequency) are indicative of a larger number of gauche defects. The surface selection rule (described in the next chapter) has been used to calculate the orientation of the methylene chains. It was found that the molecular axis of an all-trans alkane chain is tilted ~ 25-30° [96,119] with respect to the surface normal. The rotation of the C-C-C plane about the plane formed by the molecular axis in the tilt direction is ~ 48°- 55° [41,88,96,98]. This suggests that the Au-S-C bond angle is near 120°. This result is compatible with an sp^2 hybridized sulfur atom. The tilt of the alkane chains was explained by the fact that the distance between the molecules is larger than in the optimal packing density of alkane

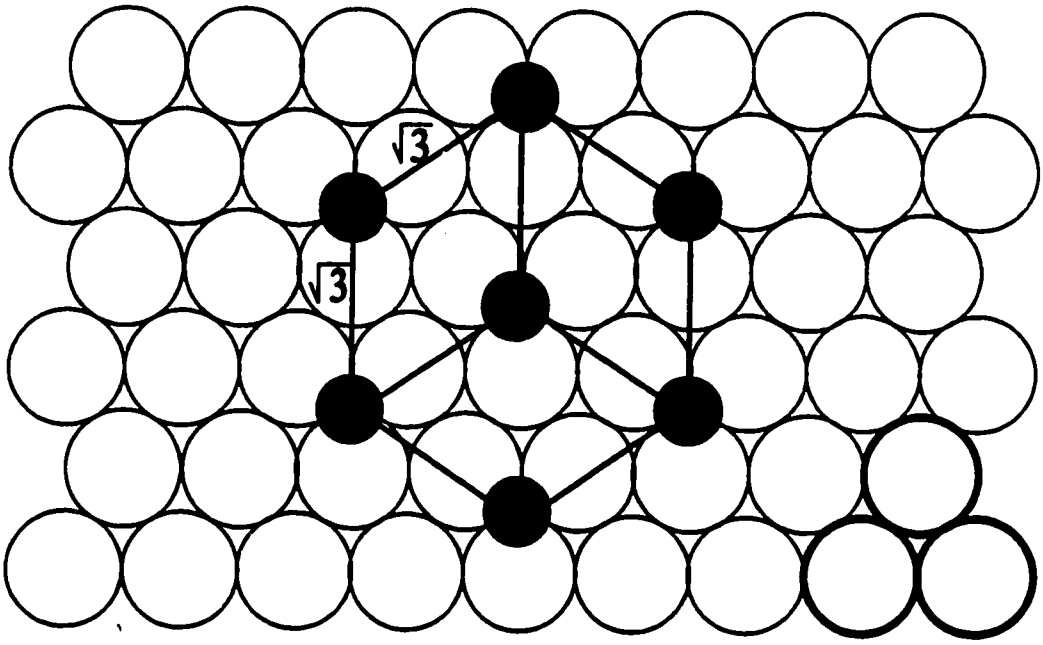

Figure 1.2 : Top view of the hexagonal gold (111) surface atom arrangement (open circles) and bound sulfur atom $(\sqrt{3} \times \sqrt{3})$ R 30° overlayer (black circles). The sulfur adsorbs on a three-fold site.

chains ($4.7x10^{-10}$ m). The molecules thus tilt in order to increase their interactions with each others.

3.3 Terminal groups :

Studies have shown that the addition of methylene groups to the alkane chains influences the orientation of the methyl-terminated group [77,96]. An odd-even chain length dependent orientation of the methyl group was observed. This effect was explained by the fact that the Au-S-C bond angle (which determines the orientation of the all-trans chain) is 120° for all alkanethiols. He-atom scattering, which is only sensitive to the outermost layer of surface atoms, revealed that chain-terminating methyl groups are ordered. Low energy He diffraction also indicates that as the chain length decreases the monolayer becomes increasingly disordered [92]. IR and molecular dynamics studies have indicated that at room temperature the concentration of gauche defects at the terminal methyl surface is greater than in the monolayer interior [120]. The surface of the SAM can be conveniently modified by using alkanethiols terminated with various groups, such as a carboxylic acid [27], ferrocene [121], azobenzene [122-124], and spiropyran [125]. The orientation of the functionalized groups have been determined in certain cases.

4. Characterization by Electrochemical Methods

Long-range electron transfer plays a very important role in many biological and technological processes. Rates of electron transfer depend on the reaction free energy, the distance between the acceptor and donor, and the molecular structure. Chidsey and co-workers [47,82] and Collard and Fox [126] carried out electrochemical studies of well-defined molecular organic thin films derived from the co-adsorption of an electroactive species, ferrocene, and methyl-terminated long-chain thiols onto gold electrodes. Chidsey [47] was able to measure both the forward and the backward electron transfer rates over a large range of potentials. He was able to determine the thermal activation and the electron tunneling parameters of the reaction separately. Other research group [127] showed that the electron

transfer rate decays exponentially with an increasing number of CH_2 groups. These data were in agreement with Marcus theory. These results will be discussed in Chapter 4.

Alkanethiol monolayers are resistant to ion penetration and form good barriers to electron transfer [128]. However, short chain thiol monolayers show more pinholes and the barrier properties are not as good as those of the longer chains. This influences the rate of the heterogeneous electron transfer [129,130]. Porter and co-workers [15] studied octadecanethiol SAMs on polycrystalline gold substrate via cyclic voltammetry. Their results showed that the fractional pinhole area is less than 6×10^{-6}. This group also characterized SAMs of different alkylthiols on gold. Their spectro-electrochemical measurements revealed that as the chain length increases, the coverage and the order increase providing substantial barriers to both electron and ion transfer processes [131].

Several electrochemical studies on the oxidation and reduction of alkanethiol self-assembled monolayers on gold surfaces [2,4,15] have been done. They revealed that both the oxidative- and reductive-removal of thiol monolayers depend strongly on the substrate crystallographic orientations, the pH and the scan rate. Alkanethiols were found to be reductively desorbed from the gold surface by a one-electron process [2,4,15,78,132]. Porter and co-workers [78,131,133] have done a series of studies of various alkanethiol SAMs chemically adsorbed onto different evaporated films of Au and Ag on mica which consists mostly of (111) domains or on Si or glass which form more disordered films. They modeled the capacitance of the electrical double layer at the electrode/SAM/electrolyte interface with two capacitors in series. A plot of the inverse of the double layer capacitance (1/C) as a function of the number of carbon atoms (N_c) of the hydrocarbon chain yields a straight line. These results were confirmed by another study [98]. According to equations (1) and (2), 1/C should increase linearly with N_c:

$$1/C = d/\epsilon\epsilon_o \qquad (1)$$

$$d = (1.3 \times 10^{-8}) N_c \cos \theta \qquad (2)$$

where d is the thickness (distance in cm) between adjacent carbons; ϵ is the dielectric constant of the SAM; ϵ_o is the free space permittivity [15]; θ is the angle between the molecular axis of the thiol and the surface normal. The charge associated with charging the double layer of a bare gold surface after the desorption was calculated to be ~ 18 ($\pm$ 2) $\mu C/cm^2$. The scan rate dependence on the amount of thiolates oxidatively redeposited was also measured. The higher the scan rate, the greater the redeposition since there is insufficient time for the species to diffuse away from the electrode surface.

The maximum reductive peak current, i_p, and the potential of this maximum peak current, E_p, were found to vary linearly with the scan rate. The reductive desorption peak potential shifts linearly to more negative potentials as the chain length increases. This behavior was assigned to the decrease of the potential drop across the sulfur head groups and the increase of the attractive interactions between methylene groups as the chain length increases. The effect of electrolyte composition was also examined for LiOH, NaOH and KOH. It revealed that a larger overpotential is required for initiating the desorption process in the order $K^+ < Na^+ < Li^+$. This was assigned to the higher solvation of the smaller ions which increase the energy required for going through the organic monolayer.

Self-assembled monolayers can also be formed by electrochemical deposition from aqueous solution containing thiolates [134-137]. The electrochemical method offers the advantages of being faster and allowing for a better control of the coverage obtained [134,135].

The solvent/thiol interaction influences the adsorption process. Lower surface coverages are observed in non-polar solvent. The lower coverages are due to the higher solubility of thiolates [138].

The solubility of the thiols also influence their electrochemistry. Reduced thiols with

less than 12 carbons give a single current peak and almost no oxidative redeposition is observed. Thiols with more than 12 carbons yield two reductive current peaks [3,133] and most of them remain physisorbed at the surface and can be oxidatively redeposited. The appearance of a fine structure in the voltammogram of the reduction of insoluble thiols is unclear. Two suggestions were made. The first one suggests that two domains with different packing densities are formed by the insoluble thiols. The difference in packing densities influences the ionic permeation and this would cause them to be reduced at different potentials. The other suggestion relates the two reductive peaks to the stabilization of a second adsorption site when the alkane chain is long enough [3]. When the thiols are not soluble, they can be quantitatively deposited by a positive-going potential scan [3,133]. This distinct property of insoluble thiols is interesting since they go from a chemisorbed state to a physisorbed state repetitively while remaining in an ordered state.

5. General Objectives of this Research

The main objectives of this work are :

1. To determine the mechanism of the reductive desorption and oxidative adsorption of insoluble thiols.
2. To examine the thermal stability of alkanethiol monolayers.
3. To determine if the thiol monolayers undergo phase transitions.

The first objective is relevant to the development of a protocol for the electrodeposition of a self-assembled monolayer. The advantages of such a protocol are numerous compared to the most commonly used spontaneous adsorption of thiols. The substrate can be electrochemically cleaned prior to the deposition of the adsorbates. The substrate cleanliness has been shown to influence the quality of the formed monolayers. Variable coverage can be obtained by a simple adjustment of the electrode potential. Selective reduction of adsorbates can help in the formation of mixed monolayers with new properties. The elucidation of this mechanism will also be useful in understanding the failure

of electrodes modified by the adsorption of SAMs. Finally we believe that the knowledge that we will gain can be applied to the electrochemistry of other organic thin films.

The second and third objectives are related to understanding the electrochemical behavior of SAM over a range of temperatures. Many applications of SAM will be as electro-sensors. It is important to establish if the sensitivity of such sensors would be influenced by a phase transition, partial desorption, etc....

To achieve these goals we used well-defined gold (111) single crystal electrodes. This should simplify the analysis of the electrochemical and spectroscopic data by restricting the number of possible adsorption sites and the structures that can be formed. We used a variety of electrochemical techniques to probe the SAMs under various conditions of pH and temperature. These techniques are described in the next chapter.

6. References

1. Ulman, A. An Introduction to Ultrathin Organic Films : from Langmuir-Blodgett to Self-Assembly ; Academic Press : New York, 1991.
2. Yang, D.-F.; Wilde, C. P.; Morin, M. Langmuir **1996**, 12, 6570.
3. Yang, D.-F.; Wilde, C. P.; Morin, M. Langmuir **1997**, 13, 243.
4. Yang, D.-F.; Al-Maznai, H.; Morin, M. J. Phys. Chem. **1997**, 101, 1158.
5. Byloos, M.; Al-Maznai, H.; Morin, M. J. Phys. Chem. B accepted.
6. Whitesides, G. M.; Laibinis, P. E. Langmuir **1990**, 6, 87.
7. Feast, W. J.; Munro, H. S., Eds.; Polymer Surfaces and Interfaces ; John Wiley & Sons : New York, 1987.
8. Andrade, J. D. Ed., Surfaces and Interfacial Aspects of Biomedical Polymers ; Plenum Press : New York, 1985.
9. Holmes-Farley, S. R.; Reamey, R. H.; McCarthy, T. J.; Deutch, J.; Whitesides, G. M. Langmuir **1985**, 1, 725.

10. Cherry, B. W. Polymer Surfaces ; Cambridge University Press : Cambridge, 1981.
11. Holmes-Farley, S. R.; Reamey, R. H.;Nuzzo, R. G.; McCarthy, T. J.; Whitesides, G. M. Langmuir **1987**, 3, 799.
12. Adamson, A. W. Physical Chemistry of Surfaces ; John Wiley & Sons : New York, 1982.
13. Miller. W. J.; Abbott, N. L. Langmuir **1997**, 13, 7106.
14. Nuzzo, R. G.; Allara, D. L. J. Am. Chem. Soc. **1983**, 105, 4481.
15. Porter, M. D.; Bright, T. B.; Allara, D. L.; Chidsey, C. E. D. J. Am. Chem. Soc. **1987**, 109, 3559.
16. Bain, C. D.; Troughton, E. B.; Tao, Y.-T.; Evall, J.; Whitesides, G. M.; Nuzzo, R. G. J. Am. Chem. Soc. **1989**, 111, 321.
17. Poirier, G. E.; Tarlov, M. J. Langmuir **1994**, 10, 2853.
18. Poirier, G. E.; Tarlov, M. J.; Rushmeier, H. Langmuir **1994**, 10, 3383.
19. Nuzzo, R. G.; Fusco, F. A.; Allara, D. L. J. Am. Chem. Soc. **1987**, 109, 2358.
20. Truong, K. D.; Rowntree, P. A. J. Phys. Chem. **1996**, 100, 19917.
21. Sato, Y.; Haba, T.; Uosaki, K. Langmuir **1996**, 12, 2726.
22. Bain, C. D.; Whitesides, G. M. Angew. Chem. Int. Ed. Engl. **1989**, 28, 506.
23. Fox, M. A.; Wooten, M. D. Langmuir **1997**, 13, 7099.
24. Al-Mohamed, A.; Smith, C. W.; Al-Saffar, I. S.; Slifkin, M. A. Thin Solid Films **1990**, 189, 175.
25. Swalen, J. D.; Allara, D. L.; Andrade, J. D.; Chandross, E. A.; Garoff, S.; Israelachvili, J.; McCarthy, T. J.; Murray, R.; Pease, R. F. ; Rabolt, K. J.; Wynne, K.J. ; Yu, H. Langmuir **1987**, 3, 932.
26. Ulman, A. Chem. Rev. **1996**, 96, 1533.
27. Kim, T.; Crooks, R. M.; Tsen, M.; Sun, L. J. Am . Chem. Soc. **1995**, 117, 3963.
28. Green, J. B.; McDermott, M. T.; Porter, M. D.; Sperko, L. M. J. Phys. Chem. **1995**, 99, 10960.
29. Mueller, W. T.; Klein, D. L.; Lee, T.; Clarke, J.; McEuen, P. L.; Schultz, P. G. Science **1995**, 268, 272.

30. Everett, W. R.; Fritsch-Faules, I. Anal. Chim. Acta **1995**, 307, 253.
31. Xu, S.; Liu, G.-Y. Langmuir **1997**, 13, 127.
32. Ohtake, T.; Mino, N.; Ogawa, K. Langmuir **1992**, 8, 2081.
33. Nuzzo, R. G.; Dubois, L. H.; Allara, D. L. J. Am. Chem. Soc. **1990**, 112, 558.
34. Ulman, A.; Eilers, J. E.; Tillman, N. Langmuir **1989**, 5, 1147.
35. Fenter, P.; Eisenberger, P.; Liang, K. S. Phys. Rev. Lett. **1993**, 70, 2447.
36. Poirier, G. E.; Tarlov. M. J. J. Phys. Chem. **1995**, 99, 10966.
37. Dubois, L. H.; Zegarski, B. R.; Nuzzo, R. G. J. Am. Chem. Soc. **1990**, 112, 570.
38. Chidsey, C. E. D.; Loiacono, D. N. Langmuir **1990**, 6, 682.
39. Tamada, K.; Hara, M.; Sasabe, H.; Knoll, W. Langmuir **1997**, 13, 1558.
40. Whitesides, G. M.; Folkers, P. J.; Zerkowski, J. A.; Laibinis, P. E.; Seto, C. T. J. Am. Chem. Soc. **1992**, 114, 6156.
41. Strong, L.; Whitesides, G. M. Langmuir **1988**, 4, 546.
42. Hickman J. J.; Ofer, D. E.; Laibinis, P. E.; Whitesides, G. M.; Wrighton, M. S. Science **1991**, 252, 688.
43. Kepley, L. J.; Crooks, R. M.; Ricco, A. J. Anal. Chem. **1992**, 64, 3191.
44. Laibinis, P. E.; Whitesides, G. M. J. Am. Chem. Soc. **1992**, 114, 9022.
45. Chailapakul, O.; Sun, L.; Xu, C.; Crooks, R. M. J. Am. Chem. Soc. **1993**, 115, 12459.
46. Banga, R.; Yarwood, J.; Morgan, A. M. Langmuir **1995**, 11, 4393.
47. Chidsey, C. E. D. Science **1991**, 251, 919.
48. Becka, A. M.; Miller, C. J. J. Phys. Chem. **1992**, 96, 2657.
49. Becka, A. M.; Miller, C. J. J. Phys. Chem. **1993**, 97, 6233.
50. Badia, A.; Back, R.; Lennox, R. B. Angew. Chem. Int. Ed. Engl. **1994**, 33, 2332.
51. Waldbilling, R. C.; Robertson, J. D.; McIntosh, T. J. Biochim. Phiophys. Acta **1976**, 448, 1-14.
52. Prime, K. L.; Whitsides, G. M. Science **1991**, 252, 1164.
53. Johnsson, B.; Lofas, S.; Lindqvist, G. Anal. Biochem. **1991**, 198, 268.
54. DiMilla, P. A. J. Am. Chem. Soc. **1994**, 116, 2225.

55. Cohen, S. R.; Naaman, R.; Sagvi, J. J. Phys. Chem. **1986**, 90, 3054.

56. Frisbie, C. D.; Martin, J. R.; Duff, R. R.; Wrighton, M. S. J. Am. Chem. Soc. **1992**, 114, 7142.

57. Gardner, T. J.; Frisbie, C. D.; Wrighton M. S. J. Am. Chem. Soc. **1995**, 117, 6927.

58. Kumar, A.; Biebuyck, H. A.; Whitesides, G. M. Langmuir **1994**, 10, 1498.

59. Schwartz, D. K.; Steinberg, S.; Israelachvili, J.; Zasadzinski, J. A. N. Phys. Rev. Lett. **1992**, 69, 3354.

60. Allara, D.L. Biosens. Bioelectron. **1995**, 10, 771.

61. Dubois, L. H.; Nuzzo, R. G. Annu. Rev. Phys. Chem. **1992**, 43, 437.

62. Poirier, G. E. J. Vac. Sci. Technol. B **1996**, 14, 1453.

63. Lopez, G. P.; Albers, M. W.; Schreiber, S. L.; Carroll, R.; Peralta, E.; Whitesides, G. M. J. Am. Chem. Soc. **1993**, 115, 5877.

64. Cooper, E.; Wiggs, R.; Hutt, D. A.; Parker, L.; Leggett, G. J.; Parker, T. L. J. Mater. Chem. **1997**, 7, 435.

65. Tidswell, C. D.; Ertel, S. I.; Ratner, B. D.; Tarasevich, B.; Atre, S.; Allara, D. L. Langmuir **1997**, 13, 3404.

66. Laibinis, P. E.; Hickman, J. J.; Wrighton, M. S.; Whitesides, G. M. Science **1989**, 245, 845.

67. Hickman, J. J.; Ofer, D. E.; Zou, C.; Wrighton, M. S.; Laibinis, P. E.; Whitesides, G. M. J. Am. Chem. Soc. **1991**, 113, 1128.

68. Fundamental Aspects of Corrosion Protection by Surface Modification ; McCafferty, E.; Clayton, C. R., Eds.; The Electrochemical Society : Pennington, NJ. 1984, Vol. 84, p.355.

69. Fontana, M. G.; Green, N. O. Corrosion Engineering, 2nd Ed.; McGraw-Hill : New York, 1978, p. 465.

70. Yamamato, Y.; Nishihara, H.; Aramake, K. J. Electrochem. Soc. **1993**, 140, 436.

71. Li, Y.-Q.; Chailapakul, O.; Crooks, R. M. J. Vac. Sci. Technol. B **1995**, 13, 1300.

72. Zamborini, F. P.; Crooks, R. M. Langmuir **1997**, 13, 122.

73. Zamborini, F. P.; Crooks, R. M. Langmuir **1998**, 14, 3279.

74. Gaines, G. L. Insoluble Monolayers at Liquid-Gas Interfaces ; John Wiley & Sons : New York, 1966.

75. Truong, K. D.; Rowntree, P. A. J. Phys. Chem. **1996**, 100, 19917.

76. Alves, C. A.; Smith, E. L.; Porter, M. D. J. Am. Chem. Soc. **1992**, 114, 1222.

77. Laibinis, P. E.; Whitesides, G. M.; Allara, D. L.; Tao, Y.-T.; Parikh, A. N.; Nuzzo, R. G. J. Am. Chem. Soc. **1991**, 113, 7152.

78. Widrig, C. A.; Chung, C.; Porter, M. D. J. Electroanal. Chem. **1991**, 310, 335.

79. Li, T. T.; Weaver, M. J. J. Am. Chem. Soc. **1984**, 106, 6107.

80. Sabatini, E.; Rubinstein, I.; Maoz, R.; Sagiv, J. J. Electroanal. Chem.**1987**, 219, 365.

81. Finklea, H. O.; Avery, S.; Lynch, M.; Furtsch, T. Langmuir **1987**, 3, 409.

82. Chidsey, C. E. D.; Bertozzi, C. R.; Putvinski, T. M.; Mujsec, A. M. J. Am. Chem. Soc. **1990**, 112, 4301.

83. Miller, C.; Cuendet, P.; Gratzel, M. J. Phys. Chem. **1991**, 95, 877.

84. Popenoe, D. D.; Deinhammer, R. S.; Porter, M. D. Langmuir **1992**, 8, 2521.

85. Creager, S. E.; Hockett, L. A.; Rowe, G. K. Langmuir **1992**, 8, 854.

86. Chiang, S. Science **1996**, 272, 1123.

87. Bryant, M. A.; Pemberton, J. E. J. Am. Chem. Soc. **1991**, 113, 3629.

88. Butt, Hans-Jurgen.; Seifert, K.; Bamberg, E. J. Phys. Chem. **1993**, 97, 7316.

89. Fenter, P.; Eberhardt, A.; Eisenberger, P. Science **1994**, 266, 1216.

90. Tidswell, I. M.; Ocko, B. M.; Pershan, P. S.; Wasserman, S. R.; Whitesides, G. M. ; Axe, J. D. Phys. Rev. B **1990**, 41, 1111.

91. Samont, M. G.; Brown, C. A.; Gordon II, J. G. Langmuir **1991**, 7, 437.

92. Chidsey, C. E. D.; Liu, G.-Y.; Rowntree, P.; Scoles, G. J. Chem. Phys. **1989**, 91, 4421.

93. Camillone III, N.; Chidsey, C. E. D.; Liu, G.-y.; Putvinski, T. M. and Scoles, G. J. Chem. Phys. **1991**, 94, 8493.

94. Toennies, T. P. J. Vac. Sci. Technol. **1987**, A5, 440.

95. Dubois, L. H.; Zegarski, B. R. J. Chem. Phys. **1993**, 98, 678.

96. Nuzzo, R. g.; Zegarski, B. R.; Dubois, L. H. J. Am. Chem. Soc. **1987**, 109, 733.

97. Gorman, C. B.; Biebuyck, H. A.; Whitesides, G. M. Langmuir **1995**, 11, 2242.

98. Nuzzo, R. G.; Korenic, E. M.; Dubois, L. H. J. Chem. Phys. **1990**, 93, 767.

99. Stole, S. M.; Porter, M. D. Langmuir **1990**, 6, 1199.

100. Tillman, N.; Ulman, A.; Penner, T. L. Langmuir **1989**, 5, 101.

101. Pylant, E. D. Science **1996**, 272, 1145.

102. Haussling, L.; Michel, B.; Ringsdorf, H.; Rohrer, H. Angew. Chem. Int. Ed. Engl. **1991**, 30, 569.

103. Widrig, C. A.; Alves, C. A.; Porter, M. D. J. Am. Chem. Soc. **1991**, 113, 2805.

104. Kim, Y.-T.; Bard, A. J. Langmuir **1992**, 8, 1096.

105. Schonenberger, C.; Sondag-Huthorst, J. A. M.; Jorritsima, J.; Fokkink, L. G. J. Langmuir **1994**, 10, 611.

106. Delamarche, E.; Michel, B.; Gerber, Ch.; Anselmetti, D.; Guntherodt, H.-J.; Wolf, H.; Ringsdorf, H. Langmuir **1994**, 10, 2869.

107. Hautman, J.; Klein M. L. J. Chem. Phys. **1989**, 91, 4994.

108. Mar, W.; Klein, M. L. Langmuir **1994**, 91, 188.

109. Harris, A. L.; Chidsey, C. E. D.; Levinos, N. J.; Loiacono, D. N. Chem. Phys. Lett. **1987**, 141 (4), 350.

110. Nuzzo, R. G.; Zergarski, B. R.; Dubois, L. H. J. Am. Chem. Soc. **1989**, 109, 733.

111. Widrig, C. A.; Alves, C. A.; Porter, M. D. J. Am. Chem. Soc. **1991**, 113, 2805.

112. McDermott, C. A.; McDermott, M. T.; Green, J.-B.; Porter, M. D. J. Phys. Chem. **1995**, 99, 13257.

113. Sellers, H.; Ulman, A.; Shnidman, Y.; Eilers, J. E. J. Am. Chem. Soc. **1993**, 115, 9389.

114. Sabaathy, R. C.; Bhattacharyya, S.; Leavy, M. C.; Cleland, W. E. Jr.; Hussey, C. L. Langmuir **1998**, 14, 124.

115. Bryant, M. E.; Pemberton, J. E. J. Am. Chem. Soc. **1991**, 113, 8284.

116. Hahner, G.; Kinzler, M.; Thummler, C.; Woll, Ch., Grunze, M. J. Vac. Sci. Technol. A **1991**, 10, 2758.

117. Evans. S. D.; Ulman, A. Chem. Phys. Lett. **1990**, 170, 462.

118. Dubois, L. H.; Zegarski, B. R. Electron Spectrosc. Rel. Phenom. **1990**, 54/55, 1143.
119. Parikh, A. N.; Allara, D. L. J. Chem. Phys. **1992**, 96, 927.
120. Hautman, J.; Klein, M. L. J. Chem. Phys. **1990**, 93, 7483.
121. Rowe, G. K.; Creager, S. E. Langmuir **1993**, 7, 2307.
122. Wolf, H.; Ringsdorf, H.; Delamarche, E.; Takami, T.; Kang, H.; Michel, B.; Gerber, Ch.; Jaschke, M.; Butt, H.-J.; Bamberg, E. J. Phys. Chem. **1995**, 99, 7102.
123. Takami, T.; Delamarche, E.; Michel, B.; Gerber, Ch.; Wolf, H.; Ringsdorf, H. Langmuir **1995**, 11, 3876.
124. Caldwell, W. B.; Campbell, D. J.; Chen, K. M.; Herr, B. R.; Mirkin, C. A.; Durbin, M. K.; Dutta, P.; Huang, K. G. J. Am. Chem. Soc. **1995**, 117, 6071.
125. Willner, I.; Blonder, R.; Dagan, A. J. Am. Chem. Soc. **1994**, 116, 9365.
126. Collard, D. M.; Fox, M. A. Langmuir **1991**, 7, 1192.
127. Finklea, H. O.; Hanshew, A. A. J. Chem. Soc. **1992**, 114, 3173.
128. Weisshaar, D. E.; Walczak, M. M.; Porter, M. D. Langmuir **1993**, 9, 323.
129. Narayamurty, V. Science **1987**, 235, 1023.
130. Stewart, K. R.; Whitesides, G. M.; Godfried, H. P.; Silvera, I. F. Surf. Sci. **1986**, 57, 1381.
131. Walczak, M. M.; Alves, C. A.; Lamp, B. D.; Porter, M. D. J. Electoanal. Chem. Soc. **1995**, 396, 103.
132. Lipkowski, J. Ion and Electron Transfer across Monolayers of Organic Surfactants. In Modern Aspects of Electrochemistry; Conway, B. E.; Bockris, J. O'M.; White, R. E. Eds.; Plenum Press : New York, 1992, Vol. 23, pp. 1-99.
133. Zhong, C.-J.; Porter, M. D. J. Electoanal. Chem. Soc. **1997**, 425, 147.
134. Weisshaar, D. E.; Lamp, B. D.; Porter, M. D. J. Am. Chem. Soc. **1992**, 114, 5860.
135. Hatchett, D. W.; Uibel, R. H.; Stevenson, K. J.; Harris, J. M.; White, H. S. J. Am. Chem. Soc. **1998**, 120, 1062.
136. Hatchett, D. W.; Stevenson, K. J.; Lacy, W. B.; Harris, J. M.; White, H. S. J. Am. Chem. Soc. **1997**, 119, 6596.
137. Stevenson, K. J.; Mitchell, M.; White, H. S. J. Phys. Chem. B **1998**, 102, 1235.
138. Schneider, T. W.; Buttry, D. A. J. Am. Chem. Soc. **1993**, 115, 12391.

Chapter 2

Experimental

This chapter contains information concerning the preparation of the single crystal gold electrodes, the design of the electrochemical cell and the specifications of the chemicals, solvents, water, and purging gases used in this work. The techniques used in the experiments are also described.

1. Preparation of Gold Single Crystal Electrodes

1.1 Crystallography :

Gold is a face-centered cubic (f.c.c) solid. We determine the orientation of the plane of interest with X-ray diffraction. The stereographic projection shown in Figure 2.1 gives the angles between crystallographic planes. The crystallographic planes are expressed in term of Miller indices. A unit projection stereographic triangle [1-5] for cubic crystals such as Au, Ag, Pt, Cu, Pd, is shown in Figure 2.1b. This allows for the orientation of the crystal along the desired crystallographic plane.

In this thesis, studies on the (111) plane of gold are reported. This choice was made because the (111) surface is the most commonly used substrate for alkanethiols. Gold (111) is the least reactive of the low Miller index planes. It has a hexagonal symmetry and is the most densely packed surface as shown in Figure 2.2. The nearest neighbor distance is 4.9 $x10^{-10}$ m. Surface reconstructions of the three low index gold faces [5-10] induced by the electric field have been reported. On gold(111) this reconstruction is small and consists of a slight expansion of the unit cell of gold.

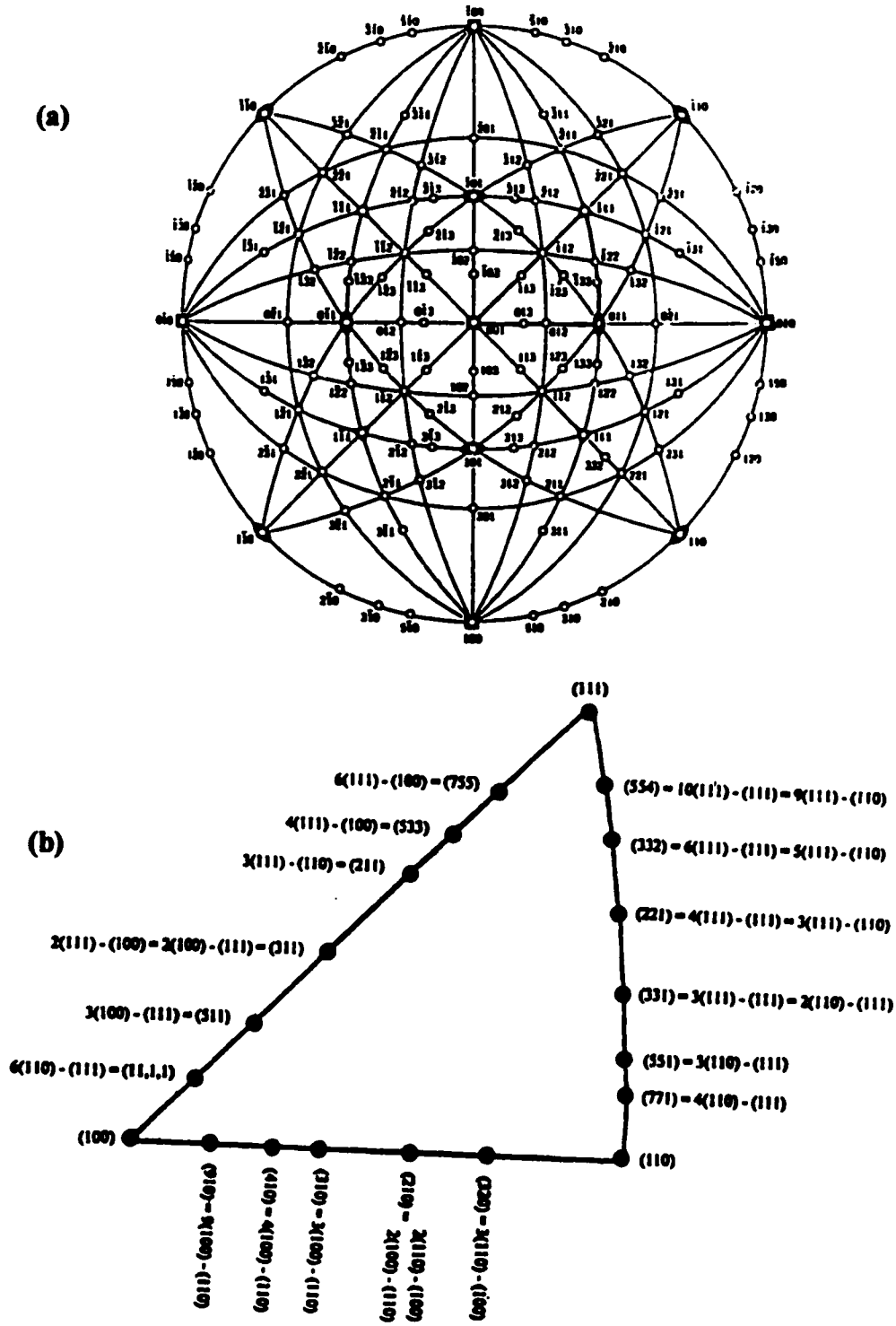

Figure 2.1 : (a) Standard (001) stereographic projection and (b) the unit face projected stereographic triangle for a f.c.c solid with the (100) at the center of the projection [From Refs. 3 and 4].

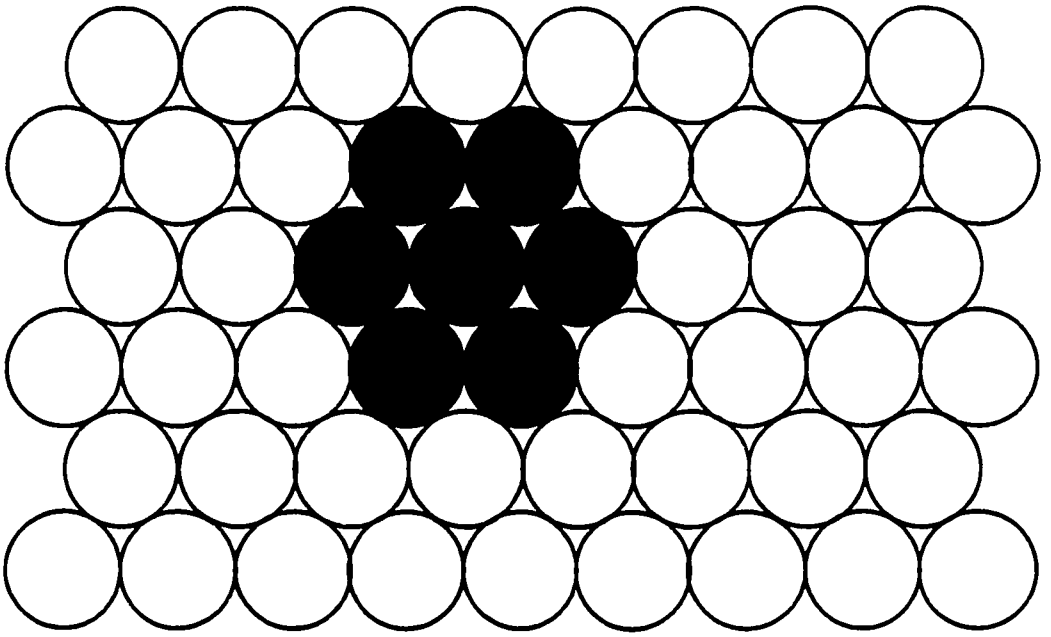

Figure 2.2 : Top view of the hexagonal gold (111) surface atom arrangements.

1.2 Cleaning of the gold :

Gold (Alfa Aesar, Puratronic grade(99.9985 %)) was purchased from Johnson Matthey. About 6.0 and 8.0 grams were used, cut into very small pieces and rinsed thoroughly with de-ionized distilled water, then etched in aqua regia for about 5-10 min in order to remove any surface impurities and then rinsed thoroughly with Milli-Q water. The nuggets are then put in a graphite crucible with a bell shape. The diameter of the crucible is approximately 8.0 mm.

1.3 Melting gold in an inductive furnace :

The furnace set-up consists of a power amplifier, a frequency generator (FG) and a vacuum pump. The crucible was put in a quartz tube. This tube was then pumped down to a pressure of a few milliTorr. Melting begins by setting the FG between 60-65 kHz. Then the power is increased at a rate of 50 watts/min from 500 watts to 1350 watts. The gold nuggets are melted at this power. The gold was kept melted for 10-15 min to ensure complete melting of the gold nuggets and to get rid of air bubbles. The next step is the cooling of the sample. This step is very crucial. It needs to cool down very slowly (especially between 1350 and 1000 watts) by step of about 25 watts every 4 minutes to allow for a proper crystallization. Once the crystallization has been initiated the power is decreased by steps of 100 watts every 2 minutes.

1.4 Gold single crystal orientation by X-ray diffraction :

The crystal is first etched in aqua regia for ~ 5-10 min then rinsed thoroughly with deionized distilled water and checked for any appearance of different domains. The grain boundaries are etched at different rates and become visible. In the absence of grain boundaries, an X-ray diffraction pattern is recorded to determine the crystallographic orientation of the top most surface. When a (111) surface is obtained, further alignment of the crystal is done using the method described by Hamelin [3]. First the crystal is placed in a plastic holder and secured in place using high melting point wax. The plastic holder was then inserted in a goniometer and adjusted parallel to the goniometer surface by means of four

screws. One complete turn (360°) of a screw corresponds to a change of 2° in the crystal surface. The goniometer was mounted in a holder and the crystallographic orientation of its main axis is determined from its X-ray diffractogram. The accuracy of the orientation is ± 0.5° of the desired plane. The Laüe X-ray diffraction pattern is recorded on a film in a lightproof holder mounted normal to the X-ray beam a few centimeter before the crystal. The radiation from a tube with a copper target bombarded by electrons with an acceleration voltage of 40 kV is used. The X-rays at well-defined energies are generated from the relaxation of valence electrons to core levels [1]. The beam of X-rays is then directed to the crystal. The X-rays are scattered by the gold atoms. When certain geometrical conditions are fulfilled, the monochromatic X-rays interfere constructively and give rise to a diffraction spot. This is illustrated in Figure 2.3. X-rays (1) and (2) reflect from atomic planes which are a distance d apart. Only if the distance traveled by X-ray (2) is an integral number of wavelengths greater than the distance traveled by X-ray (1) do the beams interfere constructively. So, from Figure 2.3, this occurs when :

$$AB = BC \qquad (1)$$

$$\sin \theta = AB/d \qquad (2)$$

therefore $$AB = d \sin \theta \qquad (3)$$

If n is an integer and λ is the wavelength of the X-rays :

$$2d \sin \theta \, (AB+BC) = n \lambda \qquad (4)$$

Equation 4 is known as the Bragg equation [1].

Prominent features of Laüe X-ray photographs are ellipses of spots originating from various planes belonging to an individual zone. All Laüe X-ray spots lie on conic sections.

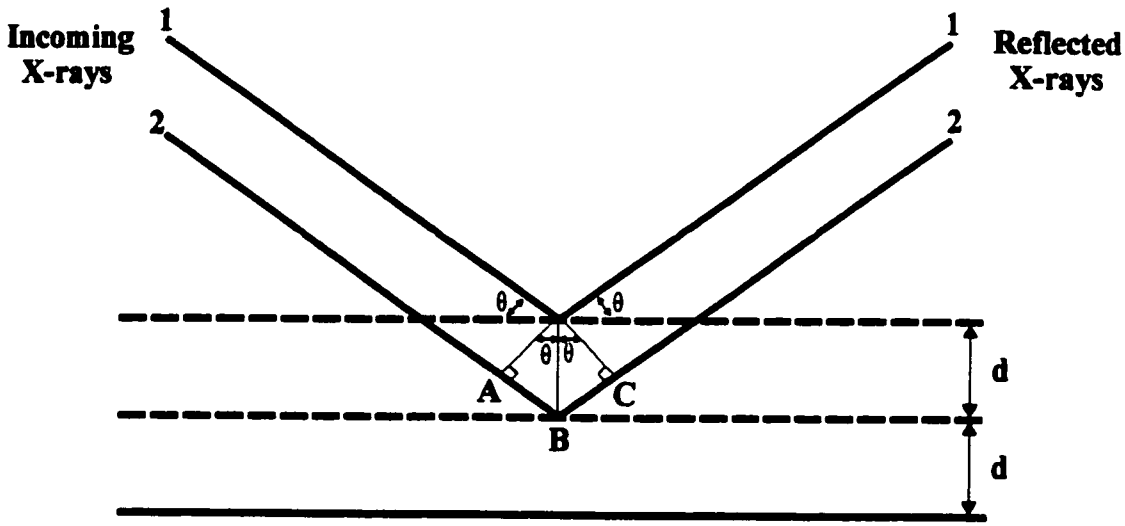

Bragg equation $n\lambda = 2d \sin\theta$

Figure 2.3 : Diffraction of X-rays from plane of atoms giving rise to diffraction maxima.

A straight line of spots signifies a zone axis normal to the beam. We only look at the X-ray scattering in the backward direction so scattering is mainly from an atomic plane perpendicular to the direction of the X-rays. In this way, we can determine the crystallographic plane perpendicular to the direction of the X-ray and use it as the electrode surface. We used a so-called Greninger net to analyze the diffraction pattern. A Greninger net is a projection of a sphere on a flat surface. This is necessary because the film is on a flat surface. The diffraction pattern of a gold (111) surface has the same 3-fold symmetry as that shown in Figure 2.2.

1.5 Mechanical polishing of the gold single crystal surface :

Once the orientation has been determined from the X-ray diffractogram, the single crystal is ready for mechanical polishing. The polishing of the single crystal is performed by holding the goniometer up-side-down so that the crystal is normal to the surface of a high quality polishing silicon carbide paper (Struers) positioned and wetted (Milli-Q water) on a flat plexiglass surface. Polishing begins with silicon carbide grinding papers of three different grades, 1200, 2400 and then 4000 grade, until the gold surface is very smooth (with a minimum of very small scratches). This is followed by polishing the gold surface with 6, 1 and 0.1 micron diamond suspensions (Buehler) to a mirror finish. The gold single crystal was sonicated (Sonicator 2210 Branson) between polishing-steps to remove the polishing material.

The gold (111) single crystal electrode in the plastic holder is removed from the goniometer. The wax is dissolved in chloroform for about 5-10 min. A gold wire (0.5 mm dia., 99.999 %, Johnson Matthey Company) is then attached to the gold single crystal stem.

1.6 Electrochemical polishing of the gold single crystal surface :

The gold single crystal was then electrochemically polished (in order to remove the first few gold layers perturbed by the mechanical polishing) in 1 M $HClO_4$ (Seastar Chemicals) for about ~ 6 - 10 min at a total current density of 100 mA/cm^2 (PINE Model AFRDE5, potentiostat/galvanostat) and dipped several times in a ~ 10 - 20 % HCl solution

(to remove the gold oxide formed) and rinsed thoroughly with Milli-Q water every 2 minutes.

1.7 Flame annealing of the gold single crystal surface :

Flame annealing in a natural gas was performed in order to eliminate any surface stress and to allow gold surface atoms to arrange themselves smoothly. The gold single crystal was heated in a flame with continuous horizontal rotational motions for a few minutes. The crystal was removed from the flame and allowed to cool down in air for about one minute and then sprayed with Milli-Q water.

1.8 Cyclic voltammetry :

A cyclic voltammogram is considered to be a "fingerprint". The electrochemical double layer region, the formation of a monolayer of oxide and its subsequent reduction and the beginning of the reduction of protons of the solvent [4,5] is characteristic of the electrode orientation. Voltammograms are used to check our gold single crystal electrodes. We recorded a cyclic voltammogram of Au(111) in 0.1 M $HClO_4$ (Figure 2.6). It is identical to the voltammogram reported by Hamelin et al.[4] which is accepted as indicating that the electrode is a well-ordered Au(111) substrate.

2. Chemicals, Water, Electrolytes, Purging Gases and Glassware

2.1 Chemicals, water and electrolyte solutions :

Butanethiol (99 + %), hexanethiol (95 %), nonanethiol (95 %), dodecanethiol (98 %), hexadecanethiol (92 %), and octadecanethiol (98 %) were purchased from Aldrich and tetradecanethiol () 98 %) from Fluka and were all used as received. Ethanol (OmniSolv grade) was the solvent.

Potassium hydroxide (99.99 %, semiconductor grade) and lithium hydroxide(99.95 %) were purchased from Aldrich and were used as received. Potassium perchlorate (ACS certified from Fisher Scientific) was recrystallized twice in water (resistivity of 18.2 Mωcm).

Potassium ferricyanide was used as received and both were purchased from BDH Chemicals. Sodium fluoride was of Suprapure grade from MERCK. Perchloric acid was from Seastar Chemicals Inc.

All the electrolyte solutions used were dissolved in water obtained from a Milli-Q purification system. The electrolyte solutions were degassed with argon or nitrogen to remove oxygen for about 15 min before starting the measurements. Argon or nitrogen was allowed to flow over the solution at all times.

2.2 Purging gases :

Argon gas (99.9993 %V, Air product Canada Ltd.) was used as received while nitrogen gas from the evaporation of a liquid nitrogen tank was purified to remove oxygen (Matheson gas products). We found no trace of oxygen in our measurements as shown in Figures 2.4 and 2.6. Oxygen reduction would be visible as a negative current increasing rapidly as the potential is scanned in the negative direction.

2.3 Glassware cleaning:

All glassware were cleaned by putting them in boiling concentrated sulfuric acid (98 %) for about 1-2 hours. It was then rinsed throughly with a Milli-Q pure water (18.2 MΩcm) before each experiment to remove any organic contaminants.

3. Electrodes and Electrochemical Cell

We used a three electrode system. The current flows between the working and the counter electrode. The current is limited by the size of the working electrode. The reference electrode is used to fix the potential applied to the working electrode relative to the reversible potential of this electrode.

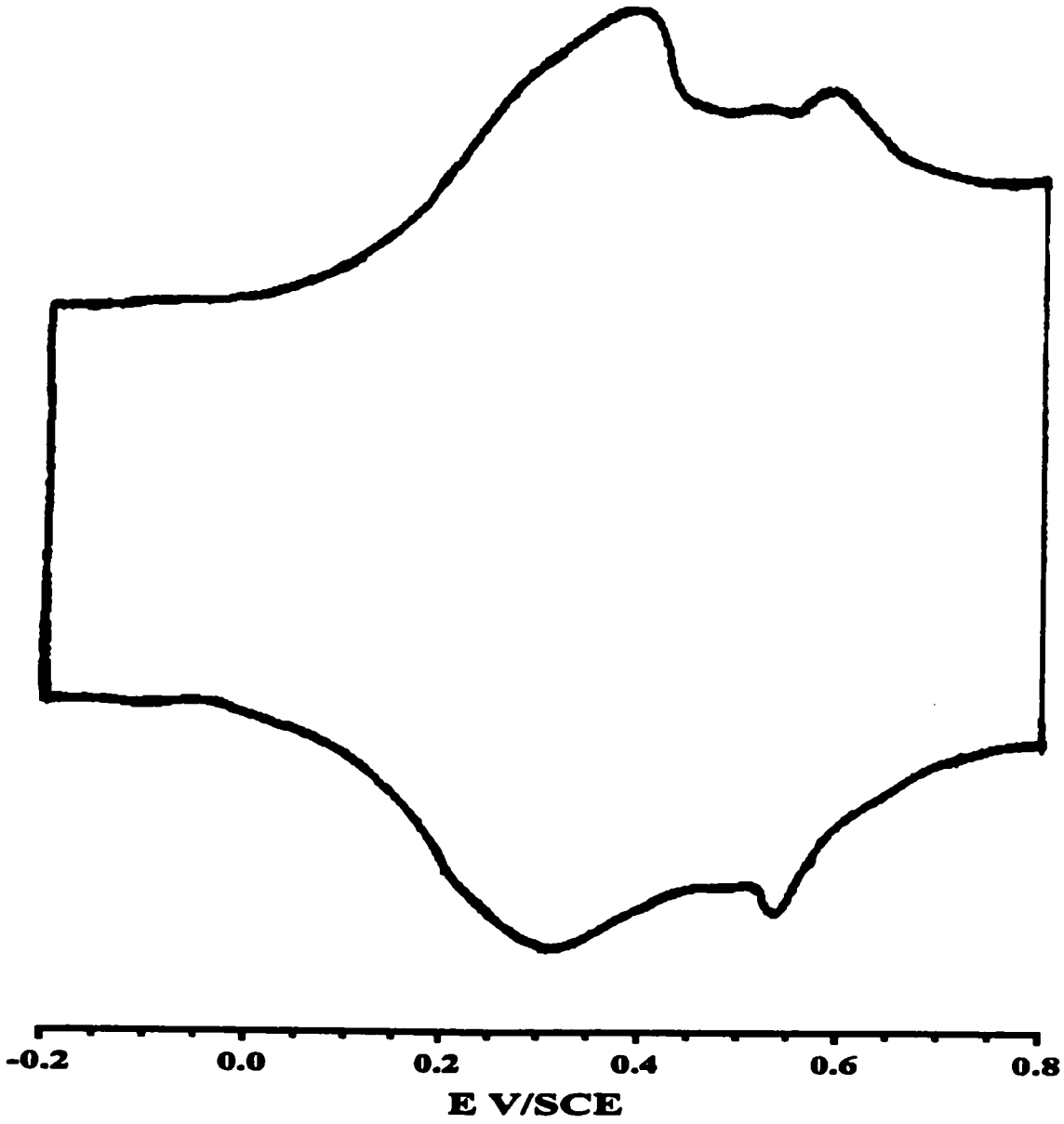

Figure 2.4 : Voltammogram of the double layer of a bare gold (111) single crystal electrode recorded in 0.1 M $HClO_4$ at a potential scan rate of 20 mV/s.

3.1 Counter electrode :

A counter electrode of the same material as the working electrode is preferred during electrochemical investigations on gold, platinum etc [11]. This prevents possible dissolution of the counter electrode material which could deposit on the working electrode [11]. Thus, the counter electrode was a 1 mm (diameter) gold wire (Premion gold Alfa Aesar grade 99.9985 % purchased from Johnson Matthey) in a coiled-shaped in order to maximize the surface area.

3.2 Reference electrode :

The reference electrode was a saturated calomel electrode (SCE) (Corning products). It was housed in an external compartment connected to the main compartment through a porous glass frit and a so-called Luggin capillary, as shown in Figure 2.5. This prevents chlorine contamination. Attention must be given to the problem of the ohmic drop in solution by a quantity iR_u, where R_u is the solution, or uncompensated, resistance between the working electrode and the position of the reference electrode. R_u is reduced to a small value by using a Luggin capillary. The tip of the Luggin is positioned close to the working electrode, and thus R_u is reduced significantly.

3.3 Working electrode :

The working electrodes were gold (111) single crystal electrodes with geometric areas of 0.71 and 0.64 cm^2, respectively.

3.4 Electrochemical cells :

A conventional three-electrode cell was used and is shown in Figure 2.5. The electrochemical cell was enclosed in a grounded Faraday cage, whereas for temperature-dependance study (see Chapters 4 and 5), the electrochemical cell was enclosed in a thermostated water bath (Model 1180A, VWR Scientific Co.). A hanging meniscus method was used to expose only the Au(111) single crystal surface and to minimize lateral wetting.

ELECTROCHEMICAL CELL SCHEMATIC DIAGRAM

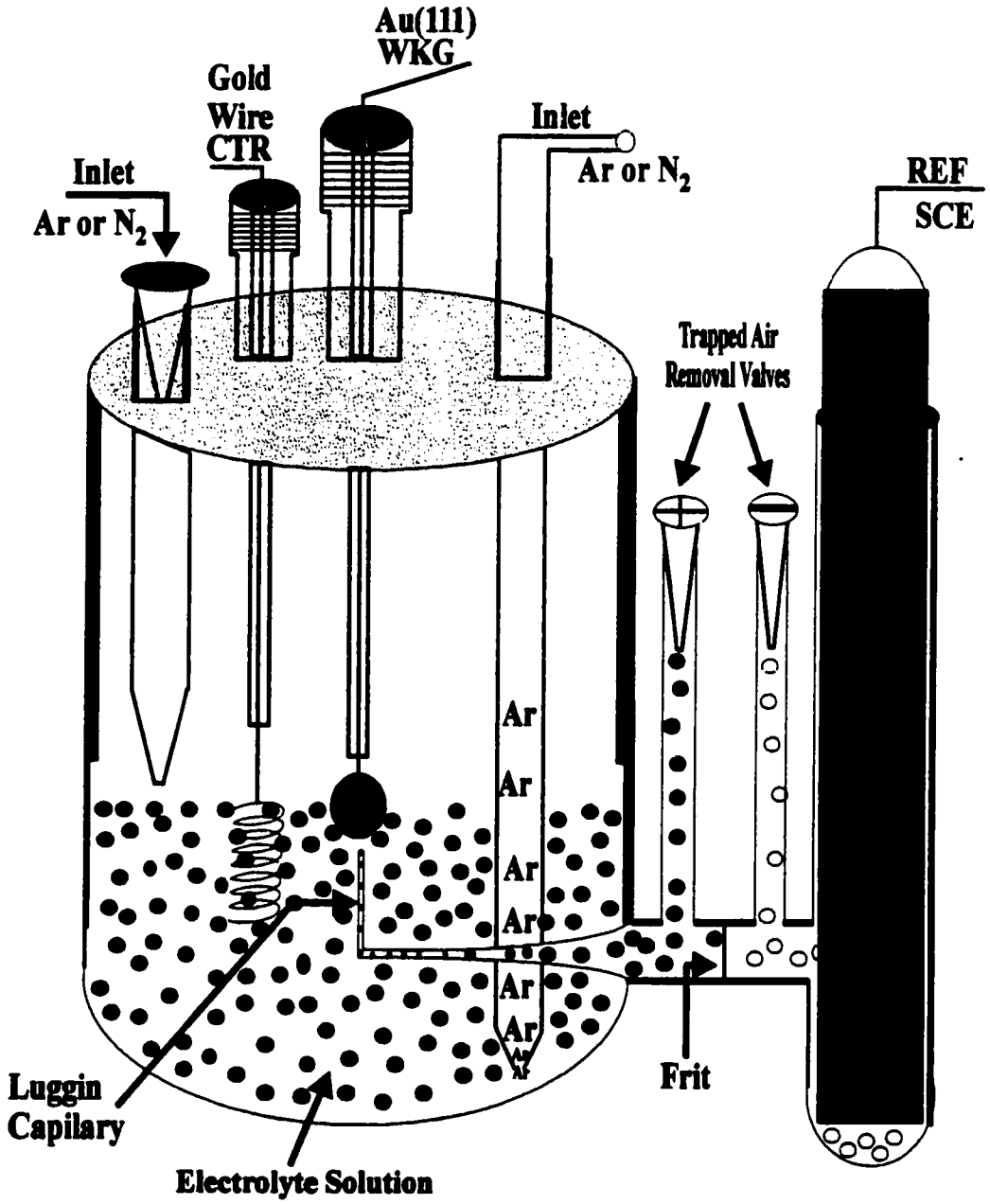

Figure 2.5 : Electrochemical cell consisting of a gold (111) single crystal electrode and a gold coil counter electrode in one compartment and, in a separate compartment, a saturated calomel electrode. The two compartments are connected via a fine grade glass frit and a Luggin capillary.

The latter would introduce undesired contributions from the sides of the single crystal which present different orientations from the one being investigated.

4. Characterization Techniques

4.1 Cyclic Voltammetry (CV) :

Cyclic voltammetry is widely used to study electrode reactions. Voltammetry is very sensitive to surface processes (electron transfer, charge of the double layer, adsorption, etc.) [12,13]. Voltammetry makes it possible to check the electroreactivity of organic molecules. Noble metal electrodes (e. g., Au, Pt, Ag, Cu, Pd, etc.) display different electrocatalytic activity towards the oxidation of many organic compounds. Cyclic voltammograms can be recorded at different scan rates and be used in thermodynamic and kinetics measurements of electrochemical reactions [4].

Cyclic voltammetry involves the application of a triangular waveform to the potential of the working electrode and the simultaneous measurement of the current [11,12]. The current is measured between the working and counter electrodes. The potential is measured between the working electrode (polarizable) and the reference electrode (non-polarizable) which has a constant potential. The potential is generated via a function generator and then applied to the electrochemical cell through a potentiostat (Omni 90 or PINE model AFRDE5 potentiostat/galvanostat). The current-potential curves such as the one in Figure 2.6 are measured with an X-Y recorder (series 200 the Recorder Company, Texas) or an analog/digital acquisition board (National Instruments, USA) and a computer.

Negative and positive final potentials, E_c^t and E_a^t, are chosen in aqueous electrolyte to lie between the hydrogen and the oxygen evolution potentials. By linearly scanning the potential between these limits, reproducible current-potential or cyclic voltammograms for gold are obtained. The potential and the potential scan rate, υ (V/s), is obtained from the equation :

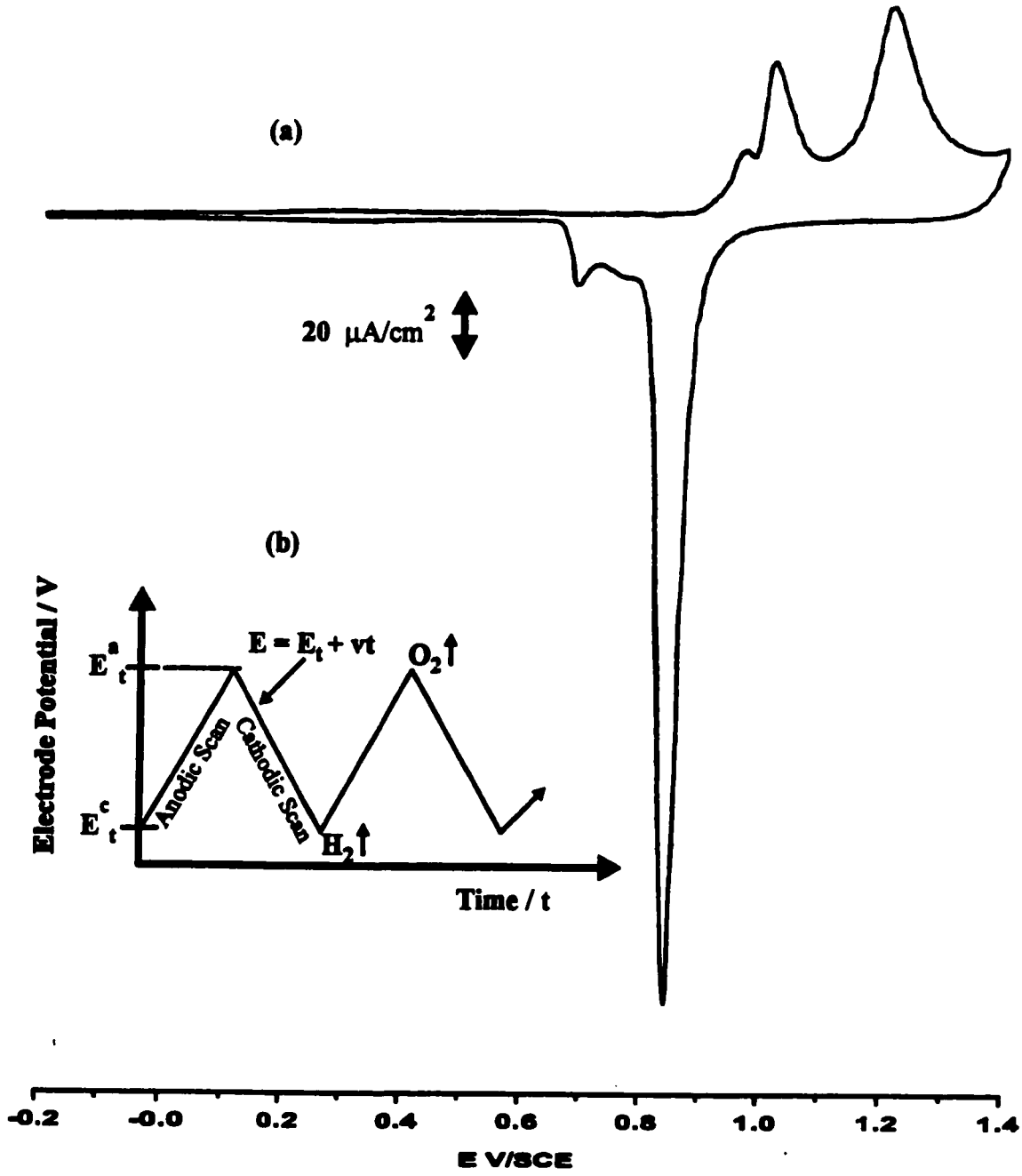

Figure 2.6 : (a) Cyclic voltammogram of a bare gold (111) single crystal electrode in 0.1 M $HClO_4$ recorded at a potential scan rate of 20 mV/s at room temperature. (b) Potential-time variation at the working electrode.

$$E = E_i + \upsilon t \qquad (5)$$

or $$dE/dt = \upsilon \qquad (6)$$

where E_i is the initial potential.

The current density response, j, to the applied potential, E, is related to the charge since the current is the time derivative of q :

$$j = dq/dt = (dq/dE) \,.\, (dE/dt) \qquad (7)$$

where $dq/dE = C$ is the capacitance in the absence of faradaic processes since $dE/dt = \upsilon$, the current response can be represented by :

$$j = C\,\upsilon \qquad (8)$$

From the current density vs potential profiles, the total charge passed between the two potential limits E_i (initial) and E_f (final) can be calculated from the following equation :

$$dq = j\,dt \qquad (9)$$

Integration gives :

$$q = \int_{Ei}^{Ef} j dt = \int_{Ei}^{Ef} C dE \qquad (10)$$

Reproducibility in cyclic voltammetry depends on the nature of the electrode, its crystallographic orientation of Miller indices of the exposed face, the electrolyte purity, the potential limits, and the potential scan rate. In the potential region between $E_c^{\,t}$ and $E_a^{\,t}$, the observed current-potential curve in aqueous solution corresponds to the formation and the

removal of chemisorbed hydride and oxide layers on the electrode surface.

4.1.1 Electrical double layer :

When the electrode is immersed in a water with non-adsorbing electrolyte species, a potential-dependent structure will form at the metal/solution interface. The formation of this interfacial structure is due to several factors including the chemical nature and concentration of the electrolyte, the metallic electrode and the applied potential at the electrode.

Several models of the interface have been reported [15]. Figure 2.7 shows a representation of the structured interface proposed by Grahame [16]. The interface consists of three parts as presented in the figure : (1) The inner Helmholtz plane; (2) The outer Helmholtz plane; (3) The diffuse layer. Numerous methods have been used to characterize the metal/solution interface, but the most common procedure is the determination of differential capacitance [17]. This method gives the relationship between the interfacial capacitance and the applied potential.

The modified gold electrode/electrolyte interface can be represented as a capacitor consisting of two parallel plates separated by a SAM. When a voltage is applied across the capacitor, there is a variation of charge. The relationship between the capacitance and the charge is given by:

$$C = \frac{Q}{V} \qquad (11)$$

where C is the double layer capacitance (Farad, F) ; Q is the charge stored in the capacitor (Coulomb, C) ; V is the voltage across the plates (Volts, V).

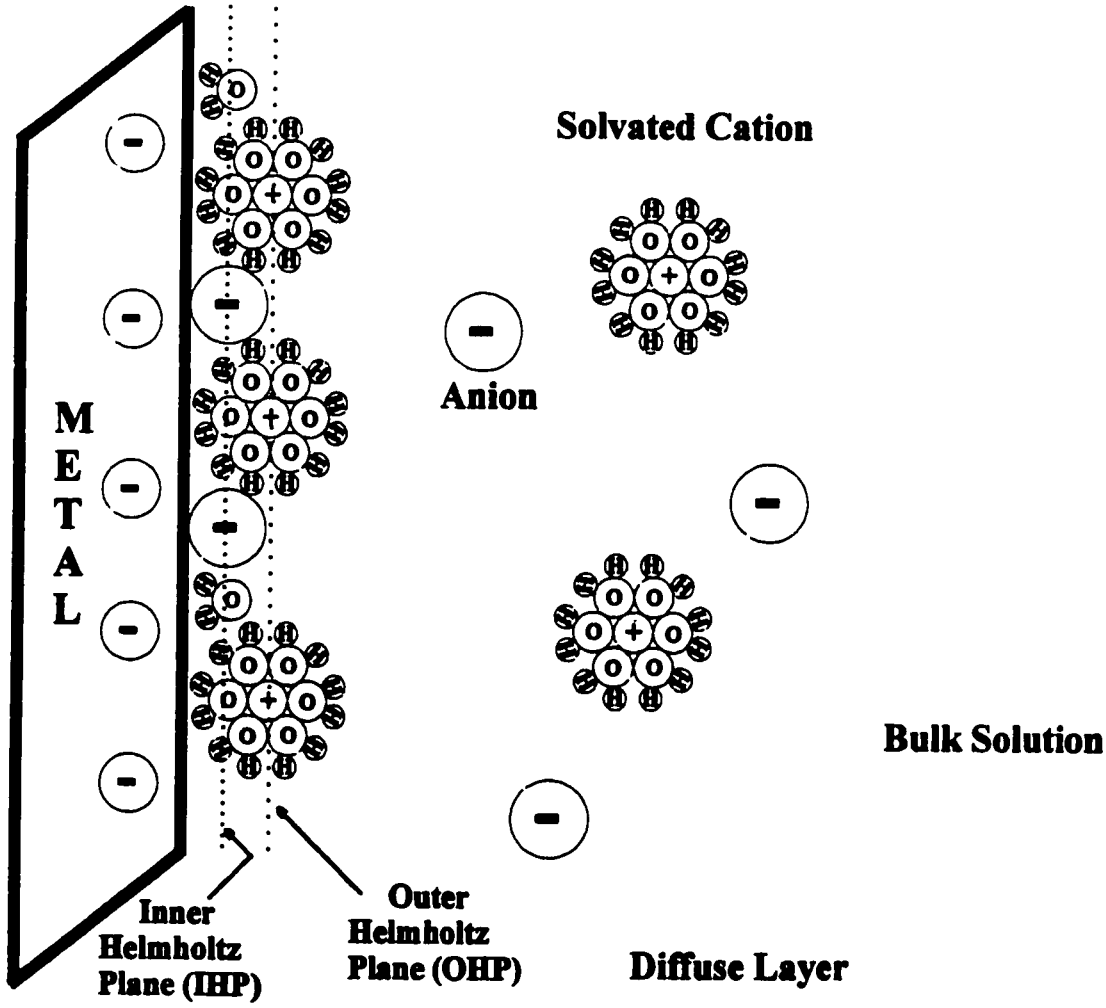

Figure 2.7 : Interfacial region with the anion specific adsorption at a metallic electrode. + and - represent the cation and the anion and the remaining spheres are water molecules either free or involved in the solvation of the ions. IHP and OHP are the inner and outer Helmholtz planes.

4.1.2 Comparison of the voltammograms as a function of the pH of the aqueous solutions:

Voltammograms in different electrolytes are different, as shown in Figures 2.6, 2.8, and 2.9. These demonstrate the high sensitivity of the technique used and are in agreement with literature [4,18-21]. Cyclic voltammograms for both acidic and alkaline aqueous solutions are the same when the solution is stirred (the solution pH does not change at the level of the electrode) or quiescent (unstirred) [4]. However, in neutral solutions, they are different [4]. Thus, it is easier to check the gold face in an acidic solution than it is in an alkaline (difficult to purify) or in a neutral solution.

4.2 Fourier Transform Infrared Reflection-Absorption Spectroscopy (FTIR-RAS) :

Ex-situ vibrational spectra were performed with a FTIR (Nicolet 550) spectrometer equipped with a MCT-B detector cooled with liquid nitrogen.

FTIR provides information on the structure of adsorbed species at the molecular level [12]. The energy levels of a harmonic oscillator are quantized and the energy can be expressed by [11]:

$$E = (n + 1/2)h\nu \qquad (12)$$

where the vibrational frequency ν is given by :

$$\nu = 1/2\pi\,[k/\mu]^{1/2} \qquad (13)$$

where the reduced mass is $\mu = m_1 m_2/(m_1 + m_2)$. Different molecules have different vibrational frequencies because of different reduced masses and force constants, k.

Not all modes are IR active. Only those that lead to a change in the dipole moment in the molecule [11] are active. Homonuclear diatomic molecules such as O_2, Cl_2, etc., are not

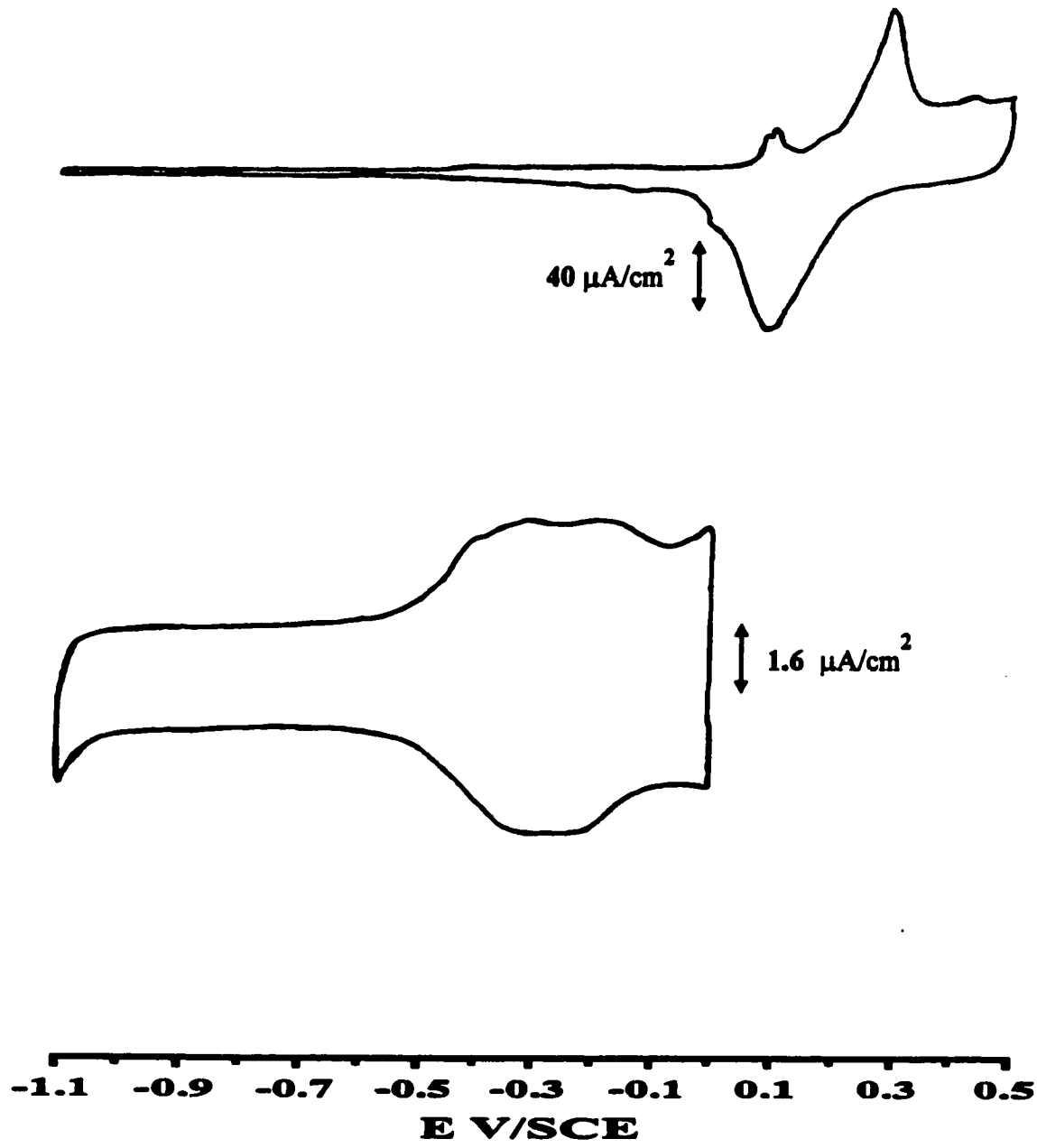

Figure 2.8 : Voltammograms of the formation and removal of a gold surface oxide and the double layer at a single crystal gold (111) electrode in 0.1 M KOH solution. Measurements were done at a scan rate of 50 mV/s.

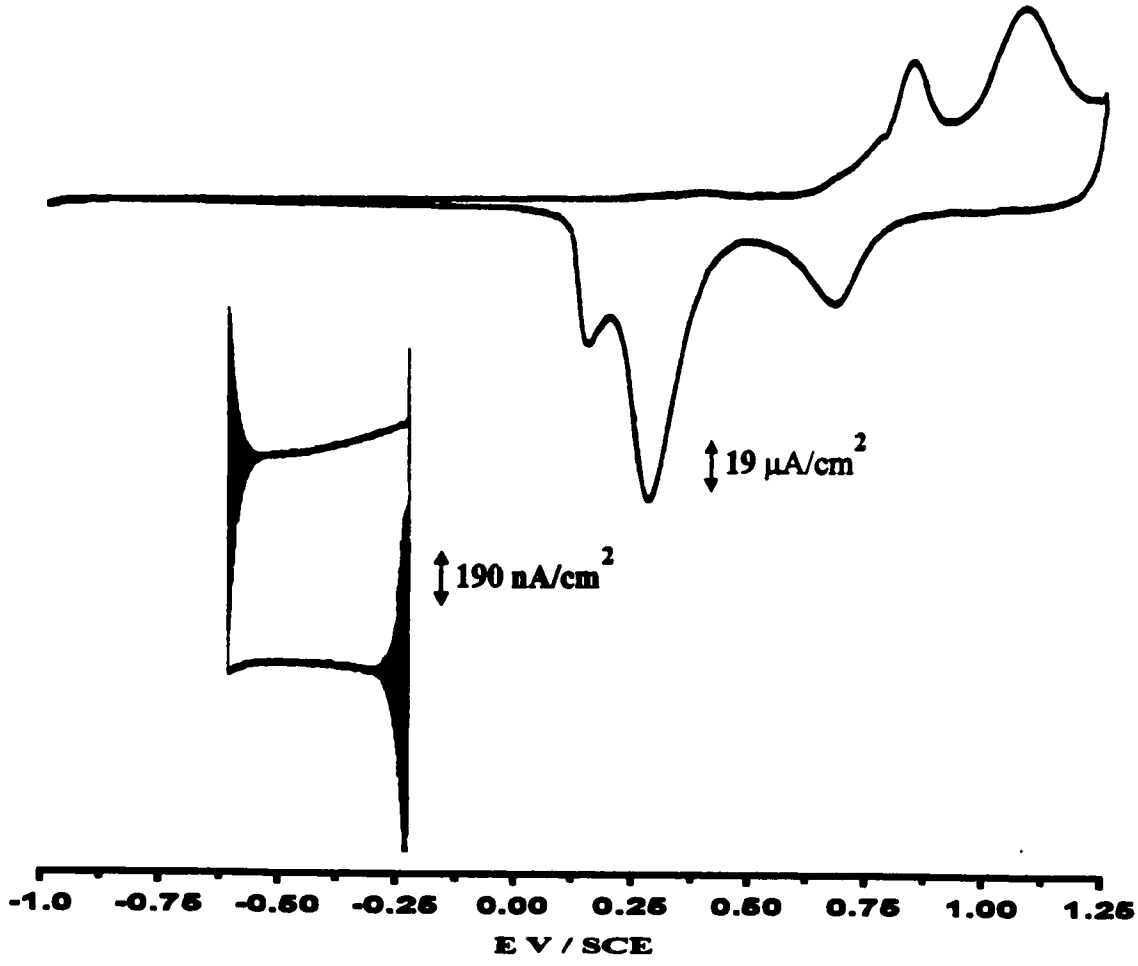

Figure 2.9 : Cyclic voltammogram of a Au(111) single crystal electrode in 0.1 M $KClO_4$ at a scan rate of 20 mV/sec. at 20 °C.

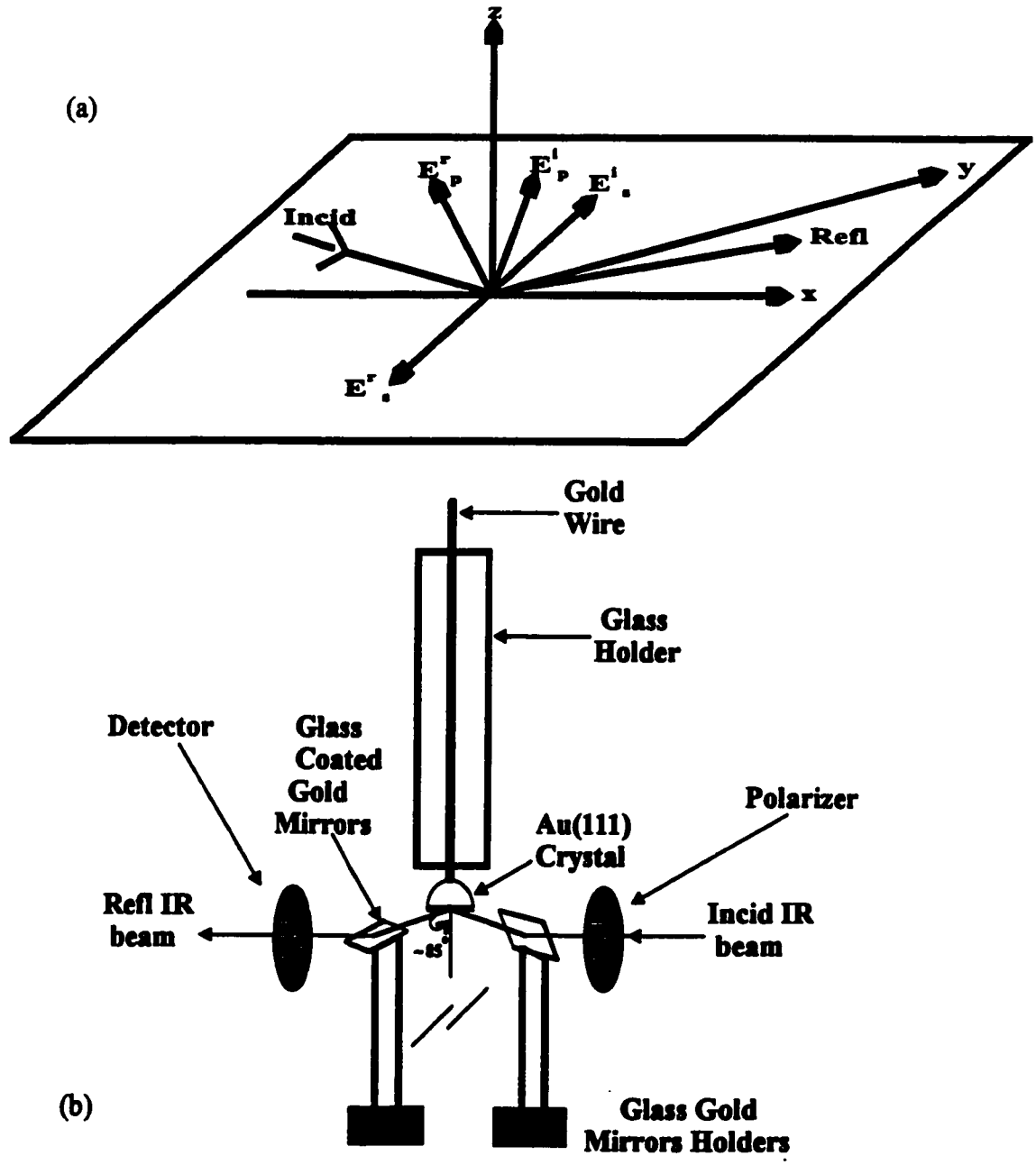

Figure 2.10 : (a) Surface selection rules : only electric fields polarized perpendicular to the metallic surface cause an IR excitation. (b) FTIR ex-situ experimental set-up.

IR active, and the totally symmetric modes of molecules such as CO_2, CH_4, etc., are IR inactive.

In the case of molecules adsorbed on a metallic substrate, only modes that have a non zero projection of the transition dipole moment perpendicular to the surface will be IR active, as shown in Figure 2.10a. This is due to the fact that the electrical field generated by an incident electric field polarized parallel to a metallic surface is out of phase with the incident field. Thus, this electric field does not cause a vibrational excitation. An electric field polarized perpendicular to the surface induces an electric field in phase. In this case the electrical field is enhanced by a factor of two. It can excite vibrational modes of adsorbed molecules. This effect is known as the surface selection rule.

$$E_{Tot}\ (\text{parallel}) = (E_s^{\,i}) + (-E_s^{\,r}) = \text{ZERO} \quad \therefore \text{IR inactive} \qquad (14)$$

$$E_{Tot}\ (\text{perpendicular}) = (E_p^{\,i}) + (E_p^{\,r}) = \text{Doubled} \quad \therefore \text{IR active} \qquad (15)$$

This rule has been used to obtain information on the orientation of adsorbates (see Chapter 1).

The FTIR spectrometer operates with a polychromatic light. Before the beam is sent to the sample, it goes through a Michelson interferometer. The beam is split in two by a KBr beam splitter. Half of the beam is sent to a fixed mirror and the other half is sent to a mobile mirror. The reflected beams recombine and are sent to the sample. The intensity of the beam is now modulated because of the interference between the beams which changes as a function of the position of the mobile mirror, as shown in Figure 2.11. If the path length difference for a beam of wavelength λ is $\lambda/2$ or any odd multiple of $\frac{1}{2}\lambda$, then, on re-combining the two beams, light of that wavelength will be zero. After reflection from the electrode surface the signal is recorded as a function of the position of the mobile mirror. This gives rise to an interferogram which is Fourier transformed to give the vibrational spectrum.

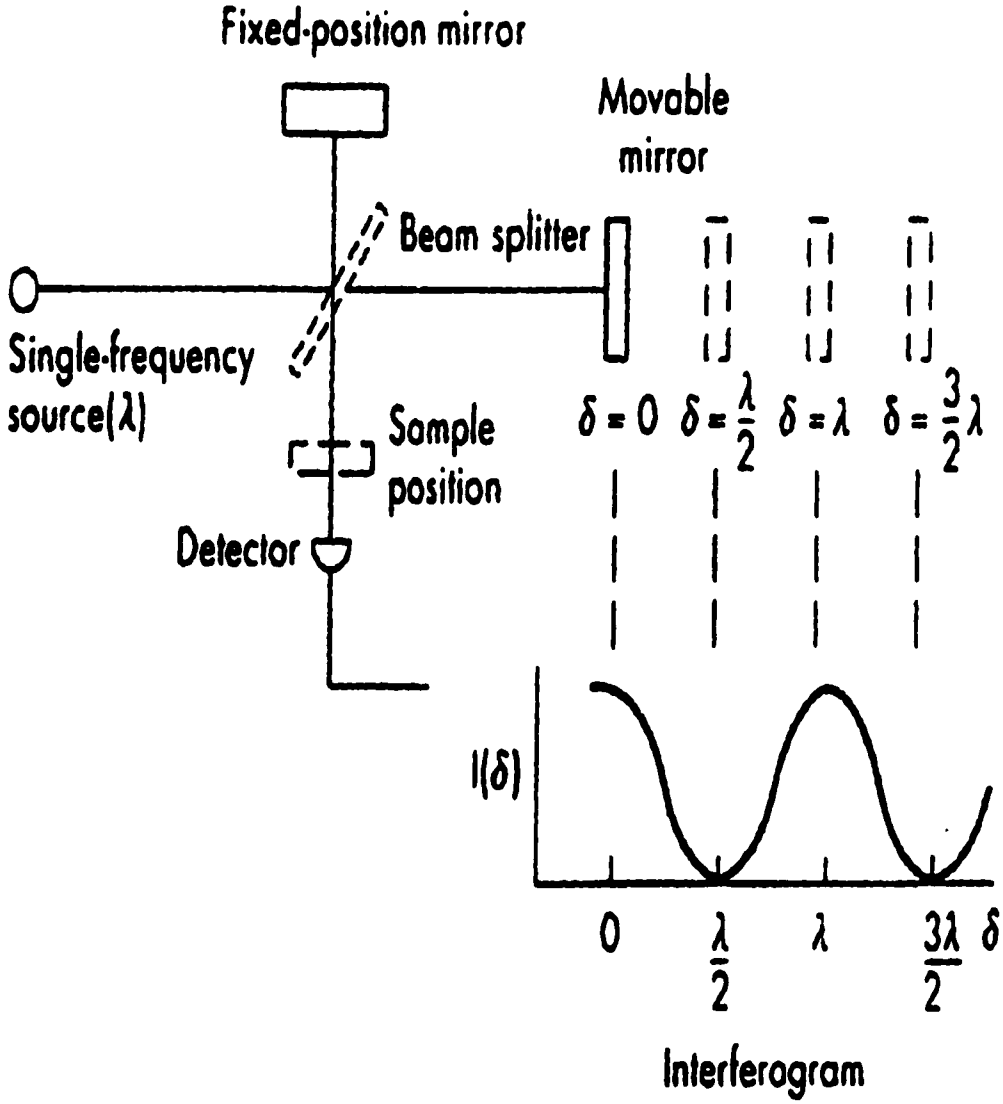

Figure 2.11 : Michelson interferometer of the Fourier transform infrared (FTIR) spectrometer.

4.3 Chronoamperometry (CA) :

Chronoamperometry is used to study the kinetics of electrochemical reactions. This is achieved by rapidly changing the potential applied to the working electrode and recording the current. The current transient is a measure of the process by which the electrochemical system reaches a new equilibrium state. It is possible with this method to distinguish multiple reactions if their time scale are sufficiently different [12]. For example, the double layer charging current is fast (μsec) and will decay exponentially with a time constant R_uC_{dl}. Thus it is sometimes possible to distinguish it from slower electron transfer reactions [22]. The study of the kinetics of electrochemical reactions is also possible by cyclic voltammetry. However, capacitive and faradaic processes are often not well resolved.

Figure 2.12a shows the waveform applied in a potential-step experiment [22]. E_1 is a potential region where no faradaic processes occur. E_2 is a potential region where there is a faradaic reaction. When the reactant is dissolved in the electrolyte solution and the electrochemical reaction is rapid, the current (i. e. the measured rate of electron transfer) is limited by the diffusion of the molecules to the electrode surface. At a sufficiently long time, a diffusion gradient is established and a constant current is measured.

The chronoamperometric measurements were carried out using a function generator (Hokuto Denko, model HB-104) and a potentiostat (EG & G, Princeton Applied Research, model 173) and recorded with a digital oscilloscope (Tektronic TDS 300 Series or Hewlett-Packard, model 54510B) and a PC or with an XY recorder .

4.4 AC Impedance Spectroscopy (ACIS) :

The AC impedance spectroscopy consists of applying a small AC potential to an electrode maintained at a constant potential. This small perturbation will give rise to a current oscillating at the same frequency as the potential if there is an electrochemical process

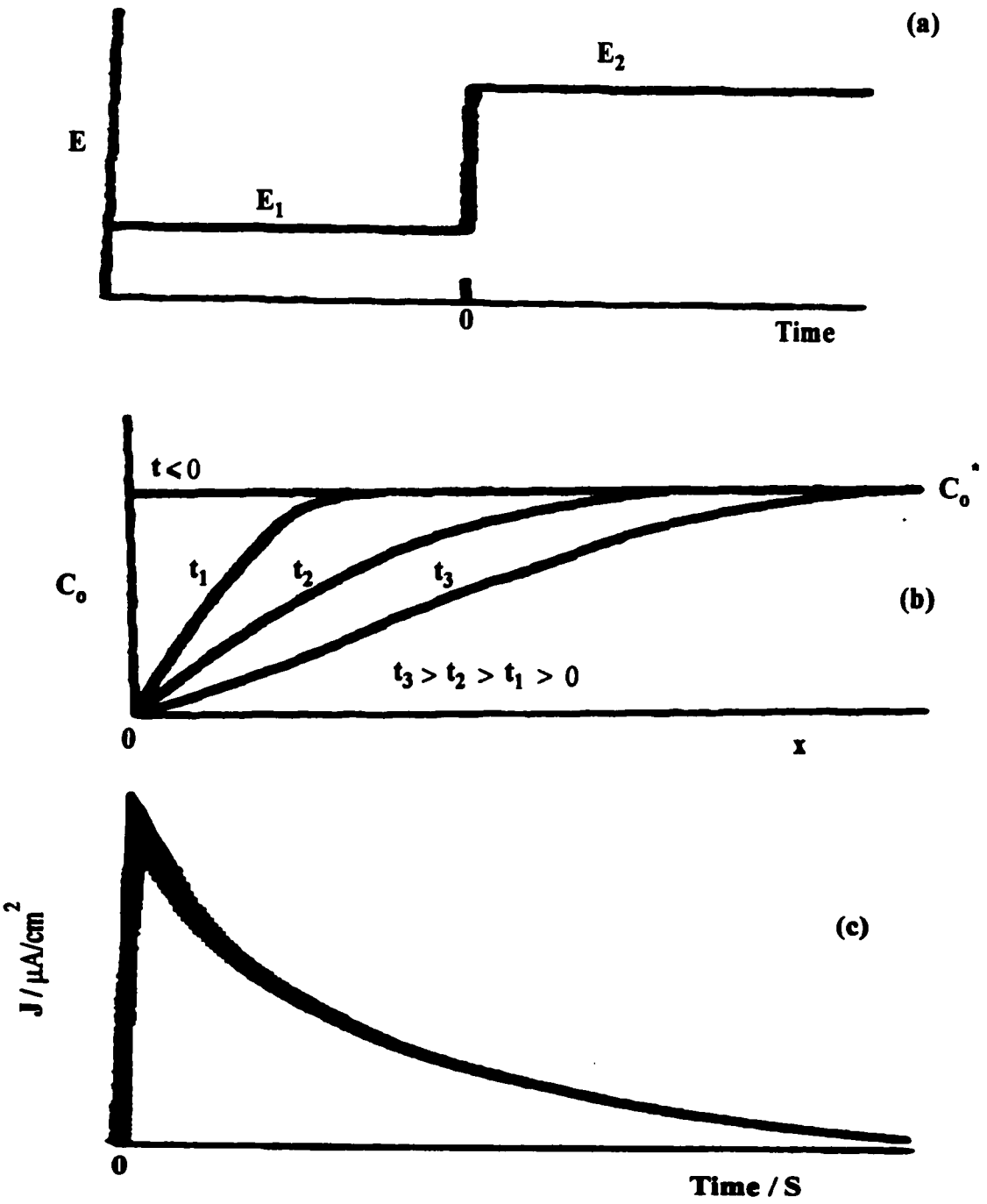

Figure 2.12 : (a) Waveform, (b) concentration profile, and (c) current-time decay for a potential-step chronoamperometry experiment.

occurring at a rate which is at least as fast as the AC perturbation. Thus the magnitude of the current response gives information on an electrochemical reaction near equilibrium conditions. By varying the frequency of the perturbation, it is possible to quantitatively extract the rates of electrochemical reactions. The analysis of the impedance data is usually done using AC circuits theory [22-24]. A brief description of models used to describe a simple electrochemical system, such as a thiol coated Au(111) electrode, is given below. A more detail discussion of the model used to analyze our results is given in Chapter 6.

4.4.1 Theory of AC impedance spectroscopy :

Figure 2.13 presents a phasor diagram for (A) an alternating voltage and (B) a current i separated by the phase angle ϕ. The sine wave (sinusoidal) voltage and current expressions are :

$$E = \Delta E \sin \omega t \qquad (16)$$

$$i = \Delta i \sin (\omega t + \phi) \qquad (17)$$

where ΔE is the maximum amplitude and ω is the angular frequency ($\omega = 2\pi f$ where f is in Hz). In impedance measurements we measure the voltage and current at a given frequency. In many cases the current will be sinusoidal and of the same frequency ω, but both the amplitude and phase angle are different from the voltage. For simple circuit elements such as in Figure 2.14a the phase angle $\phi = 0^\circ$ and Ohm's law applies for a pure resistance R:

$$i = E / R \qquad (18)$$

where the phase angle $\phi = 0^\circ$ and is shown in Figure 2.15a .

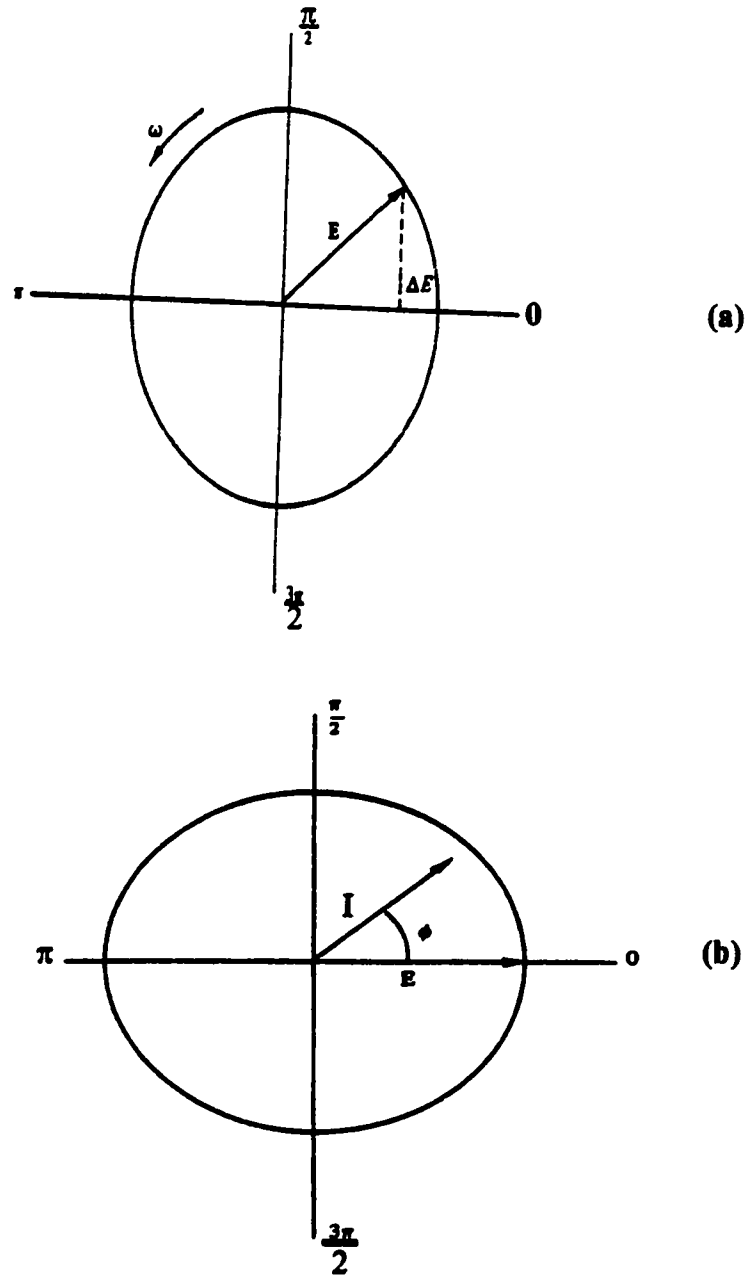

Figure 2.13 : Phasor diagrams showing the relationship between (a) alternating voltage $e = E \sin \omega t$ and (b) alternating current $i = I \sin(\omega t + \phi)$ oscillating at the same frequency ω.

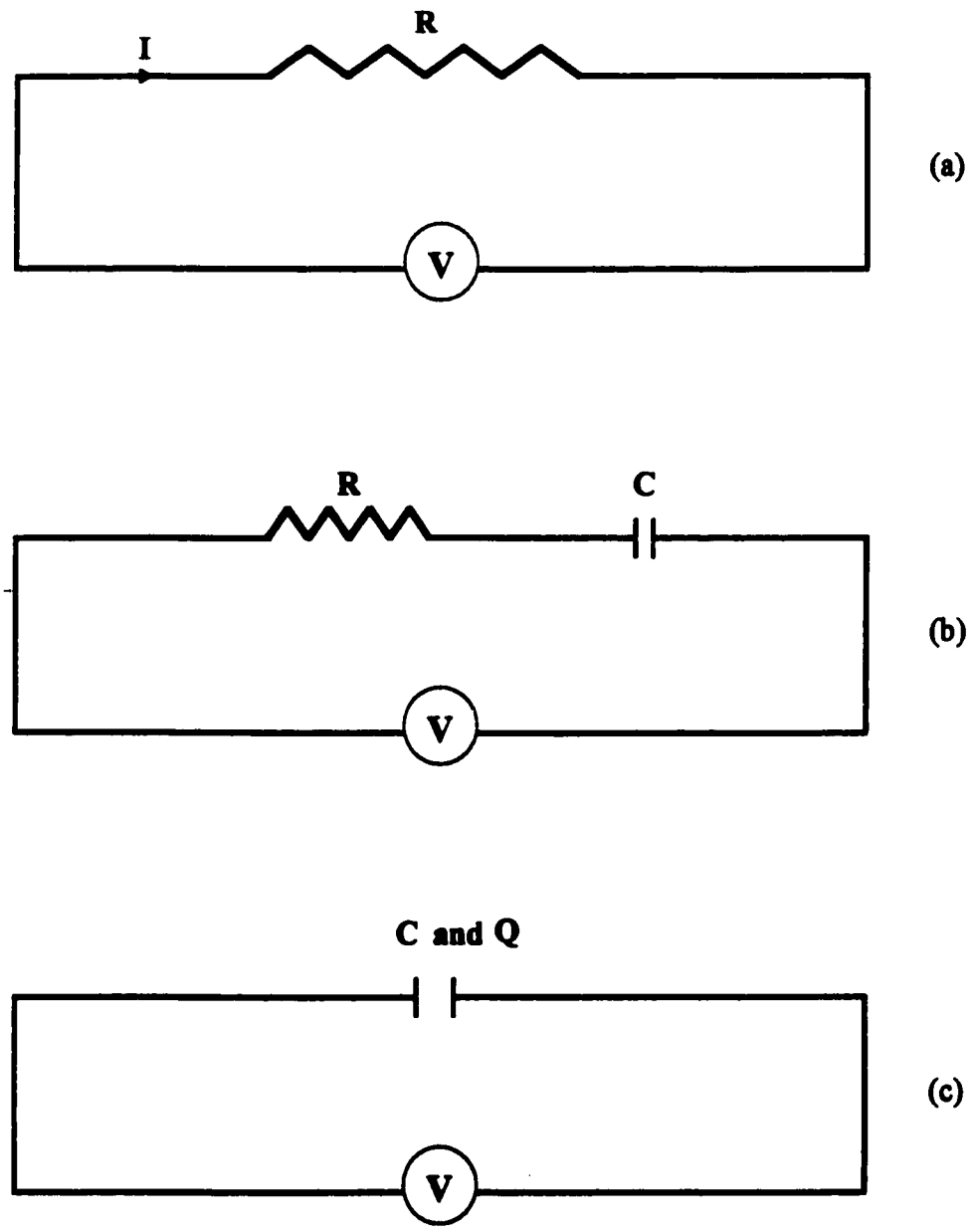

Figure 2.14 : Schematic electrical circuit diagrams of (a) purely resistive ; (b) an RC ; and (c) purely capacitive systems. Where R : resistance, C : capacitor, Q : charge, I : current and V : voltage.

For a pure capacitance C :

$$q = CE \qquad (19)$$

C is obtained from the relation between the potential E and the charge, q, stored on the plates (see Figure 2.14c). The current can be obtained by differentiation :

$$i = dq/dt = C\,(dE/dt) \qquad (20)$$

and by taking the sinusoidal voltage derivative eq. (16) the current is given by :

$$i = \omega C\, \Delta E \cos \omega t \qquad (21)$$

Replacing $1/(\omega C) = X_c$ which is called the capacitive reactance, we get :

$$i = (\Delta E/X_c) \sin (\omega t + \pi/2) \qquad (22)$$

This equation is similar to Ohm's resistance expression, but here R is replaced by X_c, the reactance, and ϕ is not zero. If the phase angle, $\phi = + \pi/2$, the current is said to "lead the voltage" as shown in Figure 2.15b. If the phase angle, $\phi = - \pi/2$, the current is said to "lag the voltage" and is presented in Figure 2.15c.

An electrochemical system in which there is only charging occurring at a given potential can be represented by a resistance R (the solution resistance) and a capacitance C connected in series (Figure 2.14b). The impedance is given by [23] :

$$Z = R + 1/(j\,\omega C) \qquad (23)$$

where Z is the impedance, R is the real part of Z and the imaginary part of Z is $1/(\omega C)$.

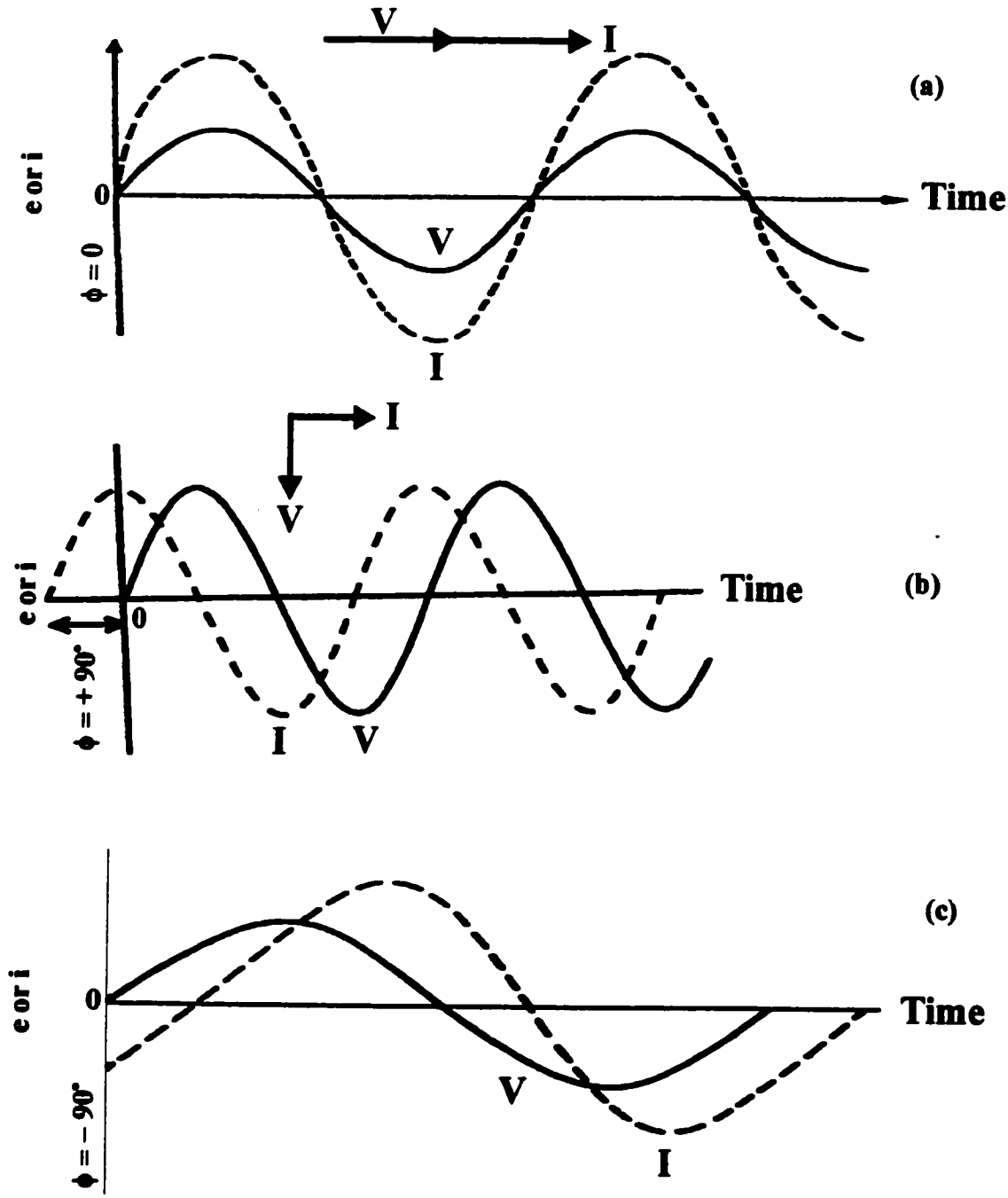

Figure 2.15 : Time variation of (a) an alternating voltage across a resistor and alternating current through the resistor; Relationship between an alternating voltage across a capacitor and the alternating current through the capacitor where (c) the current leads and (b) the current lags the voltage at frequency ω.

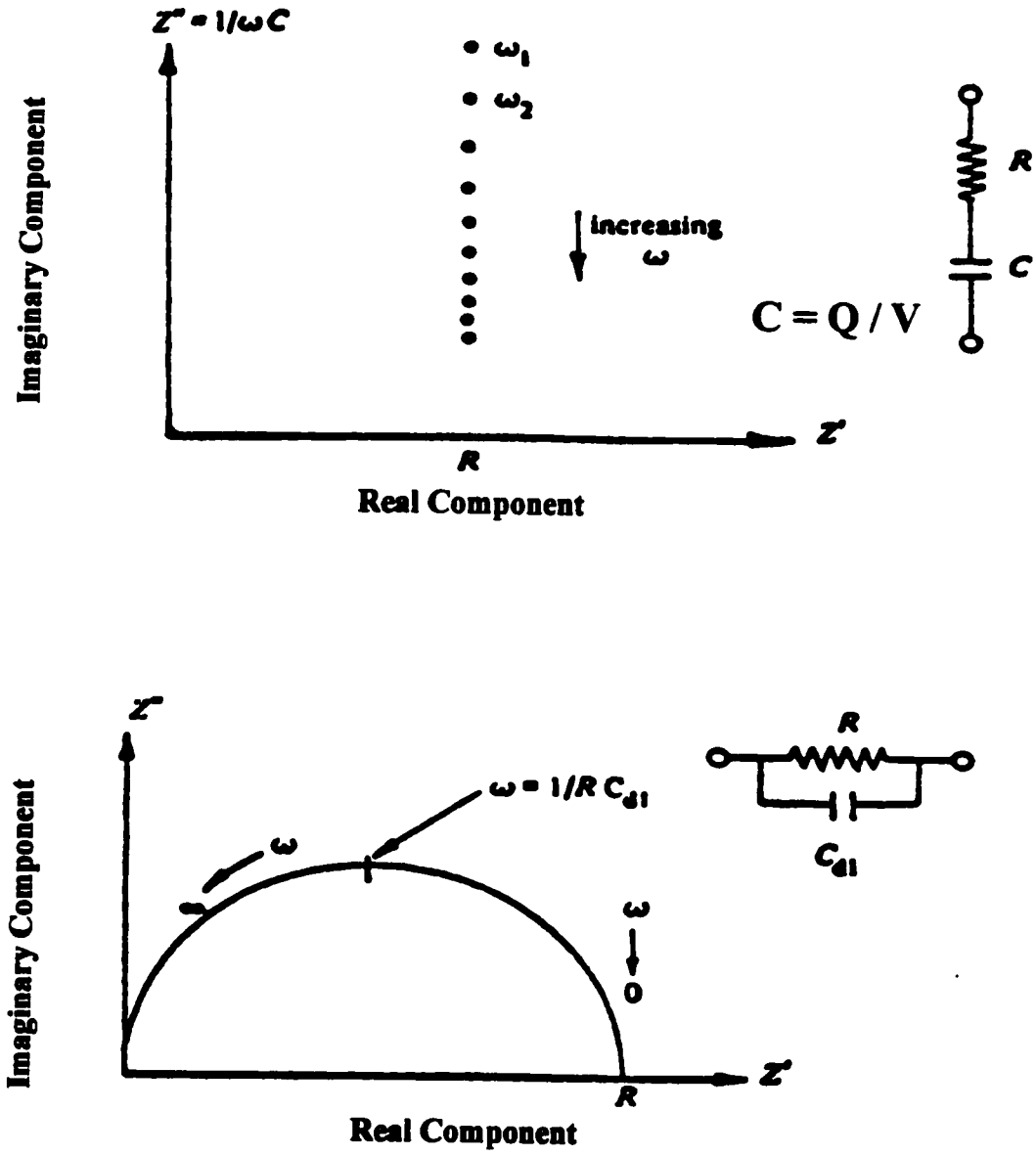

Figure 2.16 : Complex plane (Argand) plots (a) for an electrical series RC circuit; (b) for an electrical parallel RC circuit. This circuit is used to describe a faradaic reaction at an electrode with an electrical double layer capacitance C_{dl}.

Therefore,

$$Z = Z' + Z'' \qquad (24)$$

A plot of Z' vs Z'' is called an Argand diagram and is shown in Figure 2.16a in the form of a vertical series of points at different ω for RC in series. A vertical line in an Argand plot is a fingerprint of a purely capacitive system. There is no faradaic process occurring.

An electrochemical reaction can be represented by a resistance, R, and a capacitance, C, connected in parallel. The semi-circle in Figure 2.16b is the solution of this system. We see that at high frequency Z' and Z'' approach zero. A maximum is observed at a value which depends on the rate constant (RC) of the process. Data can be used to obtain the double layer capacitance. The intercept of this curve at a frequency of zero gives the value of R. A small value of R is indicative of a fast process.

A more realistic model is obtained by adding the uncompensated solution resistance R_u in series with the RC in parallel. This series-parallel combination circuit is known as "Randles equivalent circuit" [25]. The effect of the uncompensated resistance is to shift the semi-circle by R_u along the Z' axis (Figure 2.17a).

A complete analysis of the series-parallel configuration is done by considering the diffusion of the reactants to the surface. Two limiting cases need to be considered. The first case occurs at low frequencies. As $\omega \rightarrow 0$ the real part and the imaginary part of the impedance Z are given by :

$$Z' = R_u + R_{ct} + (\sigma\,\omega)^{-1/2} \qquad (25)$$

$$Z'' = (\sigma\,\omega)^{-1/2} + 2\sigma^2 C_{dl} \qquad (26)$$

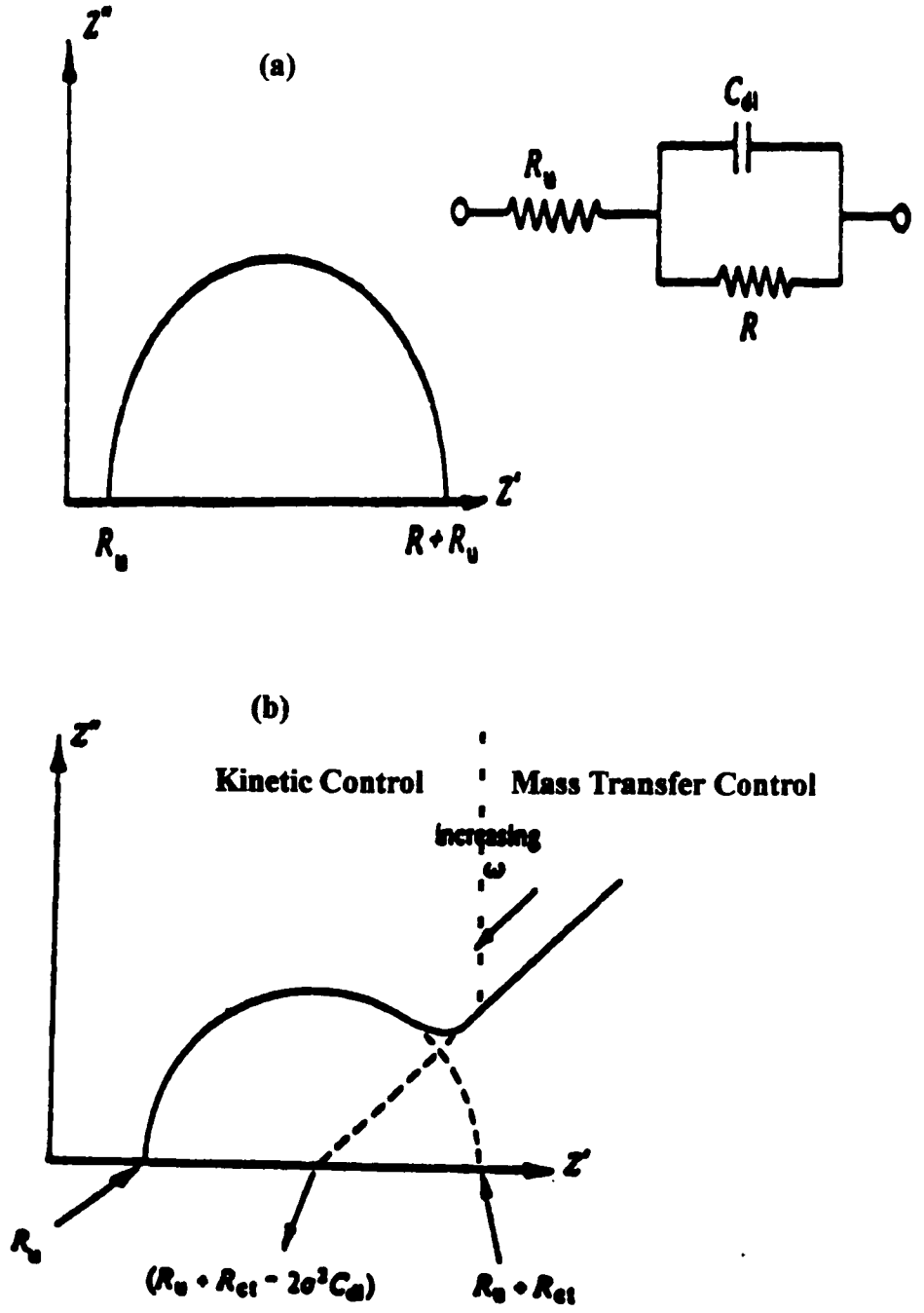

Figure 2.17 : Complex plane (Argand) diagrams (a) for an electrical parallel RC circuit with an electrical double layer capacitance C_{dl} and uncompensated solution resistance R_u; (b) The same system where the diffusion of the reactants to the surface is considered.

$$Z = Z' - R_u - R_{ct} + 2\sigma^2 C_{dl} \quad (27)$$

where R_{ct} is the charge transfer resistance. A small resistance is indicative of fast kinetics, and σ has to do with the diffusion parameters of the system under investigation. This is a straight line equation of unit slope with an intercept on the real axis of $R_u + R_{ct} - 2\sigma^2 C_{dl}$. The second limiting case occurs at high frequencies. The components Z' and Z''are :

$$Z' = R_u + [R_{ct} / (1 + \omega C^2_{dl} R^2_{ct})] \quad (28)$$

$$Z'' = C_{dl} R^2_{ct} \omega/(1 + \omega^2 R^2_{ct} C^2_{dl}) \quad (29)$$

Eliminating ω yields

$$(Z' - R_u - R_{ct}/2)^2 + (Z'')^2 = (R_{ct}/2)^2 \quad (30)$$

This is the equation of a circle centered on $Z' = R_u + R_{ct}/2$ with a radius of $R_{ct}/2$. In Figure 2.17b the kinetically controlled process is a semicircle and the diffusion controlled process is a linear region with a slope of unity.

AC impedance measurements were performed using a Solartron (Solartron Group Inc., England) electrochemical interface (SI 1287) and impedance/gain-phase analyzer (SI 1260) controlled by a computer running Corrview and Zplot software (Scribner Associates, Charlottesville, VA). Measurements were performed at either a 5 or 10 mV amplitude and impedance values were determined at five discrete frequencies per decade. The range of frequencies applied was 0.01 Hz to 10 kHz. The impedance analyzer measures the voltage and current at a given frequency and is expressed as :

$$Z(\omega) = \text{Voltage Phasor} / \text{Current Phasor} \quad (31)$$

$$Z(\omega) = V(j\omega)/I(j\omega) \quad (32)$$

$$Z(\omega) = Z'(\omega) + j Z''(\omega) \qquad (33)$$

where $Z(\omega)$ is the measured impedance of the system ; $Z'(\omega)$ is the real part of the impedance; $j Z''(\omega)$ is a complex quantity in which $j = \sqrt{-1}$ and $Z''(\omega)$ is the imaginary part of the impedance. All $Z(\omega)$, $Z'(\omega)$ and $Z''(\omega)$ are dependent of the frequency [26, 27] of the oscillating potential.

5. References

1. Wood, E. A. "Crystal Orientation Manual"; Columbia University Press : New York, 1963.
2. Nicholas, J. F. An Atlas of Models of Crystal Surfaces, Gordon and Breach, Eds.; New York, 1965.
3. Hamelin, A. In Modern Aspects of Electrochemistry ; Conway, B. E.; Bockris, J. O'M.; White, R. E.; Eds.; Plenum Press : New York, 1985, Vol. 16, Chapter 1.
4. Hamelin, A. J. Electroanal. Chem. **1996**, 407, 1-11.
5. Hamelin, A. J. Electroanal. Chem. **1982**, 142, 299.
6. Gao, X.; Hamelin, A.; Weaver, M. J. Phys. Rev. Lett. **1991**, 67, 618.
7. Gao, X.; Hamelin, A.; Weaver, M. J. J. Chem. Phys. **1991**, 95, 6993.
8. Gao, X.; Hamelin, A.; Weaver, M. J. Phys. Rev. B **1991**, 44, 10983.
9. Gao, X.; Hamelin, A.; Weaver, M. J. Surf. Sci. Lett. **1991**, 274, L588.
10. Kozlowska, H. A.; Conway, B. E.; Hamelin, A.; Stoicoviciu, L. J. Electroanal. Chem. **1987**, 228, 429.
11. Hamann, C. H.; Hamnett, A.; Vielstich, W. In Electrochemistry ; Wiley-VCH : New York, 1998, Chapter 5.
12. Amokrane, S.; Badiali, J. P. In Modern Aspects of Electrochemistry ; Conway, B. E. ; Bockris, J. O'M.; White, R. E. ; Eds.; Plenum Press : New York, 1992, Vol. 22, Chapter 1.
13. Perez, J.; Gonzalez, E. R.; Villullas, H. M. J. Phys. Chem. B **1998**, 102, 10931.

14. Strbac, S.; Hamelin, A.; Adzic, R. R. J. Electroanal. Chem. **1993**, 362, 47.

15. Lang, B.; Joyner, R. W.; Somorjai, Surface Sci. **1973**, 30, 454.

16. Kaischew, R.; Mutaftschiew, Zeit. Phys. Chem. **1955**, 204, 334.

17. Hamelin, A.; Morin, S.; Richer, J.; Lipkowski, J. J. Electroanal. Chem. **1990**, 285, 249.

18. Hamelin, A. J. Electroanal. Chem. **1986**, 210, 303.

19. Hamelin, A.; Doubova, L; Wagner, D.; Schirmer, H. J. Electroanal. Chem. **1987**, 220, 155.

20. Hamelin, A.; Sttomayor, M. J.; Silva, F.; Chang, S.-C.; Weaver, M. J. J. Electroanal. Chem. **1990**, 295, 291.

21. Angerstein-Kozlowska, H.; Conway, B. E.; Hamelin, A.; Stoicoviciu, L. J. Electroanal. Chem. **1987**, 228, 429.

22. Bard, A. J.; Faulkner, L. R. In Electrochemical Methodes, Fundamental and Applications ; John Wiley and Sons : New York, 1980, Chapter 5.

23. Greef, R.; Peat, R.; Peter, L. M.; Pletcher, D.; Robinson, J. In Instrumental Methods In Electrochemistry ; John Wiley & Sons : New York, 1985, Chapter 8.

24. Modern Aspects of Electrochemistry ; Conway, B. E.; Bockris, J. O'M.; White, R. E. ; Eds.; Plenum Press : New York, 1982, Vol. 16, Chapter 2.

25. Randles, J. E. B. Disc. Faraday Soc. **1947**, 1, 11.

26. Sondag-Huethorst, J. A. M.; Fokkink, L. G. J. J. Electoanal. Chem. **1994**, 367, 49-57.

27. Janek, R. P.; Fawcett, W. R.; Ulman, A. J. Phys. Chem. B **1997**, 101, 8550.

Chapter 3

The Role of the Solubility of Alkanethiols on the Reductive and Oxidative Electrochemistry of Alkanethiols

1. Introduction

In this chapter we present ex-situ vibrational spectroscopic measurements of self-assembled hexadecanethiol and butanethiol monolayers on Au(111). We also examined the role of the solubility of alkanethiols on the reductive and oxidative electrochemistry of alkanethiols. We will show that monolayers of alkanethiols of different solubility adsorbed on a Au(111) substrate display different electrochemical characteristics.

Potential applications of self-assembled monolayers of thiols as electrochemical sensors or organic electronics depend on the possibility of controlling the electron transfer across the organic/metallic interface [1-6]. It is therefore important to determine how defects and surface coverages influence the electrochemical properties of organic monolayers. We present a comparison of the reduction and, in the case of the less soluble thiols, their oxidative redeposition at a Au(111) single crystal electrode in an aqueous alkaline electrolyte solution. We examined the effect of the pH and ionic strength of the electrolyte solution on these processes.

The surface coverage of thiols can be obtained from simple electrochemical measurements. The measurement of the charge involved in the reduction of a monolayer of chemisorbed thiols corrected for the capacitive contribution does provide a good estimate of the surface coverage [7-13]. Such measurements have been used to estimate the surface coverages of thiols on Ag [7,13-15], Au [7,11,13,16] and Hg [17]. White et al. [14,15,17] found that ethanethiolates oxidatively adsorbed on Ag and Hg via two-step mechanisms, whereas on Au, Porter et al. reported a one-step mechanism [11]. For Ag [14,15] and Hg [17], the two steps of the

process are, respectively, the formation of a low surface coverage (gauche defects appear in the alkane chains) by a Langmuir process. This is followed by the formation of a high surface coverage (gauche defects disappear) by a nucleation and growth process (Temkin-Frumkin isotherm). White et al. [15] reported an electrosorption valency of one for the oxidative adsorption of ethanethiolates on Ag.

Numerous studies have examined electrochemical properties such as the reduction/oxidation as well as blocking properties of alkanethiols monolayers. A shift of the reduction potential of thiols was observed as the chain length increases on silver and gold substrates. This shift was assigned to the difficulty of the ion permeating through the organic monolayer as its thickness increases. This was shown by the dependance of the reduction potential on the cation of the electrolyte. Li^+, a cation that has a large solvation sphere, causes a negative shift of the reduction potential.

The total reductive charge involves a contribution of two components. The first component is the faradaic charge due to a one electron transfer from the electrode to the chemisorbed thiols. The second component is the capacitive charge owing to the formation of a double layer just after the reductive removal of thiols from the Au(111) surface. Approximately 30 % of the total reductive charge is due to the double layer charge [16].

Detailed studies of the variation of the capacitance were done recently by Fawcett et al. [18,19] using AC impedance. In the double layer where charging current occurs, the adsorbed thiols are highly stable. This result in a dramatic decrease of the capacitance because of the low dielectric constant of the monolayer. These studies concluded that a simple equivalent circuit model of a series capacitor of the double layer, C_{dl}, and solution resistence, R_s, is too simple and insufficient to accurately fit the data of all SAM modified electrodes.

Morin et al. [9] and Porter et al. [12] found that, on single crystal Au(111) substrates, a fine structure appears on the cyclic voltammogram. Two models were suggested. The first

model is the formation of two domains of slightly different packing densities. Thus, the different ionic permeabilities would give different reduction potentials for the thiol molecules in each domain. The second model is the reduction of thiols from two adsorption sites involving three-fold hollow and on-top sites. The presence of second adsorption on-top sites for long chain thiols is due to the increase of the adsorbate-adsorbate interactions. Both research teams concluded that there is no direct evidence of preferring either of these two models.

2. Results and Discussion

2.1 Vibrational spectroscopy :

A qualitative comparison of the orientation of the aliphatic chains of the chemically deposited hexadecanethiols and butanethiols was conducted by recording the ex-situ vibrational spectra of the C-H stretching region shown in Figs. 3.1 and 3.2, respectively. The vibrational spectrum of the chemically deposited hexadecanethiols in Fig. 3.1 displays five C-H stretching bands. It is identical to previously reported spectra [10,20]. The bands at 2963, 2937 and 2877 cm^{-1} are assigned to the methyl group. They are, respectively, the asymmetric out-of-plane and the symmetric mode split by a Fermi resonance with a bending mode into the two other bands [20]. The bands at 2920 and 2850 cm^{-1} are the asymmetric and symmetric modes of the methylene groups. The wavenumbers of the methylene C-H stretching bands are typical of all-trans aliphatic chains forming an ordered monolayer [10,20].

The vibrational spectrum of the chemically adsorbed monolayer of butanethiols shown in Fig. 3.2 displays four C-H stretching bands, but are shifted to higher wavenumbers (2963, 2927, 2877, and 2854 cm^{-1}). This shift is indicative of the presence of a higher number of gauche defects and consequently of a less ordered monolayer [21,22].

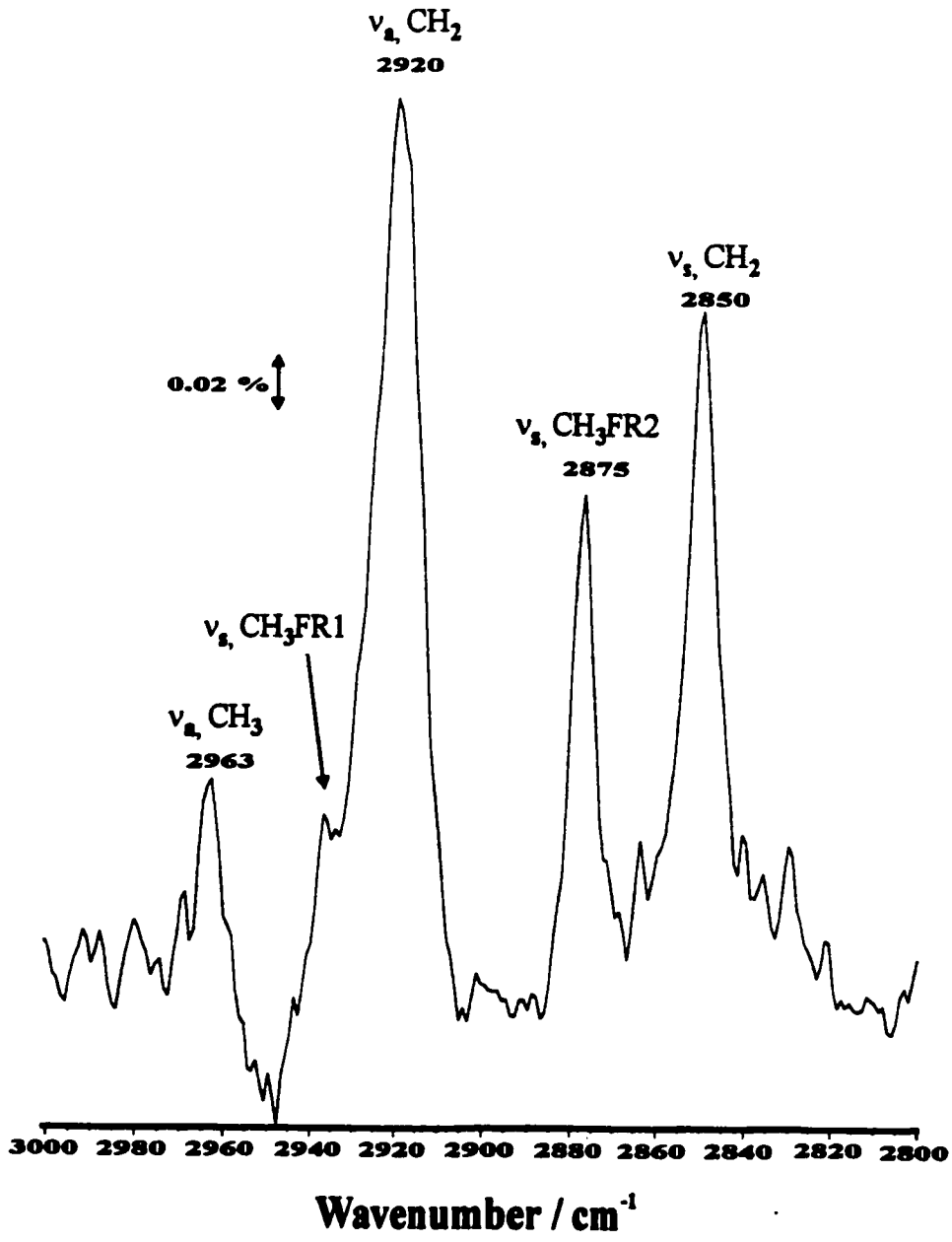

Figure 3.1 : Ex-situ vibrational FTIR spectrum of the C-H stretching modes of a hexadecanethiol monolayer on gold (111).

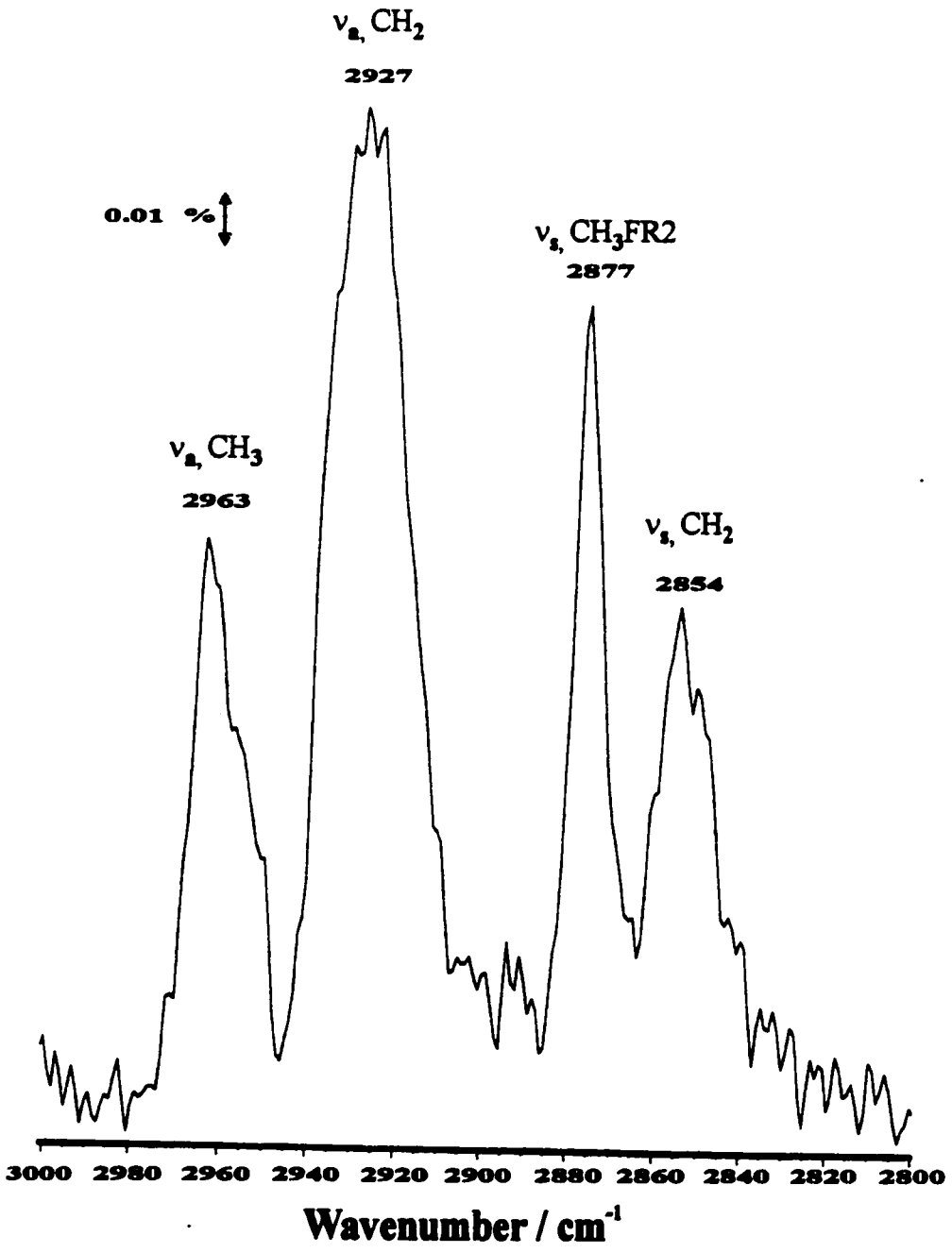

Figure 3.2 : Ex-situ vibrational spectrum of the C-H stretching modes of a butanethiol monolayer adsorbed on gold (111).

2.2 Double layer capacitance as a function of chain length :

The double layer capacitance of alkanethiols with four to sixteen carbons was calculated from the measurement of the double layer charging current measured in cyclic voltammograms recorded between -0.2 and -0.6 V in 0.1 M KOH. The current between these limits is constant. The capacitance was obtained by assuming a perfect capacitor behaviour. In this model there is accumulation of charge at the water/methyl interface. This charge is separated from an equivalent charge at the gold surface by the alkanethiols. The following equation is used to obtain the capacity of the thiol covered gold electrode C ($\mu F/cm^2$) :

$$C = J / \upsilon \qquad (1)$$

where J is the current density ($\mu A/cm^2$) and υ is the potential scan rate (mV/s). The calculated double layer capacitance as a function of chain length of thiols is presented in Fig. 3.3. The variation is linear. This suggests that the thickness of the monolayer increases linearly with the number of carbons in the alkane chains. This behaviour is also compatible with the thiol monolayer acting as a capacitor since the capacitance should decrease with the distance between the capacitor plates.

2.3 Effect of the solubility of the alkanethiols on the reductive desorption chemisorbed process :

Monolayers of various alkane thiols (butanethiol C_4, hexanethiol C_6, nonanethiol C_9, dodecanethiol C_{12}, tetradecanethiol C_{14}, hexadecanethiol C_{16} and octadecanethiol C_{18}) were formed by incubating a flame-annealed Au(111) in an ethanolic solution of the thiols. The thiol-coated Au(111) electrode was immersed in 0.5 M KOH while the applied potential was held at - 0.3 V. Cyclic voltammograms (CVs) were recorded at room temperature between -0.2V and -1.2 V. Two types of voltammograms are observed. The first type has only one

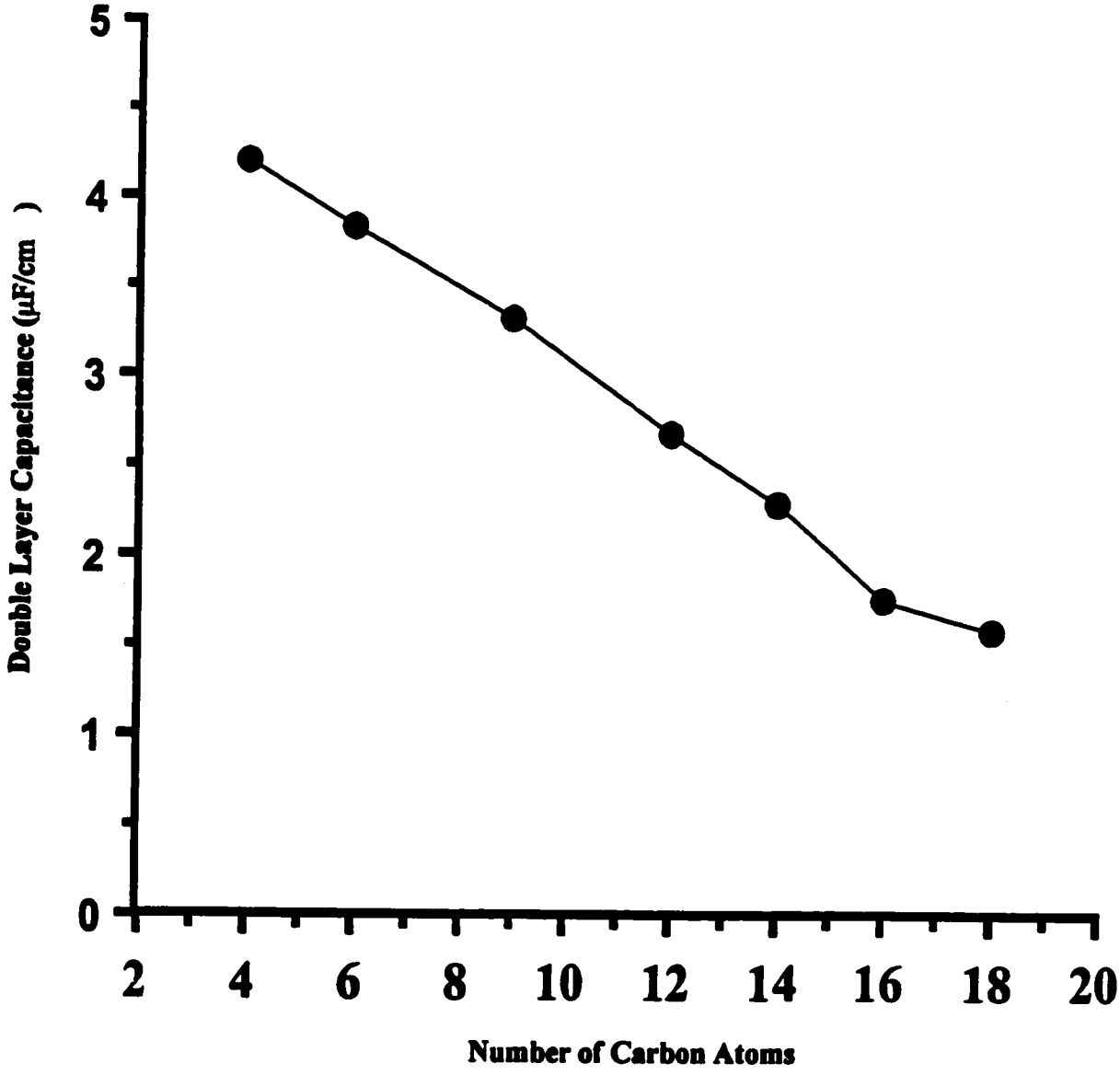

Figure 3.3 : Double layer capacitance vs number of carbon atoms for alkane thiols adsorbed on a Au(111) electrode measured at - 0.4 V in 0.5 M KOH at a potential scan rate of 20 mV/s and 20 °C.

reductive current peak. The second type is observed for the less soluble thiols, and it has two reductive current peaks and a substantial oxidative current is observed on the positive-going cycle. We will now describe each type of voltammogram. The cyclic voltammograms of butanethiol, hexanethiol and nonanethiol are shown in Fig. 3.4. We see that, for all compounds, the current is small (0.09-0.06 $\mu A/cm^2$) and constant between -0.2 V and - 0.6 V. We assign this observation to the blocking effect of the alkane thiols on the adsorption of electrolyte ions. When the potential reaches a sufficiently negative value, narrow reductive current peaks (with FWHM of 40 mV) are observed at - 0.780 (butanethiol), - 0.890 (hexanethiol) and - 0.965 V (nonanethiol). This reductive current peak is associated with one-electron reduction of the chemisorbed thiols. When the potential is reversed and scanned in the positive direction, no oxidative currents are observed at 20 mV/s. These results show that the reduced thiols are removed from the gold surface and diffuse into the bulk solution because these thiols are soluble in alkaline aqueous solutions. Butanethiol in 1 M NaOH has a solubility of 0.56 g/L in water [8,23]. The shape of the current peaks does not vary with the scan rate between 5 and 20 mV/s. The full width at half maximum (fwhm) of the reductive peak is $\approx 40 \pm 5$ mV. The width of the current peaks indicates that there is significant attractive interactions. We note that the total charge density is constant at 90 ± 5 $\mu C/cm^2$ (scan rate of 20 mV/s) for these three thiols. The observation of these constant properties suggests that these thiols are reduced by the same process.

Figure 3.5a shows the cyclic voltammograms of the longer chain thiols (dodecanethiol, tetradecanethiol, hexadecanethiol and octadecanethiol) recorded at a potential scan rate of 0.5 mV/s. This slow scan rate was used to resolve the fine structure of the reductive desorption peaks on the negative-going scan. We observed two reductive current peaks on the voltammograms of all the compounds. We note that as the chain length increases the oxidative current increases. The potential of the reductive and the oxidative current peaks associated with different chain length are listed in Table 1.

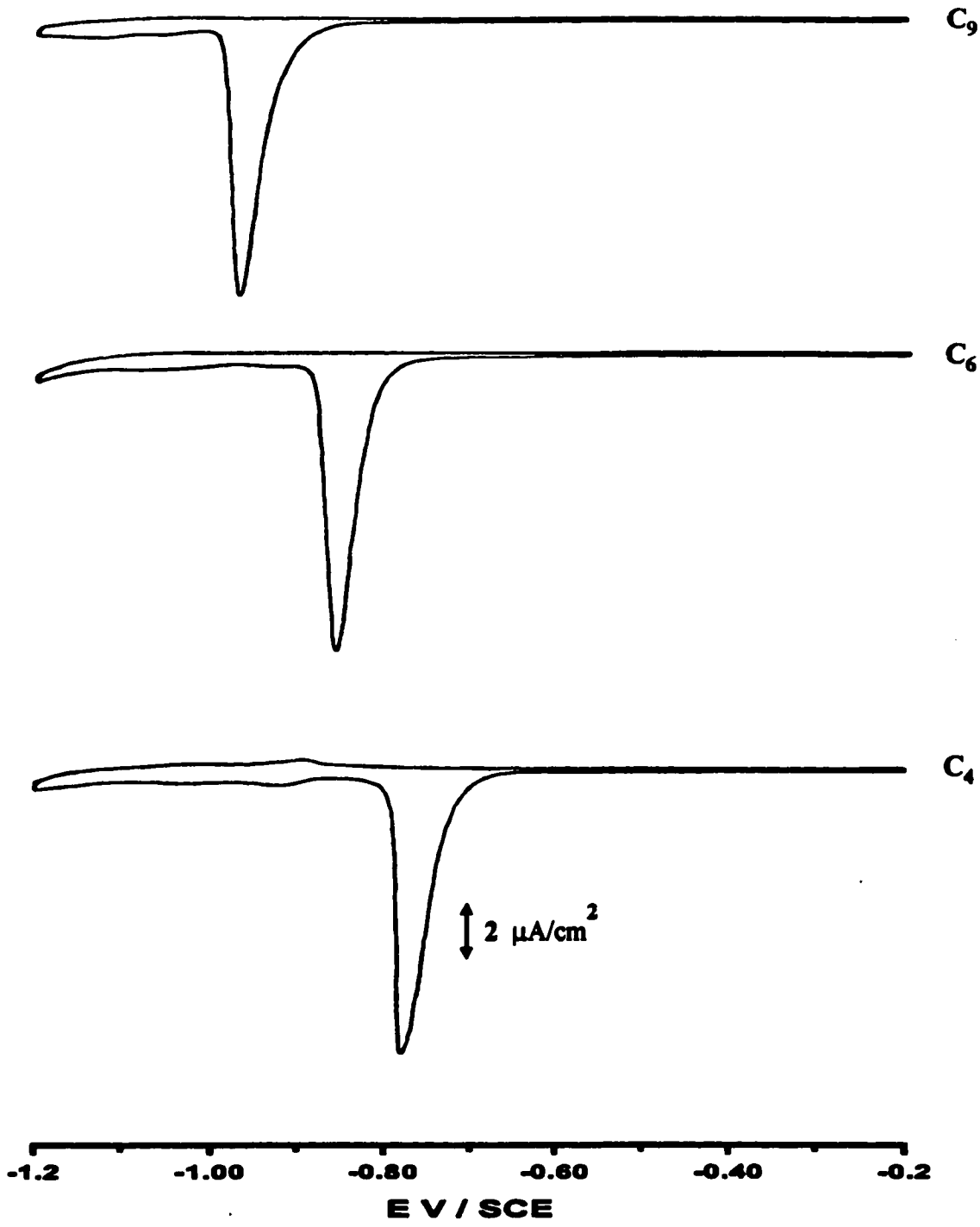

Figure 3.4 : Cyclic voltammograms of the reductive desorption and the oxidative redeposition of alkanethiols of different chain length on a Au(111) single crystal electrode measured in 0.5 M KOH at a scan rate of 20 mV/s at 20 ^{o}C.

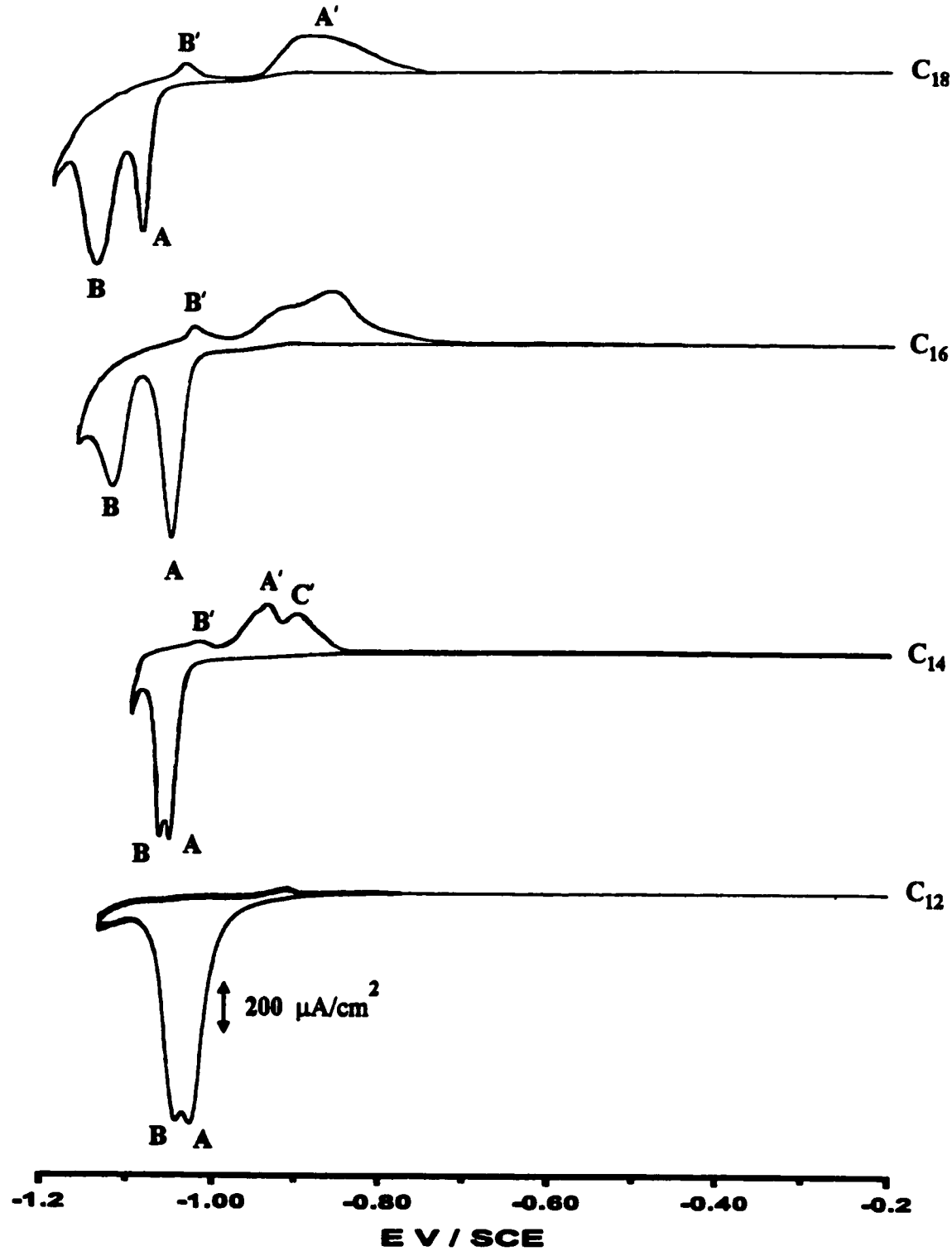

Figure 3. 5a : Cyclic voltammograms of the reductive desorption and the oxidative redeposition of alkanethiols of different chain length on a Au(111) single crystal electrode measured in 0.5 M KOH at a scan rate of 0.5 mV/s at 20 °C.

Table 1. Reductive desorption peak potentials and oxidative redeposition peak potentials of alkanethiols chemisorbed on Au(111) recorded in 0.1 M KOH :

Chain Length	Peak A (± 5 mV)	Peak B (± 5 mV)	Peak A' (± 5 mV)	Peak B' (± 5 mV)	Peak C' (± 5 mV)
Dodecanethiol	-1.025	-1.04	-0.91	———	———
Tetradecanethiol	-1.045	-1.06	-0.935	-1.015	-0.895
Hexadecanethiol	-1.05	-1.12	-0.93	-1.03	-0.865
Octadecanethiol	-1.09	-1.14	———	———	———

Table 1 shows that the reductive peaks are shifted to more negative potential. The separation between peaks A and B also increases with chain length. It changes from 15 to 70 mV. The shift of the peak B is larger than that of the peak A and is presented in Figure 3.5b. The negative shift is assigned to the increase blocking effectiveness of long chain alkanethiols and a result of more difficulty is the ion permeation process. The fact that the shifts of the reductive peaks are different suggests that they are due to different processes. Similarly to the shorter chain thiols, the reductive charge densities remain constant at 85 ± 5 $\mu C/cm^2$ for C_{12} and 88 ± 5 $\mu C/cm^2$ for C_{14}.

The oxidative current peaks grow in intensity. However, they are observed at the same potentials. We can see in Table 1 that the position of the oxidative current peaks does not change significantly with increasing chain length. However, the associated oxidative charge densities are 3 ± 1 $\mu C/cm^2$ for C_{12} and 78 ± 2 $\mu C/cm^2$ for C_{14}, respectively. The smaller value of the oxidative charge density of C_{12} is due to the fact that C_{12} thiols are more soluble and diffuse away into the bulk solution during the potential scan. To support this view, experiments were performed at 20 mV/s and are presented in Figure 3.6a. They revealed that the average reductive charge density is 90 ± 5 $\mu C/cm^2$ whereas the oxidative charge density increases to 31 ± 2 $\mu C/cm^2$ for the first cycle. Subsequent reductive cycles 2, 3 and 4 gave 33, 16, 7.7 ± 5 $\mu C/cm^2$ and are shown in Figure 3.6b. These results suggest that it is possible

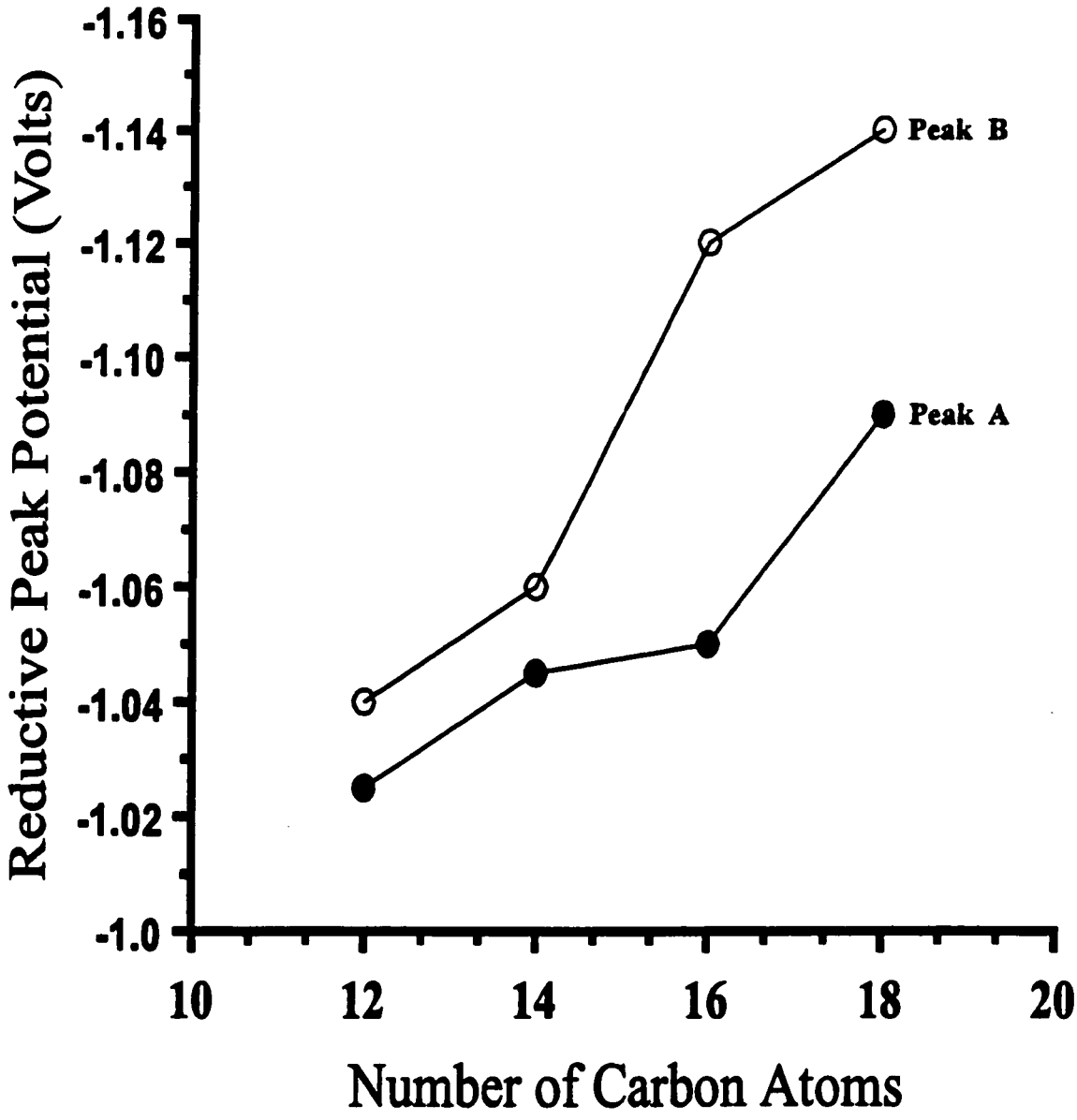

Figure 3.5b : Reductive peak potential vs the number of carbon atoms of thiols adsorbed at a Au(111) electrode measured in 0.5 M KOH at a potential scan rate of 0.5 mV/s and 20 $^{\circ}$C.

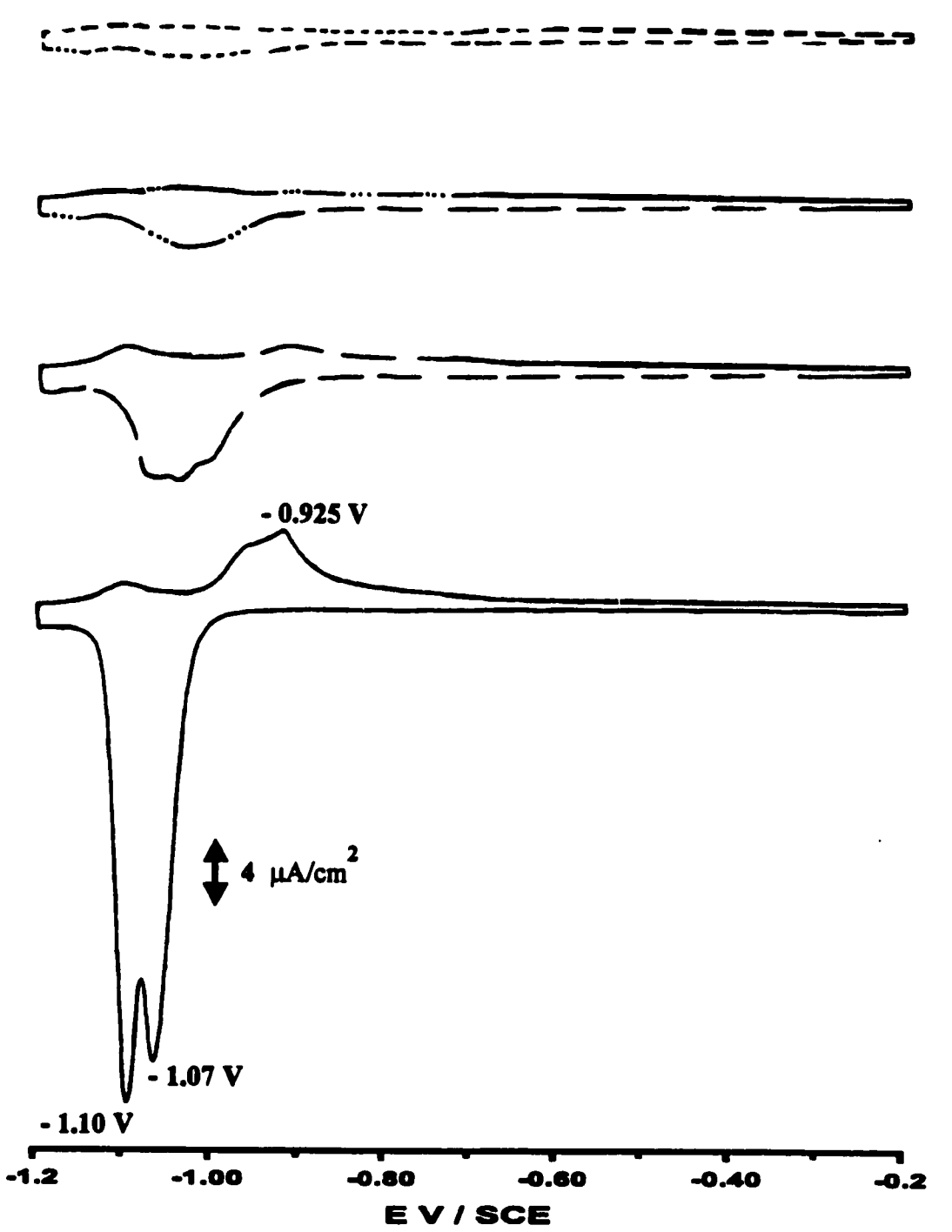

Figure 3.6a : Voltammograms of the reductive desorption of a dodecanethiol SAM at a single crystal gold (111) electrode recorded in 0.5 M KOH at a scan rate of 20 mV/s at 20 °C.

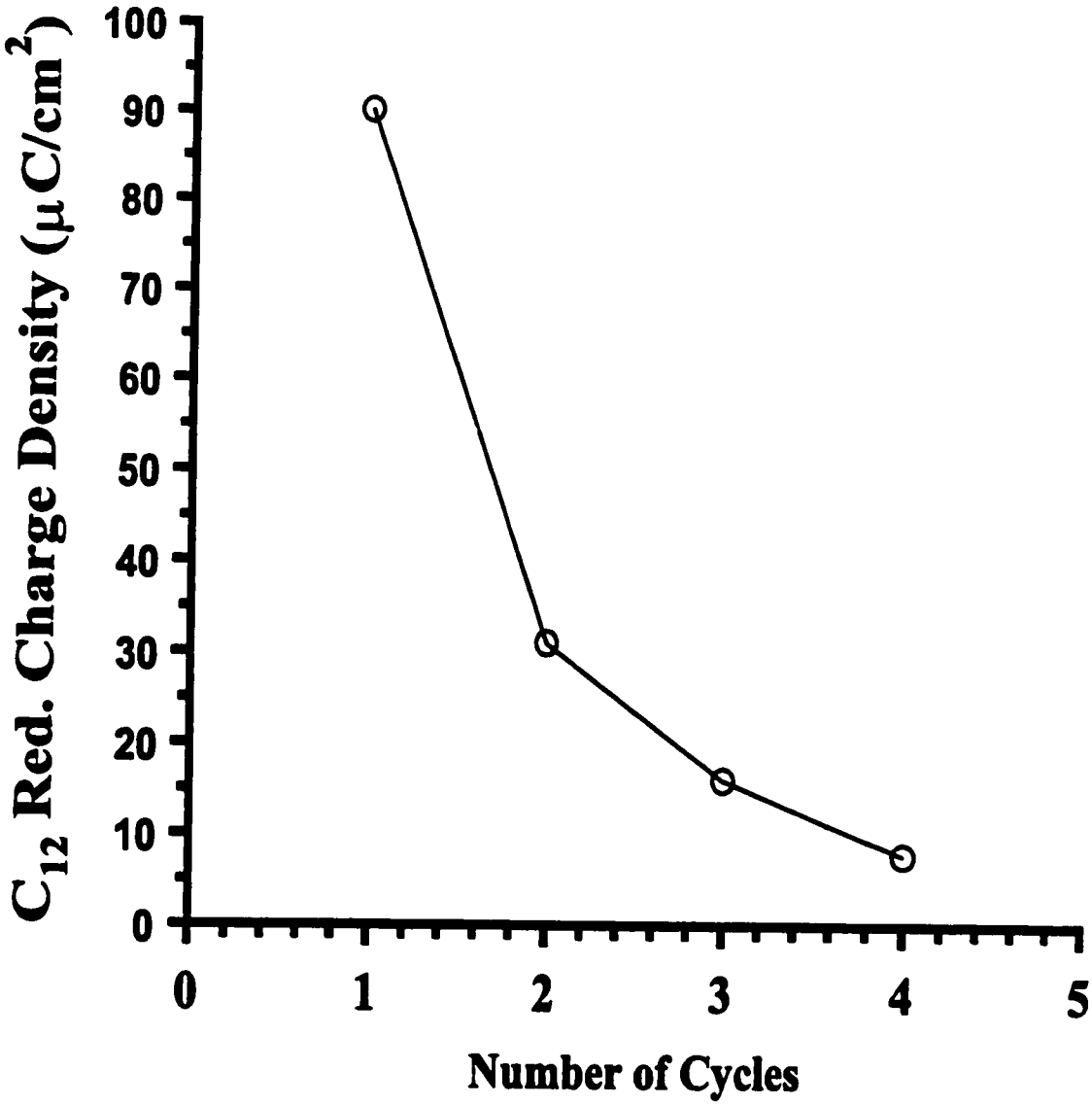

Figure 3.6b : Reductive charge density measured after various numbers of cyclic voltammograms for a dodecanethiol SAM coated single crystal Au(111) electrode. Measurements were done in 0.5 M KOH at a potential scan of 20 mV/s at 20 °C.

with even a higher scan rate than 20 mV/s to oxidatively redeposit more C_{12} before they diffuse into the bulk solution. For C_{16} and C_{18} thiols, two well separated reductive peaks and three oxidative peaks are observed. The corresponding total reductive charge densities are 88 ± 2 and $90 \pm 2\ \mu C/cm^2$. The total oxidative charge densities are 86 ± 2 and $85 \pm 2\ \mu C/cm^2$, respectively. The calculated double layer capacitances of the coated long chain thiols are in the range of 2.3 to 1.5 $\mu F/cm^2$ at a potential scan rate of 20 mV/s. We see that for these two thiols the absolute values of the reductive and oxidative charges are equal. Thus, the thiols are quantitatively redeposited. This result is quite interesting since the same molecules go from a chemisorbed state to a physisorbed state reversibly. The stability of these SAMs of thiols was tested via cycling 20 cycles between the two potential limits and getting the same CV. The appearance of multiple current peaks suggests a change in the mechanism of reduction and oxidative redeposition for the insoluble thiols.

The surface coverage, Γ : $\Gamma = Q_{RedSAM}/n\ F\ A$, of each thiolate was estimated from the charge passed for the reduction of the thiol during the cathodic sweep. Q_{RedSAM} is the charge passed in $\mu C/cm^2$; n is the number of electrons involved in the electron transfer process (here n = 1); F is the Faraday constant; A is the geometric surface area of the gold (111) working electrode in cm^2. Values of Q_{RedSAM} were obtained via integration of the area under the reductive desorption wave and were corrected for the capacitive double layer charge contributions. The thiol surface concentration found to be between 6.7 and 7.8 x 10^{-10} mol/cm^2, corresponds to an average value of 7.3×10^{-10} (± 9 %) mol/cm^2. This value is compatible with a thiol monolayer coverage of 7.6×10^{-10} mol/cm^2 from diffraction studies [24,25].

2.4 The effect of ion permeation on the reduction of chemisorbed thiols :

To further verify our assignment of the negative shift of the reductive current peaks with the increase of the chain length to the blocking effect of the monolayer, we examined this process in different electrolyte solutions. Potassium hydroxide and lithium hydroxide were used as aqueous electrolytes since their solvated radii differ. The ionic radii of the cations are

1.33 and 0.6 Å, respectively. Their solvation numbers are 4 ± 2 and 5 ± 1, whereas the diffusion coefficients (D) of K^+ and Li^+ ions in aqueous solutions are 1.569×10^{-5} and 1.028×10^{-5} cm^2/sec [26,27].

We chose the monolayer of hexadecanethiols as the model system for this study and all others in this chapter since the reductive and oxidative current peaks are relatively well resolved and the effects of the composition of the electrolyte solutions should be more clearly visible. Cyclic voltammograms of the reductive desorption and the subsequent oxidative redeposition of hexadecanethiols chemisorbed on Au(111) in 0.5 M KOH and in 0.5 M LiOH were recorded at a potential scan rate of 20 mV/s. The electrode potential is first scanned in the negative direction from - 0.2 to -1.3 V and then back to - 0.2 V. The resulting voltammograms are shown in Fig. 3.7. The reduction of thiols in KOH starts at a more positive potential than in LiOH. However, two reductive current peaks are observed in both solutions. In LiOH, the reductive peak B overlaps with the hydrogen evolution. There is a decomposition of the water molecules to produce hydrogen when the electrode is at a potential more negative than - 1.25 V. This process limits the range of potential that is accessible in aqueous solutions.

A comparison of the reductive and the oxidative peak potentials, total charge densities and peak separation of hexadecanethiol SAMs at a Au(111) electrode in aqueous KOH and LiOH solutions are presented in Table 2.

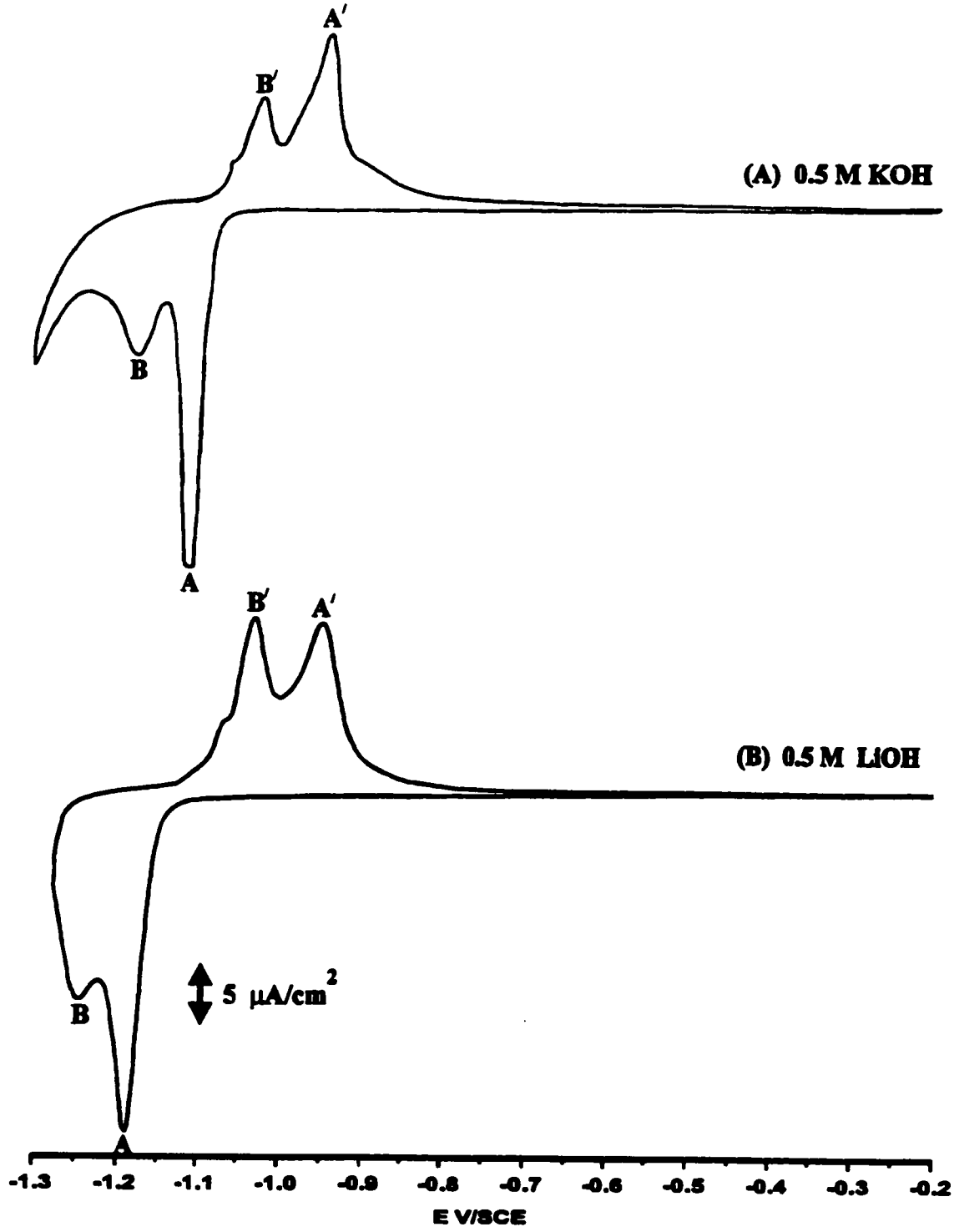

Figure 3.7 : Cyclic voltammograms of the reductive desorption and the oxidative redeposition of hexadecanethiol monolayers adsorbed on Au(111) in two different electrolytes. Measurements were done at a scan rate of 20 mV/s at 20 ^{0}C.

Table 2. Peak potentials, charge densities, and oxidative peak separation, ΔE_{ps}, of a hexadecanethiol monolayer adsorbed on Au(111) recorded in alkaline and neutral solutions:

Electrolyte Solution	Peak A (V)	Peak B (V)	Reductive σ ($\mu C/cm^2$)	Peak A′ (V)	Peak B′ (V)	Oxidative σ ($\mu C/cm^2$)	ΔEps (mV)
0.5 M KOH	-1.12	-1.18	90 ± 3	-0.94	-1.02	85 ± 3	~ 80
0.5 M LiOH	-1.19	-1.24	80 ± 3	-0.935	-1.015	79 ± 3	~ 80

The reductive peak potentials (E_{PS}) are different. The peak separations are 70 and 30 mV. The reduction process is more influenced by the cation of the electrolyte. Li^+ which has the largest solvated radii and causes the reductive current peaks to shift in the negative direction relative to the results obtained in KOH. It is more difficult for the more solvated cation to diffuse through the organic monolayer, either because of its solvated size or because it needs to be desolvated before diffusing. However, from these results we cannot say which process occurs. The observation that the relative magnitudes and separation between the peaks A and B is not modified by the electrolyte's cation suggests that the reduction process is unchanged but shifted to more negative potentials.

The potentials of the oxidative current peaks are less influenced by the cation of the electrolyte. There is only an increase in the magnitude of the peak B′ in LiOH. The small influence of the cation on the oxidative peaks indicate that the rate of the oxidative redeposition of the physisorbed thiolates is not limited by the removal of the cations from the electrode surface. This is reasonable since the cations are not chemically bound to the electrode surface.

2.5 Relationship between the reductive and the oxidative current peaks :

The relationship between the reductive peaks and the oxidative peaks was examined in closer detail by doing "window-opening" experiments. "Window-opening" is a technique in which one of the potential limits of a cyclic voltammogram is increased gradually over a

range where an oxidation or reduction occurs. A correlation between the reductive and oxidative current peaks can be established by noting at which potential reductive and oxidative current peaks are appearing.

The electrode potential is first scanned from - 0.2 to - 1.16 V, just after the first reductive peak, and scanned back to - 0.2 V. This is shown in Figure 3.8. This potential range clearly shows that the reductive peak A at E_p - 1.14 V and the oxidative peak A′ at - 0.930 V are related. The associated charge densities are 50 ± 5 and 36 ± 5 $\mu C/cm^2$, respectively. Increasing the negative switching potential unveils the correlation between the second reductive peak B and the second oxidative peak B′. When the E_λ is increased to - 1.26 V, just before the onset of the hydrogen evolution, two reductive peaks and two oxidative peaks are observed and shown in Figure 3.8b. The E_{ps} for the new reductive peak B and the oxidative peak B′ occur at - 1.20 and - 1.00V, respectively. The total reductive and the total oxidative charge densities are 88 ± 5 and 74 ± 5 $\mu C/cm^2$. Furthermore, octadecanethiol SAMs were also examined (not shown) and they gave results consistent with those of hexadecanethiol SAMs. The reductive charge densities are equal to the oxidative charge density within the experimental error of ± 6-7 %.

The relationships between the reductive desorption peak A and the oxidative redeposition peak A′ and between peak B and peak B′ of hexadecanethiol SAMs at single crystal gold (111) electrode are examined in 0.5 M KOH at 5°, 20°, 35° and 55 °C at a scan rate of 20 mV/s. These window opening experiments were performed by the variation of the positive E_λ switching potential and are shown in Figures 3.9-3.12. The electrode potential is first scanned from - 0.2 to - 1.2 V and then scanned back. In the way back, the positive E_λ switching potential is increased gradually start switching at - 1.0 then back to -1.2 then to - 0.9 V and so on. Finally, a complete voltammogram is recorded between - 0.2 and - 1.2 V. These data clearly confirm the relationship between the reductive and oxidative peaks. When only peak B′ is seen on the anodic scan, one reductive peak B is observed. These results also reveal that increasing the temperature causes the peaks to shift toward more

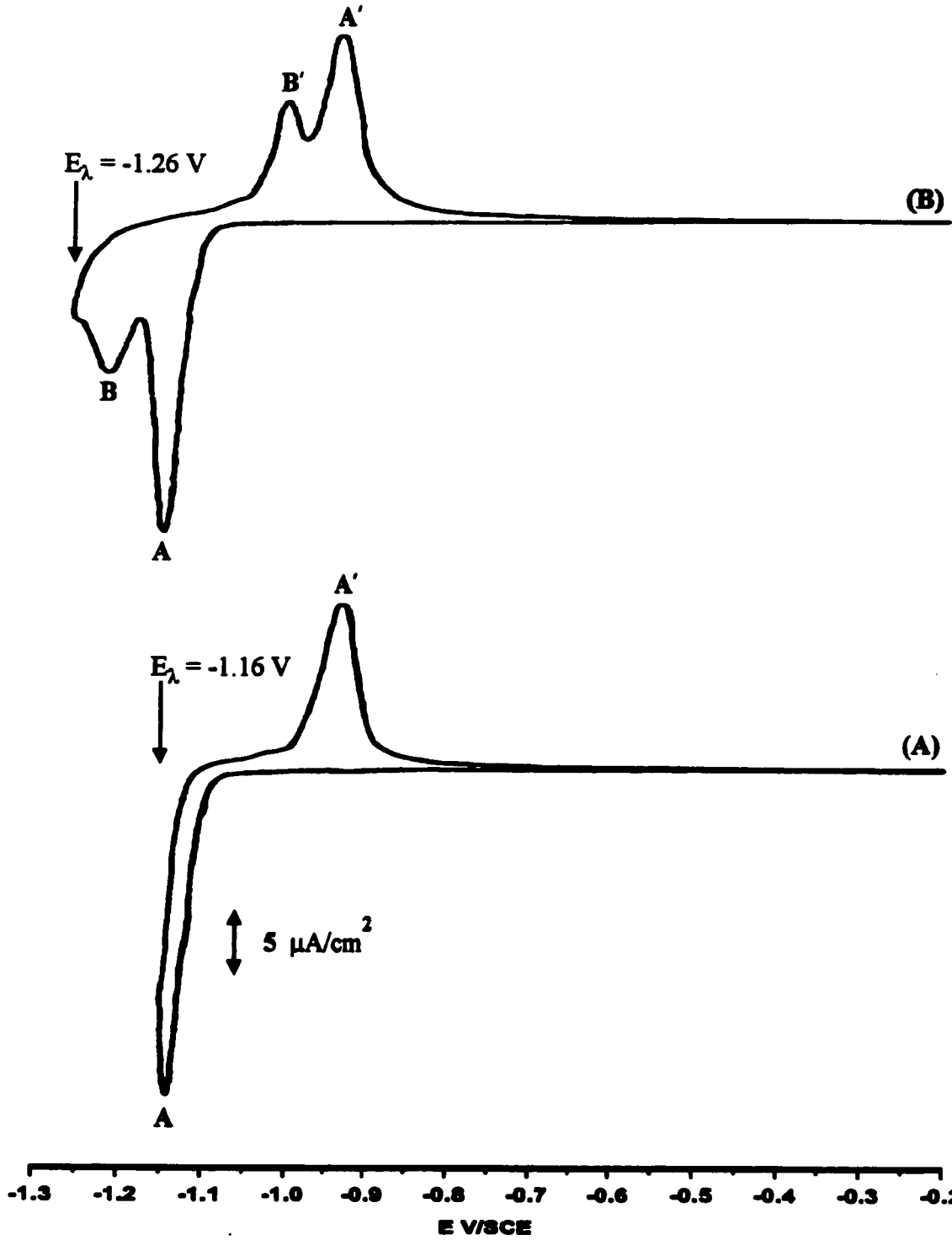

Figure 3.8 : Window opening voltammograms of the reductive desorption and the oxidative redeposition of an hexadecanethiol monolayer adsorbed on Au(111). Measurements were done in 0.1M KOH at a scan rate of 20 mV /s at 20 $^{\circ}$C. E_λ is the negative limit of the potential.

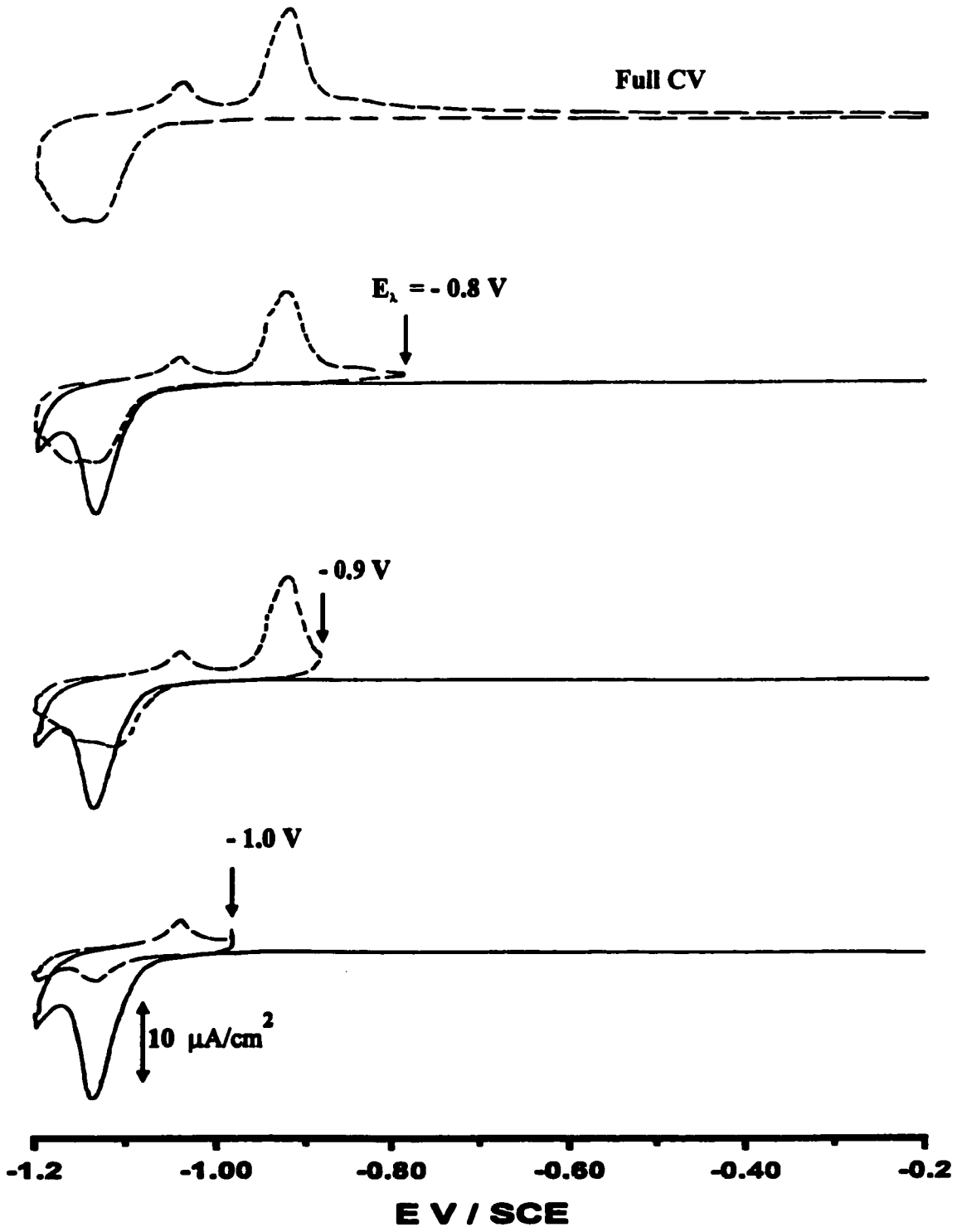

Figure 3.9 : Window opening voltammograms of a Au(111) single crystal electrode modified with a monolayer of hexadecanethiols recorded in 0.5 M KOH at a scan rate of 20 mV/s at 5 $^{\circ}$C (see text for detail).

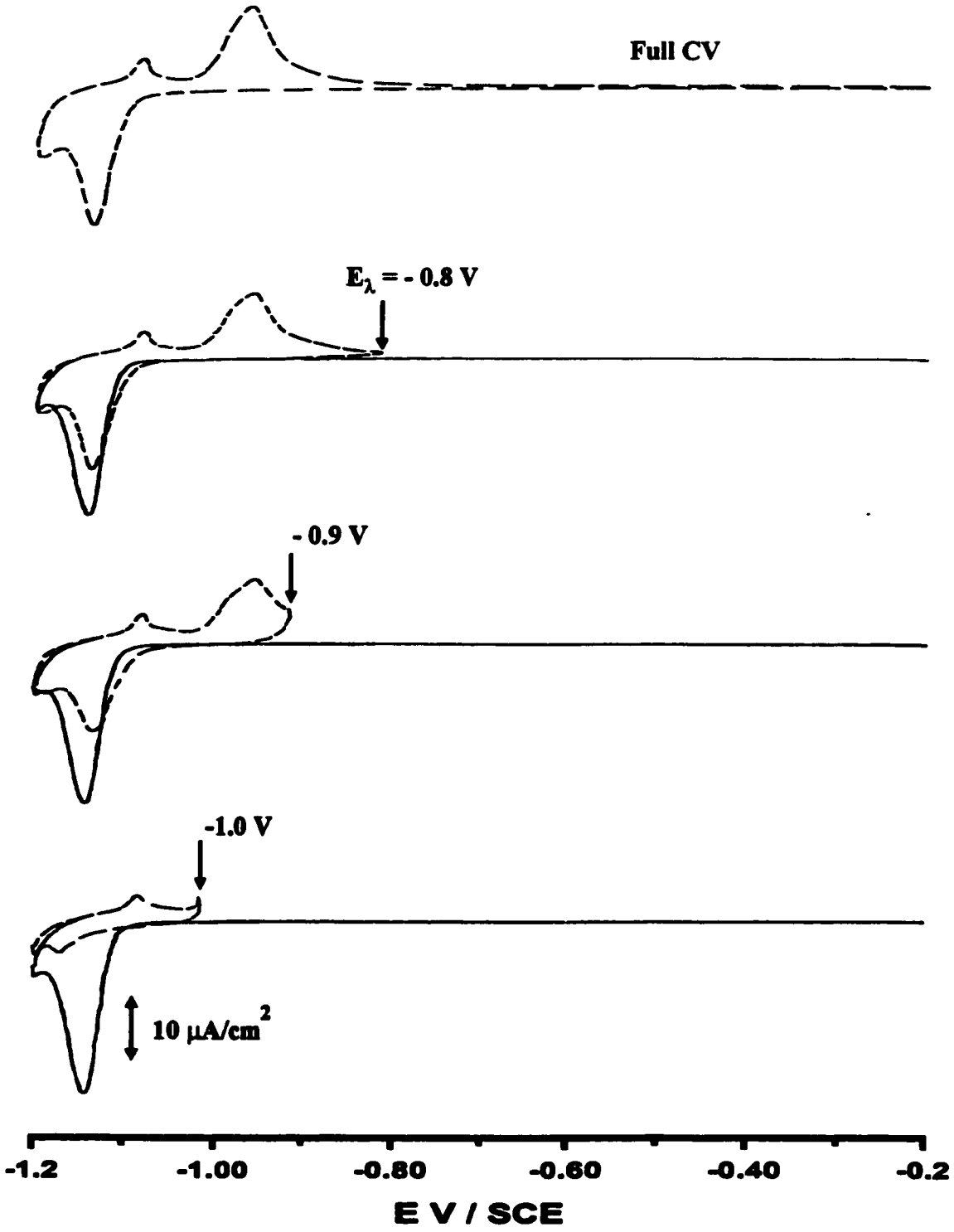

Figure 3.10 : Window opening voltammograms of a Au(111) single crystal electrode modified with a monolayer of hexadecanethiols recorded in 0.5 M KOH at a scan rate of 20 mV/s at 20 °C (see text for detail).

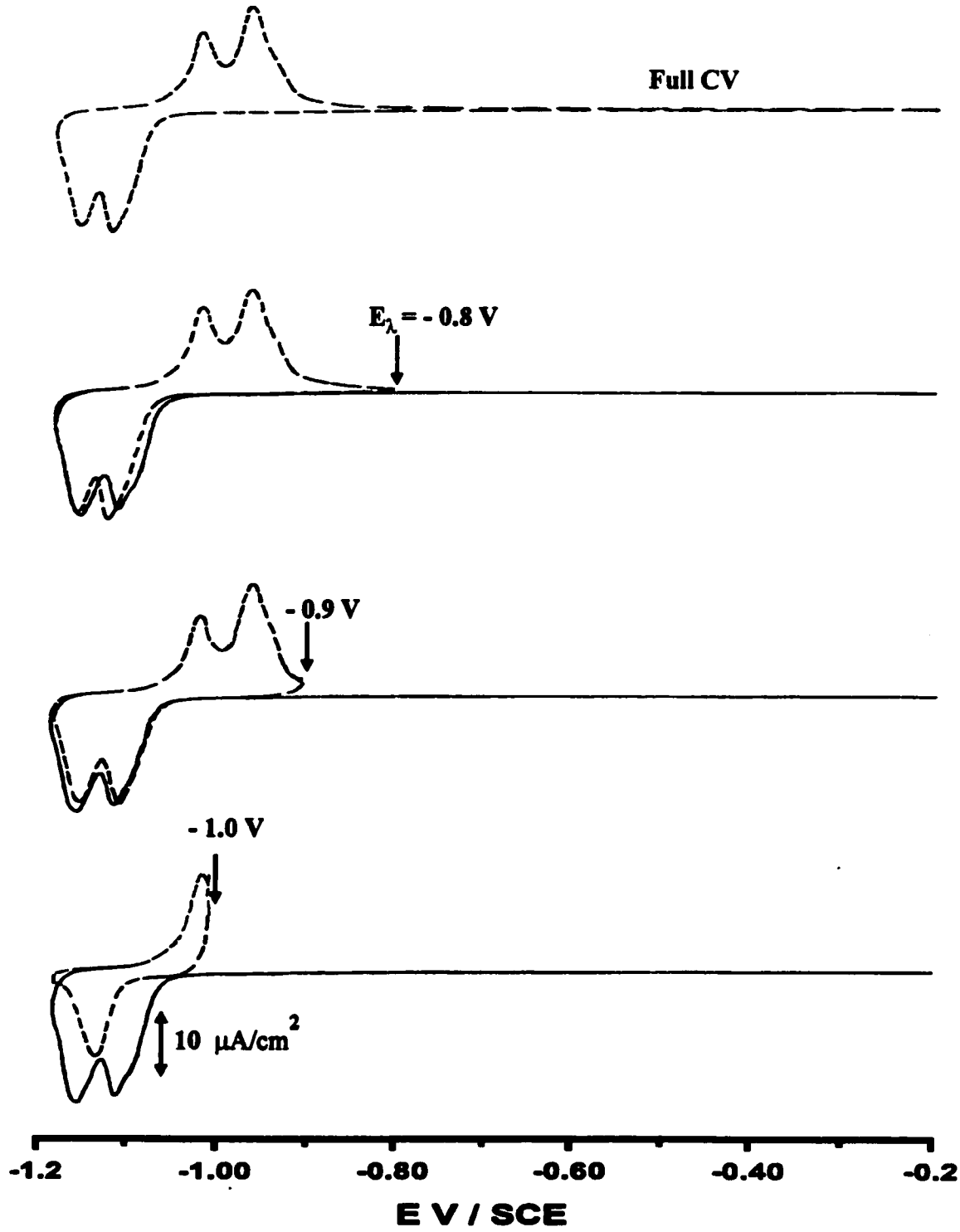

Figure 3.11 : Window opening voltammograms of a Au(111) single crystal electrode modified with a monolayer of hexadecanethiols recorded in 0.5 M KOH at a scan rate of 20 mV/s at 35 ^{o}C (see text for detail).

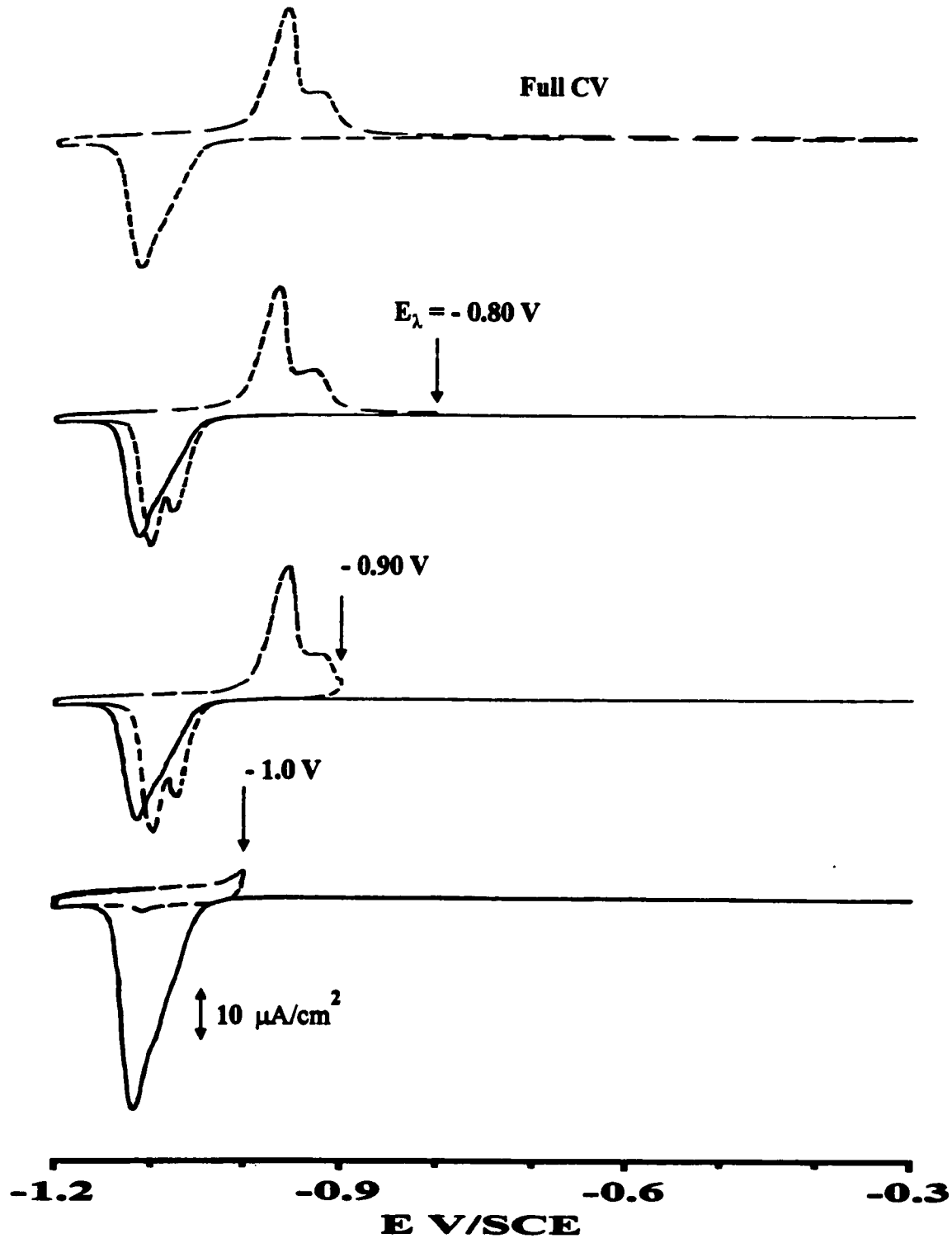

Figure 3.12 : Window opening voltammograms of a Au(111) single crystal electrode modified with a monolayer of hexadecanethiols recorded in 0.5 M KOH at a scan rate of 20 mV/s at 55 $^{\circ}$C (see text for detail).

positive potentials (in chapter 5, we examine the temperature effects in more detail).

Figures 3.13a, 3.13b and 3.13c are potential scan/potential hold/oxidative cyclic voltammetric measurements of Au(111) modified with a hexadecanethiol SAM in 100 mM KOH solution at a potential scan rate of 20 mV/s . The potential scan is initiated at - 0.3 V down to various final reductive potentials between - 1.06 and - 1.2 V . This is followed by holding the working electrode potential at different reductive potentials for one minute and then recording the oxidative redeposition process. Holding the reductive potential at - 1.06 V and above does not show any oxidative peak since these final potentials are still within the double layer region and the gold surface is blocked effectively by the hexadecanethiol monolayer.

However, between the - 1.08 and - 1.10 V reductive potential range, the oxidative going direction voltammograms show a single oxidative redeposition peak A′ at - 0.94 V, indicative of two related processes. Potential scan and hold experiments at - 1.14 V and up to - 1.2 V show two oxidative redeposition peaks, B′ at - 0.99 V and A′ at - 0.94 V. The average normalized charge densities as a function of the final reductive potential with error bars are shown in Fig. 3.13c. The reductive peak A has a charge of $45 \pm 3\ \mu C/cm^2$ while peak B has a charge of $25 \pm 3\ \mu C/cm^2$.

2.6 The effect of pH and ionic strength on the oxidative redeposition of physisorbed thiolates :

The reductive current peaks are influenced by the nature of the electrolyte's cation. The reduced thiols are negatively charged and they also have a basic character (pK_a = 10-12). We can thus expect that the voltammogram will be influenced by the pH and the ionic strength of the electrolyte solution. The pH could have a bigger influence on the oxidative current peaks since the thiolates are only physisorbed.

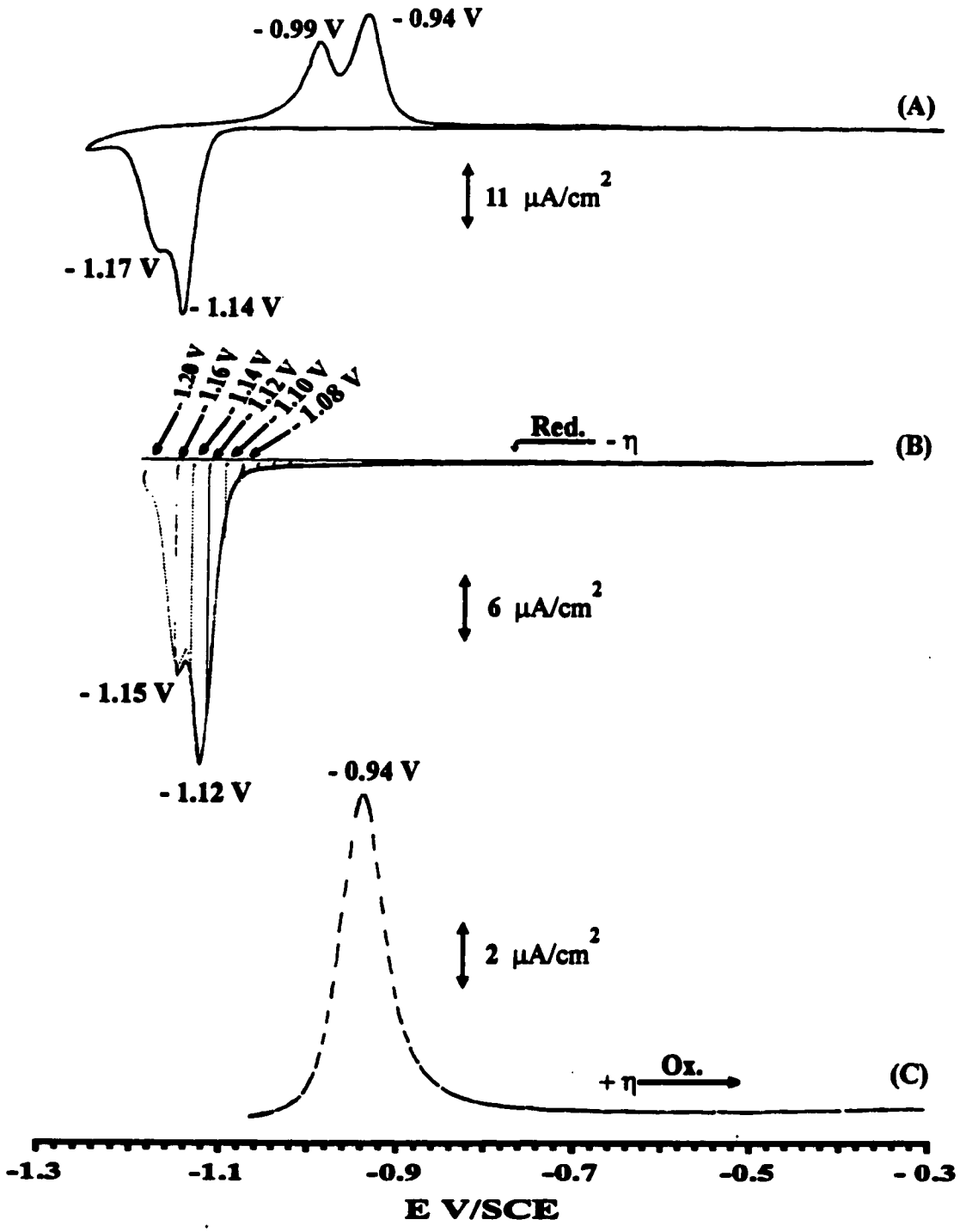

Figure 3.13a : (a) Voltammogram of the reductive desorption and the oxidative redeposition of hexadecanethiols adsorbed on Au(111); (b) Reductive desorption "window-opening" potentials; (c) Oxidative redeposition associated with the reductive final potential of - 1.08 V. All measurements were done in 0.1M KOH at a scan rate of 20 mV/s.

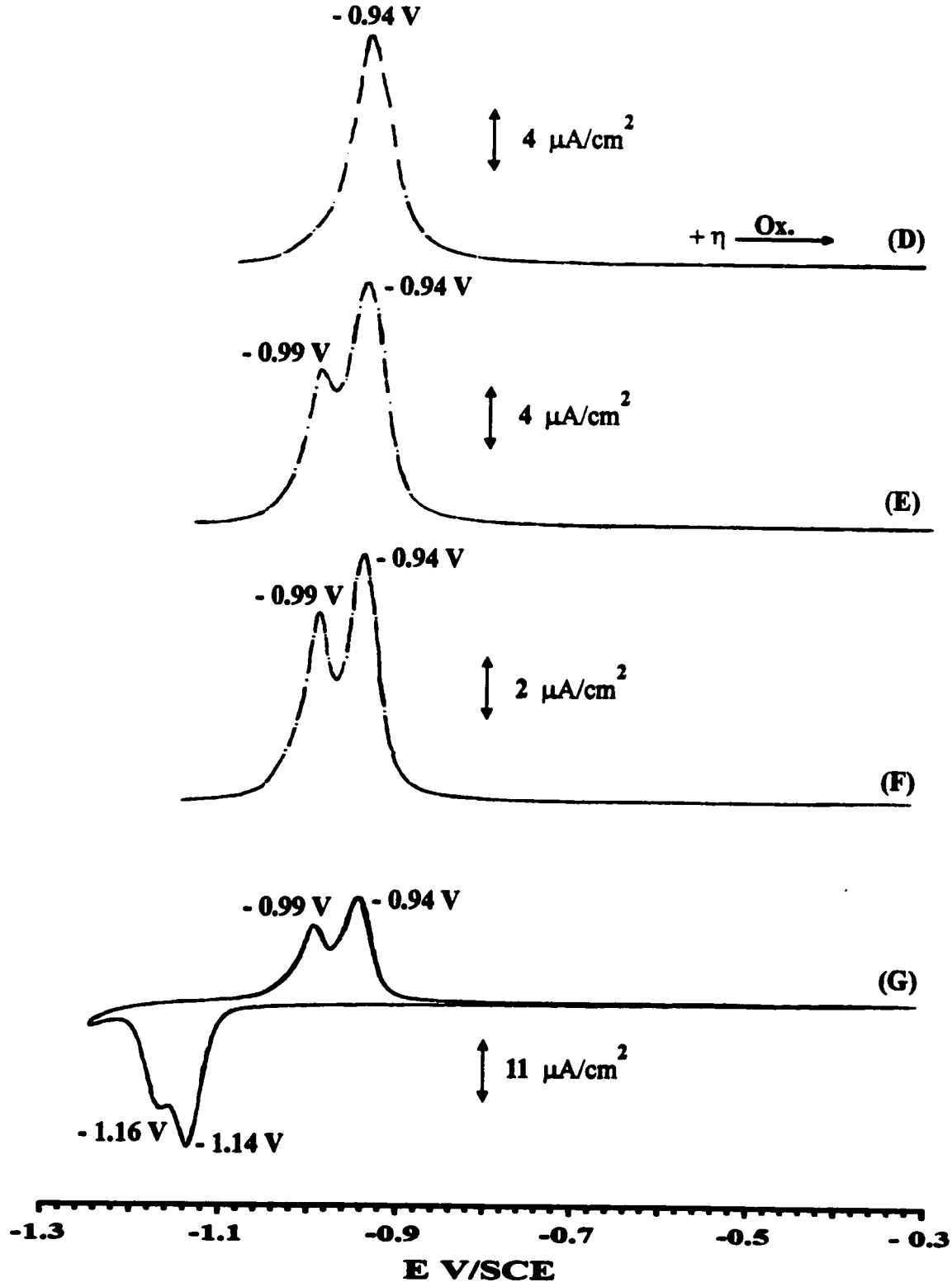

Figure 3.13b : (d) - 1.10 V; (e) - 1.12 V; (f) - 1.14 V; (g) - 1.16 to - 1.2 V. All measurements were done in 0.1 M KOH and a potential scan rate of 20 mV/s.

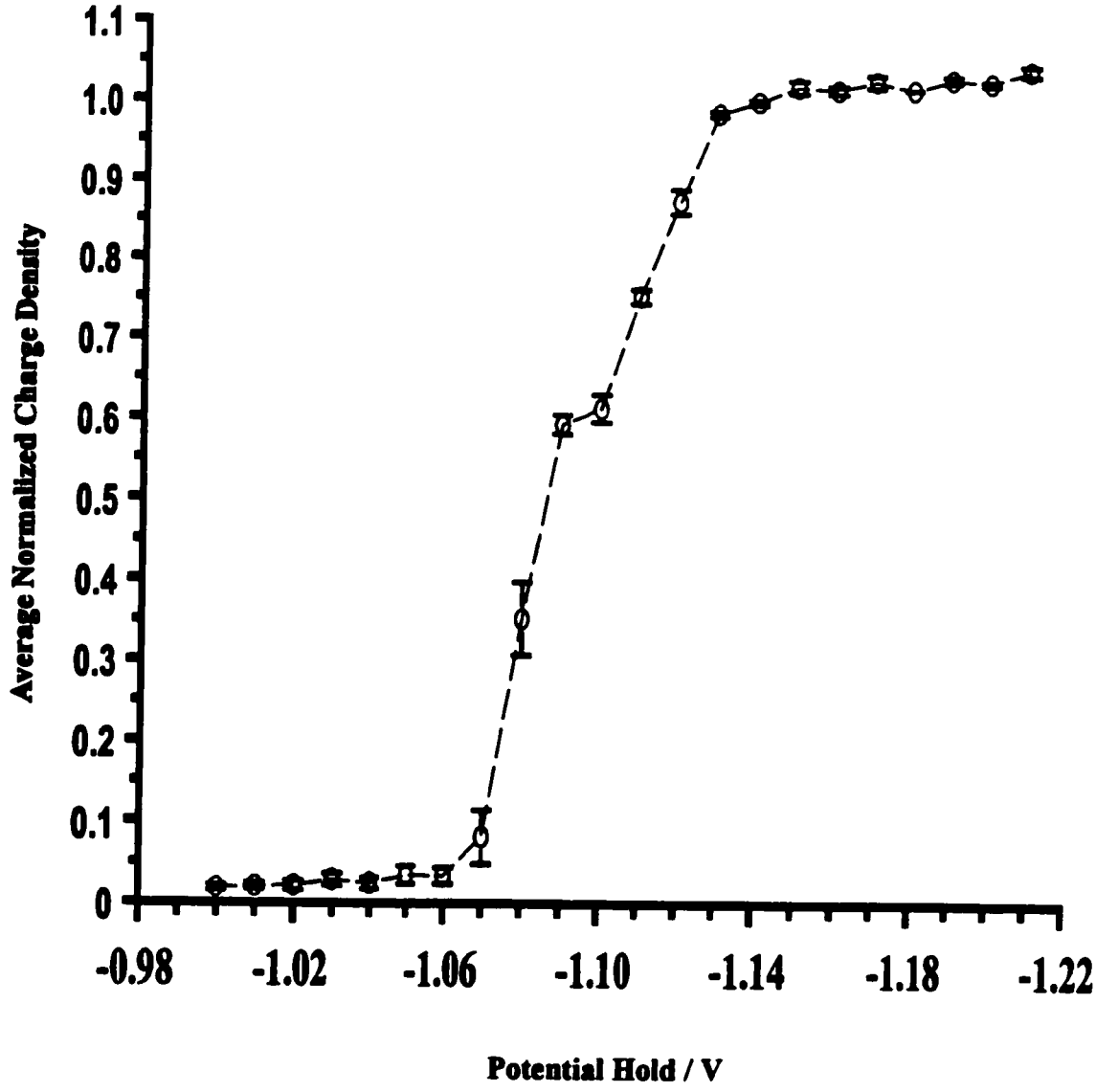

Figure 3.13c : Normalized charge density measured by integrating the oxidative current of potential scan from - 0.3 V to various negative potentials and then holding for 1 min and then recording the oxidative re-deposition voltammogram of a Au(111) electrode modified by hexa-decanethiol in 0.1 M KOH at a potential scan rate of 20 mV/s at room temperature. The oxidative charge is then divided by the oxidative charge of a voltammogram recorded between - 0.3 and - 1.3 V.

A series of voltammograms were recorded in solutions of KOH at different concentrations. The potential is first scanned from - 0.2 to - 1.3 V and then reversed back to - 1.1 V (just before the onset of the oxidative peaks). The potential was then held at - 1.1 V for various times (t_H) : 1, 5, 15 and 30 min. The holding time was used to examine the stability of the physisorbed monolayer of hexadecanethiolates.

Figure 3.14 presents voltammograms of a hexadecanethiol modified Au(111) electrode in 1.0 M KOH solution. Holding the working electrode at - 1.1 V on the positive potential scan direction for 1 to 5 min shows no change. However, after 5 min the oxidative peaks are influenced more strongly than the reductive peaks. The overlap of the oxidative peaks increases gradually with increasing holding times until they merge into a broad oxidative peak with a long tail. This broad oxidative peak shifts toward more positive overpotential at longer holding time.

Figure 3.15 shows cyclic voltammograms of hexadecanethiols adsorbed on gold (111) in 0.5 M KOH as a function of holding time. A comparison of Figures 3.15a-d reveals important changes as the holding time increases from 1 min to 30 min. The oxidative current peaks A′ and B′ observed for holding times of up to 5 minutes, are quite similar to the one obtained with no holding time (see Fig. 3.7a). Their peaks' potentials are the same at - 0.94 V for A′ and - 1.02 V for B′ (± 10 mV). However, we note an increase in the positive going tail of peak A′. We also see that there is no measurable change of the total oxidative charge measured between - 1.1 and - 0.3 V relative to the one measured in one continuous cycle (90 ± 5 and 85 ± 5 $\mu C/cm^2$). The potentials at which the reductive peaks A and B are observed are also similar to the ones observed in Fig. 3.7a. (Two reductive current peaks are observed at - 1.12 and - 1.17 V after t_H of 1 min). These results show that the physisorbed monolayer of thiolates is quite stable over a period of at least 5 minutes. When the potential is held for 15 min only one broad oxidative current peak is observed. Its maximum is located at ~ - 0.88 V. A very small current peak is visible at ~ - 1.00 V. There is also a decrease in the integrated oxidative charge to 70 ± 5 $\mu C/cm^2$. Thus, a small quantity of thiolates has left

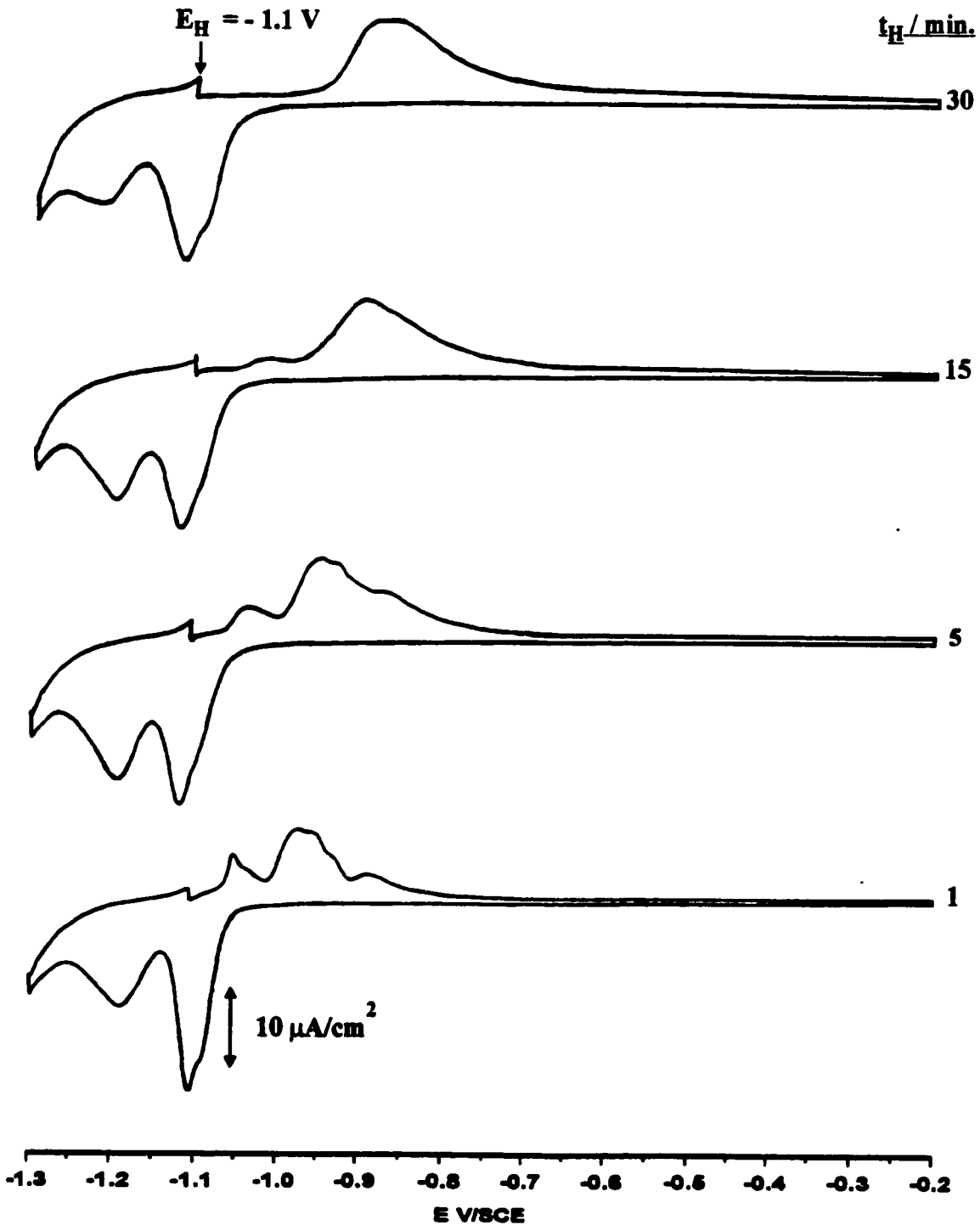

Figure 3.14 : Cyclic voltammograms of the reductive desorption and the oxidative redeposition of hexadecanethiols adsorbed on Au(111) recorded in 1.0 M KOH at a scan rate of 20 mV/s at 25 °C. E_H and t_H are the potential hold and the hold time (see text).

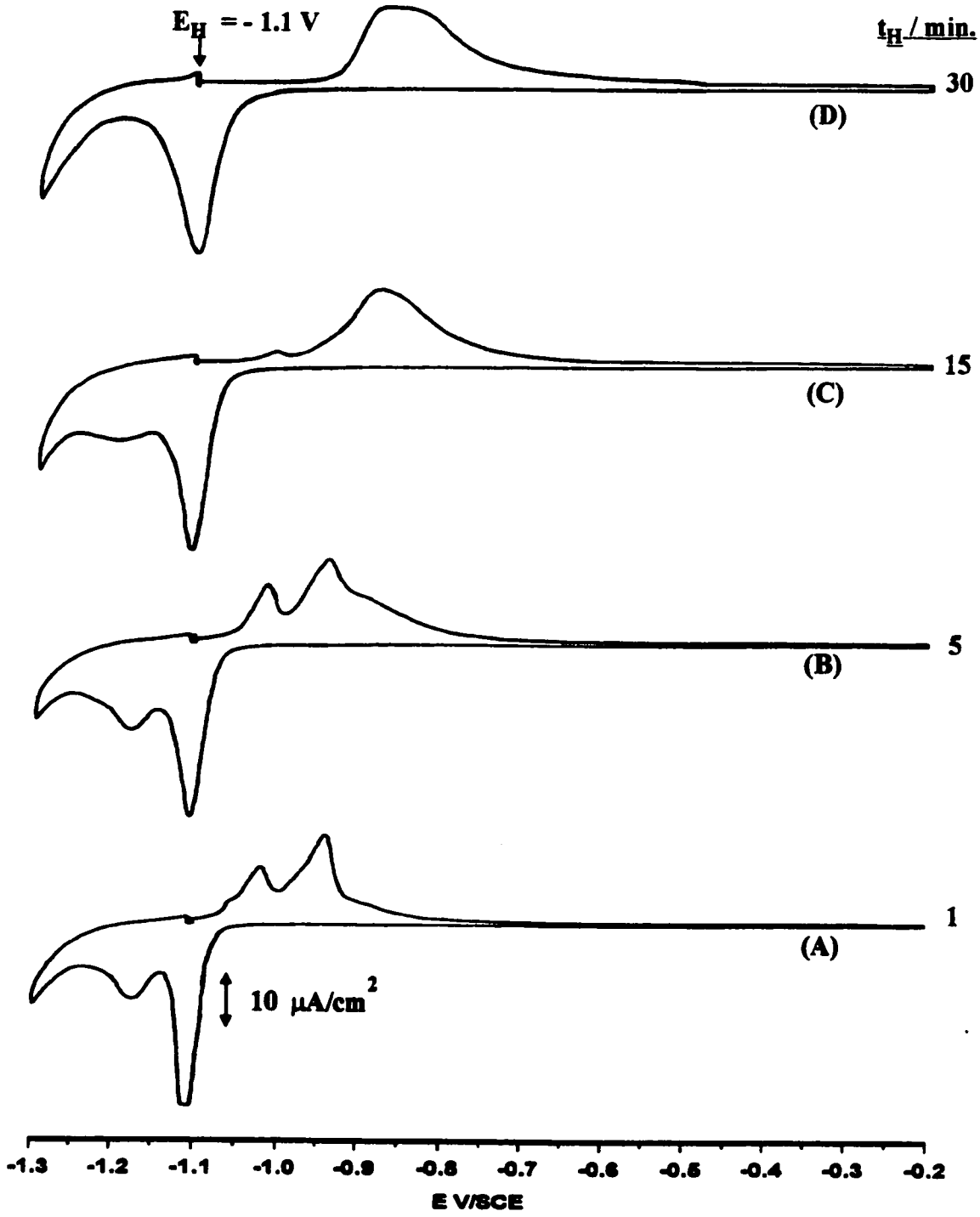

Figure 3.15 : Cyclic voltammograms of the reductive desorption and the oxidative redeposition of hexadecanethiols adsorbed on Au(111) recorded in 0.5 M KOH at a scan rate of 20 mV/s at 25 °C. E_H and t_H are the potential hold and the hold time (see text).

the electrode surface. The reductive current peaks A and B only decrease in intensity. Their relative magnitudes and the potentials at which they are observed do not change. Thus, the changes in the oxidative redeposition does not influence the reduction. We can conclude that, once the thiolates are redeposited they form a monolayer with a packing density similar to the original monolayer. A holding time of 30 minutes leads to a further shift of the oxidative current peak to more positive potentials and to a decrease of the oxidative charge to 67 ± 5 $\mu C/cm^2$. The reductive current peak B is absent from the negative-going potential scan. Only peak A is observed at - 1.1 V. The shift toward a positive potential of the oxidative current peak for the longer holding time shows that the reduced thiols become more difficult to redeposit whereas the reductive current peaks shift to a positive potential of ~ 20 mV which is indicative of an easier reductive desorption process. The integrated total reductive and total oxidative charge densities are equal (66 and 67 ± 5 $\mu C/cm^2$) at the holding time of 30 min.

Voltammograms recorded in 0.1 M KOH confirm the effect of the pH. Figure 3.16 shows the presence of a single reductive peak, sometimes with a small shoulder and two oxidative peaks. As the holding times increases the oxidative peaks show a significant change as well. These changes are very similar to what we have said earlier with small changes worth mentioning here. That is shown in Figure 3.16c where a third peak appears at ~ - 0.840 V after t_H of 15 min. It then dominates in Figure 3.16d. Its E_p is at ~ - 0.835 V after t_H of 30 min.

Figure 3.17 presents voltammograms in 0.05 M KOH solution. As the holding time (t_H) increases (depicted in Figures 3.17a-d) the reductive peaks do not change substantially. The reductive current peak potential (E_p) shifts about 40 mV from - 1.18 V after t_H of 1 min to - 1.14 V after t_H of 30 min. The oxidative current peaks are affected by the holding times. Two oxidative current peaks are observed at - 0.915 and - 0.950 V. They are separated at shorter times. They change shape and shift to a higher positive potential as a function of increasing time. A third oxidative current peak appears at - 0.850 V (t_H of 30 min).

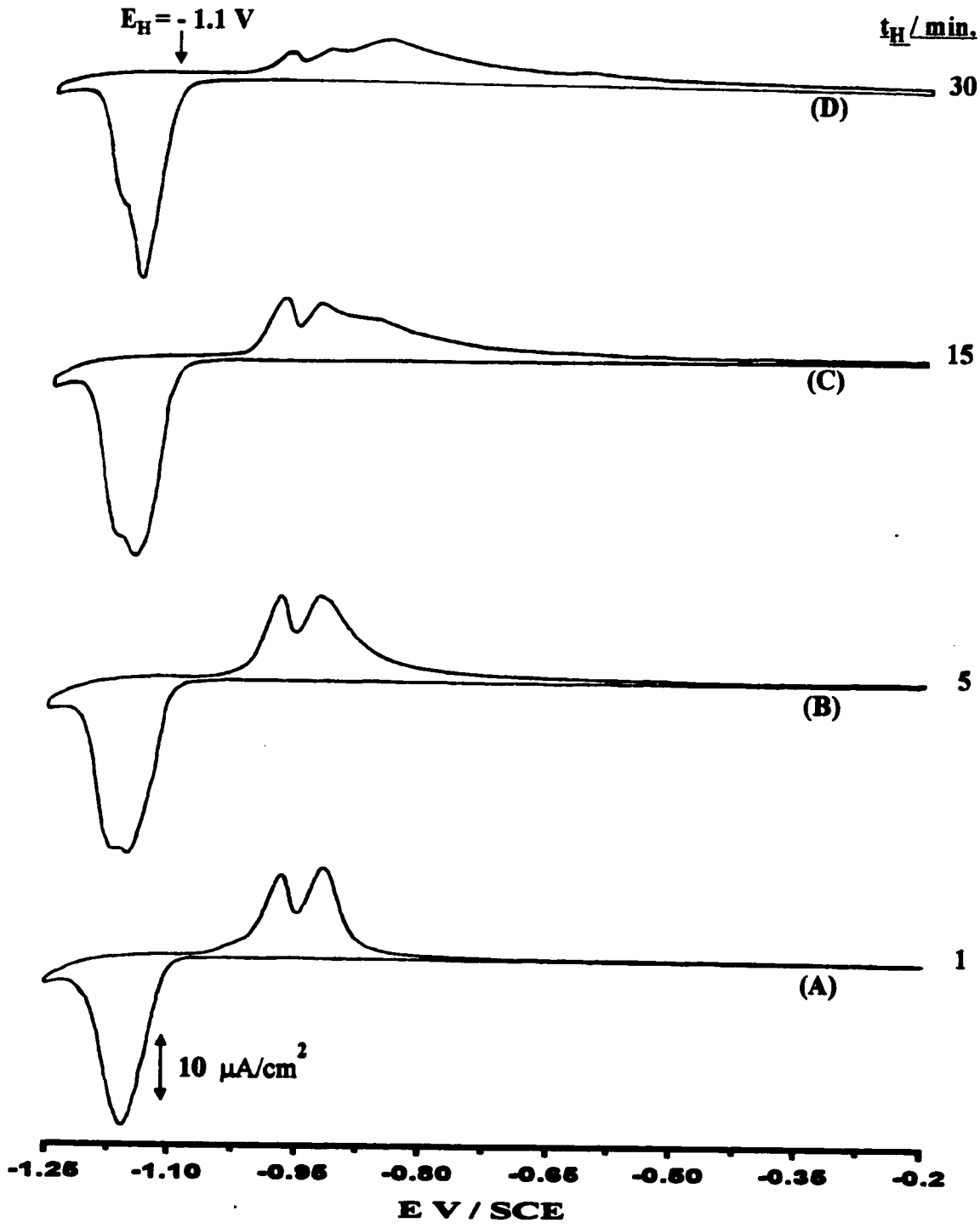

Figure 3.16 : Cyclic voltammograms of the reductive desorption and the oxidative redeposition of hexadecanethiols adsorbed on Au(111) recorded in 0.1 M KOH at a scan rate of 20 mV/s at 25 °C. E_H and t_H are the potential hold and the hold time (see text).

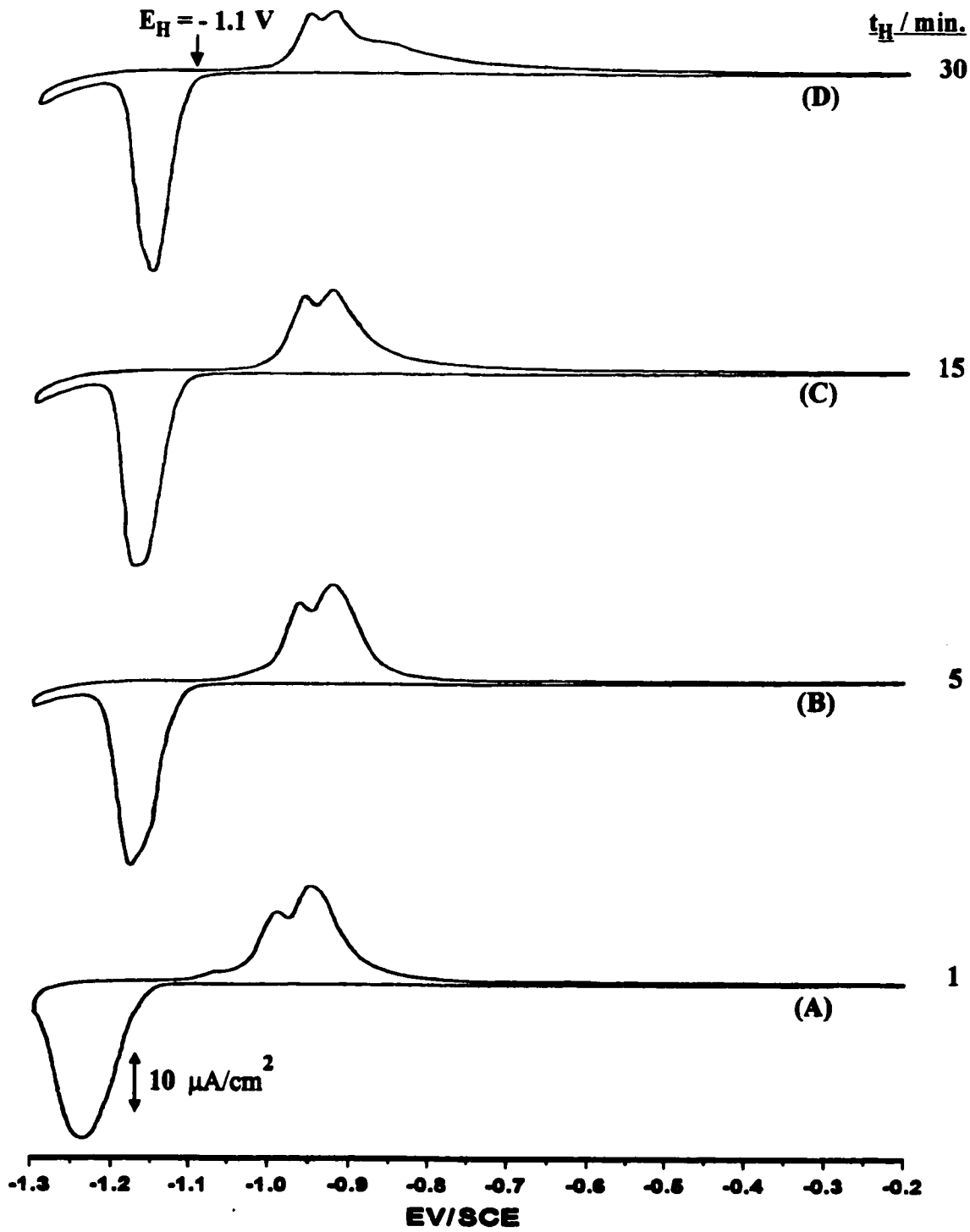

Figure 3.17 : Cyclic voltammograms of the reductive desorption of hexadecanethiols from Au(111) followed by holding the potential at E_H for various times t_H. The potential was scanned to - 0.2 V to oxidatively redeposit the hexadecanethiolates. Measurements were done in 0.05 M KOH at a potential scan rate of 20 mV/s at 25 °C.

The variation of the ionic strength does influence the peaks much less than the pH. The effect of the pH is measured by decreasing the pH by a factor of 10 while keeping the ionic strength constant. This was done by recording voltammograms in a solution of 0.45 M $KClO_4$ and 0.05 M KOH under the same settings as those used for the voltammograms in Figure 3.15. The voltammograms are presented in Fig. 3.18. A comparison of Figs. 3.15a-d with Figures 3.18a-d shows that the lowering of the pH by 1 has a noticeable effect on the voltammograms. There are still two oxidative current peaks but they are much closer in potentials. The reductive current peaks are also much closer. The change of the oxidative current peaks is occurring at longer holding times of 15 minutes. The amplitude of peak A′ diminishes relative to that of B′ as the holding time increases. However, both peaks remain at the same potentials. A very long tail develops on the positive potential side of peak A′ for holding times longer than 15 minutes.

Voltammograms recorded in 0.05 M KOH shown in Figure 3.17 under the same conditions are almost identical to those in Fig. 3.18. This indicates that the pH causes the change in the voltammograms and not the ionic strength. We note that the shift of the peaks A′ and B′ after a holding time of 30 minutes in 0.05 M KOH is similar to that observed in 0.05 M KOH + 0.45 M $KClO_4$. This raises the possibility that in the high pH solution the thiolates are slowly protonated at a potential of - 1.1 V. The protonation is more rapid in a lower pH solution since the pK_a of thiolates is 10-12. We thus assign the positive shift of the oxidative current peaks to the fact that physisorbed thiols must be deprotonated before they are oxidatively adsorbed and this makes the adsorption more difficult.

The associated integrated charge densities of the reductive desorption and the oxidative deposition as a function of holding time are shown in Table 3 and Figure 3.19.

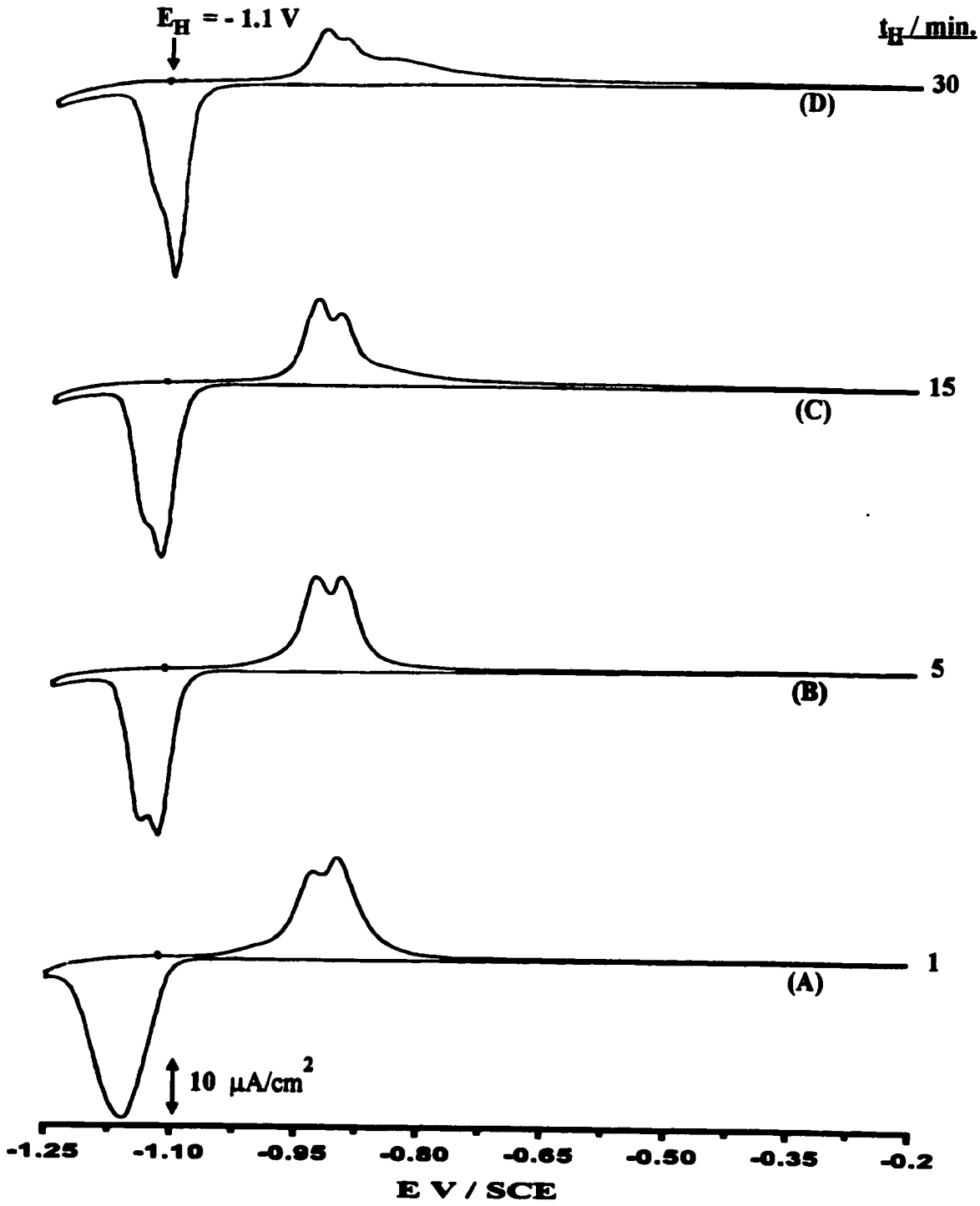

Figure 3.18 : Cyclic voltammograms of the reductive desorption of hexadecanethiols from Au(111) followed by holding the potential at E_H for various times t_H. The potential was then scanned to - 0.2 V to oxidatively redeposit the hexadecanethiolates. Measurements were done in 0.05 M KOH + 0.45 M $KClO_4$ at a potential scan rate of 20 mV/s at 25 °C.

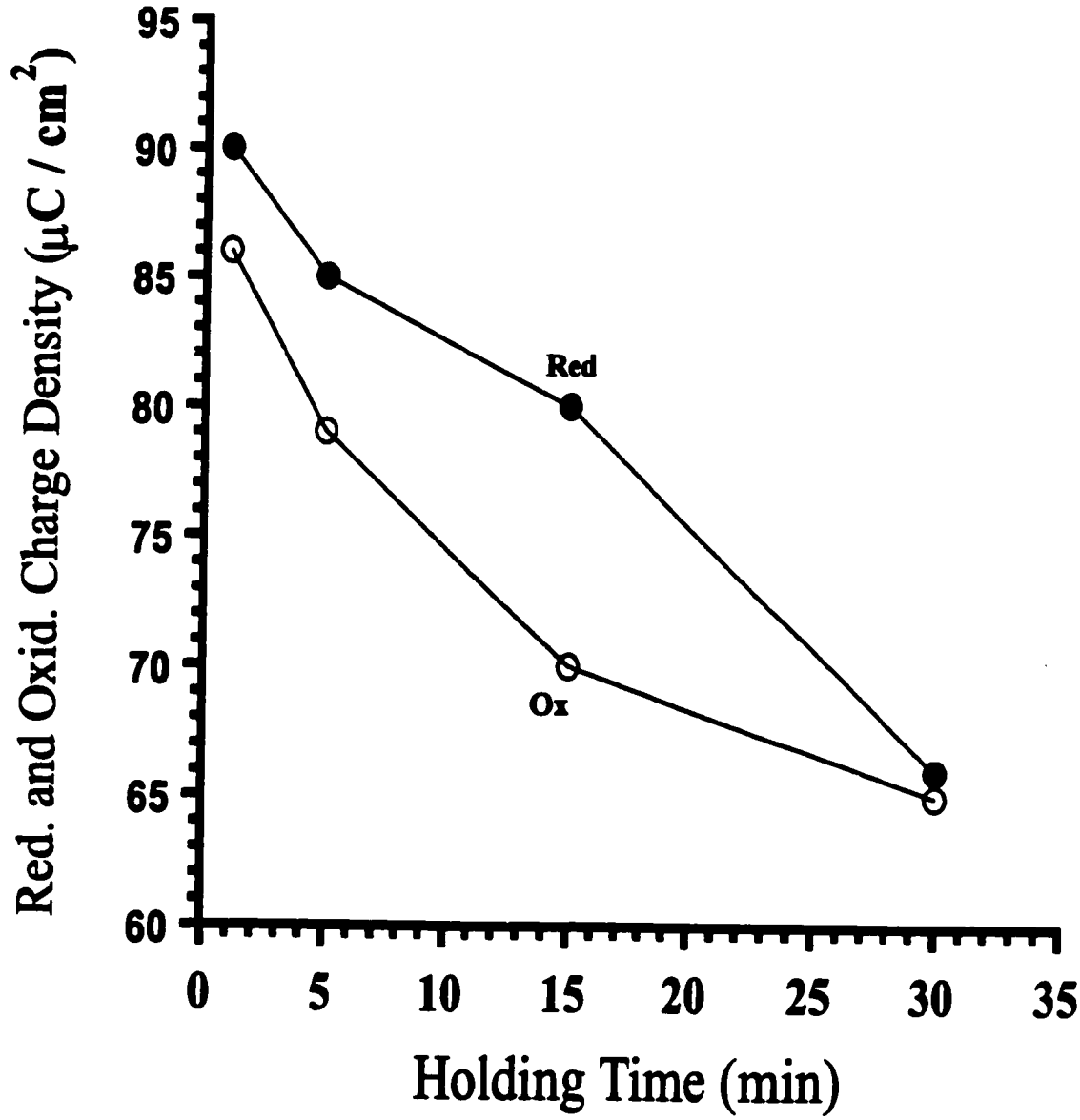

Figure 3.19 : Absolute integrated reductive and oxidative charge densities as a function of holding time of a Au(111) electrode modified with hexadecanethiols in 0.1 M KOH at a scan rate of 20 mV/s and 25 °C.

Table 3. Total reductive and oxidative charge densities for different holding times at - 1.10 V in 0.1 M KOH :

Holding Time / min.	Total Red. σ (± 5 μC / cm^2)	Total Oxid. σ (± 5 μC / cm^2)
1	90	86
5	85	79
15	80	70
30	66	65

Approximately 25 % of the alkanethiol monolayer is lost after holding the potential at - 1.1 V for 30 minutes.

2.7 The effect of holding the potential on the negative potential scan at - 1.08 V on the reductive desorption peaks :

The reductive desorption peaks A and B of an adsorbed hexadecanethiol SAM at a gold (111) electrode were examined in 0.1 M KOH at a potential scan rate of 20 mV/s at 25°C. Voltammograms are shown in Figures 3.20a and 3.20b. The potential of - 1.08 V was chosen as the potential just before the onset of thiol reduction potential. Holding time range between 1 sec and about 1 or 2 min, a single and broad reductive peak (at ~ - 1.15 V and 1 sec) is observed at shorter holding times. This peak gradually narrowed and shifted toward more negative potentials (to - 1.18 V at 1 min) as the holding time increases. In contrast, the two oxidative desorption peaks do not change much (from - 0.915 peak A′ and - 0.975 V peak B′ at 1sec to - 0.925 peak A′ and - 0.98 V peak B′ at 1 min). After 3 min, the reductive peak gradually overlapped with the hydrogen evolution. This peak disappeared around 5 min. Simultaneously to this observation, significant changes and shifts of the oxidative peaks occur. This suggests that the two processes (reductive and oxidative) are different and whatever is happening is a very slow process.

2.8 The oxidative peak A′:

We have tried to separate the two oxidative peaks A′ and B′ by holding the potential

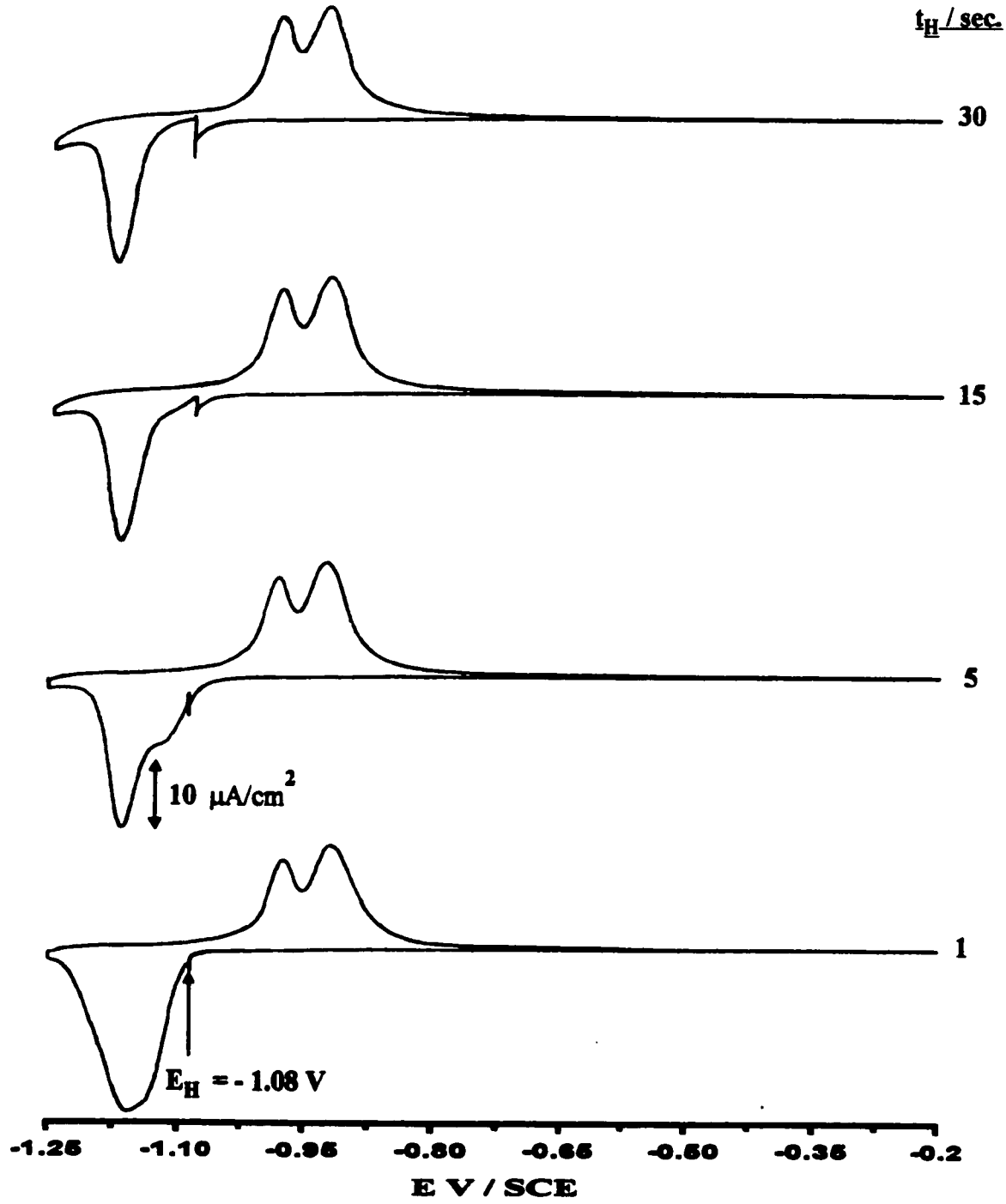

Figure 3.20a : Cyclic voltammograms of holding the potential of Au(111) modified with hexadecanethiols at E_H for various times t_H. The potential was then scanned to - 0.2 V to oxidatively redeposit the hexadecanethiolates. Measurements were done in 0.1 M KOH at a potential scan rate of 20 mV/s at 25 °C.

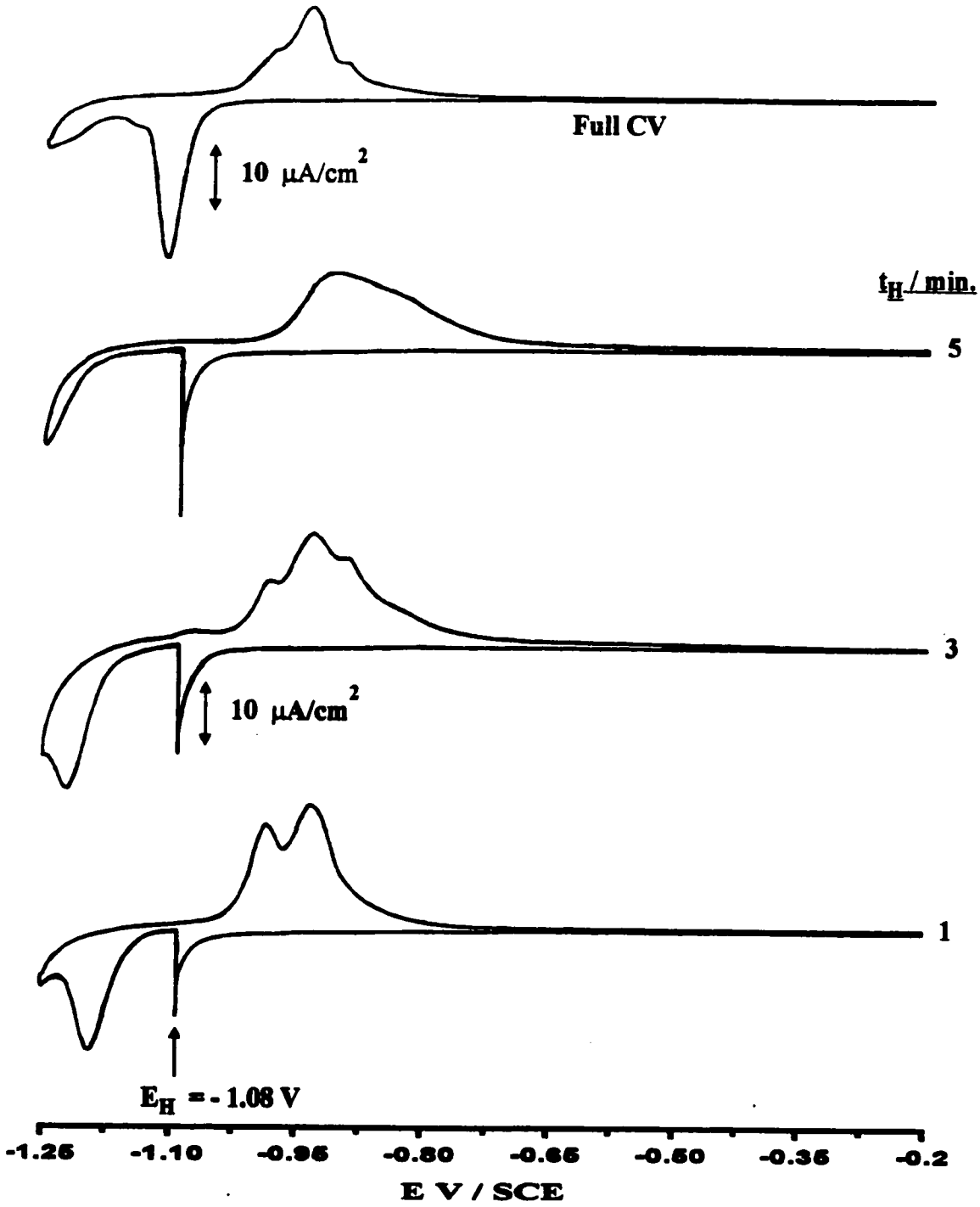

Figure 3.20b : Cyclic voltammograms of holding the potential of Au(111) modified with hexadecanethiols at E_H for various times t_H. The potential was then scanned to - 0.2 V to oxidatively redeposit the hexadecanethiolates. Measurements were done in 0.1 M KOH at a potential scan rate of 20 mV/s at 25 °C.

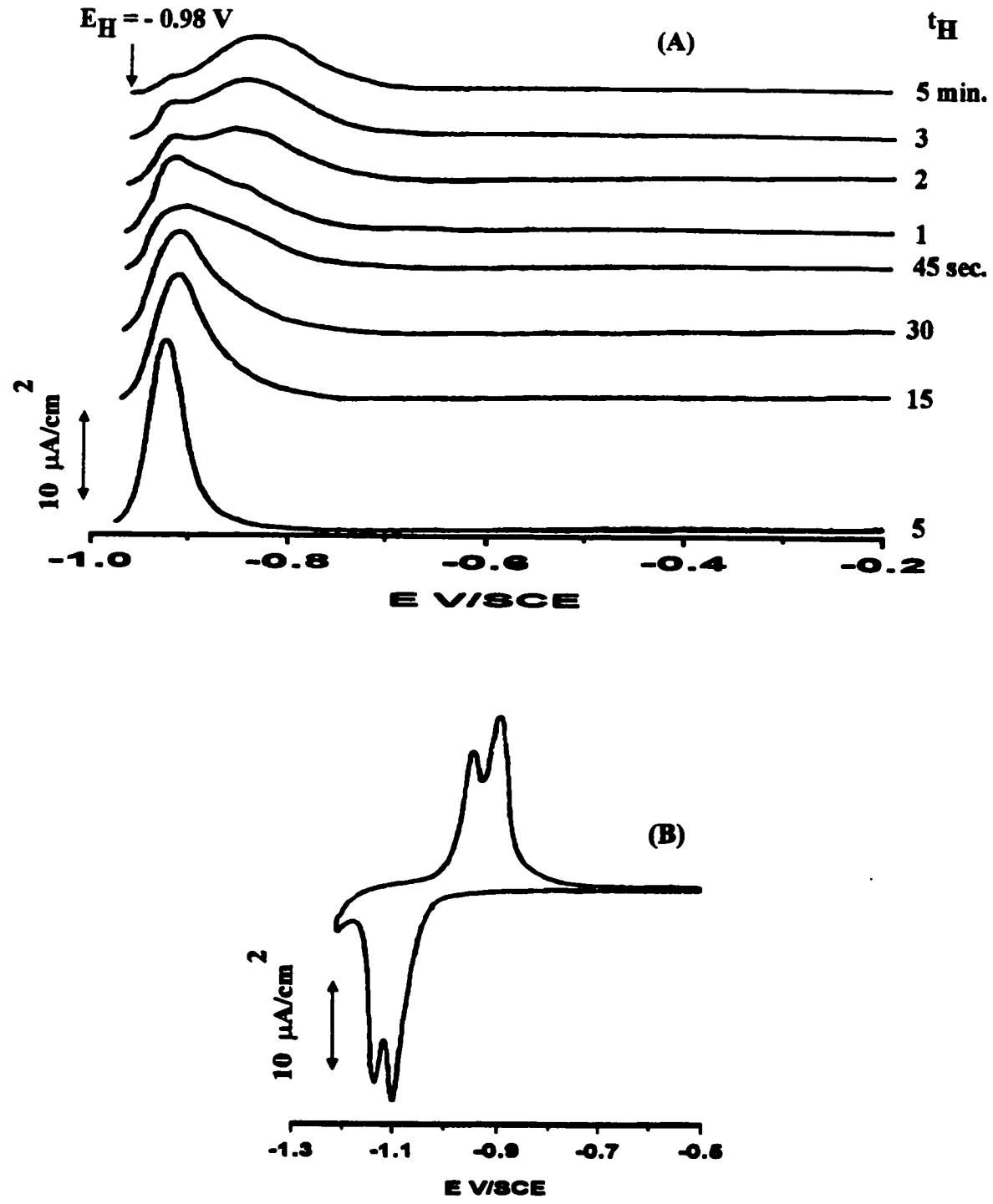

Figure 3.21 : (a) Voltammograms recorded after reducing the hexadecanethiols and holding the potential (E_H) at - 0.98 V for various holding times (t_H). Measurements were done in 0.1 M KOH at a potential scan rate of 20 mV/s at 25 ^{0}C. (b) Cyclic voltammogram recorded after a 5 min t_H.

at - 0.98 V, just passed peak B', in order to calculate the charge associated with peak A'. Figure 3.21 shows the gradual shift of peak A' with increasing holding time. Peak A' occurs at - 0.92 V and is associated with $45 \pm 5\ \mu C/cm^2$ (total reductive charge is $90 \pm 5\ \mu C/cm^2$) at 1 sec and finishes at - 0.83 V ($\Delta E_p \approx 90$ mV) and is associated with $35 \pm 5\ \mu C/cm^2$ (total reductive charge is $74 \pm 5\ \mu C/cm^2$) at 5 min. This positive peak shift suggests that thiol deposition is harder than at shorter times. Octadecanethiol SAMs were also investigated and they showed a similar behaviour.

2.9 Model for the reductive desorption and the oxidative redeposition process :

Short-chain alkanethiol SAMs with $4 \leq C_nSH \leq 10$ (n is the number of carbon atoms) adsorbed from dilute alkanethiol ethanolic solution at single crystal gold (111) electrode show one reductive desorption current peak and the complete absence of oxidative redeposition peak(s). The reductive peak potential shifts toward a more negative overpotential as the chain length increases. This reflects the gradual increase of the van der Waals interactions between alkanethiol molecules.

SAMs of C_{12} mark the line at which two well-defined reductive desorption peaks and a small broad oxidative redeposition are observed. More energy is required for longer chain lengths to begin the reductive desorption faradaic process. Van der Waals forces also hold the alkanethiols together in the physisorbed state as micelles near the electrode surface. Short chains show a single reductive desorption peak while longer chains show two reductive desorption peaks and two or three oxidative redeposition peaks. These results suggest that soluble thiols are reduced in one step. The second peak is observed only when some thiolates remain physisorbed at the surface. Thus, this peak seems to be associated with the formation of a physisorbed monolayer of thiolates. The previous models used to explain the fine structure observed in the voltammograms of insoluble thiols are not compatible with our results. The two reductive peaks are not due to the formation of domains with different ionic permeabilities. The formation of such domains would occur randomly since it probably depends on very small changes in the adsorption process. These changes are likely to be

related to surface defects. Thus, the ratio of the surface covered by each type of domains would vary from one experiment to the other and from one single crystal to the other. However, the ratio of the current peaks is found to be quite reproducible. The second model assigned the peaks to the presence of two adsorption sites. The infrared spectrum of hexadecanethiols chemisorbed on gold is compatible with a tilt of the alkane chains molecular axis of 35° relative to the surface normal. The surface coverage is also found to be independent of the chain length. These two results are compatible with the formation of a ($\sqrt{3}$ x $\sqrt{3}$)R30°. The adsorption of thiols on two sites should lead to significant changes in the surface coverage and thus to an increase in the reduction current relative to the one measured for soluble thiols. We also expect the infrared spectra to undergo changes. The tilt angle of the molecular axis should decrease if the surface coverage increases. Such changes have not been reported in the literature nor seen in our measurements.

We proposed an alternative model for the reduction of insoluble thiols from gold. This model described the reduction as two processes occurring consecutively as shown in Figure 3.22. The important interadsorbate interactions causes a separation of the total reductive current into its two components. The Faradaic process (the transfer of one electron from the substrate to the adsorbate) occurs first. The thiolates however do not change their orientation. They remain physisorbed in their original orientation. Only when the potential is made more negative do the thiolates form micelles. Upon the formation of micelles, a significant fraction of the gold surface is made free of adsorbates. This allows the formation of an electric double layer at the metal surface which gives rise to the observed capacitive current. In this model the oxidative adsorption occurs via the reverse process.

Our results are in quantitative agreement with this model. The total charge densities associated ($90 \pm 5\ \mu C/cm^2$) with the reductive desorption peak(s) from cyclic voltammograms for each chain studied is independent of the chain length, within experimental uncertainty. Slow scan rates of 0.5 and 1.0 mV/s (not shown) at two single crystal gold (111) electrodes modified with hexadecanethiol and octadecanethiol SAMs, respectively, allowed a good

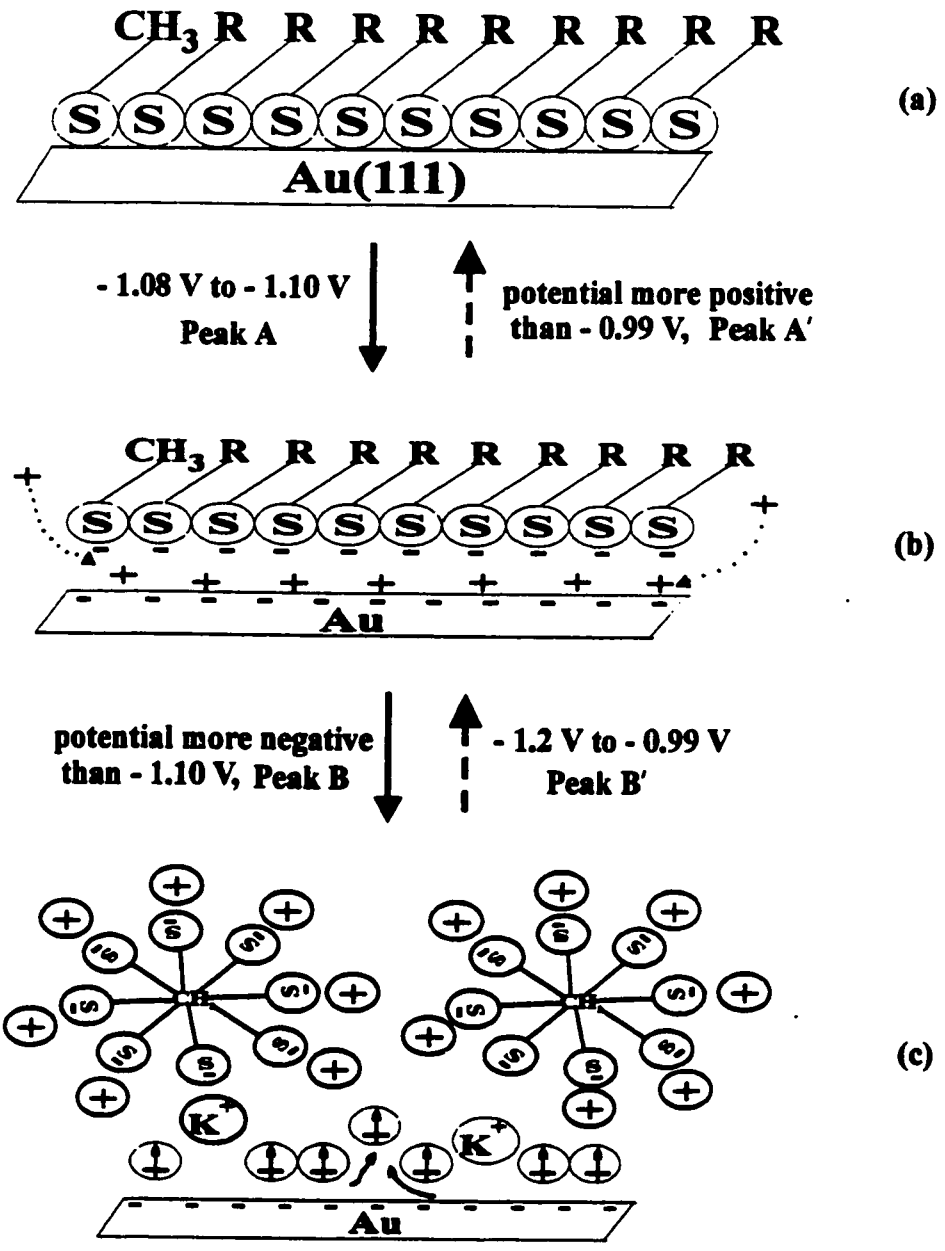

Figure 3.22 : Mechanism of the reductive desorption and oxidative deposition of insoluble thiols from Au(111) (a) Chemisorbed thiols; (b) The reduction of the thiols causes peak A, but the thiolates remain in the same orientation; (c) When the potential is more negative than - 1.10 V, micelles of thiolates are formed. The oxidative redeposition occurs by the reverse mechanism under the conditions shown on the Figure.

separation of the two reductive desorption peaks. These experiments show that reductive peak A is associated with 60 % (~ 50-55 $\mu C/cm^2$) and peak B with 40 % (~ 30-35 $\mu C/cm^2$) of the total charge density. Examining both the short and the long alkanethiol chain carefully and correcting for the double layer charging current revealed that the former had about 20-25 $\mu C/cm^2$ and the latter had ~ 25-30 $\mu C/cm^2$.

The magnitude of the charges is in quantitative agreement with our model. The first peak is assigned to the reduction of thiols. The reduction of a full monolayer of chemisorbed thiols requires 73 $\mu C/cm^2$. This corresponds to approximately 70 % of the total charge. This value is quite consistent with the fact that peak A accounts for 60%. The second step of the reduction process occurs at more negative potentials and is assigned to the formation of micelles of thiolates. The capacitive current arising from the formation of micelles should be equal to the difference between the capacitive charging current of the thiol coated surface and the uncoated surface. This difference is approximately 25 $\mu C/cm^2$. It corresponds to the remaining 30 % of the charge. The physisorbed micelles of thiolates are oxidatively redeposited when the applied potential is reversed in the positive potential scan by the same two steps, but in the reverse order.

Recent in-situ FTIR measurements done in our laboratory [16] give further support to the proposed model. The variation of the intensity of the C-H stretching bands was found to occur mainly over the potential ranges of peaks B and B'. This is explained by the formation of micelles which causes a reorientation of the micelles. Whereas the reduction of the thiols causes minimal reorientation of the adsorbates.

3. References

1. Creager, S. E.; Olsen, K. G. Anal. Chim. Acta **1995**, 307, 277.
2. Steinberg, S.; Tor, Y.; Sabatini, E.; Rubinstein, I. J. Am. Chem. Soc. **1991**, 113,

5176.

3. Schoer, J. K.; Zamborini, F. P.; Crooks, R. M. J. Phys. Chem. **1996**, 100, 11086.
4. Malem, F.; Mandler, D. Anal. Chem. **1993**, 65, 37.
5. Abbott, N. L.; Gorman, C. B.; Whitesides, G. M. Langmuir **1995**, 11, 16.
6. Gorman, C. B.; Biebuck, H. A.; Whitesides, G. M. Langmuir **1995**, 11, 2242.
7. Yang, D. -F.; Al-Maznai, H.; Morin. M. J. Phys. Chem. B **1997**, 101, 1158.
8. Yang, D. -F.; Wilde, C. P.; Morin, M. Langmuir **1996**, 12, 6570.
9. Yang, D. -F.; Wilde, C. P.; Morin, M. Langmuir **1997**, 13, 243.
10. Porter, M. D.; Bright, T. B.; Allara, D. L.; Chidsey, C. E. D. J. Am. Chem. Soc. **1987**, 109, 3559.
11. Weisshaar, D. E.; Lamp, B. D.; Porter, M. D. J. Am. Chem. Soc. **1992**, 114, 5860.
12. Zhing, C. J.; Porter, M. D. J. Electroanal. Chem. **1997**, 425, 147.
13. Widrig, C. A.; Chung, C.; Porter, M. D. **1991**, 310, 335.
14. Hatchett, D. W.; Stevenson, K. J.; Lacy, W. B.; Harris, J. M.; White, H. S. J. Am. Chem. Soc. **1997**, 119, 6596.
15. Hatchett, D. W.; Uibel, R. H.; Stevenson, K. J.; Harris, J. M.; White, H. S. J. Am. Chem. Soc. **1998**, 120, 1062.
16. Byloos, M.; Al-Maznai, H.; Morin, M. J. Phys. Chem. B in press.
17. Stevenson, K. J.; Mitchell, M.; White, H. S. J. Phys. Chem. B **1998**, 102, 1235.
18. Janek, R. P.; Fawcett, W. R.; Ulman, A. J. Phys. Chem. B **1997**, 101, 8550.
19. Janek, R. P.; Fawcett, W. R.; Ulman, A. Langmuir **1998**, 14, 3011.
20. Nuzzo, R. G.; Dubois, L. H.; Allara, D. L. J. Am. Chem. Soc. **1990**, 112, 558.
21. Fenter, P.; Eisenberger, P.; Liang, K. S. Phys. Rev. Lett. **1993**, 70, 2447.
22. Toennies, T. P. J. Vac. Sci. Technol. **1987**, A5, 440.
23. Reid, E. E. Organic Chemistry of Divalent Sulfur ; Chemical Publishing Co. Inc. : New York, 1958, Vol. 1.
24. Camillone, N. III; Chidsey, C. E. D.; Eisenberger, P.; Fenter, P.; Li, J.; Liang, K. S.; Liu, Y. G.; Scoles, G. J. Chem. Phys. **1993**, 99, 744.
25. Fenter, P.; Eberhardt, A.; Eisenberg, P. Science **1994**, 266, 1216.

26. Desnoyers, J. E. and Jolicoeur, C. in Modern Aspects of Electrochemistry ; Conway, B. E.; Bockris, J. O'M., Eds.; Plenum Publishing Company : New York, 1969.

27. Bockris, J. O'M.; Reddy, A. K. in Modern Aspects of Electrochemistry; vol. 1, Plenum Publishing Company : New York, 1970.

Chapter 4

Electron Transfer Across SAM

1. Introduction

In this chapter the electron transfer barrier properties of SAMs are examined using potassium ferricyanide as a redox probe. Chemisorbed alkanethiols prevent ionic and electronic transfer between the redox centers and the underlying metal electrode [1-4]. As mentioned in the previous chapters, thiol modified surfaces have been proposed as biosensors. In this application the thiols are used to control the rate of electron transfer and to obtain selectivity. It is therefore important to minimize the number of defects which are deleterious for these applications. Two mechanisms of electron transfer between thiol modified electrodes and electroactive redox species have been reported. A limited number of studies found that electron transfer occurs through tunneling while more numerous studies suggested that it proceeds through ion permeation. It is important to determine the conditions which favor one of the processes since ion permeation at defects could be used to form microelectrodes which are useful sensors. Electron tunneling can be used to form a selective electrode or possibly to form an organic conductor. Before discussing these various studies, the models used to analyze the electrochemical properties will be presented.

1.1 Marcus Theory of Electron-Transfer :

Marcus's theory is widely used to analyze electron transfer processes in electrochemistry. This theory takes into account the solvent-molecule interactions. In a polar media, such as water, there are strong interactions (10-100 kJ mol^{-1}) between ions (redox species) and solvent dipoles. The magnitude of these interactions changes significantly when an electron transfer occurs. Fundamental work on electron transfer reactions, either homogeneous (in solution) or heterogeneous (between an electrode and a redox species in solution) redox reactions, were made by Marcus [5-11], Hush [12-14], Levich [15] and Dogonadze[16].

In this work we are interested in heterogeneous electron transfer between a molecule that can be reversibly oxidized and reduced on a Au(111) electrode. Fig. 4.1 shows the metal's electronic density of states and the adsorbate's energy levels. E_{redox} is the reversible redox potential [17]. The oxidized form of the molecule will be reduced spontaneously since the Fermi level is higher than E_{redox}. Applying a positive potential to the electrode will make the reduction more difficult whereas a negative potential will make the reduction faster. If the heterogeneous electron transfer is fast compared to nuclear displacement it can be described by the Frank-Condon principle (vertical transition). After the electron transfer has occurred the solvation shell will reorganize since the oxidized and the reduced forms have different charges. This solvent reorganization energy will change the overall electron transfer activation free energy ΔG. When there are strong interactions between the redox molecules and the electrode surface, such as chemisorption, the electron transfer is difficult to model since the structure of the redox species adsorbed at the electrode surface is in general unknown. This is not the case for the redox probe that we have chosen. There are weak interactions between the redox molecules and the electrode surface except for the sulfur terminal group. The Marcus theory is thus appropriate to describe this process.

The total activation free energy and reorganization energy are given by summing the energy due to the inner and outer shell processes :

$$\Delta G_{total} = \Delta G_{is} + \Delta G_{os} \qquad (1)$$

$$\lambda_{total} = \lambda_{is} + \lambda_{os} \qquad (2)$$

where ΔG_{is} is the redox molecule inner-shell activation free energy and λ_{is} is the redox molecule inner-shell reorganization energy which is determined by the composition of the

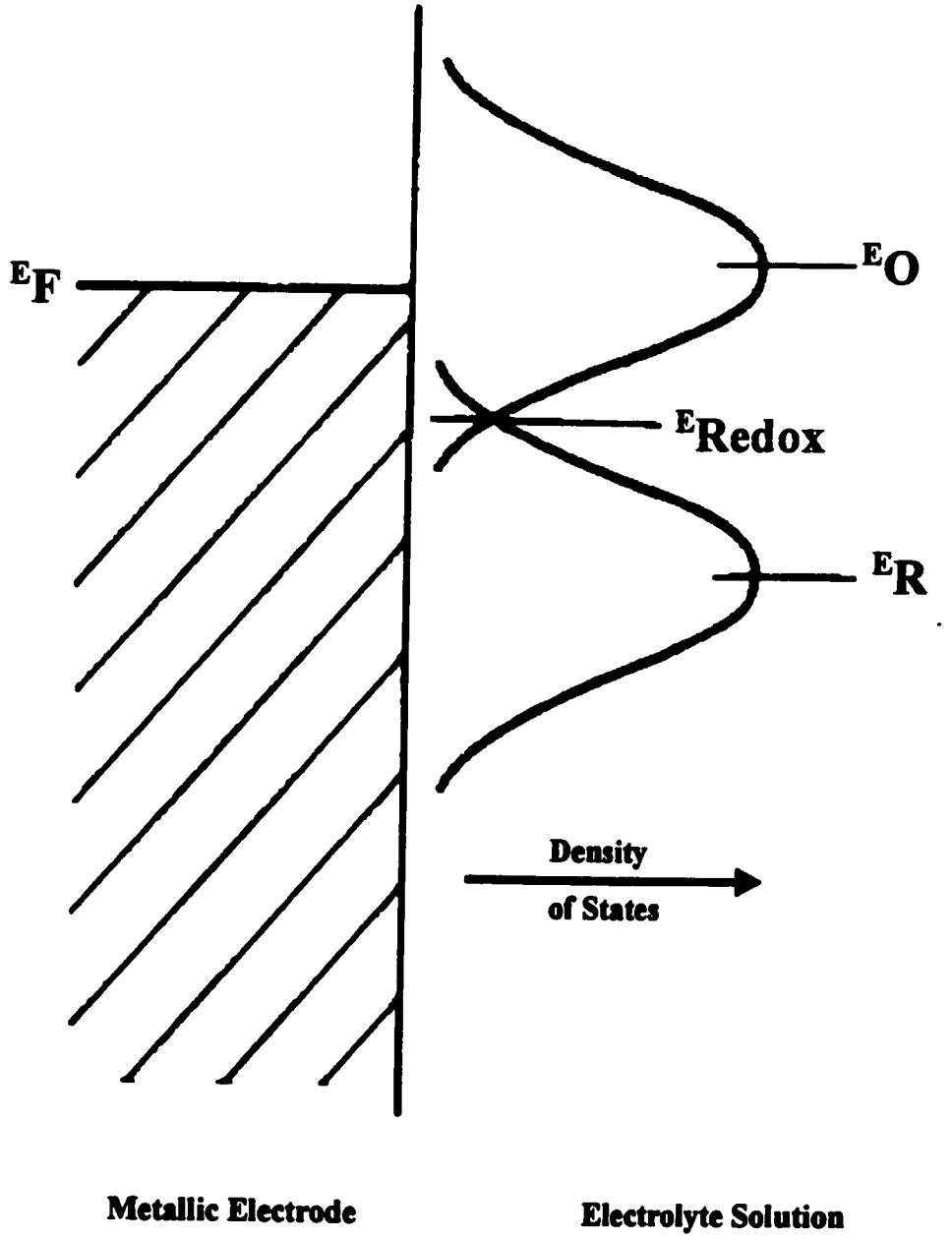

Figure 4.1 : Electronic density of states of a metal and the energy levels of the molecules (from Reference 17).

redox center. ΔG_{os} is the surrounding solvent outer-shell activation free energy and λ_{os} is the surrounding solvent outer-shell reorganization energy which is determined by the structure of the solvent.The outer shell process can be modeled by calculating the energy U required to charge a sphere in a uniform dielectric medium:

$$U = n^2e^2/(8\pi r\epsilon_o\epsilon) \qquad (3)$$

where n is the number of electrons transferred, e is the electronic charge in coulombs, r is the radius of the sphere in meters, ϵ_o is the permittivity of the space (8.85×10^{-12} C $V^{-1}m^{-1}$) and ϵ is the relative dielectric constant of the medium.

However, the electron transfer depends on the difference between the optical ϵ_{op} [ϵ_{op} = (solvent refractive index)^2] and the static ϵ_{st} dielectric constants :

$$\Delta G_{os} = n^2e^2/8\pi r\epsilon_o\,(1/\epsilon_{op} - 1/\epsilon_{st}) \qquad (4)$$

At short times after the reduction only the solvent's high frequency electronic modes respond to the redox molecule's charge change. At longer times after the charge transfer, the solvent dipoles and the nuclear positions can reorient.

If we assumed ½ e is transferred at the transition state, the outer shell free energy becomes :

$$\Delta G_{os} = e^2/32\pi r\epsilon_o\,(1/\epsilon_{op} - 1/\epsilon_{st}) \qquad (5)$$

For polar solvents like water, the solvent used in our experiments, $\epsilon_{op} \ll \epsilon_{st}$ and ΔG_{os} become:

$$\Delta G_{os} = e^2/(32\pi r\epsilon_o\epsilon_{op}) \qquad (6)$$

$$\Delta G_{os} \alpha 1/(r\epsilon_{op}) \quad (7)$$

If an ion is brought to a distance **d** from the conducting metallic surface, an image dipole is created by a redistribution of the electrons inside the conductor. So, an equal but opposite charge image is formed inside the metal surface. This image charge screens the redox molecule's charge and consequently reduces the outer-shell activation free energy :

$$\Delta G_{os} = e^2/32\pi\epsilon_o [(1/r - 1/2d) (1/\epsilon_{op} - 1/\epsilon_{st})] \quad (8)$$

The reorganization energy becomes :

$$\lambda_{os} = (e^2N/2) [(1/r - 1/2d) (1/\epsilon_{op} - 1/\epsilon_{st})] \quad (9)$$

According to Marcus theory, the activation barrier to electron transfer is due to solvation changes. It can be shown that :

$$\Delta G^{\#} = (\Delta G_s + \Delta G)^2 / 4\Delta G_s \quad (10)$$

In the above, $\Delta G^{\#}$ represents the activation free energy, ΔG_s is the solvation energy change between reagents and products, and ΔG is the energy difference between that of the products and reagents. These terms are illustrated in Fig. 4.2.

The charge transfer coefficient, α, is defined as :

$$\alpha = RT/F (\partial \ln k/\partial E) = \partial \Delta G^{\#}/\partial E \quad (11)$$

Considering a system where there is only the oxidized form in the solution, the reduction rate is :

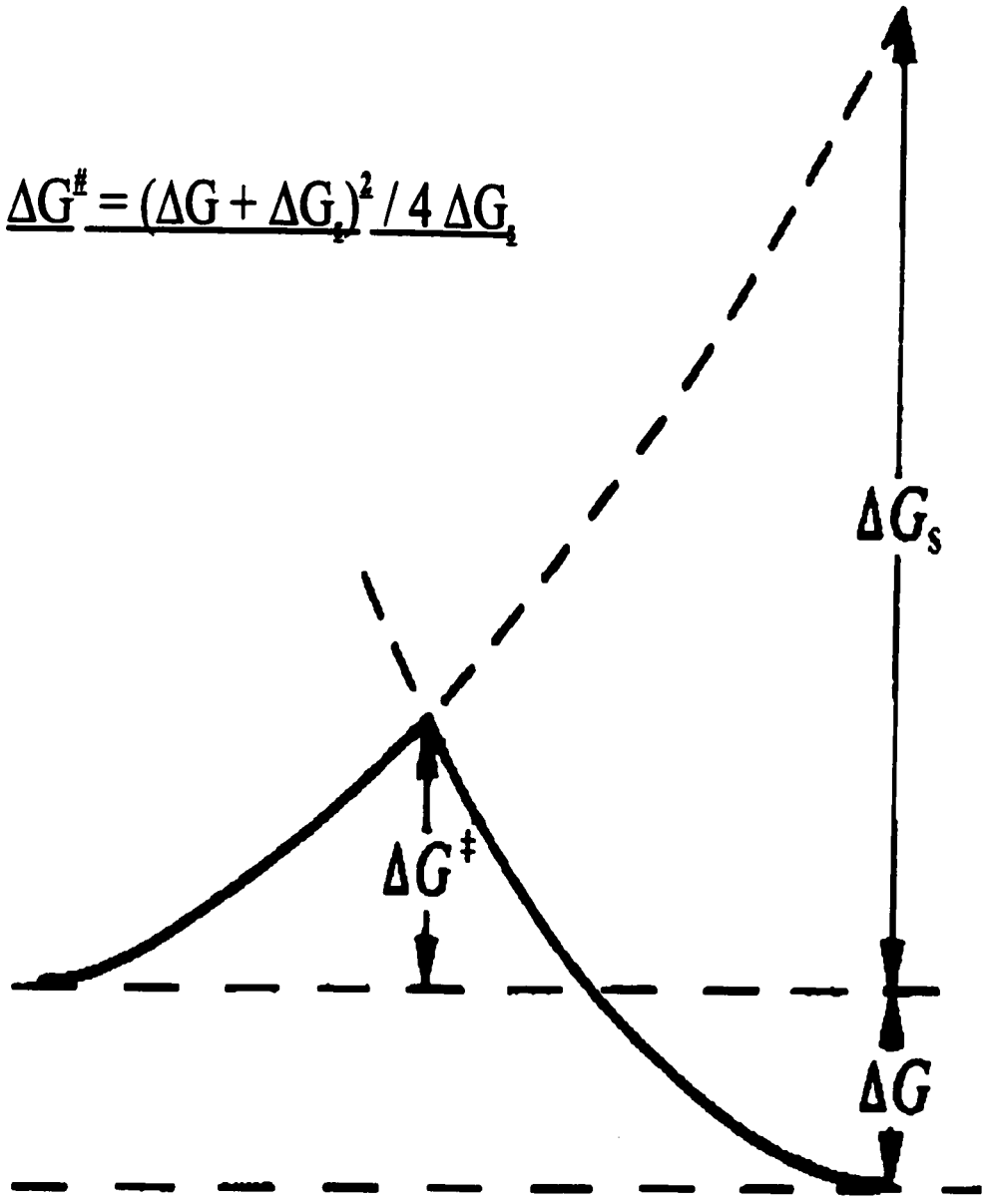

Figure 4.2 : Activation energy barrier to electron transfer due to solvent reorganization (from Reference 17).

$$k_c = k_o \exp [-\alpha_c nF/RT(E - E^{o'})] \quad (12)$$

$$\ln k_c = \text{const} - \alpha_c nFE/RT \quad (13)$$

Eq. 13 is called the Tafel relation. ln k varies linearly with a thermodynamic parameter (E). Substituting in eq. 10 we find :

$$\alpha = - 1/2F (1 + \Delta G/\Delta G_s) \partial\Delta G/\partial E \quad (14)$$

$$\alpha = ½ (1 + \Delta G/\Delta G_s) \quad (15)$$

Limiting cases are shown in Fig. 4.3 :

(1) ΔG_s is much larger than ΔG :

If $\Delta G_s \rangle\rangle \Delta G$ then $\alpha = ½$, and the kinetics is slow.

(2) ΔG_s is much smaller than ΔG :

If $\Delta G_s \langle\langle \Delta G$ then $\Delta G \approx 0$ $\alpha = ½$

$\Delta G \approx \Delta G_s$ $\alpha = 1$

$- \Delta G \approx \Delta G_s$ $\alpha = 0$

Marcus theory predicts a linear relationship between charge transfer α and potential for fast electron transfer reactions.

Adiabatic electron transfer occurs when the electron transfer and the nuclear changes occur at similar rates. Thus the adiabatic process depends on the vibrational frequencies of the nuclear reorganization of the system. The low frequencies vibrational modes can be thermally excited when $\omega \langle\langle kT / \hbar$.

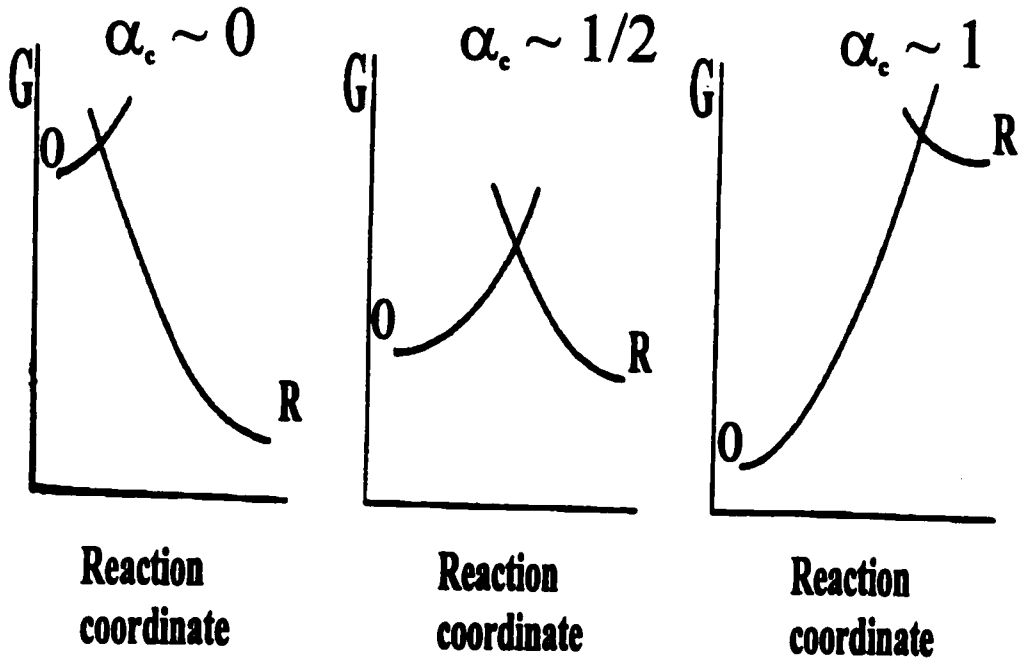

Figure 4.3 : Energy distribution of a redox couple of species O and R on the surface of a metallic electrode (from Reference 17).

In Marcus theory, the reorganization of the system involves :

1. Changes in the bond length and angles that cause energy and entropy changes.
2. Changes in the particle size.
3. Changes in the vibrational and orientational polarization of the molecule in the solvation sphere.

The adiabatic electron transfer is characterized by strong electronic coupling between the molecules and the electrode. This is shown in Fig. 4.4a where the molecules density of electronic states distribution has been distorted by this interaction[18]. The electron transfer involves a limited number of electronic states. The electron transfer rate (only at the Fermi level) can be approximated by :

$$k = \upsilon_n D_{ox} (E_f) \qquad (16)$$

$$k = \upsilon_n N_{ox} (4\pi\lambda_{ox} kt)^{-1/2} \exp[(\lambda_{ox} - E)/4\lambda_{ox} kT] \qquad (17)$$

where D_{ox} is the density of states of the redox couple; E_f is the energy at the Fermi level; N_{ox} is the number of redox centres participating in the e-transfer.

Non-adiabatic electron transfer is defined as the reorganization occurring at a slower or faster rate than the electron transfer. This process is characterized by a smaller electronic coupling between the molecule and the electrode. Fig. 4.4b shows that the molecule's electronic density of states is undistorted. The overlap between the electrode and the molecules density of electronic states occurs over a wider range of energy. The electron transfer rate is obtained by summing over all the electron energies rather than only at the Fermi level :

$$k = \upsilon_n N_{ox} (4\pi\lambda_{ox} kt)^{-1/2} \int_{-\infty}^{+\infty} \{ \exp -[(\lambda_{ox} - E)^2 / 4\lambda_{ox} kT] / \exp [(E-E_f)/kt] + 1 \} dE \qquad (18)$$

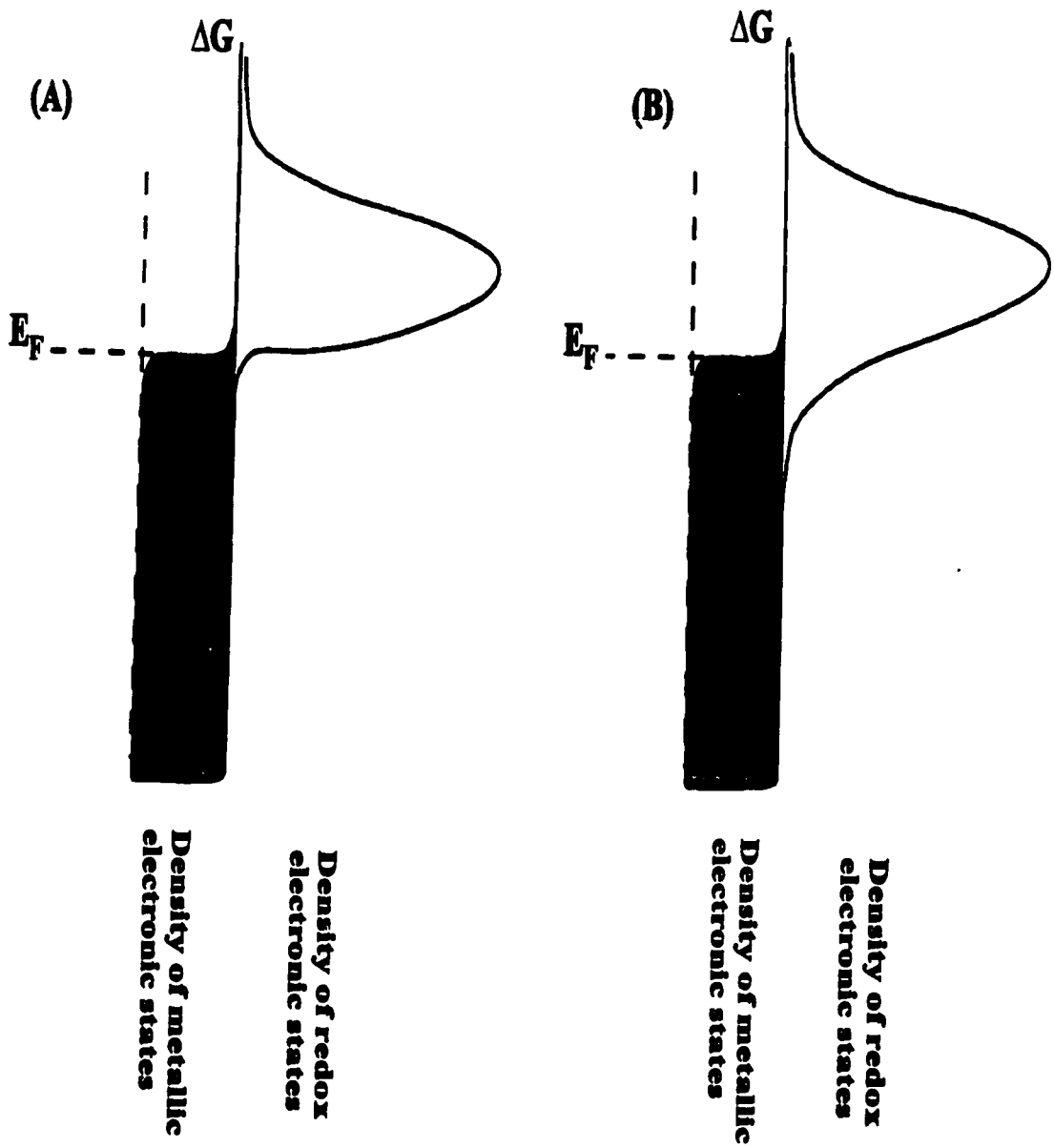

Figure 4.4 : Density of electronic states plots for the reduction of Ox. (a) Distorted density of electronic states distribution for Ox caused by an adiabatic electron transfer reaction. (b) Undistorted density of electronic states distribution for a non-adiabatic electron transfer reaction(from Reference 22).

The frequency factor (the pre-exponential) in the case of non-adiabatic electron transfer, where the transition state region is sharp, is :

$$\upsilon_n = \sum_{\text{all modes}} (\nu_i^2 \Delta G_i/\Delta G_{TOTAL})^{1/2} \qquad (19)$$

The transition state is broad for adiabatic electron transfer. The electron exchange occurs near the transition state and results in the reduction of the crossing rate across the barrier region.

The rate of electron transfer for adiabatic and non-adiabatic electron transfer are shown in Fig. 4.5, obtained by eqn.16, and summarized as :

1. Far from λ_{ox} (λ_{ox} ⟩ $E^{o'}$), both adiabatic and non-adiabatic transfers give identical potential dependence on the heterogeneous electron transfer rate. At lower over potentials, the electron transfer rate is strongly temperature dependent.
2. Near λ_{ox}, adiabatic and non-adiabatic transfers are different but show exponential increase of the rate of electron transfer with $E^{o'}$.
3. When the electrode potential = λ_{ox}, the rate of electron transfer is maximum and electron transfer becomes temperature independent.
4. Beyond λ_{ox} (high negative electrode potential), the rate of adiabatic electron transfer decreases exponentially which predict the existence of the "inverted" reaction free energy region. The rate of electron transfer is slow and varies as a parabola when the potential is made more negative. For non-adiabatic electron transfer, the rate of electron transfer approaches a limited value since the overlap between the metal filled electronic states and the unfilled redox electronic states is complete. The electron transfer becomes less dependent upon the electrode potential.

The prediction of an inverted region was recently confirmed by measurement of the electron transfer rate across alkanethiols chemisorbed on a metallic electrode. Prior attempts

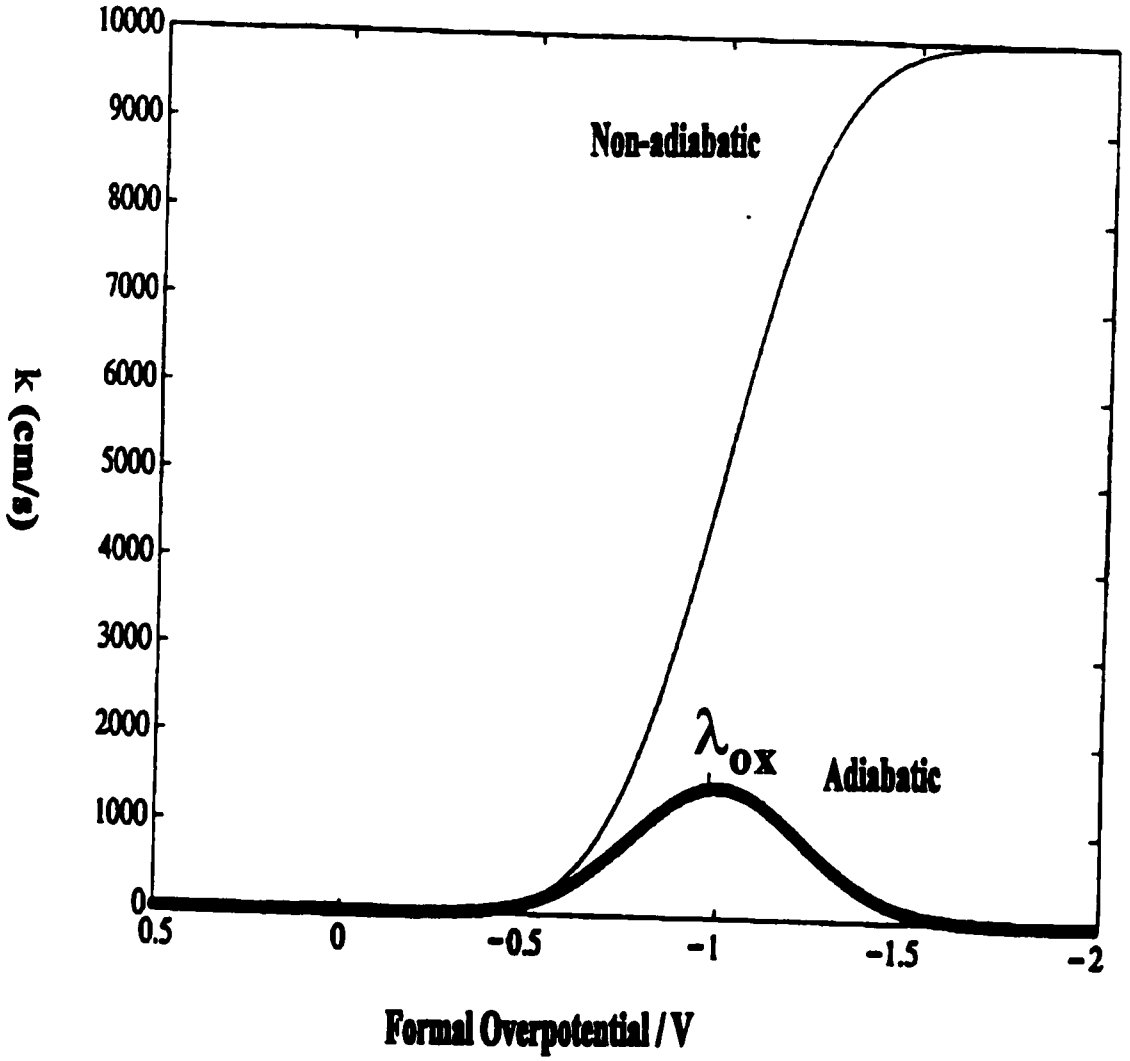

Figure 4.5 : Heterogeneous electron transfer rate constant as a function of the formal overpotential for adiabatic and non-adiabatic electron transfer reactions (from Reference 22).

had failed because the electron transfer rate was faster than the diffusion rate. Chidsey [19] used ferrocene terminated alkanethiols to eliminate the problem of diffusion and to slow down the electron transfer by controlling the distance between the electrode and the redox centre.

$$k^{o}_{app} = k^{o} \exp(-\beta d) \qquad (20)$$

where k^{o} is the apparent standard rate constant, d is the barrier thickness and β is the tunneling constant and is expressed as :

$$\beta = [2(2m)^{1/2}/\hbar][E_B - E + e\eta/2] \qquad (21)$$

where E_B is the energy barrier at $\eta = 0$, e is the electric charge and η is the overpotential. This equation assumes that all of the potential drop occurs across the energy barrier and therefore changes in the average barrier height E_B are proportional to $\eta/2$. As the overpotential becomes more positive, the average barrier height E_B increases as well. The barrier height depends upon the electrode potential. It increases as the overpotential becomes more positive and decreases as the overpotential becomes more negative.

Chidsey [19] studied the rate constant of electron transfer of chemisorbed ferrocenethiols. The shape of the cyclic voltammograms were compatible with a reversible redox process. Tafel plots were measured at 1°, 25°, 47 °C and for overpotentials of up to 1 volt. Higher scan rates show a large splitting of the current peaks which indicates that the rate of electron transfer is comparable to the scan rate. Tafel plots at very negative overpotentials show a curvature, as predicted by Marcus. Only two parameters, λ, the reorganization energy and, k^{o}_{app}, the apparent standard rate constant were needed to fit the Tafel plots at all temperatures.

Marcus relation $\quad \Delta G^{\neq}_{f,b}(E_i) = [\lambda \pm e(E_i - E^{0\prime})]^2 / 4\lambda \qquad (22)$

Becka and Miller [20] and Finklea and co-workers [21,22] used the fact that alkanethiols form ordered and compact monolayers to experimentally verify the Marcus theory of electron transfer. They have used two approaches : the redox center attached directly to an alkane thiol [23-31] and the redox species dissolved in the electrolyte [32,33,34-37].

Finklea and co-workers [35] investigated the kinetics of $Fe(CN)_6^{3-/4-}$, $Fe^{3+/2+}$, and $Ru(NH_3)_6^{3+/2+}$ redox reactions at gold surfaces modified with alkyl thiols (C_{12}, C_{14}, C_{16}, and C_{18}). They reported mercaptan monolayers with a low number of defect and pinholes. They proposed the redox molecule can approach the electrode surface at defects sites. This gives a distribution of rate constants. The faster rate of electron transfer occurs at defect sites. Smaller rates are observed at collapsed sites. The smallest rate occurs at well oriented monolayers.

Finklea and Hanshew [21] varied the distance between the electrode and the redox centers by using different chain lengths. They found that the electron transfer rates decrease exponentially with distance. These results are compatible with electron tunneling across the alkane chain.

Mixed monolayers of $HS(CH_2)_{15}CONHCH_2 pyRu(NH_3)_5^{2+}$ and $HS(CH_2)_{15}COOH$ on gold surfaces in aqueous electrolyte at pH = 4 and temperatures ranging up to 60 °C were studied by Finklea and co-workers [22]. The e-transfer kinetics are found to be independent of the anion type (1 M Na_2SO_4, NaCl, $NaNO_3$, or $NaClO_4$) in the electrolyte. Cyclic voltammetry, chronoamperometry and AC impedance spectroscopy all confirm that one standard rate constant and one reorganization energy describes the e-transfer kinetics of the majority of the redox centers. Chronoamperometry plots [ln(i) vs t] are linear for all four electrolytes examined and at all temperatures at longer times (once the redox centers at defects sites have been reduced). Their Tafel plots agree qualitatively with the predictions of the Marcus model.

Miller and co-workers [2] have generated films of alkanethiol hydroxyl terminal groups on gold substrates with a low number of defects. In this case, the dominant mechanism of e-transfer is by electron tunneling through the monolayer. Miller et al. suggested that the hydroxy terminal groups stabilize the monolayer by the formation of hydrogen bonding between adjacent hydroxy groups and between hydroxy groups and the aqueous solution. This should decrease the monolayer/aqueous surface energy when compared to a methyl terminal groups. They reported that the standard rate constant, k_o, for the $Fe(CN)_6^{3-}$ reduction on a bare gold electrode is about 0.031 cm /s [38]. The current can be described by the following equation :

$$I = i_o \exp(-\beta d) \qquad (23)$$

where I and i_o are the currents measured at a coated and a bare electrodes, respectively. β is the tunneling barrier coefficient and d is the monolayer thickness. $Fe(CN)_6^{4-/-3}$ redox rates across a gold electrode modified with $HS(CH_2)_{16}OH$ show no strong dependance on the temperature at high overpotentials (> 0.4 V). Whereas at low overpotential values (-0.1 to 0.3 V), there is a slight increase of the rate with increasing temperature. They found that the overpotential dependence of the rates of e-transfer of the redox couples studied deviated from Butler-Volmer kinetics and were in agreement with Marcus theory predictions [8]. For gold surfaces coated with hydroxy thiol monolayers, the heterogeneous e-transfer rate of a redox probe is reduced by about 2.5 for each CH_2 added. Miller et al. have also examined many redox molecules [$Fe(CN)_6^{3-}$, $Fe(bpy)(CN)_4^-$, $W(CN)_8^{3-}$, $Ru(NH_3)_6^{3+}$, Fe^{3+}, and Ce^{4+}]. They reported that the heterogeneous e-transfer rate increases exponentially with the electrode potential. When the electrode potential is increased, the rate varies linearly and finally becomes independent of the overpotential at sufficiently negative potentials, in agreement with the predictions of Marcus theory of the "inverted" region. This "inverted" region is more noticeable in a first derivative diagram [20].

French and Creager [39] used a new approach to examine the alkanethiol barrier layers on gold electrodes. Dodecanethiol coated gold electrodes were investigated in aqueous electrolyte solution saturated with 1-octanol and containing either ferrocyanide or hydroxymethylferrocene as the redox species. This work revealed that octanol significantly improves the alkanethiol barrier properties by filling the defects sites. The two redox species exhibit very different behavior that can be explained by the fact that the ferrocyanide has poor solubility in organic solvents and its large negative charge will be very difficultly come closer to the electrode. Hydroxymethylferrocene is neutral and highly soluble in organic solvents, and therefore should have a greater affinity to come closer to the electrode and promote electrooxidation.

It is clear from the results presented above that there is a distribution of electron transfer rates. This is caused by the presence of defects in the thiol monolayer. We now discuss models developed by Amatore et al. [40] to analyze voltammetric and chronoamperometric measurements on a partially blocked electrode.

The partially blocked electrode is treated as a series of active sites forming a microelectrode array surrounded by an inactive (blocked) surface. The active sites may have different forms such as a disc or a rectangle. In both cases, the separation between the active centers is small compared to the thickness of the diffusion layer. As the active area decreases and the separation between the active sites increases, the peak currents are attenuated. For a sufficiently low concentration of active sites of small size, the voltammograms exhibit a limiting current independent of the potential scan rate.

The theoretical model for diffusional behavior of microelectrode assemblies predicts three types of behavior depending on the microelectrode average size and distribution and the relaxation time scale of the electrochemical technique used. In cyclic voltammetry the relaxation time is given by $t_c = RT/F\upsilon$ where R, T and F have their usual definition whereas υ is the scan rate. At relatively short times, the diffusion layer thickness δ is small compared

to the microelectrode diameter Φ and the distance **d** between the centers of the two adjacent microelectrodes Φ, $\mathbf{d} \geq \delta$. This situation leads to semi-infinite linear diffusion and a macroelectrode behavior is expected. At longer times, ($\delta > \Phi$ but still $\delta < \mathbf{d}$). There is a spherical diffusion of the reactants to individual active sites. This is a microelectrode behavior. At even longer times, $\delta > \Phi$ and **d**, the individual spherical diffusion layers overlap and a semiinfinite linear diffusion is again expected.

Estimates of the average size of the active sites and the spacing between them can be obtained from voltammetry by $1 - \theta = (r_1/r_2)$, where r_1 is the size of the active centers and r_2 is the radius of the inactive sites [41].

The larger the peak separation between the anodic and the cathodic processes, the larger the coverage (θ coverage). If θ is not close to unity, the diffusion to the active sites can be perpendicular and parallel to the electrode surface and the electrochemical response will be the same as at a bare electrode surface but with a reduced apparent standard rate constant of e-transfer. For θ very close to unity, the diffusion is spherical type, and the larger the coverage, the slower the apparent e-transfer.

Finklea et al. [34] studied blocking properties of octadecyltrichlorilane (OTS) on gold electrodes by various electroactive species ($Fe(CN)_6^{3-}$, $Fe^{3+/2+}$, $Fe(EDTA)^{2-}$, and $Ru(NH_3)_6^{3+}$) in solution. These monolayers were characterized by cyclic voltammetry as highly compact, hydrophobic monolayers and with pinholes due to structural imperfections. This study reveals that e-transfer is dominated by permeation of the electroactive species through the defects present in the film.

Sabatini et al. [36,37] used a mixture of a polymerizable component octadecyl trichlorosilane, OTS, which provides the desired structural stability and compactness, and octadecyl mercaptan, OM, to fill imperfections formed by the polymeric component. A $Fe(CN)^{4-/3-}$ redox couple was employed as a quantitative measure of the average pinhole size

and distribution at a sputter-deposited gold surface. A behavior typical of microelectrodes was found. Porter et al.[1] studied the long chain monolayers that provide substantial barriers to electron-transfer and are strongly resistant to ion permeation but not defect free.

Lennox et al.[42] investigated the reduction of $K_3Fe(CN)_6$ through films of various alkyl mercaptans of long hydrocarbon chains containing C_{16} to C_{20} SAMs at gold polycrystalline surfaces. They reported good blocking of the gold surfaces by the monolayer films. They suggested that ion permeation is the only process of e-transfer between the electroactive species in solution and the modified electrode surfaces.

McCrindle et al.[41] used 4-pentadecylpyridine film deposited at a gold (111) electrode to investigate the reduction of $Fe(CN)_6^{3-}$ from the electrolyte solution. The rate of Fe $(CN)_6^{3-}$ reduction at the film covered electrode is characteristic of non-linear mass transport diffusion to active pores (sites). McCrindle et al. used the model of a partially blocked electrode surface consisting of a set of N circular active centers of size r_1 surrounded by larger inactive sites covered by a surfactant of radius r_2. This model predicts that the inverse of the current density (1/j) vs the square root of the time ($\sqrt{t}$) plots could be used to obtain the concentration and size of defects. This study reported an average pore size range between 10 and 30 μm and pore spacing between 200 and 500 μm.

2. Results and Discussion

The reduction of $Fe(CN)_6^{3-}$ at a metal electrode is a first order one electron process and can be described as :

$$Fe(CN)_6^{3-} + e\ (electrode) \underset{k_b}{\overset{k_f}{\rightleftharpoons}} Fe(CN)_6^{4-} \qquad (24)$$

where k_f and k_b are the forward and backward rate constants. The reaction free energy ΔG^o is :

$$\Delta G^o = -nF(E - E^{o'}) \qquad (25)$$

where E is the electrode potential and $E^{o'}$ is the formal potential of the electroactive redox species. When $E = E^{o'}$, $k_f = k_b$. Generally, k_f is expected to increase rapidly with decreasing reaction free energy while k_b is expected to increase rapidly with increasing reaction free energy [19] :

$$k = A \exp(-E_a/RT) \qquad (26)$$

where k is the rate constant, A is the pre-exponential factor and E_a is the free energy which can be determined from an Arrhenius plot (ln k vs. 1/T).

Voltammograms of the reduction current of $Fe(CN)_6^{3-}$ redox species on a Au(111) surface in 0.1 M NaF solution at three different scan rates are shown in Figure 4.6a. Before describing the effect of the scan rate, we will describe one voltammogram. The potential is first scanned in the negative direction. The ferricyanide is reduced to ferrocyanide, and there is an increase in the current. A maximum value, i_{pc}, is reached. There is then a decrease of the current because of the depletion of ferricyanide in the double layer. The current then reaches a limiting value due to the diffusion of ferricyanide to the surface. When the potential is scanned in the reverse (positive) direction, the ferrocyanide molecules created on the cathodic scan are oxidized. The shape of the positive going voltammogram is similar to that recorded on the negative going potential scan. A maximum current, i_{pa}, is observed and then a limiting current. $E_{1/2}$ is the half-wave potential. This is the average value of the potentials of the maximum anodic and cathodic current (see Fig. 4.6a). i_{pc} is found to increase as $(\text{scan rate})^{1/2}$, as shown in Figures 4.6b.

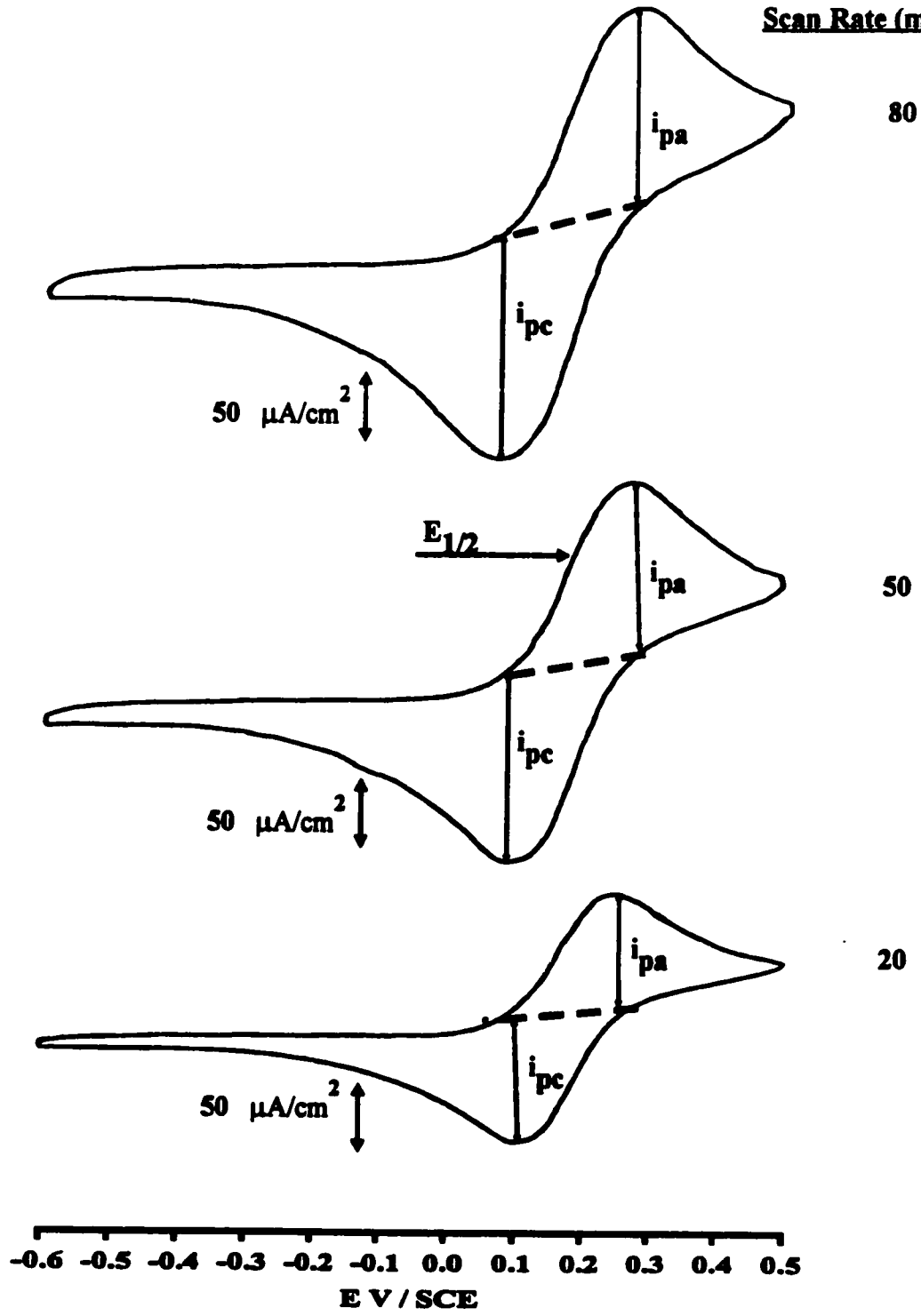

Figure 4.6a : Voltammograms recorded in 0.1 M NaF + 1 mM $Fe(CN)_6^{3-}$ at three different scan rates at 21 °C.

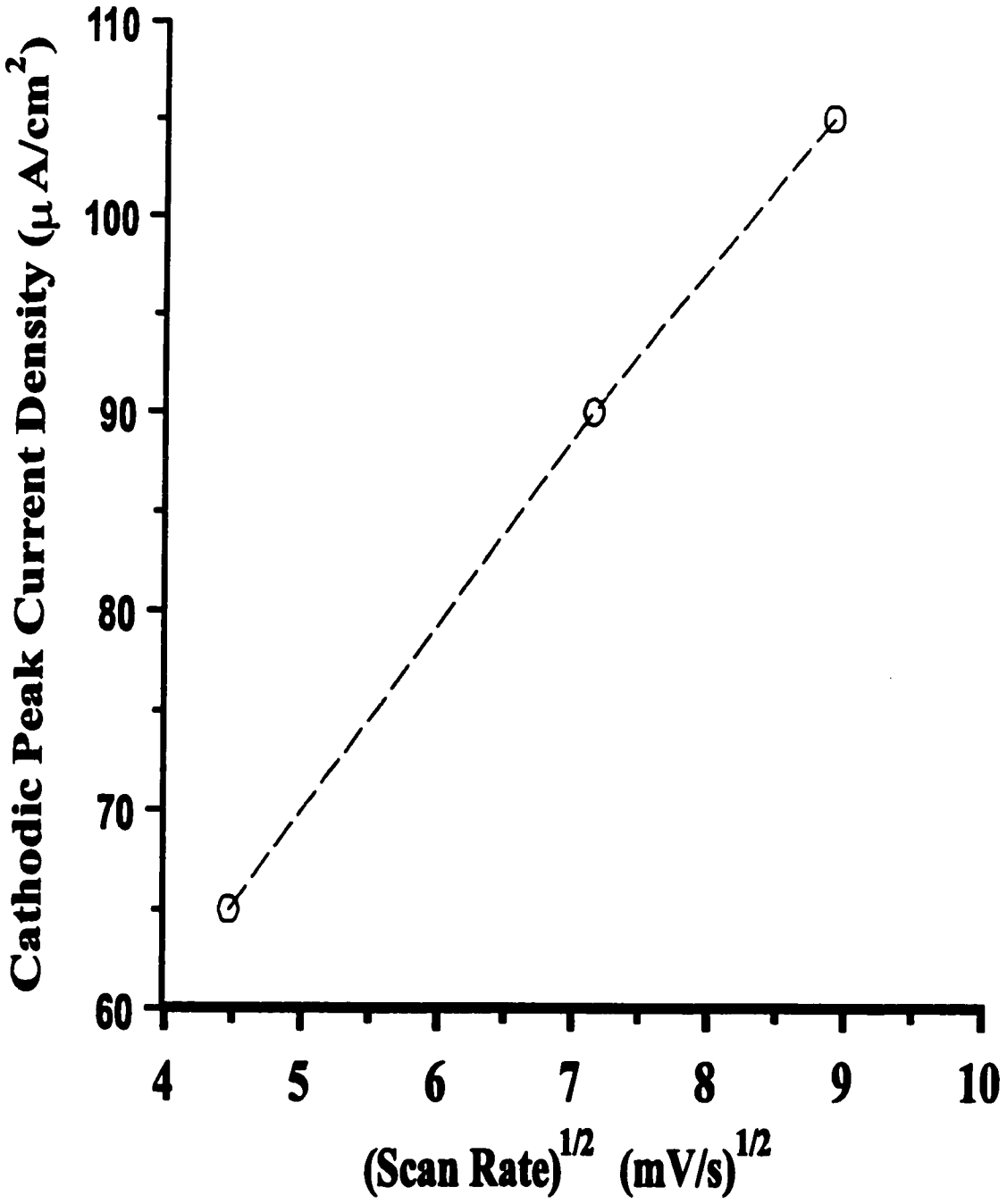

Figure 4.6b : Corrected cathodic peak current density of the reduction of $Fe(CN)_6^{3-}$ as a function of the square root of the potential scan rate. Measurements were done in 0.1 M NaF + 1.0 mM $Fe(CN)_6^{3-}$ at a gold (111) electrode and 21 ^{o}C.

2.1 Ion permeability of a monolayer of hexadecanethiols formed by a single incubation:

The effect of a 30 minute incubation of a Au(111) electrode in 1 mM hexadecanethiol ethanolic solution on the reduction of ferricyanide was examined in 1 mM $K_3Fe(CN)_6$. Figure 4.7 shows the clean gold and the thiol-coated gold. The i_{ps} are reduced by two orders of magnitudes. The reductive current peak is shifted by approximately -400 mV when the thiols are adsorbed. Thus, most of the surface is covered by thiols and the kinetics of the reduction is considerably slowed down. These characteristics are compatible with the presence of small defects. Thus the monolayer obtained from a single incubation has a few defects where the reduction of ferricyanide occurs. The voltammograms obtained after a single incubation vary significantly as a function of temperature (see Fig. 4.8).

In order to better understand the defects, we examined them indirectly by looking at the change of the reduction of ferricyanide as a function of temperature. The reduction peak is barely visible. It is followed by a limiting current. The oxidative peak is also attenuated. The redox peak separation (ΔE_p redox) at 5°C is about 320 mV. This is twice what is observed on bare gold (160 mV). The i_p is approximately three times smaller than that observed on bare gold. As the temperature increases, the peaks separation decreases and the i_p increases as is shown in Figs. 4.8 and 4.9. In Fig. 4.9 we see that the cathodic peak potential E_{pc} appears at 0 mV at 5 °C and then shifts to positive potential until 25 °C. Then it slowly moves to 60 mV at 60 °C . The anodic peak potential E_{pa} starts at about 320 mV at 5 °C and drops sharply between 5° and 25 °C and then decreases slowly to reach around 140 mV at 60 °C. The separation between the peaks decreases rapidly (at a similar rate for both peaks). After 25 °C the separation remains constant as they both shift towards more negative potentials. This trend is similar to the shift of the reduction peaks of the thiols. It is likely that this is an order to disorder transition. The fact that the peaks separation remains constant probably indicates that the size and/or shape of the defects do not change significantly after 25 °C.

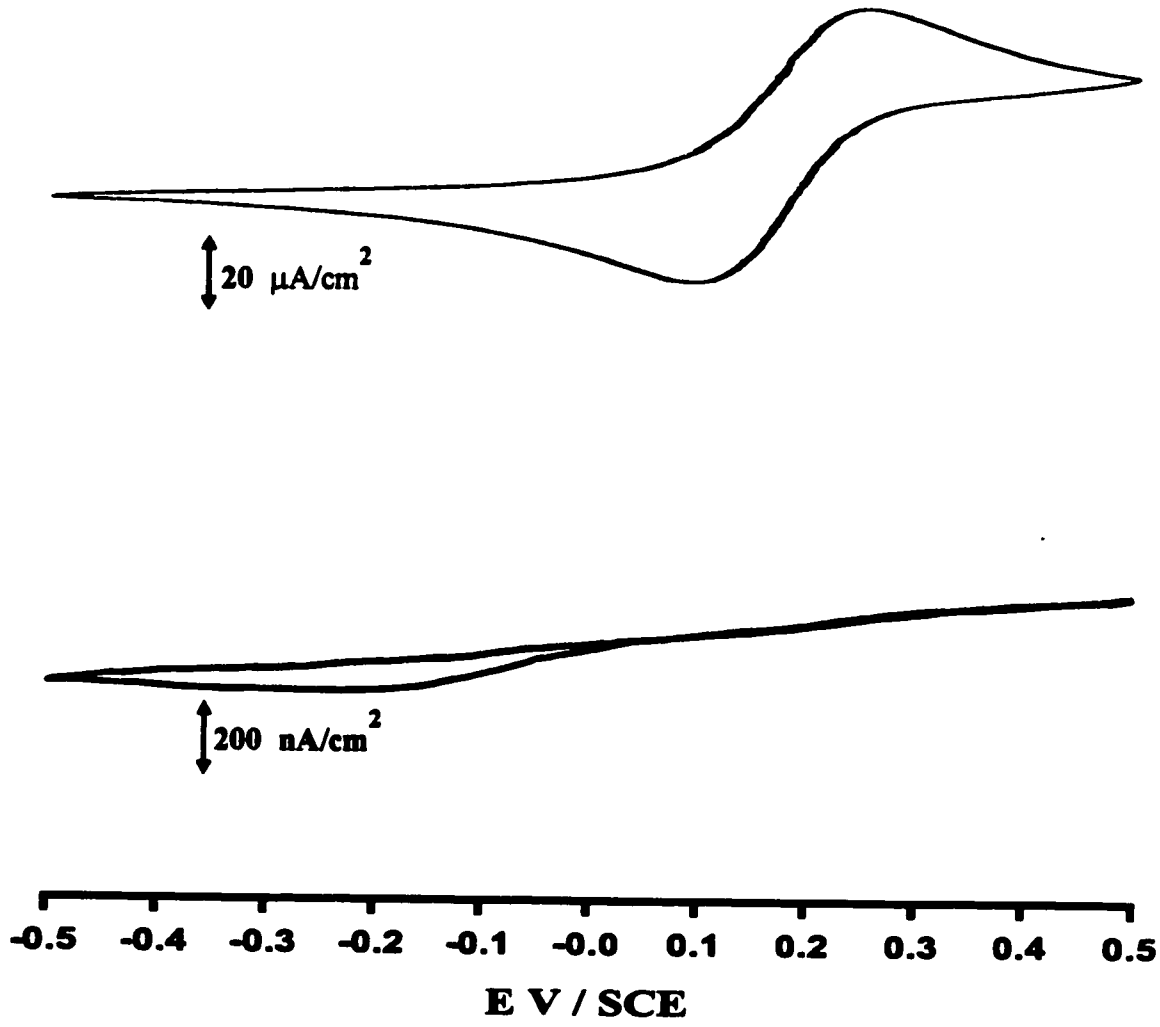

Figure 4.7 : A comparison of cyclic voltammograms for (a) a clean and (b) a hexadecanethiol modified gold (111) surface in 0.1 M NaF + 1.0 mM $Fe(CN)_6^{3-}$ redox species at a potential scan rate of 20 mV/s at room temperature.

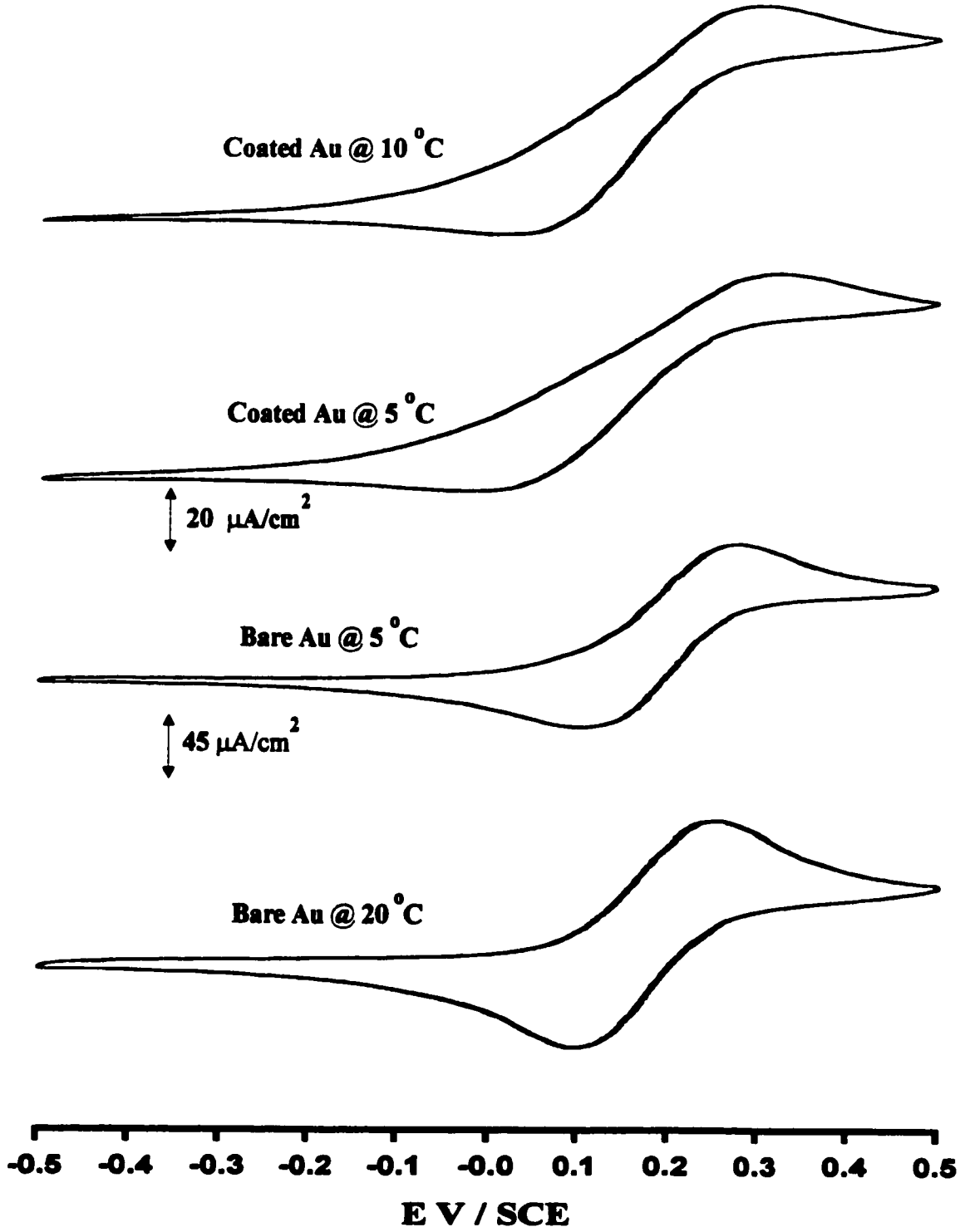

Figure 4.8a : Cyclic voltammograms of a bare Au(111) single crystal electrode and modified with hexadecanethiols recorded in 0.1 M NaF + 1.0 mM $K_3Fe(CN)_6$ at a scan rate of 20 mV/s as a function of temperature.

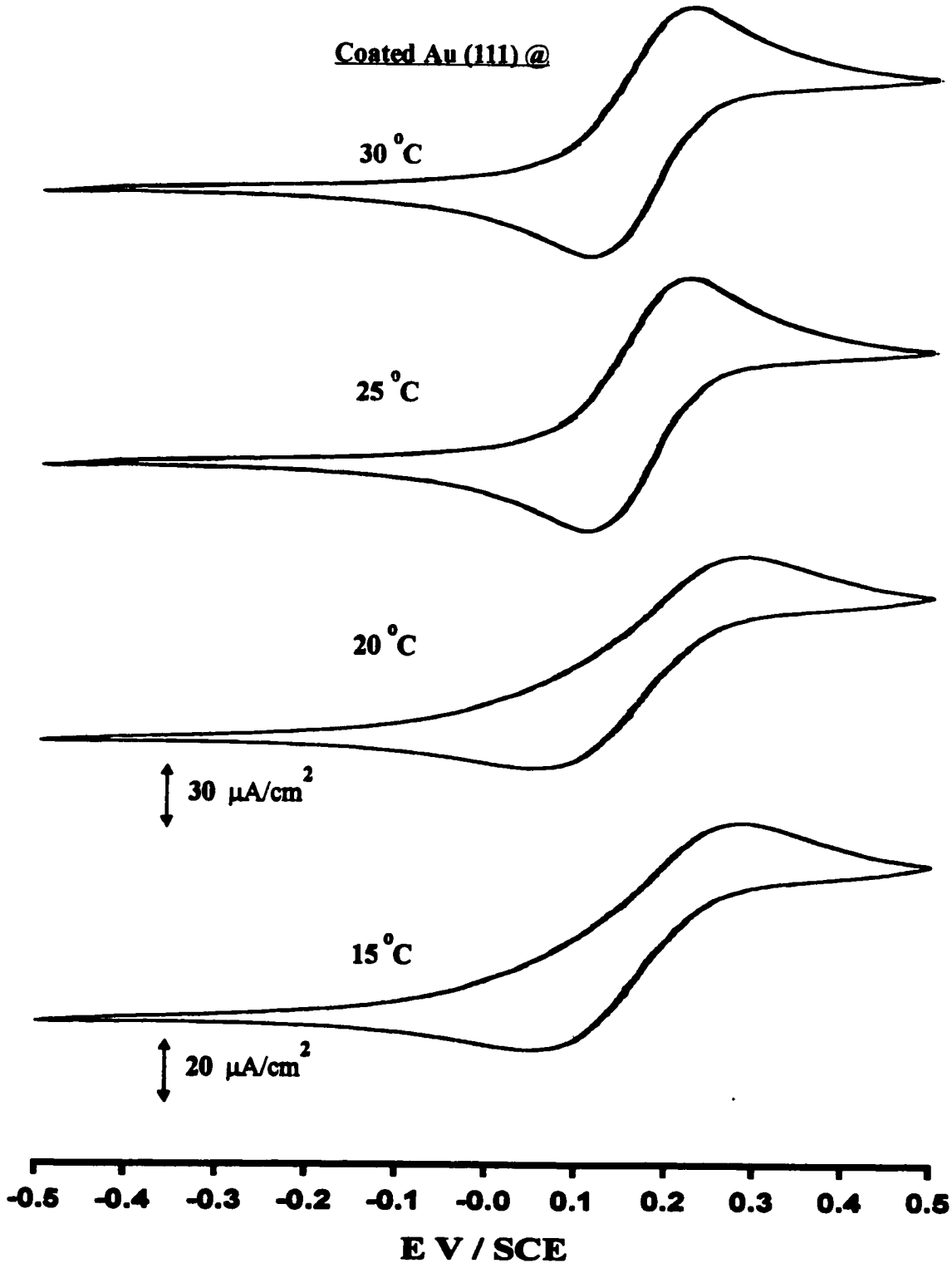

Figure 4.8b : Cyclic voltammograms of a Au(111) single crystal electrode modified with hexadecanethiols recorded in 0.1 M NaF + 1.0 mM $K_3Fe(CN)_6$ at a scan rate of 20 mV/s as a function of temperature.

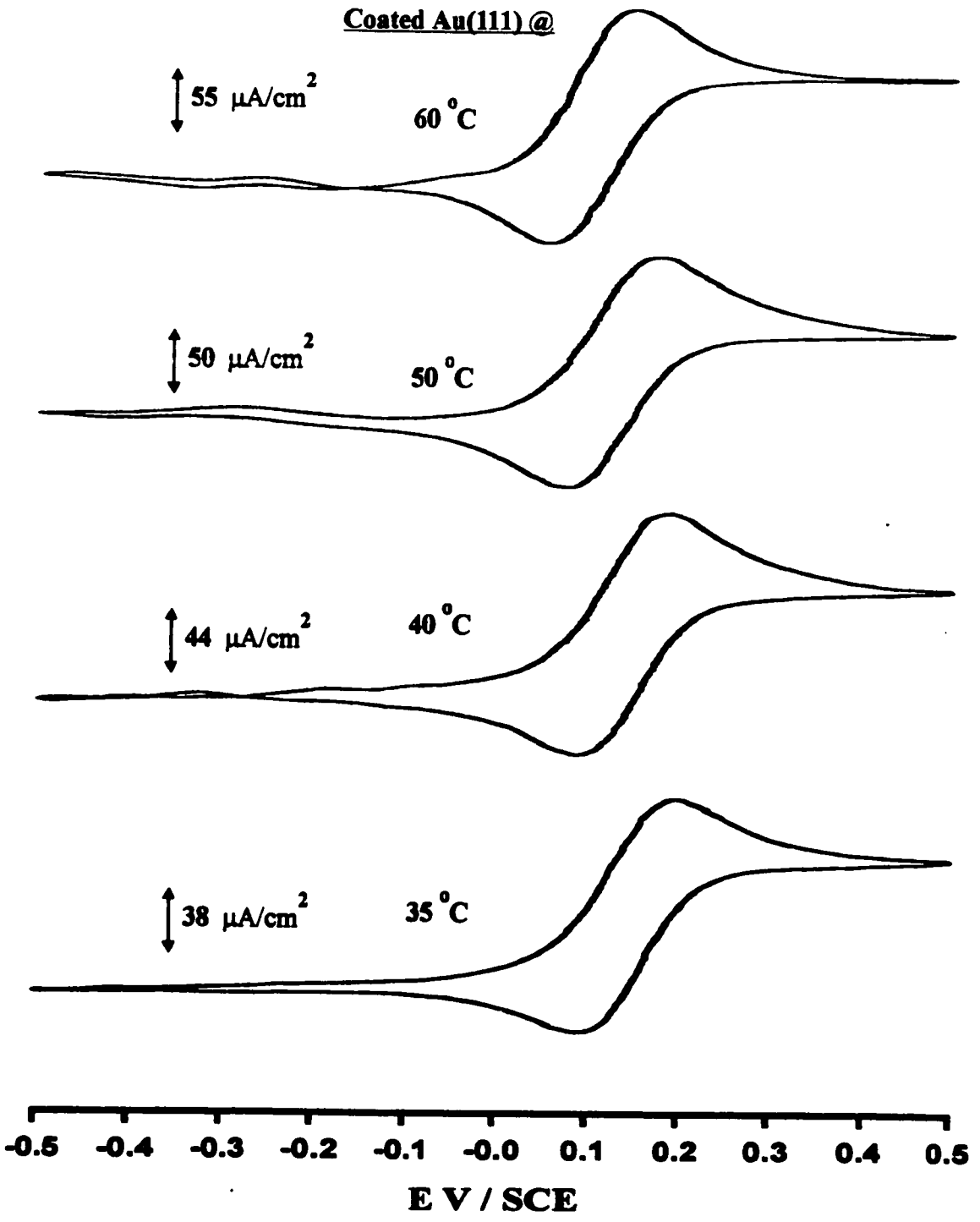

Figure 4.8c : Cyclic voltammograms of a Au(111) single crystal electrode modified with hexadecanethiols recorded in 0.1 M NaF + 1.0 mM $K_3Fe(CN)_6$ at a scan rate of 20 mV/s as a function of temperature.

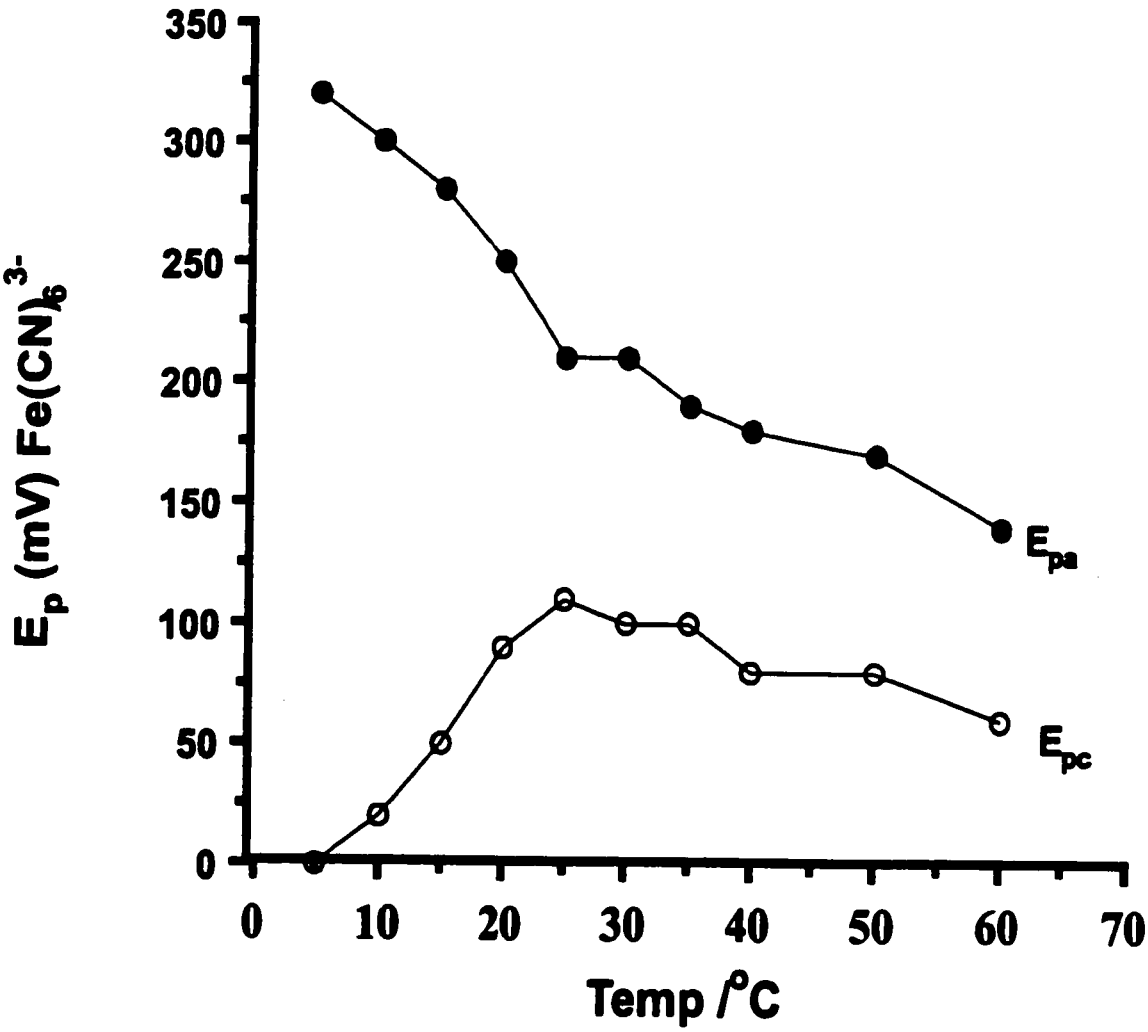

Figure 4. 9 : Anodic and cathodic peak potentials of ferricyanide as a function of temperature for a gold (111) single crystal electrode modified with hexadecanethiols after a single incubation in a solution of 10^{-2} M hexadecanethiol. Measurements were done in 0.1 M NaF containing 1.0 mM$Fe(CN)_6^{3-}$ at a scan rate of 20 mV/s.

The displacement towards more negative potentials indicates that the reduction is more difficult as the temperature is increased. We suggest that this is caused by a decrease of the average size of defects in this temperature range.

In Fig. 4.8 we see that the variation of the current density with the temperature first increases up to 25 °C, indicating an increase in the electroactive area. There is then a decrease of i_p between 30° and 35 °C. This is consistent with a collapse of the aliphatic chains that could partially block the surface and thus decrease the electron transfer rate. The increase of i_p after 35 °C is assigned to an increased desorption and/or increased mobility of the thiols at the surface. These results also indicate that there is a significant change of the monolayer structure between 25° and 35 °C. This result is compatible with the results described in Chapter 5 which show an increase with temperature of the ion permeability in the double layer region.

A comparison of the current density of a clean and a coated Au(111) surface as a function of temperature is shown in Figure 4.10. A bare gold surface displays a linear relationship. A coated gold surface exhibits a more complicated behavior. It shows the possibility of the existence of two temperature regions: one between 5° and 25 °C and a second one between ~ 25 °C and 35 °C. In the first phase, as the temperature increases, the current density increases from ~ 4 $\mu A/cm^2$ at 5 °C to ~ 30 ± 5 $\mu A/cm^2$ at 25 °C. The constant current between 25° and 35 °C suggests that the thiols at the edge of defects become disorder. This causes a reduction of the electroactive area and a decrease of the current. In the second temperature region, the current density gradually increases from ~ 25 $\mu A/cm^2$ at 35 °C to ~ 50 ± 5 $\mu A/cm^2$ at 60 °C. This behavior is assigned to the increase of the ion permeation through defects within the monolayer.

In the range of potentials used in these measurements, it is unlikely that the increase of the reduction of ferricyanide is due to the desorption of thiols. This would create more defects.

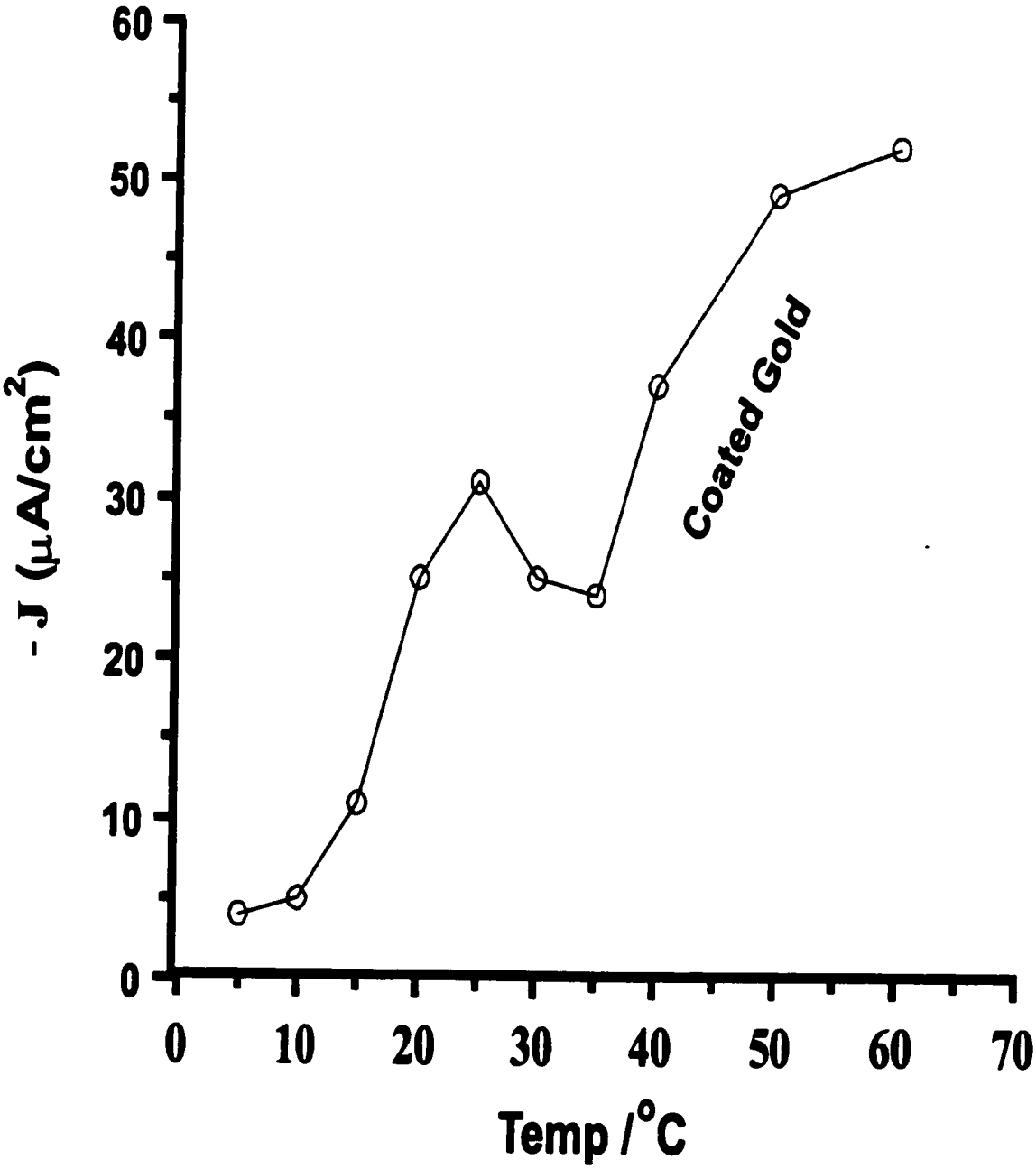

Figure 4.10 : Current density at 0.0 V as a function of temperature of a hexadecanethiol modified gold (111) electrode in 0.1 M NaF + 1.0 mM $Fe(CN)_6^{3-}$ solution at a scan rate of 20 mV/s.

Our results disagree with the results of Lennox et al.[42]. They observed two phase transitions that lead to two variations of the reduction current of ferricyanide. The first transition is assigned to a transition from a crystalline to a liquid phase. They see a second transition above 320 K which they assign to a liquid to liquid disorder transition similar to what is observed for a Langmuir-Blodgett film. This transition requires an expansion of the monolayer (i.e. an increase of the adsorbate-adsorbate separation). We do not see a second transition. We believe that this difference is linked to the fact that they used polycrystalline gold which would give rise to a lower thiol coverage and thus allow for an expansion of the monolayer. This could also be due to the desorption of thiols at a higher temperature.

2.2 Multiple Incubation:

Figure 4.11 shows the variation of the double layer charging current at - 0.1 V as a function of the number of incubations. There is a slow decrease of the double-layer current. We note that the double layer is acting as a perfect capacitor since the anodic and cathodic currents are equal and constant from 0.5 to -0.6 V. From these results we can say that after 4 one-hour incubations the monolayers are efficiently blocking the surface.

Adding the $Fe(CN)_6^{3-}$ redox probe into the 0.1 M $KClO_4$ solution confirms that there is a significant improvement of the monolayer upon successive incubations. In Fig. 4.12 we see that after the first incubation, the s-shape characteristic of a micro-electrode array is visible. There is also an exponential increase of the current when the potential is scanned past -0.3 V. The exponential increase is compatible with electron-tunneling. A second incubation decreases both the microelectrode and tunneling currents. After three incubations the microelectrode behavior disappears and only an exponential increase of the current is seen at potentials more negative than -0.3 V. Subsequent incubations do not lead to significant changes. We note that the exponential increase of the current is the same at 20 and 50 mV /s.

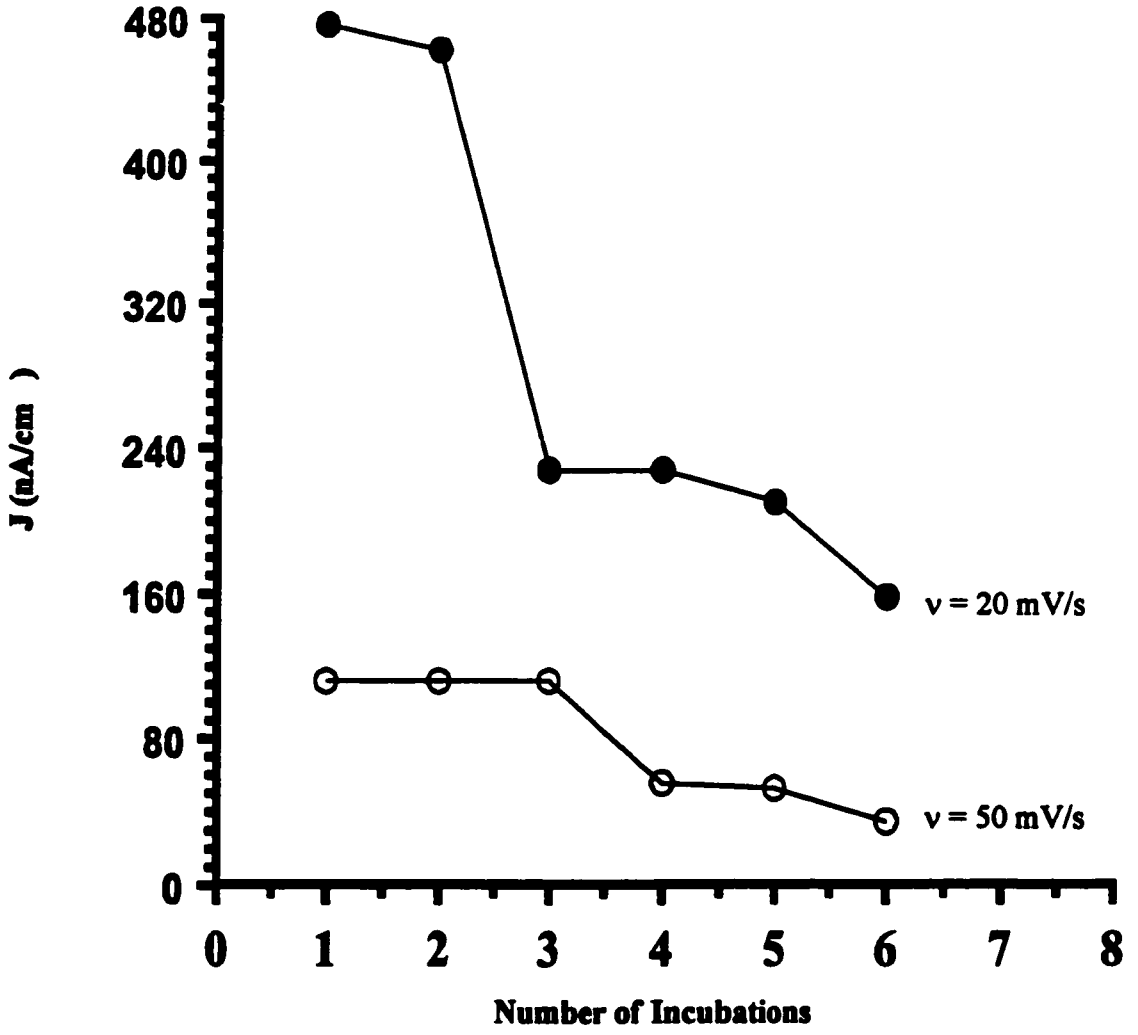

Figure 4.11 : Current density at - 0.1 V of a hexadecanethiol modified Au(111) electrode as a function of the number of incubations. Measurements were done in 0.1 M $KClO_4$ at room temperature.

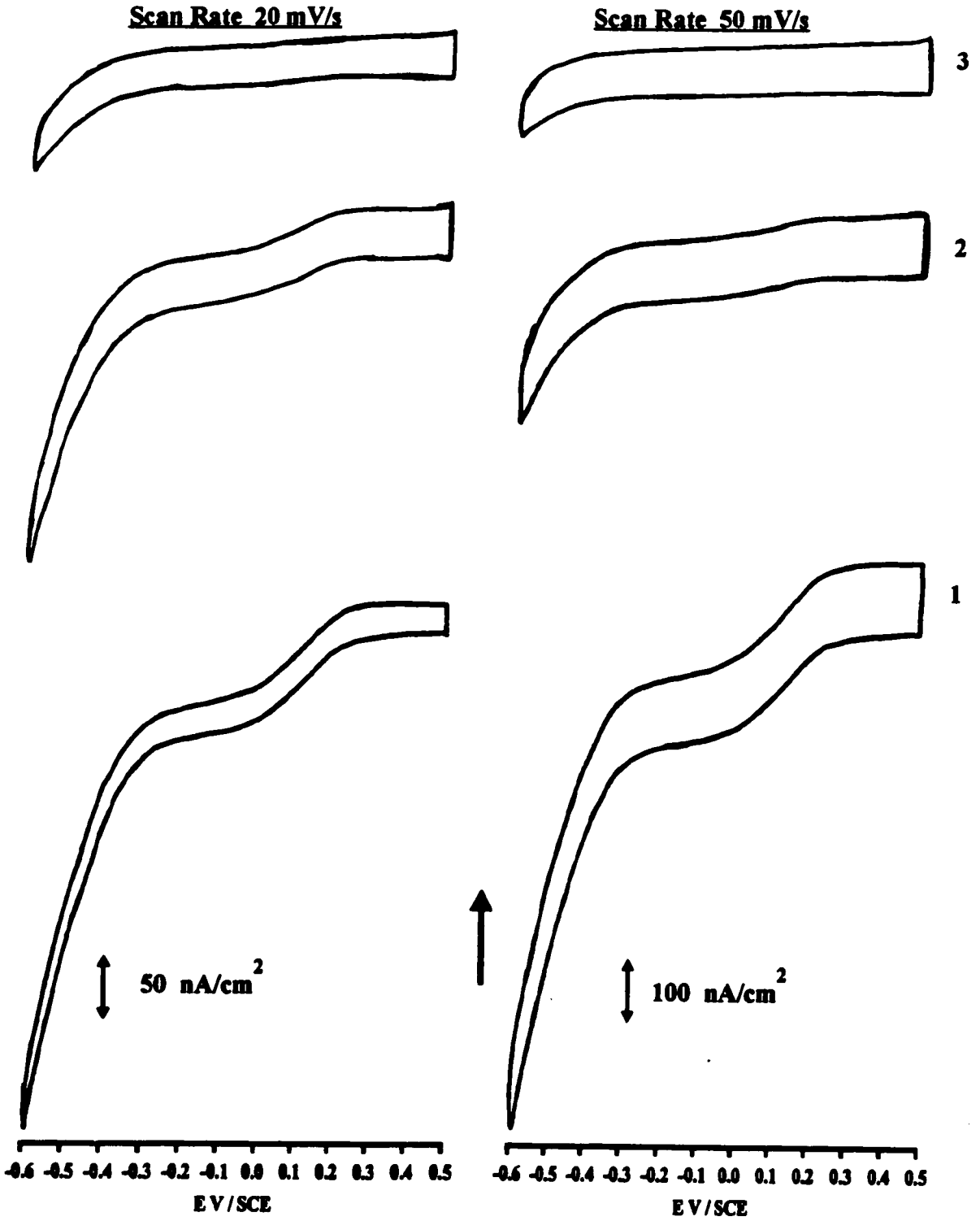

Figure 4.12a : Cyclic voltammograms of a gold (111) single crystal surface coated with a monolayer of hexadecanethiols after subsequent incubations recorded at two different scan rates in 0.1 M $KClO_4$ + 1.0 mM $Fe(CN)_6^{3-}$ at room temperature (see text).

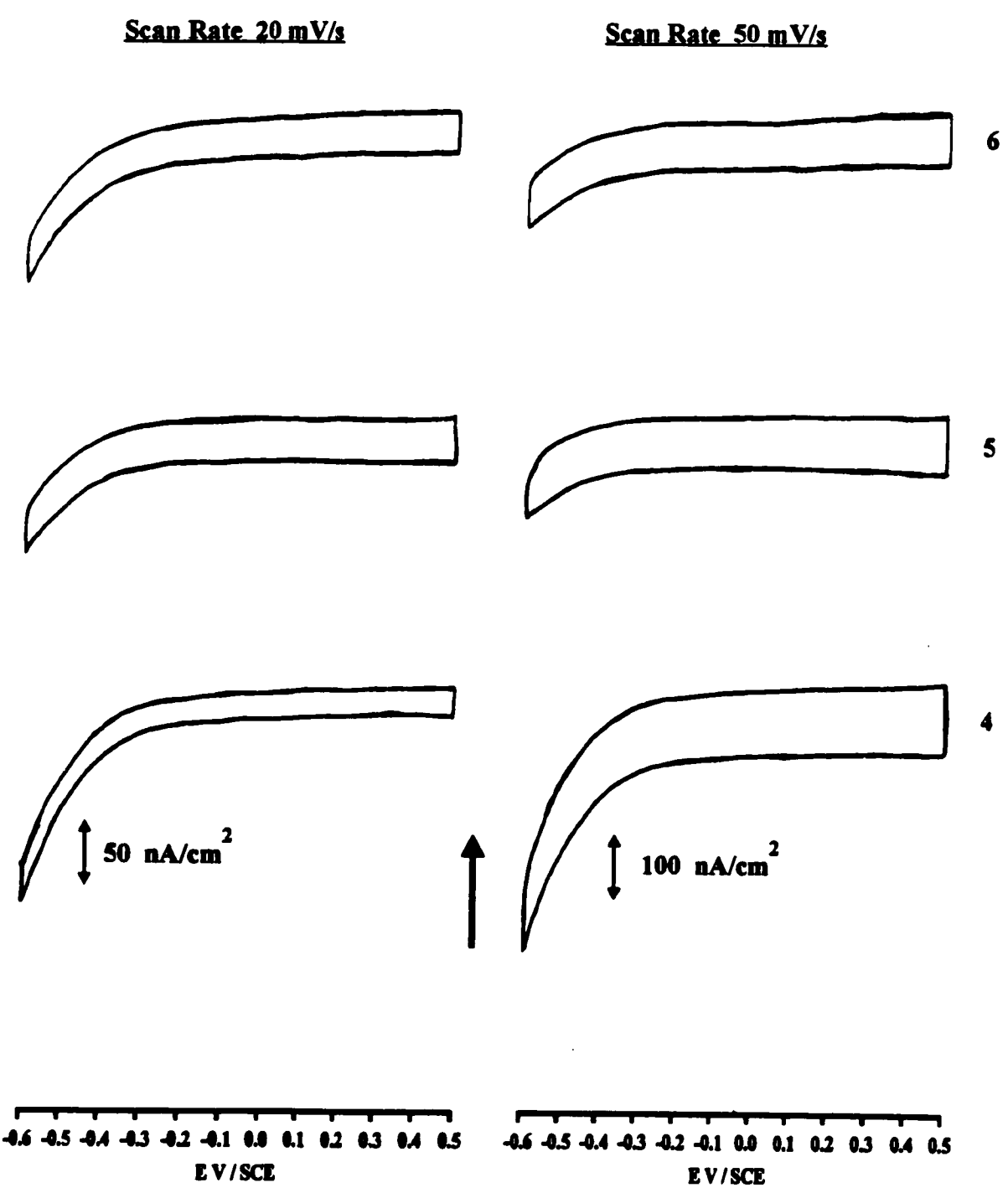

Figure 4.12b : Cyclic voltammograms of a gold (111) single crystal surface coated with a monolayer of hexadecanethiols after subsequent incubations recorded at two different scan rates in 0.1 M $KClO_4$ + 1.0 mM $Fe(CN)_6^{3-}$ at room temperature (see text).

The exponential shape of the current suggests that the electron transfer occurs via tunneling. The rate of electron transfer should be independent of the scan rate of the electrode potential in the case of tunneling. Fig. 4.13 shows that in the range of 20 to 80 mV/s the exponential increase of the current does not vary significantly. There is a linear increase of the double layer charging current between 0.5 and -0.2 V. This indicates a very low number of defects. This result supports the mechanism of electron tunneling.

The double layer charging current of a HDT SAM obtained after multiple (at least 6) one-hour immersions was measured in 0.1 M $KClO_4$ as a function of temperature. Figure 4.14 shows the measured double layer charging currents at - 0.4 V from 5° to 70 °C. The current density of the gold surface in the double layer region is approximately 12-times bigger than that of the modified gold surface. The current density of the coated gold surface as a function of temperature is independent of temperature. There is no major change in the structure that would lead to an increase in the capacitance of the modified electrode. However, beyond 70 °C there is indication of desorption of thiols.

The electron tunneling mechanism was confirmed by examining the temperature dependance of the rate of electron transfer of monolayers obtained via 6 successive one-hour incubations. In Fig. 4.15 we see that, from 5° to 40 °C, the voltammograms are identical. They show a double layer region with no current where the reduction of ferricyanide occurs. This perfect capacitor region is followed by an exponential increase of the current. This behavior is compatible with electron tunneling since it is temperature independent. Above 40 °C there is a slow increase of the current starting at - 0.2 V. This could be caused by increased disorder of the monolayer. The exponential increase does not change significantly. Fig. 4.16 represents the current density, J, measured at - 0.1 V on the voltammograms in Fig. 4.15. We see that J remains constant. We also did measurements at 50 mV s^{-1} and they are shown in Fig. 4.17. These results show the independence of the reduction current on the scan rate. The various electrochemical results described in this section are compatible with the

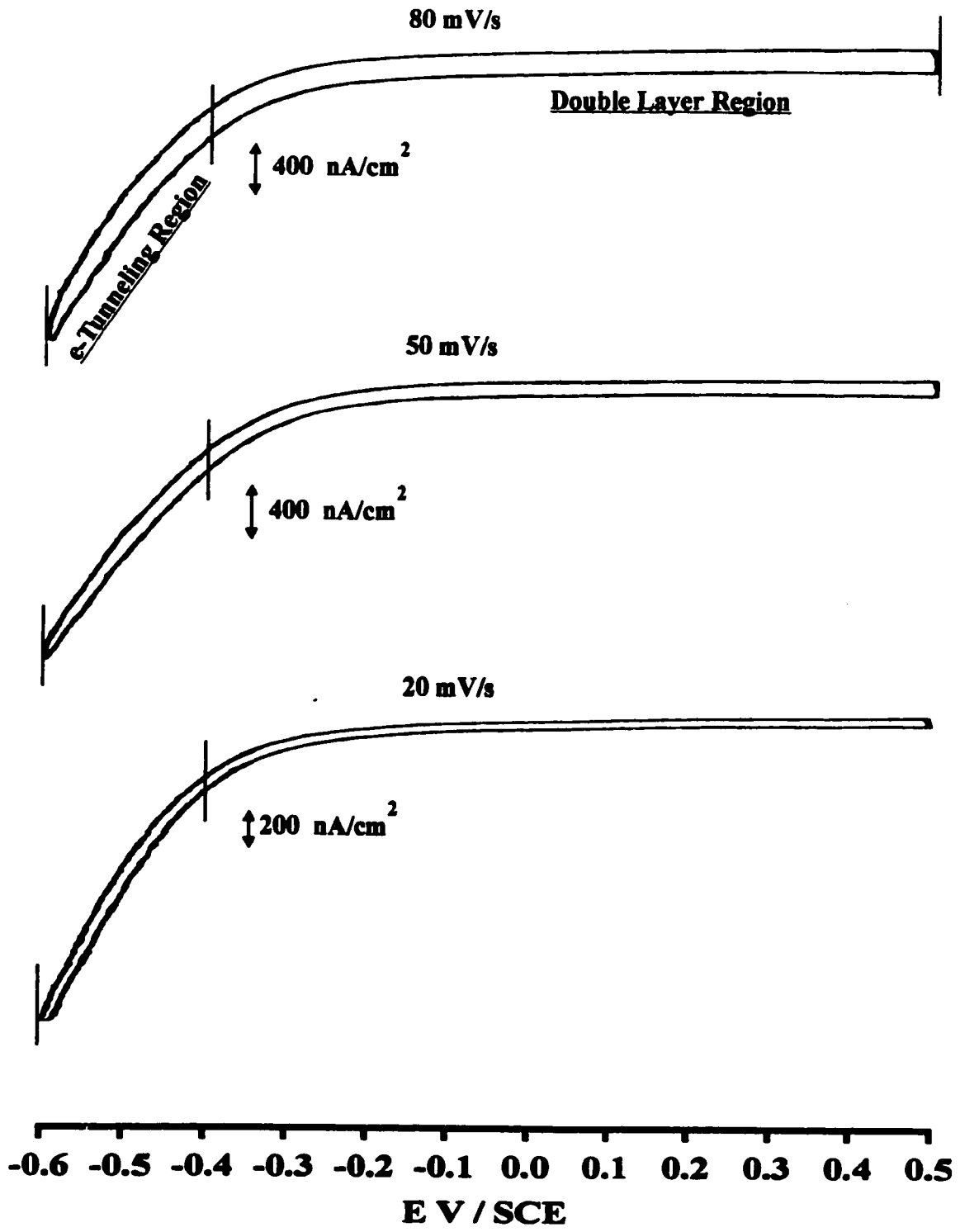

Figure 4.13 : Voltammograms of a Au(111) single crystal electrode modified with hexadecanethiols after multi-incubations in a solution of 10^{-2} M hexadecanethiol as a function of scan rate. Measurements were done in 0.1 M NaF + 1.0 mM $K_3Fe(CN)_6$ at 20 °C (see text).

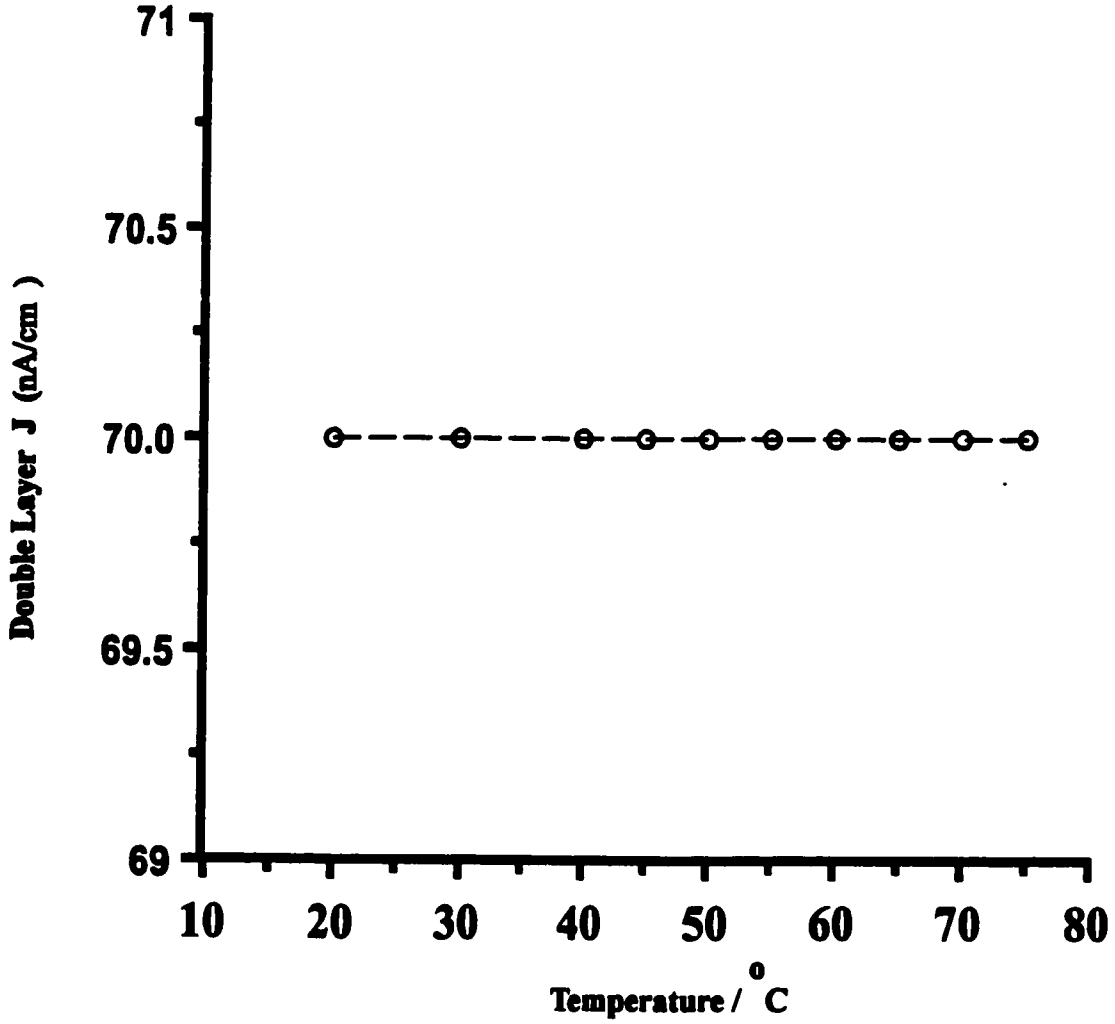

Figure 4.14 : Double layer current density as a function of temperature of a hexadecanethiol modified Au(111) electrode after multi-incubations in 10^{-2} M hexadecanethiol solution. Measurements were done in 0.1 M $KClO_4$ at a potential scan rate of 20 mV/s.

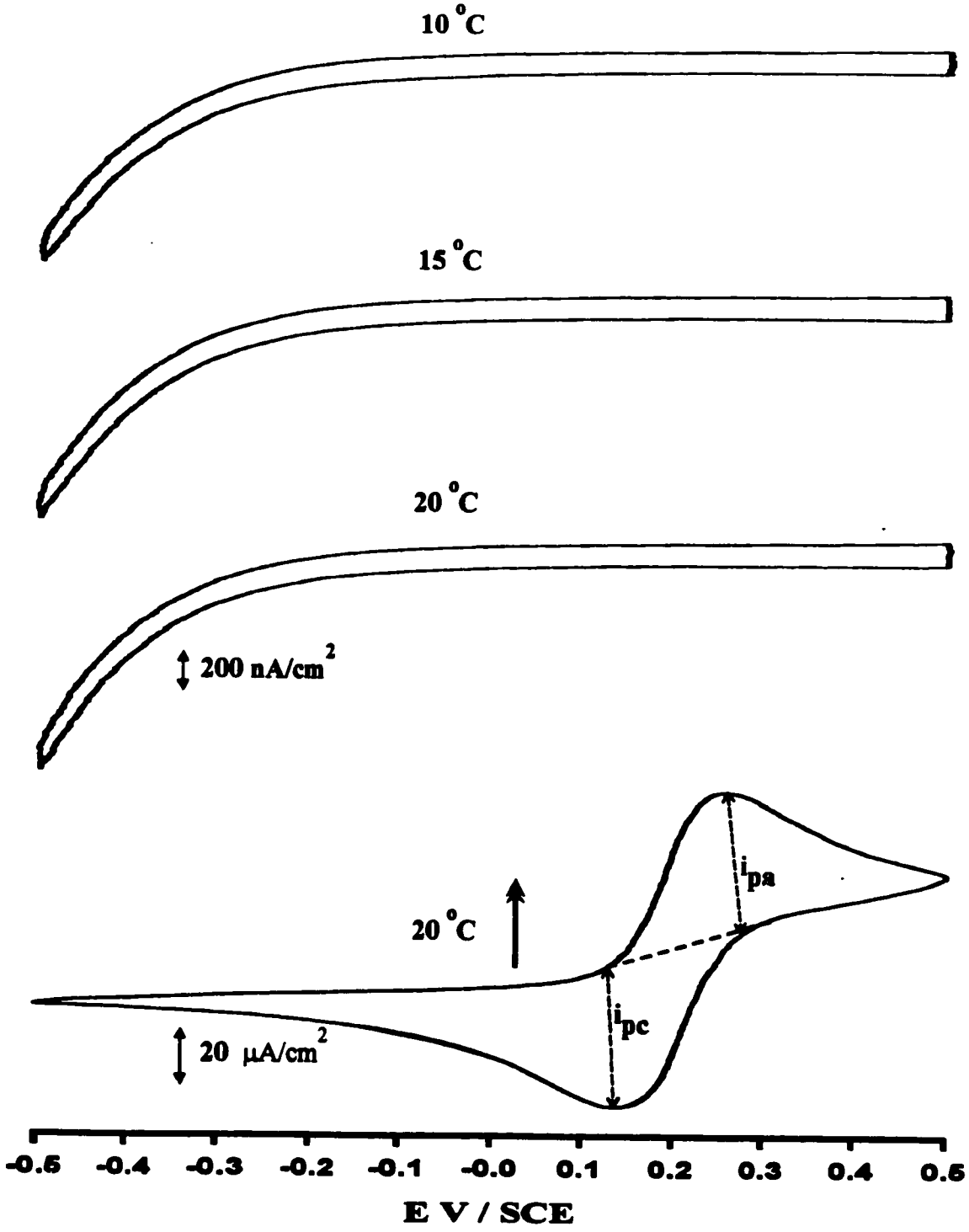

Figure 4.15a : Cyclic voltammograms of a Au(111) electrode coated with hexadecanethiol after multiple incubations in 10^{-2} M hexadecanethiol solution as a function of temperature. Measurements were done in 0.1 M NaF + 1.0 mM $K_3Fe(CN)_6$ at a scan rate of 20 mV/s (see text).

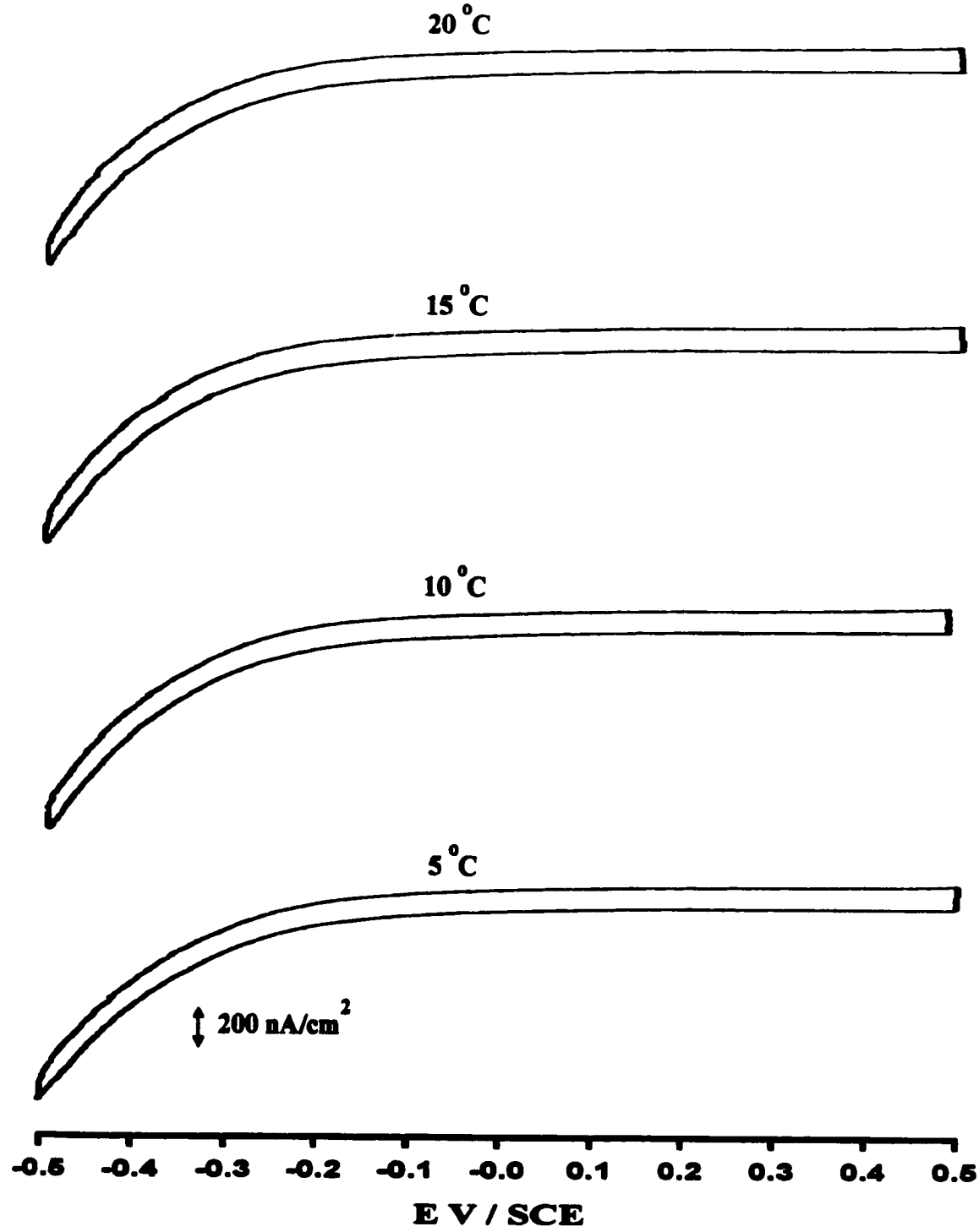

Figure 4.15b : Cyclic voltammograms of a Au(111) electrode coated with hexadecanethiol after multiple incubations in 10^{-2} M hexadecanethiol solution as a function of temperature. Measurements were done in 0.1 M NaF + 1.0 mM $K_3Fe(CN)_6$ at a scan rate of 20 mV/s (see text).

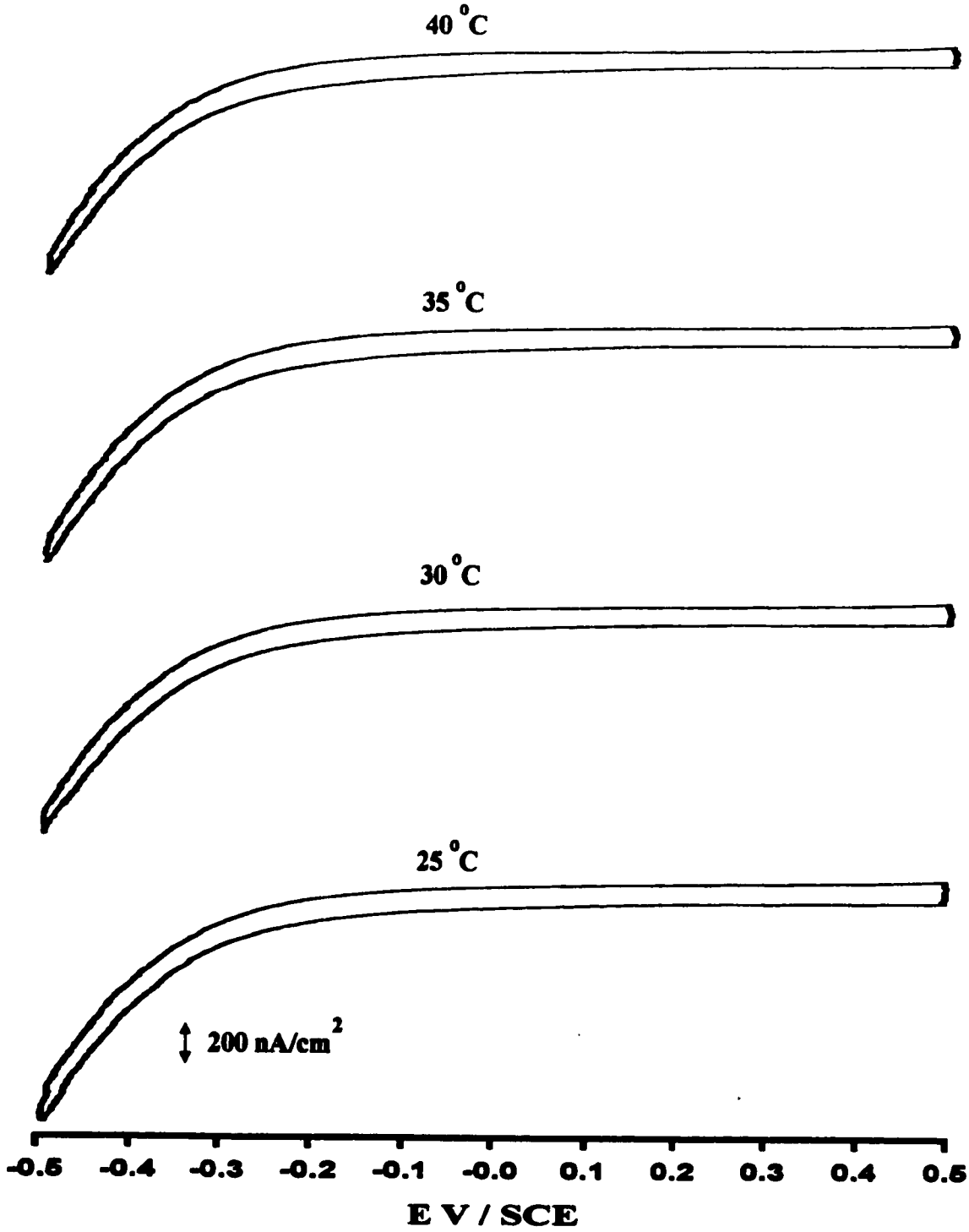

Figure 4.15c : Cyclic voltammograms of a Au(111) electrode coated with hexadecanethiol after multiple incubations in 10^{-2} M hexadecanethiol solution as a function of temperature. Measurements were done in 0.1 M NaF + 1.0 mM $K_3Fe(CN)_6$ at a scan rate of 20 mV/s (see text).

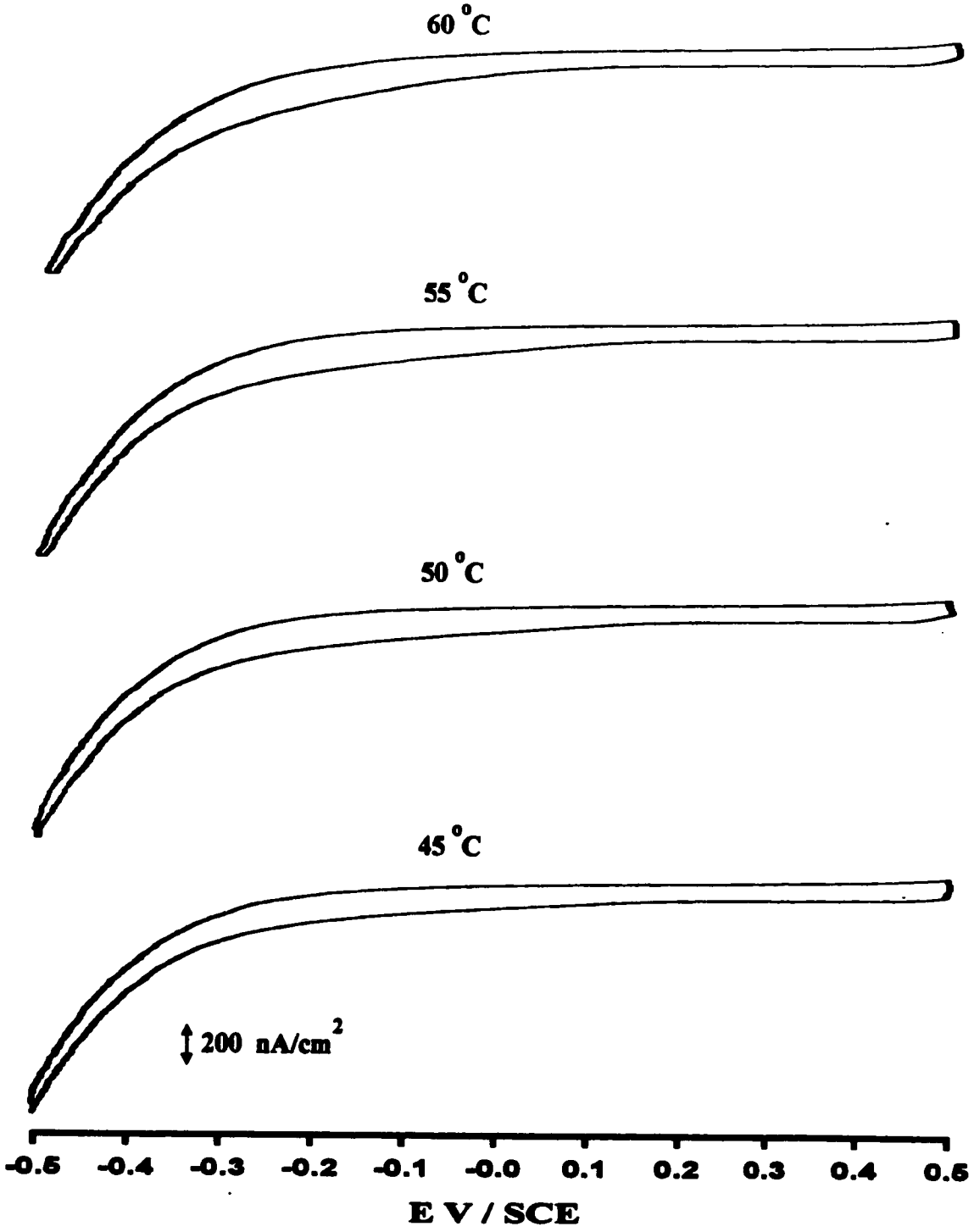

Figure 4.15d : Cyclic voltammograms of a Au(111) electrode coated with hexadecanethiol after multiple incubations in 10^{-2} M hexadecanethiol solution as a function of temperature. Measurements were done in 0.1 M NaF + 1.0 mM $K_3Fe(CN)_6$ at a scan rate of 20 mV/s (see text).

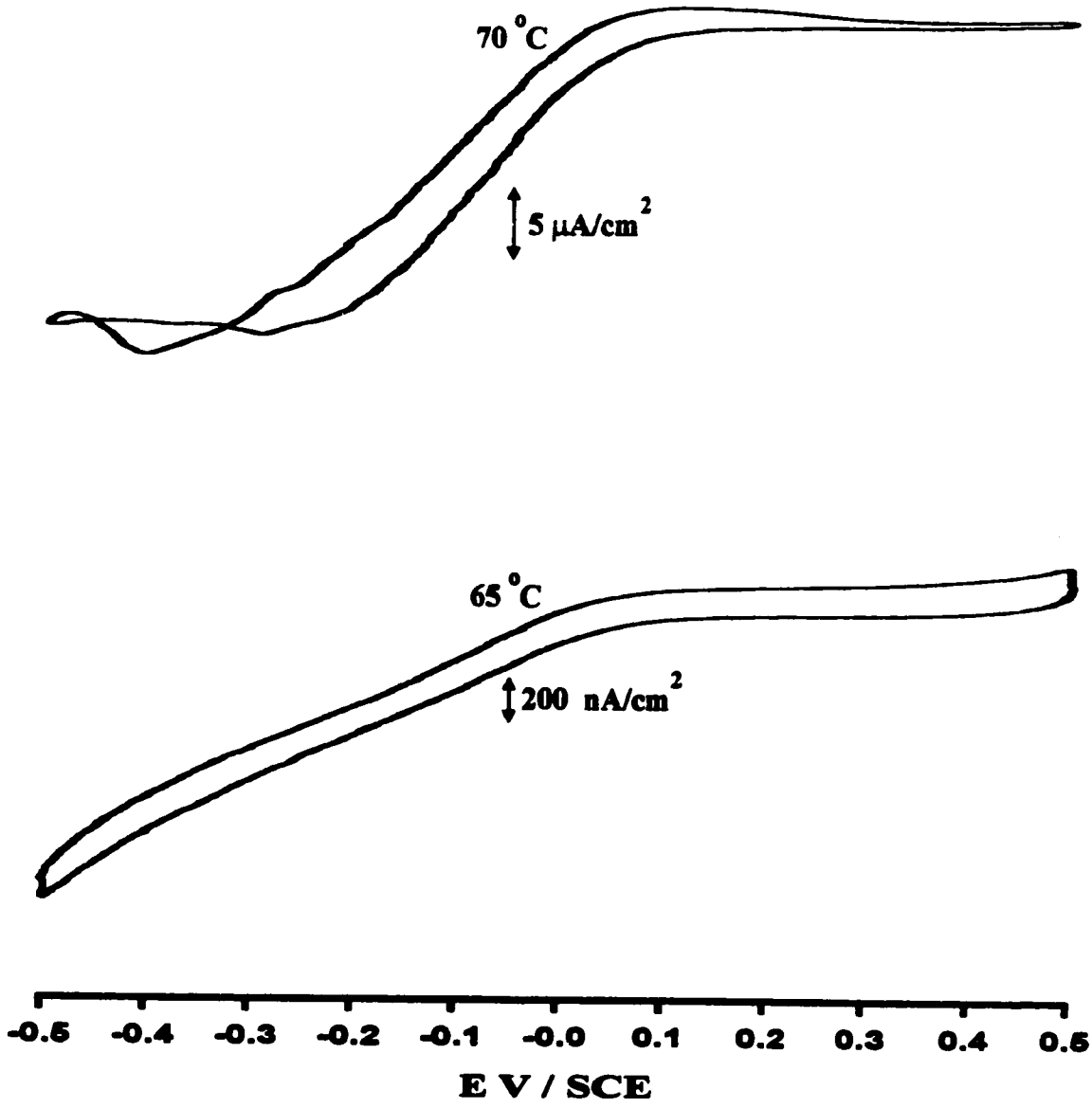

Figure 4.15e : Cyclic voltammograms of a Au(111) electrode coated with hexadecanethiol after multiple incubations in 10^{-2} M hexadecanethiol solution as a function of temperature. Measurements were done in 0.1 M NaF + 1.0 mM $K_3Fe(CN)_6$ at a scan rate of 20 mV/s (see text).

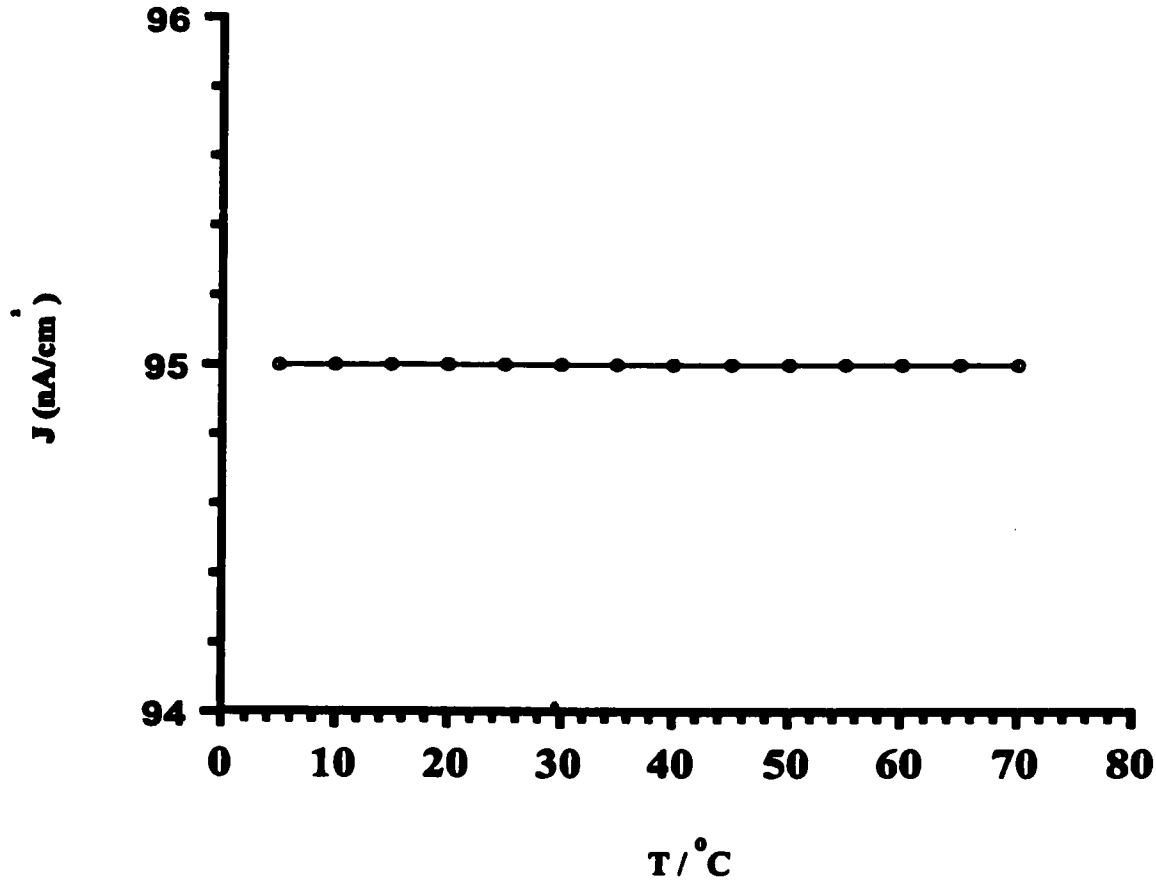

Figure 4.16 : Current density at a potential of - 0.1 V as a function of temperature of a hexadecanethiol modified Au(111) electrode. Measurements were done in 0.1 M NaF + 1.0 mM $Fe(CN)_6^{3-}$ at a potential scan rate of 20 mV/s.

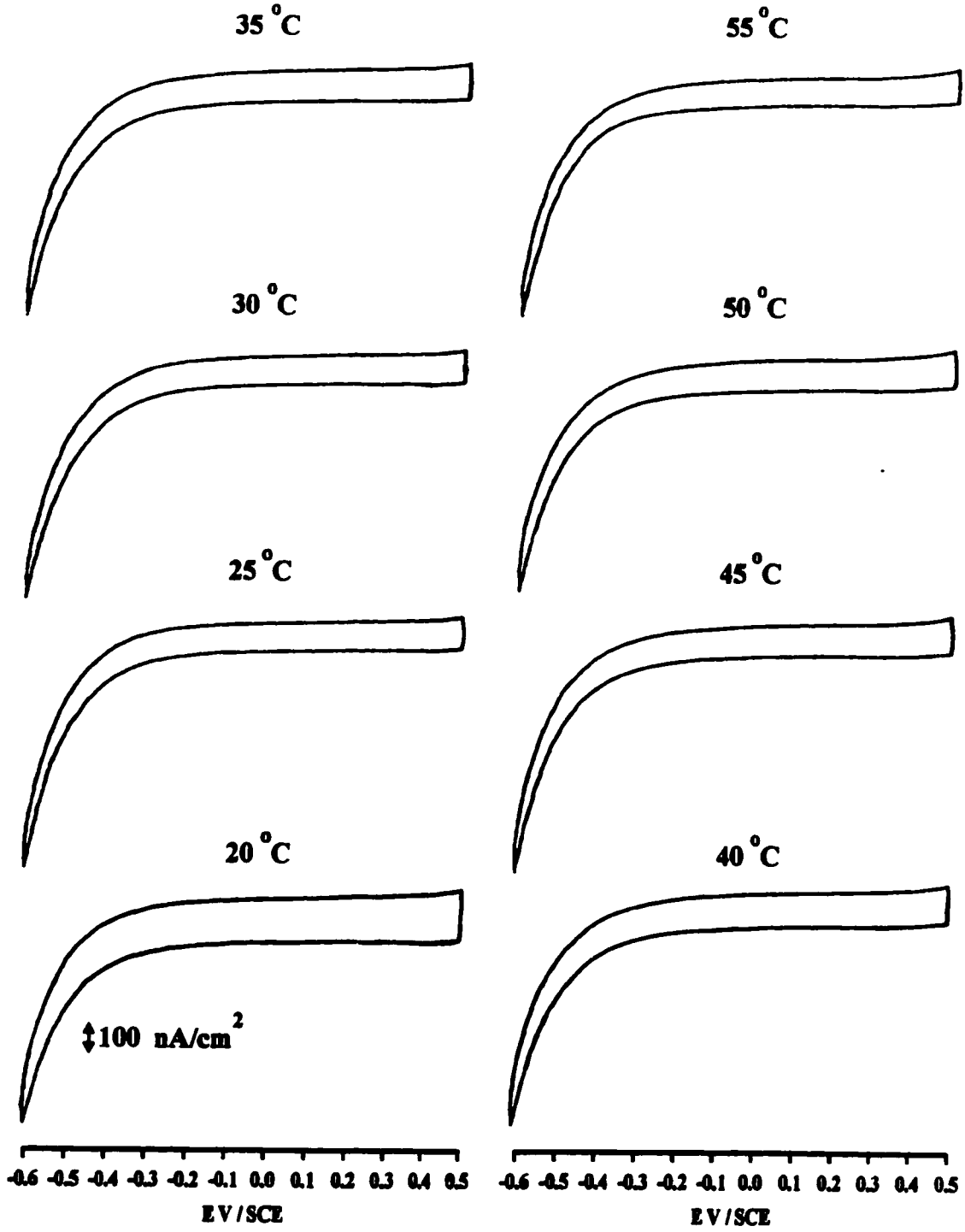

Figure 4.17a : Cyclic voltammograms of a Au(111) electrode modified with hexadecanethiols recorded in 0.1 M NaF + 1.0 mM $K_3Fe(CN)_6$ at 50 mV/s as a function of temperature.

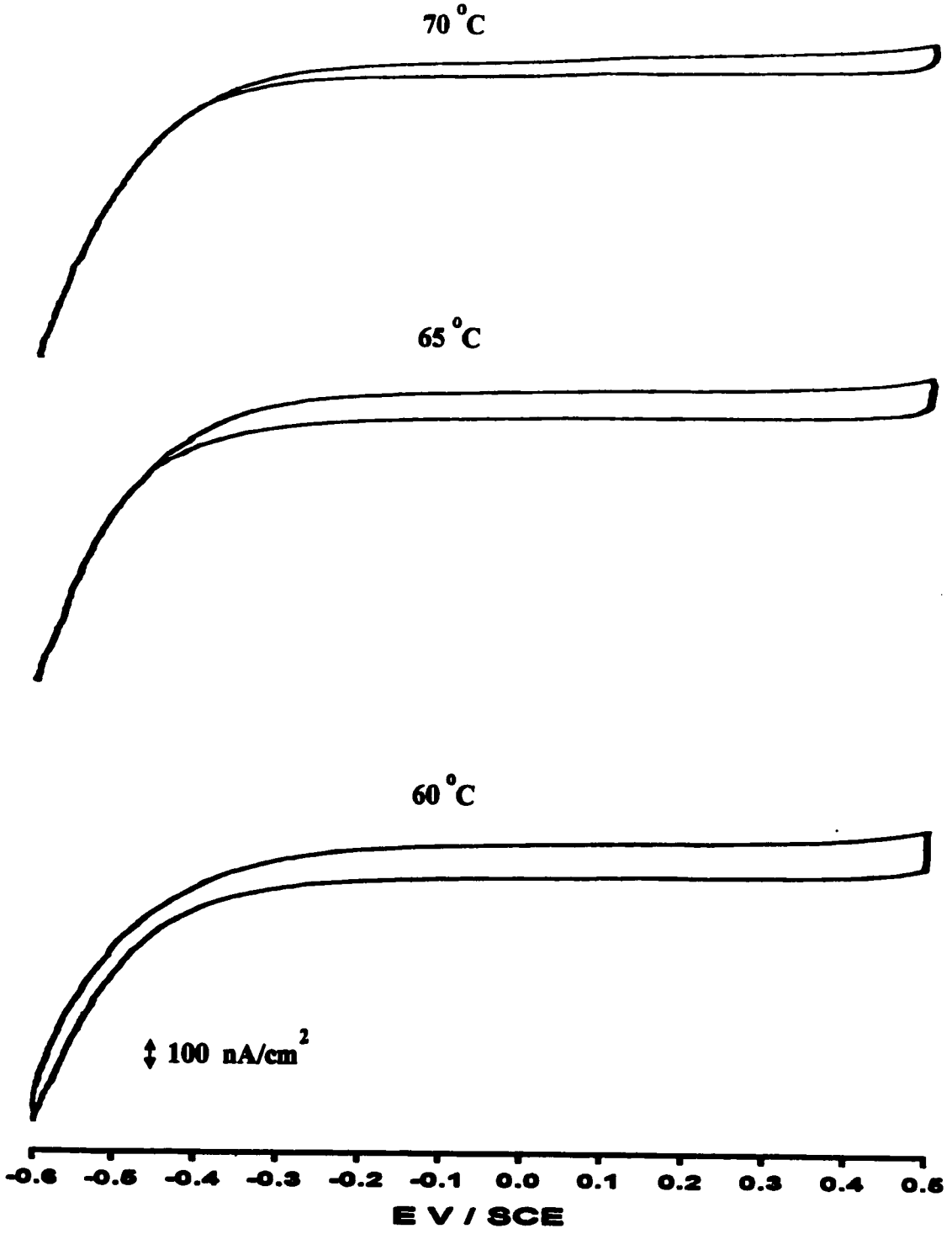

Figure 4.17b : Cyclic voltammograms of a Au(111) electrode modified with hexadecanethiols recorded in 0.1 M NaF + 1.0 mM $K_3Fe(CN)_6$ at 50 mV/s as a function of temperature.

reduction of ferricyanice via electron tunneling across the hexadecanethiol monolayer. These results are the first ones to show that methyl terminated thiol monolayers with very low numbers of defects can be formed. This is probably due to the use of an ordered single crystal Au(111) electrode which helps reduce the number of defects.

3. Summary

The results presented in this chapter show that the monolayer obtained after a single incubation has defects. These defects are in variable concentration but their size and concentration are often low enough that they act as microelectrodes. The temperature dependence of the reduction of ferricyanide reveals a significant change in the monolayer structure between 25 ° and 35 °C. This result is similar to what was observed for the reduction of thiols. We found no evidence of a second phase transition above 35 °C. This result disagrees with that of Lennox [42]. The second phase transition was assigned to a disorder-disorder transition. This could be caused by the lower amount of defects and the higher coverage which prevents the diffusion of the thiols since the separation between the thiols in the phase at 40 °C is larger than 5 Å.

Multiple incubations lead to a monolayer which has a very low number of defects. The measurements of electron transfer for the reduction of ferricyanide are found to be independent of the scan rate and of the temperature. This is compatible with electron-tunneling. Our results are the first ones showing that methyl terminated alkanethiol monolayer can block metallic surfaces very efficiently. They show that more attention must be given to the substrate in model studies of electron transfer mechanisms. They also show that the method of deposition of thiols influence the electrochemical properties.

4. References

1. Porter, M. D.; Bright, T. B.; Allara, D. L.; Chidsey, C. E. D. J. Am. Chem. Soc. **1987**, 109, 3559.
2. Miller, C.; Cuendet, P.; Gratzel, M. J. Phys. Chem. **1991**, 95, 877.
3. Miller, C.; Gratzel, M. J. Phys. Chem. **1991**, 95, 5225.
4. Lipkowski, J. Ion and Electron Transfer across Monolayers of Organic Surfactants. In Modern Aspects of Electrochemistry : Conway, B. E.; Bockris, J. O'M.; White, R. E., Eds.; Plenum Press : New York, 1992, Vol. 23, pp. 1-99.
5. Marcus, R. A. J. Chem. Phys. **1954**, 24, 4966.
6. Marcus, R. A. J. Chem. Phys. **1956**, 24, 966.
7. Marcus, R. A. Ann. Rev. Phys. Chem. **1964**, 15, 155.
8. Marcus, R. A. J. Chem. Phys. **1965**, 43, 679.
9. Marcus, R. A. Ann. Rev. Phys. Chem. **1968**, 13, 955.
10. Marcus, R. A. Theory and Application of Electron Transfer at Electrodes and in Solutions, in Special Topics in Electrochemistry (P. A. Rock, ed.); Elsevier : Amsterdam, 1977, p. 161.
11. Marcus, R. A. Biochim. Biophys. Acta **1985**, 811, 265.
12. Hush, N. S. J. Chem. Phys. **1958**, 28, 962.
13. Hush, N. S. Trans. Faraday Soc. **1961**, 57, 577.
14. Hush, N. S. Electrochim. Acta **1968**, 13, 1005.
15. Levich, V. G. Adv. Electrochem. Eng. **1966**, 4, 249.
16. Dogonadze, R. R. in "Reactions of Molecules at Electrodes," Hush, N. S. , Ed.; Wiley-Interscience : New York, 1971, Chapter 3.
17. Brett. C. M. A.; Brett, A. M. O. in "Electrochemistry, Principles, Methods, and Applications," Oxford University Press Inc. : New York, 1994, Chapter 4.
18. Miller, C. J. in "Physical Electrochemistry, Principles, Methods, and Applications," Rubinstein, I., Ed.; Marcel Dekker, Inc. : New York, 1995, Chapter 2.
19. Chidsey, C. E. D. Science **1991**, 251, 919.

20. Becka, A. M.; Miller, C. J. J. Phys. Chem. **1992**, 96, 2657.
21. Finklea, H. O.; Hanshew, D. D. J. Am. Chem. Soc. **1992**, 114 (9), 3173.
22. Finklea, H. O.; Ravenscroft, M. S.; Snider, D. A. Langmuir **1993**, 9, 223.
23. Miller, C. J.; Majda, M. J. Am. Chem. Soc. **1986**, 108, 3118.
24. Miller, C. J.; Majda, M. J. Electroanal. Chem. **1986**, 207, 49.
25. Daifuku, H.; Aoki, K.; Tokuda, K.; Matsuda, H. J. Electroanal. Chem. **1985**, 183, 1.
26. Fujihira, M.; Araki, T. J. Electroanal. Chem. **1986**, 205, 329.
27. Facci, J. S.; Falciguo, P. A.; Gold, J. M. Langmuir **1986**, 2, 732.
28. Widrig, C. A.; Miller, C. J.; Majda, M. J. Am. Chem. Soc. **1988**, 110, 2009.
29. Lee, C. W.; Bard, A. J. J. Electroanal. Chem. **1988**, 239, 441.
30. Matsuda, H.; Aoki, K.; Tokuda, K. J. Electroanal. Chem. **1987**, 217, 15.
31. Laviron, E. J. Electroanal. Chem. **1979**, 105, 25.
32. Li, T.; Liu, H. Y.; Weaver, M. J. J. Am. Chem. Soc. **1984**, 106, 6107.
33. Hupp, J. T.; Weaver, M. J. J. Phys. Chem. **1984**, 88, 1463.
34. Finklea, H. O.; Robinson, L. R.; Blackburn, A.; Richter, B.; Allara, D.; Bright, T. Langmuir **1986**, 2, 239.
35. Finklea, H. O.; Avery, S.; Lynch, M.; Furtsch, T. Langmuir **1987**, 3, 409.
36. Sabatini, E.; Rubinstein, I.; Maoz, R.; Sagiv, J. J. Electroanal. Chem. **1987**, 219, 365.
37. Sabatini, E.; Rubinstein, I. J. Phys. Chem. **1987**, 91, 6663.
38. Marecek, V.; Samec, Z.; Weber, J. J. Electroanal. Chem. **1978**, 94, 169.
39. French, M.; Creager, S. E. Langmuir **1998**, 14, 2129.
40. Amatore, C.; Savéant, J. M.; Tessier, D. J. Electroanal. Chem. **1983**, 147, 39.
41. Bizzotto, D.; McAlees, A.; Lipkowski, J.; McCrindle, R. Langmuir **1995**, 11, 3243.
42. Badia, A.; Back, R.; Lennox, R. B. Angew. Chem. Int. Ed. Engl. **1994**, 33 (22), 2332.
43. Laidler, K. J.; Meiser, J. H., Physical Chemistry, The Benjamin/Cummings Publishing Company, Inc. : California, 1982, p. 831.

Chapter 5

The effect of temperature on the Reversible reduction/oxidative deposition of Hexadecanethiol SAMs Adsorbed at a Single Crystal Gold (111) Electrode

1. Introduction

Electrochemical sensors made with self-assembled monolayers of thiols are being developed [1-7]. Bio-electrochemical sensors, based on organic monolayers, will have to be thermally stable since they will be used at 35°- 40° Celsius and stored at room temperature. Their specificity and sensitivity must remain constant over this range of temperatures. The importance of having thermally stable monolayers is more crucial than it is for thick (1 μm) polymer coated electrodes since defects and changes in the ionic permeation can lead to detrimental effects. In other suggested applications, organic monolayers would be used as organic electronics. For example, they can be used in microelectronic devices [8-13] and in sensing chemically different regions on the nanometer scale [14-16]. The thermal stability of such devices will also be important.

The thermal stability of monolayers of alkanethiols chemisorbed on gold in air and under UHV conditions has been studied. These studies have been summarized in Chapter 1. In summary, annealing monolayers of thiols was found to improve their order. The increased temperature allowed a greater mobility of the thiols and thus reduced the number of defects in the monolayer. UHV studies using well-ordered Au(111) substrates allowed the identification of an order-disorder transition at 100 K [17-19].

Fewer studies have been done on the effect of temperature on the electrochemical properties of electrodes covered with thiols. In most of these electrochemical studies, the self-

assembled monolayer of thiols has been used as a model system to study electron tunneling and ion permeation [17-24]. Conflicting results were obtained on the process of electron transfer across alkane thiol monolayers. Miller et al. [24] showed electron tunneling occurs across hydroxyl-terminated alkanethiols monolayers. In contrast, Lennox et al. [20-22] concluded that electron transfer is due to permeation of the redox group through the alkanethiols monolayer. This group also identified a series of phase transitions similar to those of Langmuir-Blodgett film [25-27].

Miller and co-workers [24] have generated films of alkanethiol hydroxyl terminal groups on gold substrates with a low number of defects such that the dominant mechanism of electron transfer is tunneling through the monolayer. Miller et al. suggested that the hydroxy terminal groups stabilizes the monolayer by the formation of hydrogen bonding between adjacent hydroxy groups and between hydroxy groups and the aqueous solution. This should decrease the monolayer/aqueous surface energy when compared to methyl terminal groups. They reported that the standard rate constant k_o for the $Fe(CN)_6^{3-}$ reduction on a bare gold electrode is about 0.031 cm /s [28]. The current for this reaction on a thiol coated electrode was found to follow this equation :

$$I = i_o \exp(-\beta d) \qquad (1)$$

where I and i_o are the currents measured at a coated and a bare electrode, respectively, β is the tunneling barrier coefficient and d is the monolayer thickness. $Fe(CN)_6^{4-/-3}$ redox rates across a gold electrode modified with $HS(CH_2)_{16}OH$ showed no strong dependance on the temperature at overpotentials larger than 0.4 V. Whereas at low overpotential values (-0.1 to 0.3 V), there is a slight increase of the rate with increasing temperature. They found that the overpotential dependence of the rates of e-transfer of the redox couples studied deviated from Butler-Volmer kinetics, in agreement with Marcus theory predictions [29]. For gold surfaces coated with hydroxy thiol monolayers, the heterogeneous e-transfer rate of a redox probe is reduced by about 2.5 for each CH_2 added. Miller et al. have also examined many

redox molecules [$Fe(CN)_6^{3-}$, $Fe(bpy)(CN)_4^-$, $W(CN)_8^{3-}$, $Ru(NH_3)_6^{3+}$, Fe^{3+}, and Ce^{4+}]. The heterogeneous electron transfer rate increases exponentially with the electrode potential. When the electrode potential is increased, the rate varies linearly and finally becomes independent of the overpotential at sufficiently negative potentials, in agreement with the predictions of Marcus theory of an "inverted" region.

IR spectroscopy has been used by Ellis and co-workers [21,22] to investigate the thermal stability of SAMs on gold polycrystalline electrodes. The IR measurements done in the temperature range 283 to 338 K, has revealed a phase transition in SAMs. They found a chain length dependence of the melting temperature, the values of which ranged between 313 and 338 K. The chains gradually untilt up to ~ 350 K, followed by an ir-reversible transition to a liquid like phase characterized by a large number of gauche conformational defects.

Scoles and co-workers have performed a series of temperature dependence studies in UHV [17-19] using He-beam diffraction (which probes the surface CH_3 groups only) of alkanethiol SAMs of different chain lengths, $CH_3(CH_2)_nSH$ ($5 \leq n \leq 21$), on a Au(111) single crystal substrates and a Au(111)/mica surface between 30 and 100 K. The conclusions obtained from these studies are summarized below : (1) At low temperatures, the terminal methyl groups are arranged in a hexagonal domain with a nearest neighbor spacings of ~5Å; (2) No diffraction peaks were observed for n = 5 while n = 9 showed weak diffraction peaks; (3) The disappearance of the diffraction peaks suggests thermal motion of the terminal CH_3 groups (an increase of the amount of disorder) because the van der Waals stabilization at the interface is weaker than in the bulk. This results in a decrease of the diffraction peak intensities because thermal vibrations reduce; (4) No phase transition is detected in the temperature range between 30 and 100 K; (5) At about 100 K and above, the He-diffraction peaks disappeared, which indicates a phase transition from ordered domains into disordered structures of the surface groups; (6) The decreasing order with decreasing chain length is consistent with spectroscopic and electrochemical experimental results [23,30].

In Chapter 3 we have shown that reduced hexadecanethiols remain physisorbed at the surface of the electrode due to their low solubility in alkaline solution. Physisorbed thiolates might form different organized structures at different temperatures similar to Langmuir-Blodgett monolayers [25-27].

Rabolt et al. [25] have studied a Langmuir-Blodgett film of cadmium arachidate by waveguide Raman spectroscopy (WRS) on a Pyrex substrate. They concluded that, at low temperatures, molecular mobility is reduced because of lattice contraction. At elevated temperatures, however, rotation about the chain axis was observed. Gauche defects are introduced in the all-trans chain as the temperature reached the order-disorder phase transition at 110 °C.

Riegler [26] used electron diffraction to study the temperature dependence of the structure of cadmium fatty acid salts, namely Cd stearate, Cd arachidate and Cd behenate LB films. At temperatures below the melting temperature of the head group lattice, there is a sharp decrease of the diffraction peak intensities due to the thermally induced tilt orientational disorder of the chains. The reduction of the diffraction peaks is chain length dependent. It occurs at ~ 35 °C for Cd stearate (C_{16}), ~ 55 °C for Cd arachidate (C_{18}) and about 75 °C for Cd behenate (C_{20}).

Piézolet and LeBihan [27] have studied the thermal behavior of dipalmitoyl phosphatidylcholine (DPPC) using both transmission and polarized attenuated total reflection infrared spectroscopy in order to characterize the sub- and the pre-transition states. At the low sub-transition temperature (Ts 17 °C), a big variation in chain packing occurs, characterized by IR bands due to the methylene scissoring mode. Below the sub-transition, they observed an increase of the hydrocarbon chain rotational disorder. At the pre-transition temperature (Tp 35 °C), the extended hydrocarbon chains show a significant decrease of the tilt angle with respect to the bilayer normal and an increase of the hydration (swelling of the lipid) of the DPPC bilayer and the appearance of ripple structure.

The physisorbed micelles of thiolates formed after the reduction of the chemisorbed thiolates are likely to be influenced by the temperature in a way similar to that which has been reported for LB monolayers. Their sizes and the structures that they form could change. Although the micelles are physisorbed, it is useful to examine the thermal behavior of ionic micelles in aqueous solutions.

At a given temperature the difference in the free energies (cal/mol : 1 cal = 4.184 J) of having a monomer in solution and a micelles is [31,32] :

$$\mu^\circ \text{ (micelle)} - \mu^\circ \text{ (water)} = -1934 - 771\, n_c \qquad (2)$$

The enthalpy is : $$\frac{d\,[\mu^\circ \text{ (micelle)} - \mu^\circ \text{ (water)}/T]}{d\,(1/T)} \qquad (3)$$

The entropy is given by :

$$\mu^\circ \text{ (mic)} - \mu^\circ (H_2O) = H^\circ \text{ (mic)} - H^\circ (H_2O) - T\,(S^\circ \text{ (mic)} - S^\circ (H_2O)) \quad (4)$$

An empirical relation between the changes in free energy for the transfer of an aliphatic thiol from the surface to an aqueous solution and the number of carbons, n_c, in the chain was derived [33] and is given below :

$$\Delta G \text{ (kJ mol}^{-1}) = A - 5.9\, n_c \qquad (5)$$

where A is a constant related to the free energy of adsorption of the thiol. The transfer of a monomer from the organic phase (i. e. the micelles) to the water phase causes important disruption of the hydrogen bonding network between the water molecules. This often leads to a negative entropy change because of the ordering of the water molecules near the ionic charge.

Short chains thiol molecules are in the form of monomers. The critical micelle concentration (CMC) is reached in the case of longer alkane chains, and micelles can be formed. Micelles of amphiphiles with long chain hydrocarbons were found to form ordered structures.

The size of the micelles and their shapes are determined by two opposing forces. In aqueous solution there is the hydrophobic effect which favors the aggregation. There is also a repulsive force between the ionic groups or head groups which determines the micelle's size [31]. The size of a micelle increases with the length of the alkane chain due to the hydrophobic effect.

There is a transition from small micelles (less than 100 molecules) to large micelles (more than 1000 molecules) with increasing ion concentration in the sequence spherical-cylindrical-hexagonal-lamellar. The ionic group has a very important effect on the size of micelles. A small ionic group favors the formation of large micelles since the counter ions can come closer to the ionic group and lead to a better neutralization. The size of ionic micelles does not change with the temperature[31].

Different shapes of micelles have been suggested. The most common shapes are disklike, spherical, rodlike, or lamellar. Thermodynamically, spherical shapes are preferred because they minimize the solvent-micelle interface. Neutron scattering studies [34] found that spherical micelles are formed by many amphiphilic compounds.

2. Results and Discussion

2.1 Effect of the temperature on the cyclic voltammetry :

Cyclic voltammograms of the reductive desorption and the oxidative redeposition of hexadecanethiol chemisorbed on a Au(111) single crystal electrode in 0.5 M KOH were recorded at from 5° to 70 °C at 5 °C intervals. Typical voltammograms at selected

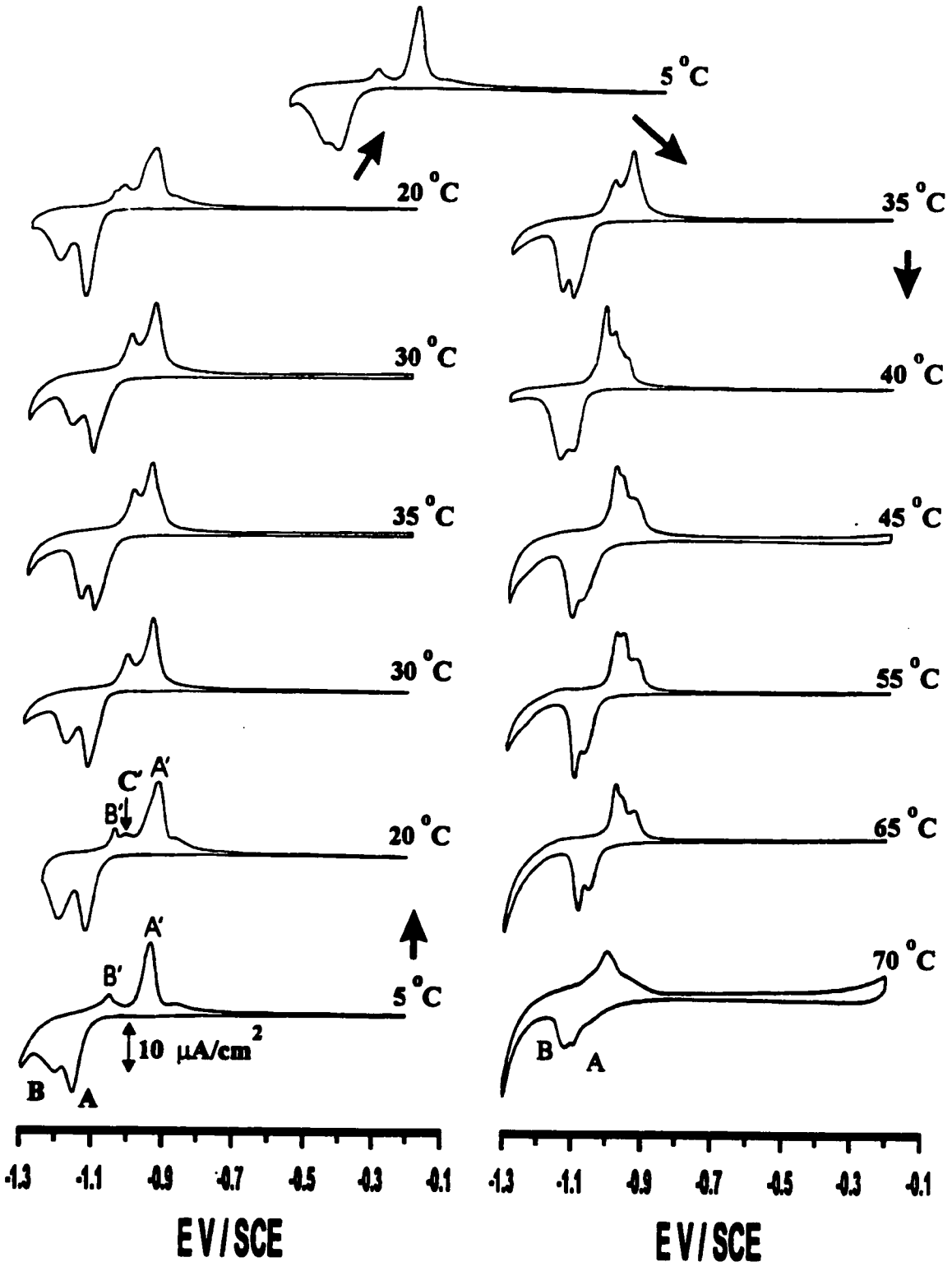

Figure 5.1 : Cyclic voltammograms of the reductive desorption and the oxidative redeposition of a hexadecanethiol SAM at a Au(111) single crystal electrode as a function of temperature recorded in 0.5 M KOH at a scan rate of 20 mV/s.

temperatures are shown in Figure 5.1.

At 5 °C two reductive peaks and three oxidative peaks are observed. The first reductive current peak is narrow and the second reductive current peak is broad. The reductive current peaks are labeled as peak A at - 1.14 V and peak B at - 1.19 V. The anodic scan consists of three current peaks. There is a narrow oxidative peak A′ at - 0.930 V, and a smaller peak B′ at - 1.05 V. The total charge densities associated with the reductive and the oxidative peaks are 90 ± 5 and 85 ± 5 $\mu C/cm^2$, respectively.

At 20 °C, the two reductive current peaks move toward more positive potentials (E_{ps} are - 1.12 V for peak A and - 1.18 V for peak B). This indicates that the reduction of chemisorbed thiols is easier probably because of the increase of the ion permeation with temperature. A new oxidative peak C′ appears at - 1.015 V on the anodic potential scan.

At 30 °C, the oxidative peak A′ is still the largest at - 0.935 V. The peak C′is narrower and appears at - 1.005 V. The peak B′ disappeared completely. The reduction peaks gradually move toward more positive E_{ps} at - 1.11 V for peak A and - 1.165 V for peak B. This result reveals an easier ion permeation through the monolayer.

At 35 °C, the reductive peaks are closer than at lower temperatures. The oxidative peak C′ continues to grow. The reductive and the oxidative peaks are very similar. Decreasing the temperature from 35° to 5 °C, in 5 °C steps yields similar voltammograms as shown in Figure 5.1. This indicates that the reductive desorption/oxidative redeposition are reversible between 5° and 35 °C.

At 40 °C the reductive peak B at - 1. 12 V is larger than the peak A at - 1.09 V. Three oxidative peaks are observed at - 0.985, - 0.95 and - 0.93 V. There is not much change in the voltammogram between 45° and 65 °C. At 70°C the oxidative peaks merge into a single broad peak at - 0.980V.

As the temperature increases gradually from 5° to 70° C, the total charge densities decrease from 90 ± 5 to ~ 40 ± 5 $\mu C/cm^2$ for the reductive peaks and from 85 ± 5 to 32 ± 5 $\mu C/cm^2$ for the oxidative current peaks. Half of the total charge is lost due to the increased solubility of the hexadecanethiolates at higher temperatures. The presence of a long tail on the positive side of the current peak A shows that the reduction starts at a much more positive potential. This is assigned to the increase of the ionic permeability at higher temperature. Some of the C_{16} monolayers are completely removed from the surface at different temperatures ranging from 55° to 90°C. We suggest this behavior may be related to the amount of defects of the original self-assembled monolayers.

The double layer charging current was measured at temperatures between 5° and 55 °C for the coated C_{16} SAM on Au(111) in 0.5 M KOH between - 0.2 and - 0.5 V. It was found to increase with temperature from 10 to 580 nA/cm^2. Thus the double layer capacity of the coated electrode increases with the temperature. This is consistent with the decrease of the surface coverage and the corresponding increase of the number of defects observed at higher temperatures.

Fig. 5.2 shows that the reductive current peak A and peak B potentials (E_p) do not have the same temperature dependance. Between 5° and 25 °C, the separation between the peaks A and B remains approximately constant at about 75 mV while they move towards more positive potential. The potential of peak B rapidly becomes more positive above 25 °C. At 35 °C the separation between the peaks has decreased to only 30 mV. It remains at this value up to 60 °C while both peaks continue to move to more positive potentials.

There are clearly two ranges of temperatures where the separations between the peaks are constant. The first one is between 5° and 25 °C and the second one is between 35° and 60 °C. The transition from one range to the other occurs between 25° and 35 °C.

The linear shift of peak A with temperature suggests that the onset of the reduction follows the same mechanism (reduction initiated by ions permeating through the monolayer)

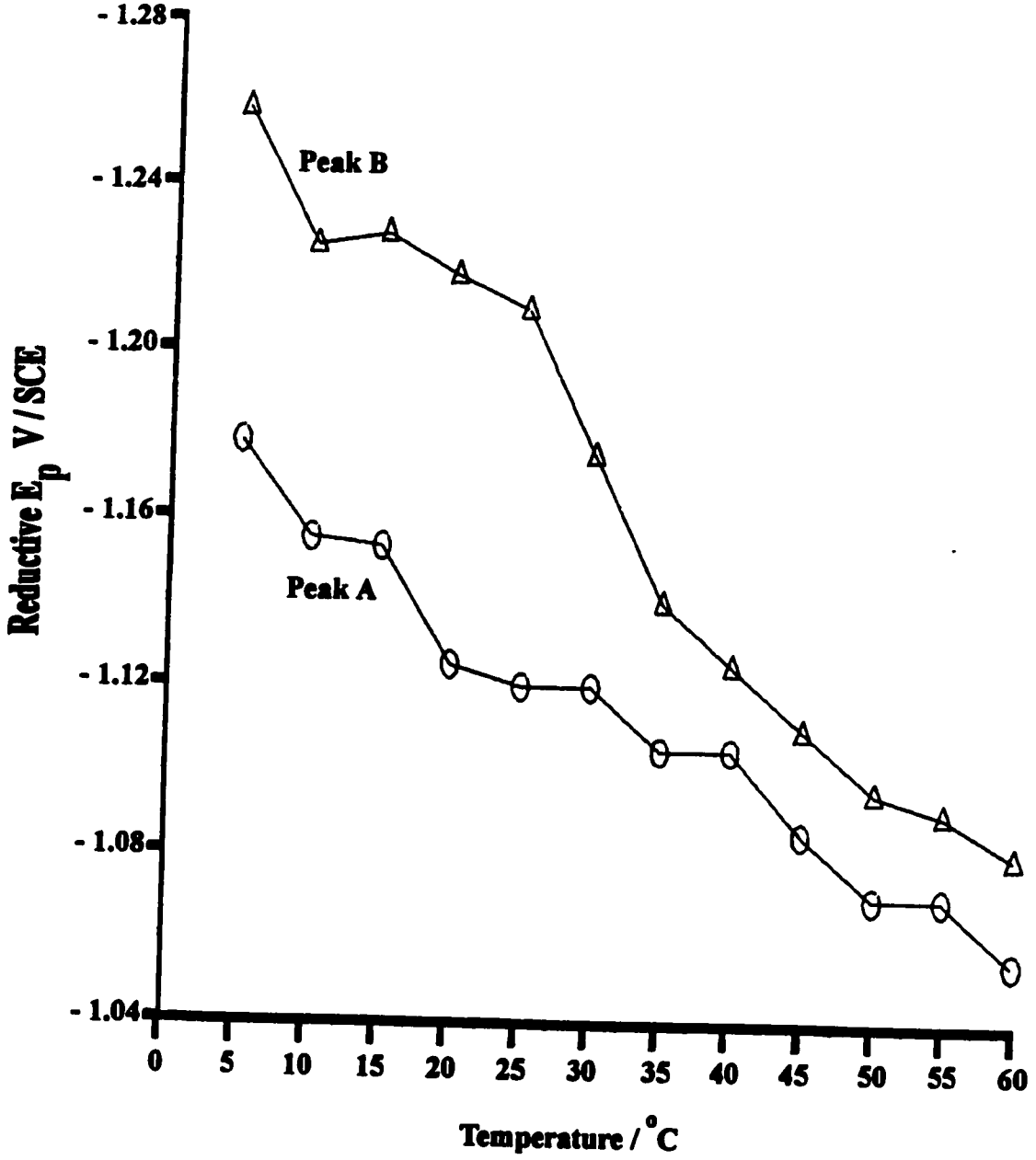

Figure 5.2 : Potentials of the reductive desorption peaks A and B (E_p) as a function of temperature measured in 0.5 M KOH at a scan rate of 20 mV/s.

over the whole range of temperatures. The fact that peak B becomes closer to peak A can be interpreted as indicating that the activation for this process (peak B) decreases. Peak B was assigned to the formation of physisorbed micelles. Hence, the transition from a laminar structure to a micellar structure of the physisorbed hexadecanethiolates would become easier at higher temperatures. We note that the transition region is approximately at the melting temperature of hexadecanethiols (20° C).

A comparison of the voltammograms between KOH and LiOH electrolytes solution reveals the following differences. At 5 °C the reductive desorption process begins at more negative potential and only one reductive desorption peak A is observed as shown in Figure 5.3. The second peak B overlaps with the hydrogen evolution. Two oxidative redeposition peaks A′ (narrow peak at - 0.93 V) and B′ (small peak at - 1.05 V) are observed. At 20 °C, the second reductive peak, B, is visible at - 1.23 V while peak A is observed at - 1.17 V. A large oxidative peak C′ appears at - 1.015 V. The oxidative peak A′ is still at - 0.93 V. The oxidative peak B′ appears as a small shoulder. At 30 °C the oxidative part of the voltammogram is similar to the one recorded at 40 °C in 0.5 M KOH. The reductive current peaks A and B are much closer than in KOH. Between 40 °C and 70 °C, the voltammograms do not change significantly. The reductive and the oxidative peaks are more well-defined and mirror images in LiOH for this range of temperatures.

Peak A shifts from - 1.19 V at 5 °C to - 1.07 V at 70 °C (~ 120 mV) in KOH. In LiOH the peak A begins at - 1.22 V at 5 °C and ends at - 1.07 V at 70 °C (~ 150 mV shifts). This observation suggests that at elevated temperature the nature of the cation (K^+ or Li^+) is not important. The effect of the cation on the reductive current peak B is quite important. There is a larger positive shift of this peak at lower temperature in LiOH (peak B shifts from - 1.25 V at 5 °C to - 1.10 V at 70 °C ≈ 150 mV) than in KOH (peak B shifts from - 1.19 V at 5 °C to - 1.10 V at 70 °C ≈ 80 mV).

The reductive peak A and peak B potentials in 0.5 M LiOH at a scan rate of 20 mV/s

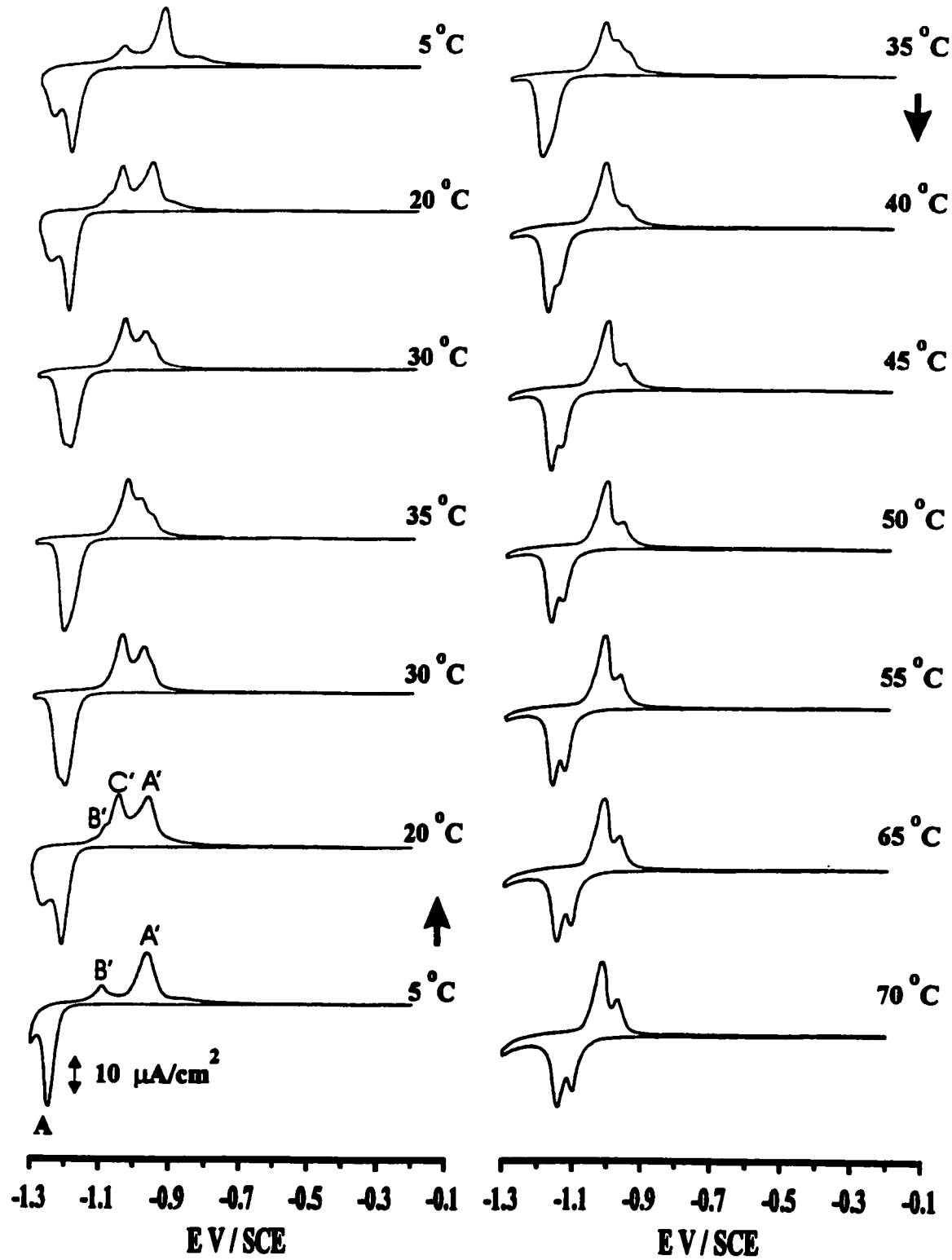

Figure 5.3 : Cyclic voltammograms of the reductive desorption and the oxidative redeposition of a hexadecanethiol SAM at a Au(111) single crystal electrode as a function of temperature recorded in 0.5 M LiOH at a scan rate of 20 mV/s.

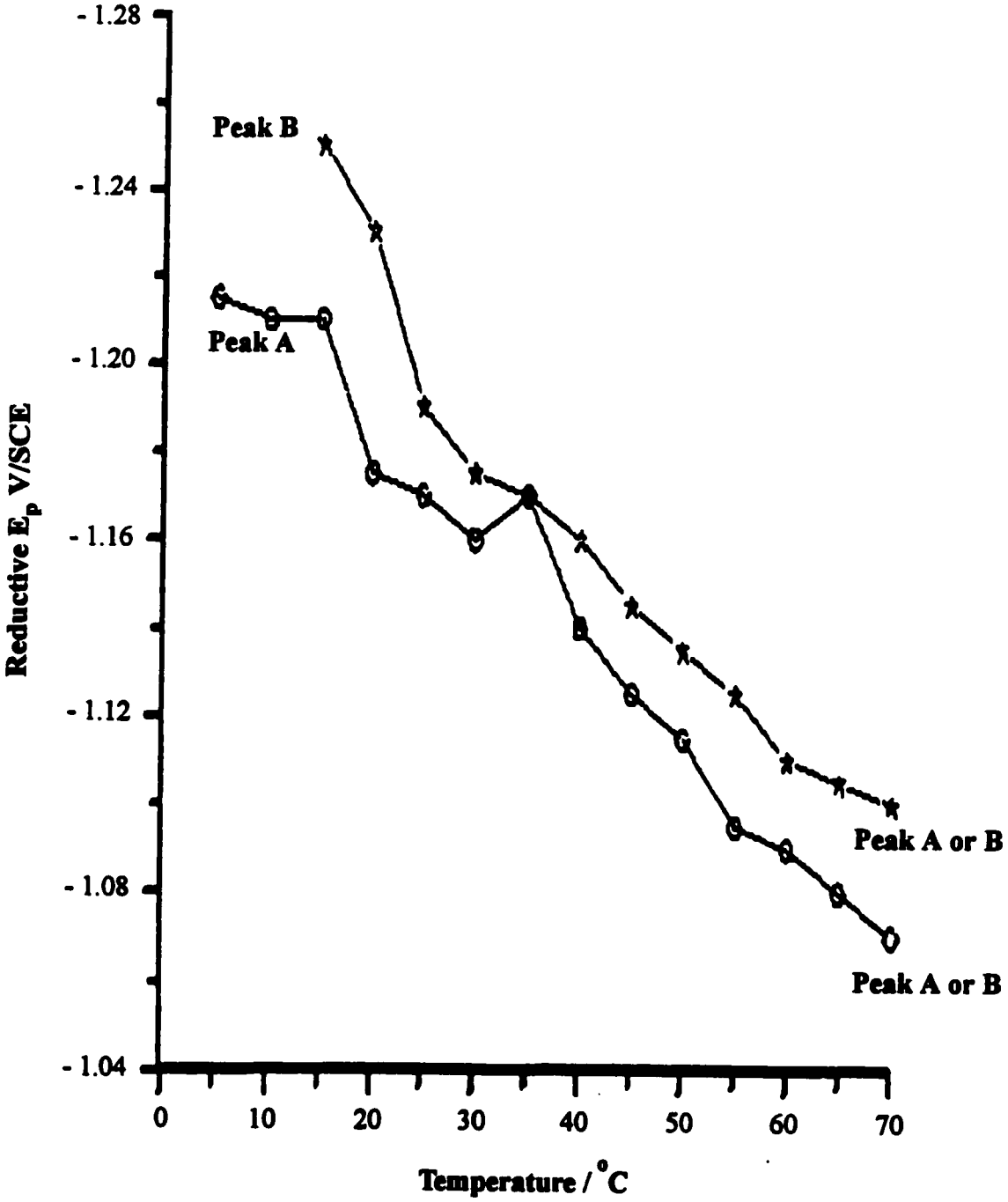

Figure 5.4 : Potentials of the reductive desorption peaks A and B (E_p) of hexadecanethiols as a function of temperature measured in 0.5 M LiOH and a potential scan rate of 20 mV/s.

as a function of temperature is presented in Figure 5.4. Only the reductive peak A is visible below 15 °C, whereas peak B overlaps with the hydrogen evolution at potentials more negative than - 1.26 V. Similarly to what was observed in KOH, the reductive peak B shifts more rapidly to positive potentials than the peak A. At 35 °C, the two reductive desorption peaks merged to give a single peak at ~ - 1.18 V. At 40 °C, the single reductive peak splits again and two reductive peaks A and B are observed. It is uncertain whether the reductive peaks reappear as before as peaks A and B, respectively or as peaks B and A. However, a comparison of the peak potentials before and after the merge gave the same peak potentials ± 10 mV. The shift of the peak's potentials is constant from 45° to 70 °C.

The similarities of the changes in the voltammograms in LiOH and KOH provide more support to the possibility of a phase transition from one structure below 25 °C to a different structure above 35 °C.

The effect of pH was examined by doing the same measurements in 0.14 M KOH. Voltammograms (not shown) show three oxidative redeposition peaks between 5° and 10 °C. Two reductive and two oxidative peaks were obtained between 15° and 35 °C, while at 40 °C, a single reductive peak at - 1.12 V and one oxidative peak at - 0.935 V are observed. The separation between them decreases gradually with increasing temperature. Decreasing the temperature gradually from 35° to 5 °C yields the same voltammograms, which again shows reversibility or reproducibility. This feature indicates that the film undergoes electrodesorption and electroadsorption repeatedly and its properties are easily restored. Increasing the temperature beyond 40 °C shows an irreversible behavior. The peaks split into two unresolved peaks up to 60 °C without any further changes with increasing temperature. At this temperature, the reductive peaks reappear at - 1.09 and - 1.11 V while the oxidative side shows a peak at - 0.935 V and a small shoulder at ~ - 0.96 V.

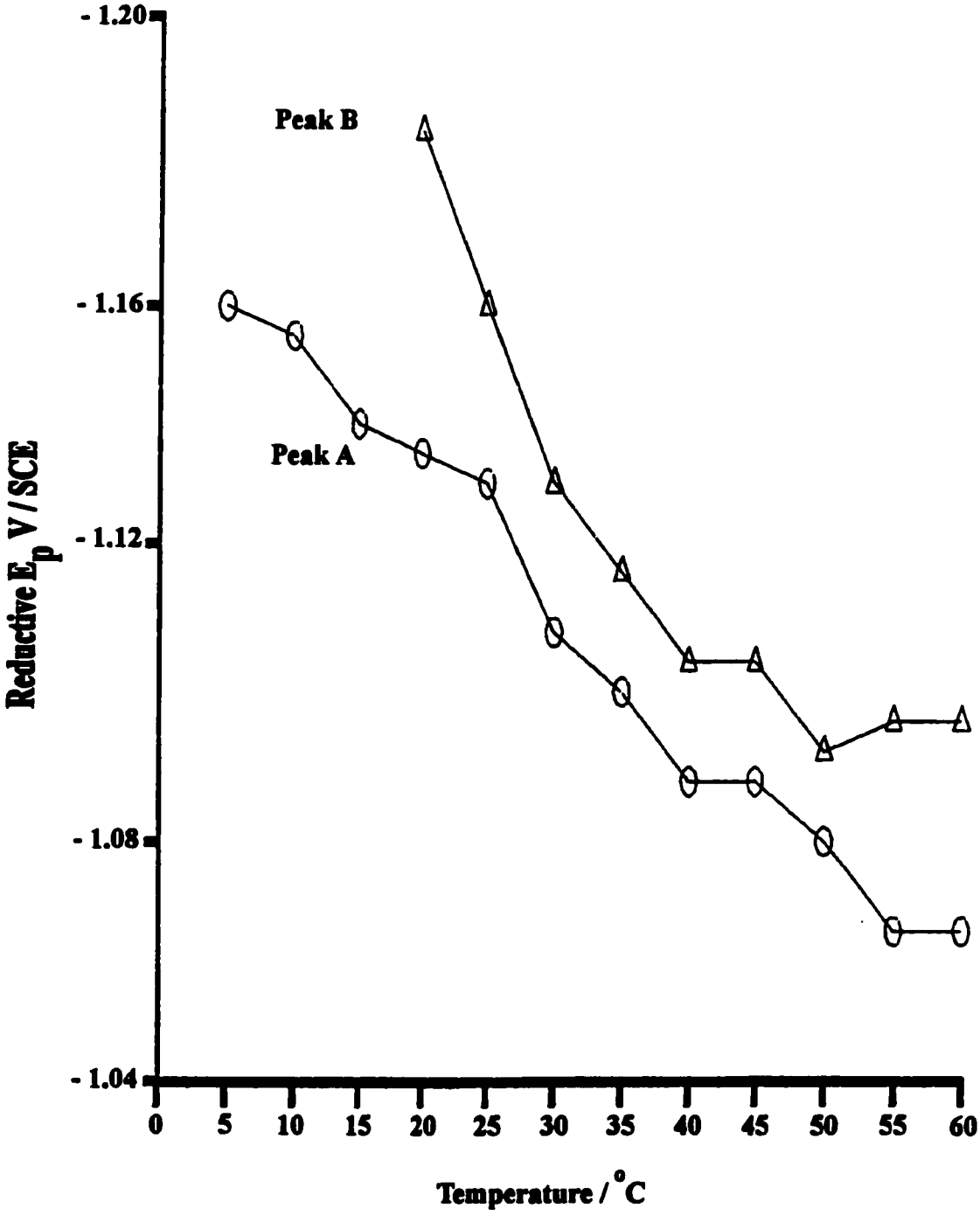

Figure 5.5 : Potentials of the reductive desorption peaks A and B (E_p) of hexadecanethiols as a function of temperature measured in 0.14 M KOH at a scan rate of 20 mV/s.

The reductive peaks' potentials at different temperatures at a scan rate of 20 mV/s in 0.14 M KOH are shown in Figure 5.5. Peak B is absent at the lower temperatures, 5° to 15 °C, because of the overlap with the hydrogen evolution at lower pH. The E_p-temperature plot shows a large slope for the reductive peak B and smaller slope for the reductive peak A between 5° and 35 °C. Thereafter, both peaks show very similar slopes.

Two regions of temperature have been observed in all the electrolyte solutions. There is one at temperatures below 20°-25 °C where the separation between the two reductive peaks is large. The processes giving rise to the two current peaks have different activation energies. There is a transition range between 20° and 30°-35 °C. In this range, peak B moves more rapidly to positive potentials. At temperature higher than 35 °C, and up to 60 °C, the separation between the peaks remains constant while they continue to move towards more positive potentials.

The larger separation of the reductive peaks occurs at temperature below the melting point of hexadecanethiols (18°-20 °C). If peak A is due to the reduction of the thiols, its positive shift is probably due to the increase in the permeation of the ions. The peak B was assigned to the formation of micelles we can expect that the transition from a laminar to a micellar structure will require more energy if at low temperature the monolayer is in a crystalline state.

The potentials of the oxidative current peaks do not change significantly with temperature. From 5° to 20 °C there is a lot of change in the number of peaks and their magnitudes. Above 40 °C the oxidative peaks do not change noticeably. This behavior is similar to the reduction peaks. At even higher temperatures the reduction/oxidation is more reversible. In LiOH the reduction peaks are a mirror image of the oxidation peaks. This strongly suggests that the reduction and oxidation are occurring via similar mechanisms. This agrees with our model described in Chapter 3. However, discrepancies with this model are observed above 40 °C where the reductive peak B and the oxidative peak B′ are more intense

than peaks A and A′. This behavior may be due to the loss of some thiols and the formation of a different shape of micelles of thiolates.

2.2 Effect of the potential scan rate on the fine structure of the voltammograms :

The goal of examining the scan rate dependence is to obtain information on the kinetics of the reductive desorption and the oxidative adsorption of the hexadecanethiols from the Au(111) electrode. Voltammograms recorded at potential scan rates in the range between 1.0 and 500 mV/s in 0.5 M KOH at 20° and 35 °C are presented in Figure 5.6. A comparison of the voltammograms at 20° and 35 °C revealed that the reductive peaks are affected more significantly than the oxidative peaks. The reductive peaks are shifted to more negative potentials as the scan rate increases from 1.0 to 500 mV/sec. At slower the scan rates there is a better separation between the reductive peaks. At faster the scan rates there is a greater overlap of the reductive peaks. Two distinct behaviors are strongly connected with 35 °C. First, the reductive desorption peak A shows splitting at very slow scan rates of 1.0 and 5.0 mV/s. Second, at a scan rate of 500 mV/s the two reductive desorption peaks A and B are not merged completely, in contrast to what occurs at 20 °C. These voltammograms suggest that ion permeation, which is necessary for the reduction to occur, is slow. The oxidative peaks A′ and B′ display faster kinetics. They are not affected by the increase of the scan rate from 1.0 to 500 mV s^{-1}. This is probably due to the fact that the species are physisorbed at the electrode surface.

Plots of the peak potentials as a function of scan rate of the reductive desorption and the oxidative redeposition at 20° and 35°C are shown in Figure 5.7. The oxidative peaks A′ and B′ show very small changes at very slow scan rates and then remain unchanged at faster scan rates. The reductive peaks A and B are greatly affected by increasing the scan rate. At

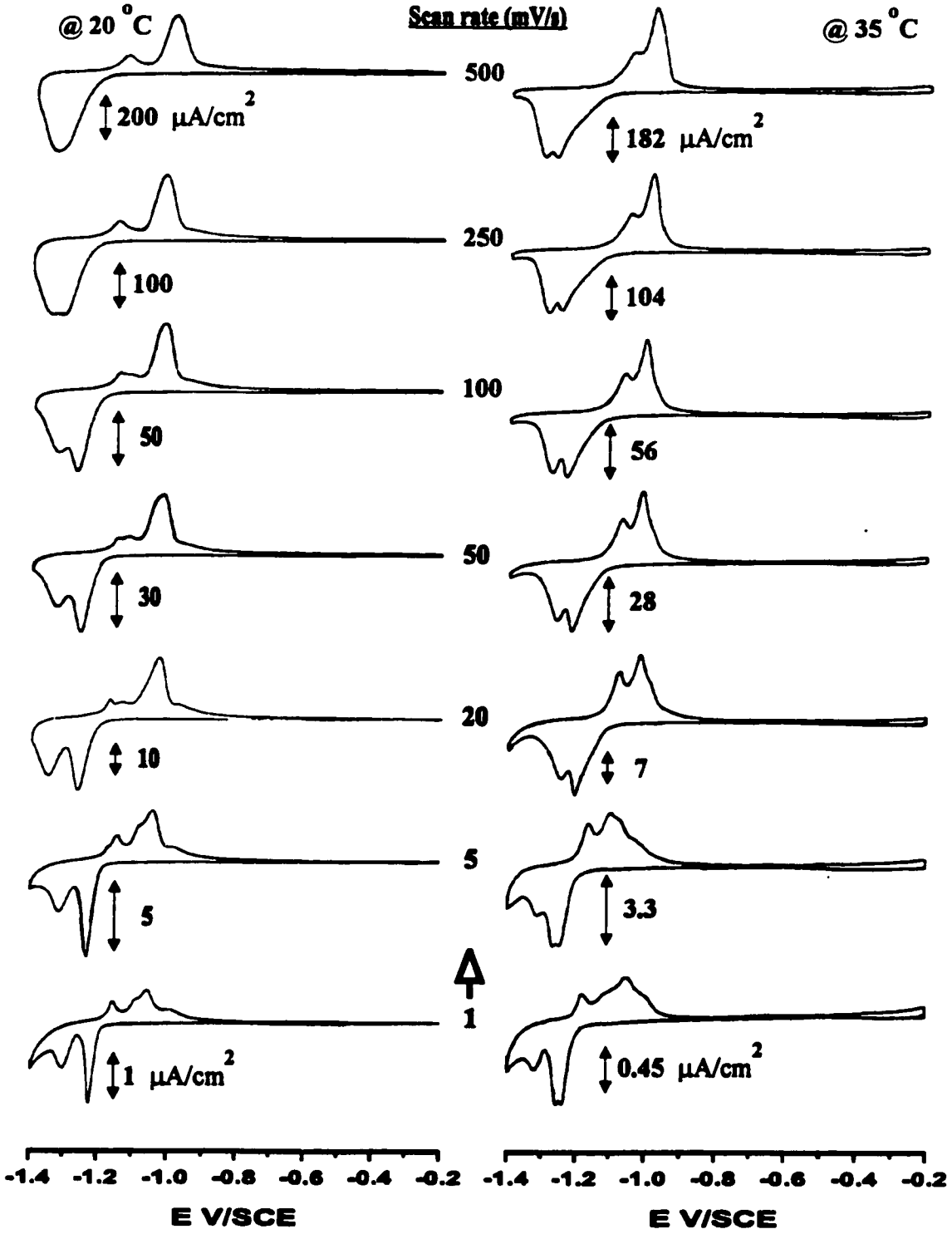

Figure 5.6 : Cyclic voltammograms of the reductive desorption and the oxidative redeposition of a hexadecanethiol SAM at a Au(111) single crystal electrode as a function of scan rate recorded in 0.5 M KOH at 20° and 35 °C.

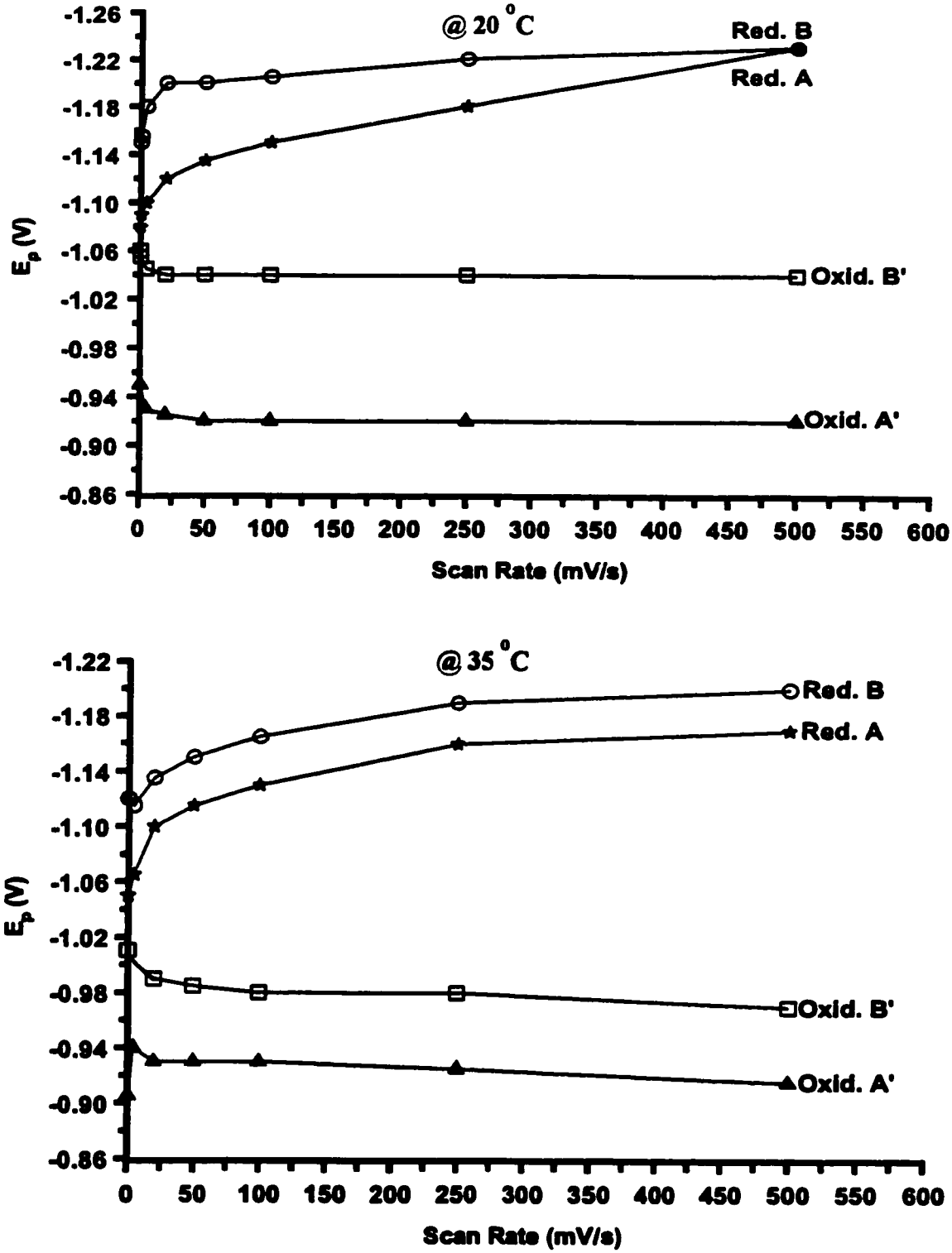

Figure 5.7 : Peak potentials, E_p, of hexadecanethiols adsorbed on a Au(111) as a function of potential scan rate measured in 0.5 M KOH at 20 °C and 35 °C.

20° C and a scan rate of 500 mV/s, both reductive peaks overlap and a single rounded reductive peak is observed. The reductive peaks are well-separated at 35° C. The peak separation, ΔE_p (reductive) = E_p (B) - E_p (A) or ΔE_p (oxidative) = E_p (B') - E_p (A'), as a function of scan rate in the range studied show that, at 20°C, the ΔE_p (reductive) decreases from 70 mV at 1.0 mV s^{-1} to 0 mV at 500 mV/s. We noted that peak A displays slower kinetics than peak B. Peak B displays a smaller potential shift and is thus significantly faster than peak A. The oxidative peaks' separation shows small changes. ΔE_p (oxidative) is 110 mV at 1.0 mV s^{-1}. It then increases to 125 mV for the faster scan rates. At 35 °C, ΔE_p (reductive) drops from around 70 mV at a scan rate of 1.0 mV/s to about 35 mV at 20 mV/s. It then remains constant. ΔE_p (oxidative) drops from 105 mV at a scan rate of 1.0 mV/s to 50 mV at 20 mV/s and then remains constant. The E_p's shift to more negative potentials when the scan rate increases. These observations are compatible with the formation of micelles. Peak A is related to the rate at which ions go across the monolayer. This rate is relatively slow and is responsible for the shift to more negative potentials. Peak B, which corresponds to the formation of physisorbed micelles of thiolates, is faster. As expected from our model, the oxidative redeposition is fast.

The relationships between the total charge densities of the reductive and oxidative current peaks as a function of the scan rate at 20° and 35°C are shown in Figure 5.8. At very slow scan rates, there is a sharp decrease in the charge densities of the reductive and the oxidative peaks, more pronounced for the oxidative peak. The oxidative charge densities are usually about 10 % less than the corresponding charge densities of the reductive peaks as a function of scan rate. The reductive charge densities drops from 90 ± 5 $\mu C/cm^2$ at a scan rate of 0.5 mV/s to about 70 ± 5 $\mu C/cm^2$ at 5.0 mV/s and thereafter stays constant. The oxidative charge density drops at 20° C from 85 ± 5 $\mu C/cm^2$ at a scan rate of 0.5 to about 68 ± 5 $\mu C/cm^2$ at 5.0 mV/s. At 35 °C it drops from 75 ± 5 $\mu C/cm^2$ at a scan rate of 0.5 mV/s to about 60 ± 5 $\mu C/cm^2$ at 5.0 mV/s. These changes are due to a partial reduction of the monolayer at the higher scan rates.

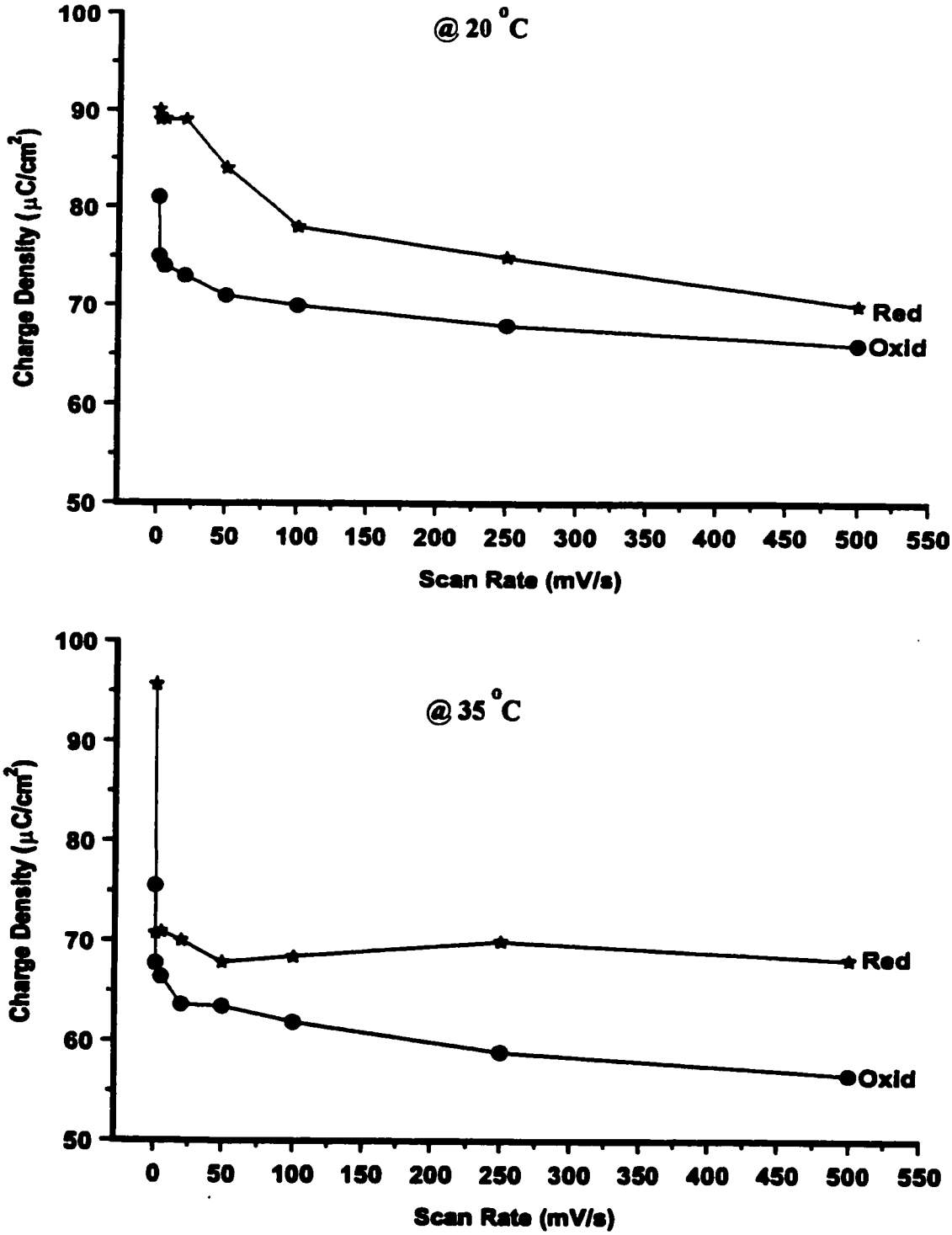

Figure 5.8 : Reductive desorption and oxidative redeposition charge densities of a hexadecanethiol monolayer as a function of scan rate at a Au(111) single crystal electrode. Measurements were done in 0.5 M KOH at 20° and 35 °C.

The relationship between the peak current and the potential scan rate can provide information on electrochemical reactions. If the reduction and the oxidative redeposition are considered as irreversible reactions, it can be shown that the rate of the forward reaction is [35].

$$\frac{i}{nFA} = -(\partial \Gamma_o(t)/\partial t) = [\partial \Gamma_o(t)/\partial E]\upsilon \qquad (6)$$

$$\frac{i}{nFA} = k_f \Gamma_o(t) \qquad (7)$$

where F is the Faraday's constant, A is the electrode surface area, υ is the sweep rate. k_f and k_{fi} are the reaction rate constants. Here $\Gamma_o(t)$ is the surface concentration of the species o at time t. k_f is given by :

$$k_f = k_{fi}\, e^{at} \qquad (8)$$

In the above, $k_{fi} = k^o \exp[-\frac{\alpha n F}{RT}(E_i - E^{o'})]$, where α is the transfer coefficient and $a = \frac{\alpha n F \upsilon}{RT}$. By combining equations (6), (7) and (8), we obtain:

$$d\Gamma_o(t)/dt = k_{fi}\, e^{at}\, \Gamma_o(t) \qquad (9)$$

With the initial condition that at $t = 0$, $\Gamma_o(t) = \Gamma_o^*$, the expressions for $\Gamma_o(t)$ and the i-E curve become :

$$\Gamma_o(t) = \Gamma_o^* \exp(k_f/a) \qquad (10)$$

and $$i = nFAkf\,\Gamma_o^* \exp\left[\left(\frac{RT}{\alpha nF}\right)(k_f/\upsilon)\right] \qquad (11)$$

Assuming that the scan rate begins at positive potentials and that $k_{fi} \longrightarrow 0$ (since $e^{k_{fi}} \longrightarrow 1$), the peak current and potential are given by [35] :

$$i_p = (n^2\alpha F^2 A\Gamma_o^*/2.718\,RT)\,\upsilon \qquad (12)$$

$$i_p \;\alpha\, \upsilon \qquad (13)$$

The peak current is found to vary linearly with the scan rate υ.

$$E_p = E^{o'} + \frac{RT}{\alpha nF}\,Ln\left(\frac{RT}{\alpha nF}\right) + \frac{RT}{\alpha nF}\,Ln\,(k^o/\upsilon) \qquad (14)$$

$$E_p = \text{Constant} + \frac{RT}{\alpha nF}\,Ln\,(k^o/\upsilon) \qquad (15)$$

$$E_p = C + m\,Ln\,(1/\upsilon) \qquad (16)$$

The peak currents of the reductive peak A and the oxidative peak A′ at 20° and 35 °C are a linear function of the scan rate as shown in Figure 5.9. This is indicative of a fast surface redox process. This is compatible with a Langmuir process where the reduction of the chemisorbed thiols occurs randomly on the surface.

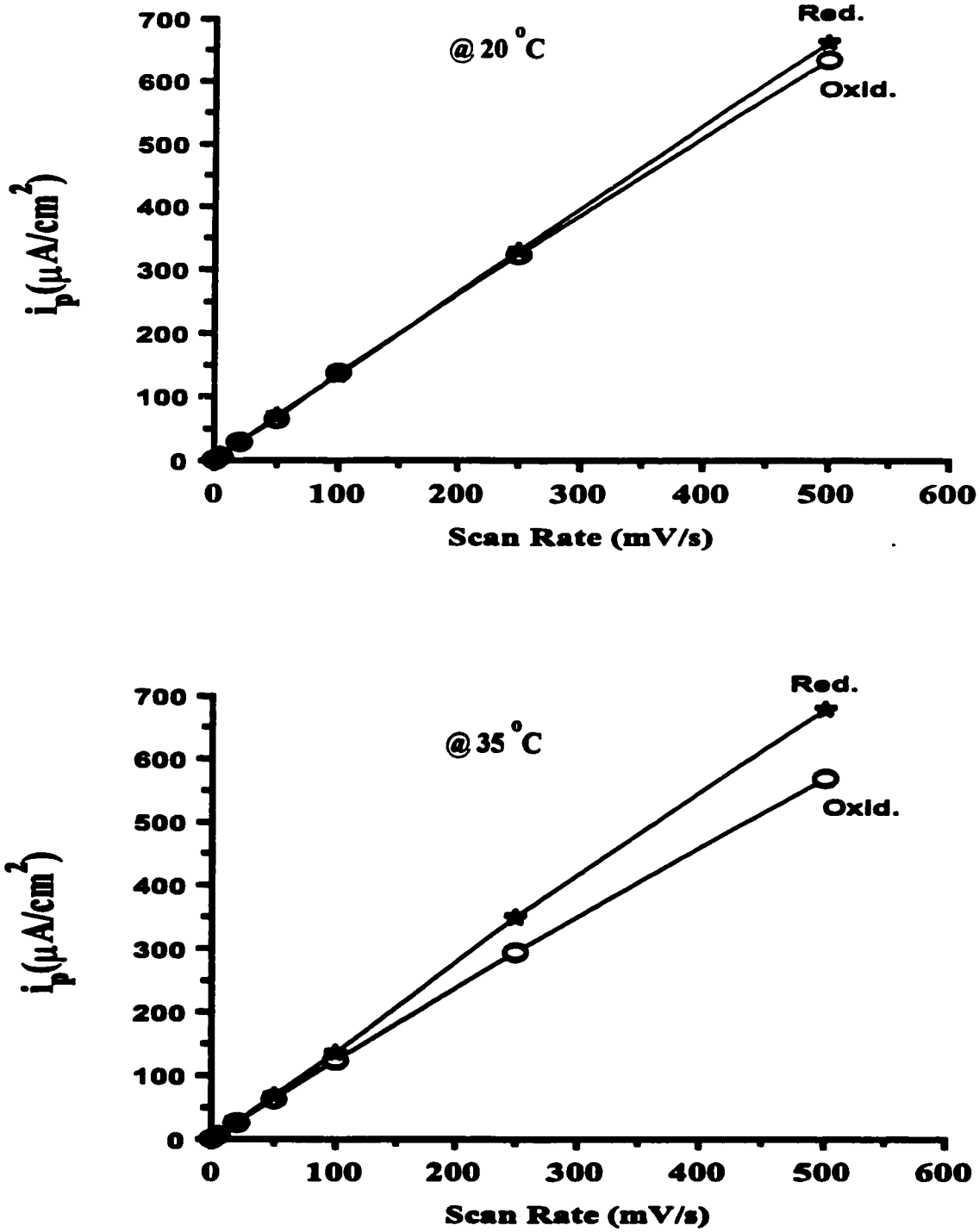

Figure 5.9 : Peak current densities of the reductive desorption and the oxidative redeposition of a hexadecanethiol monolayer adsorbed on Au(111) as a function of scan rate. Measurements were done at a Au(111) in 0.5 M KOH at 20° and 35 °C.

Figure 5.10 shows the linear relationship of the oxidative redeposition peak A′ current density as a function of scan rate for C_{16} SH and C_{18} SH on a single crystal gold (111) electrode in 0.1 M KOH at 25 °C. As the scan rate increases from 5 to 500 mV/sec, the oxidative peak A′ current density increases linearly. For C_{16} SH, i_p varies between 4 and 425 $\mu A/cm^2$. For C_{18}SH, i_p varies between 4.5 and 418 $\mu A/cm^2$. The average charge densities are, respectively, 44 and 43 $\mu C/cm^2$. Thus the longer chains thiolates are oxidatively redeposited by the same mechanism.

Figure 5.11a shows voltammograms recorded after scanning the electrode potential between -0.2 to -1.3 V and holding the potential on the anodic direction at - 0.98 V for 5 sec and then recording the oxidative redeposition peak A′ at different scan rates in 0.1 M KOH at 25° C. The aim of this experiment is to study the effect of the scan rate on the oxidative peak A′. Fig. 5.11a shows that as the scan rate increases the oxidative current peak A′ increases and shifts toward more positive potentials.

Figure 5.11b presents the oxidative peak A′ potential as a function of ln(1/scan rate). The line is a fit to eq. 16. This shows that the oxidative peak A′ varies linearly with the logarithm of the inverse of the scan rate. As the scan rate increases from 5 to 500 mV/sec, the oxidative peak potential shifts toward more positive potentials ~50 ± 5 mV while the peak current increases from ~ 4 to ~ 425 $\mu A/cm^2$ and the average charge density does not change ≈ 44 $\mu C/cm^2$ (all values have been corrected for the double layer charging current).

3. Summary

The temperature-dependence cyclic voltammetry study revealed the presence of one phase transition between 25° and 35 °C. In contrast, Lennox et al. [20-22] identified a series of phase transitions similar to those of Langmuir-Blodgett film [25-27]. Our temperature study concluded that this transition involves the physisorbed thiolates. We believe that this could be related to the transition of physisorbed thiolates from a laminar structure to a micellar

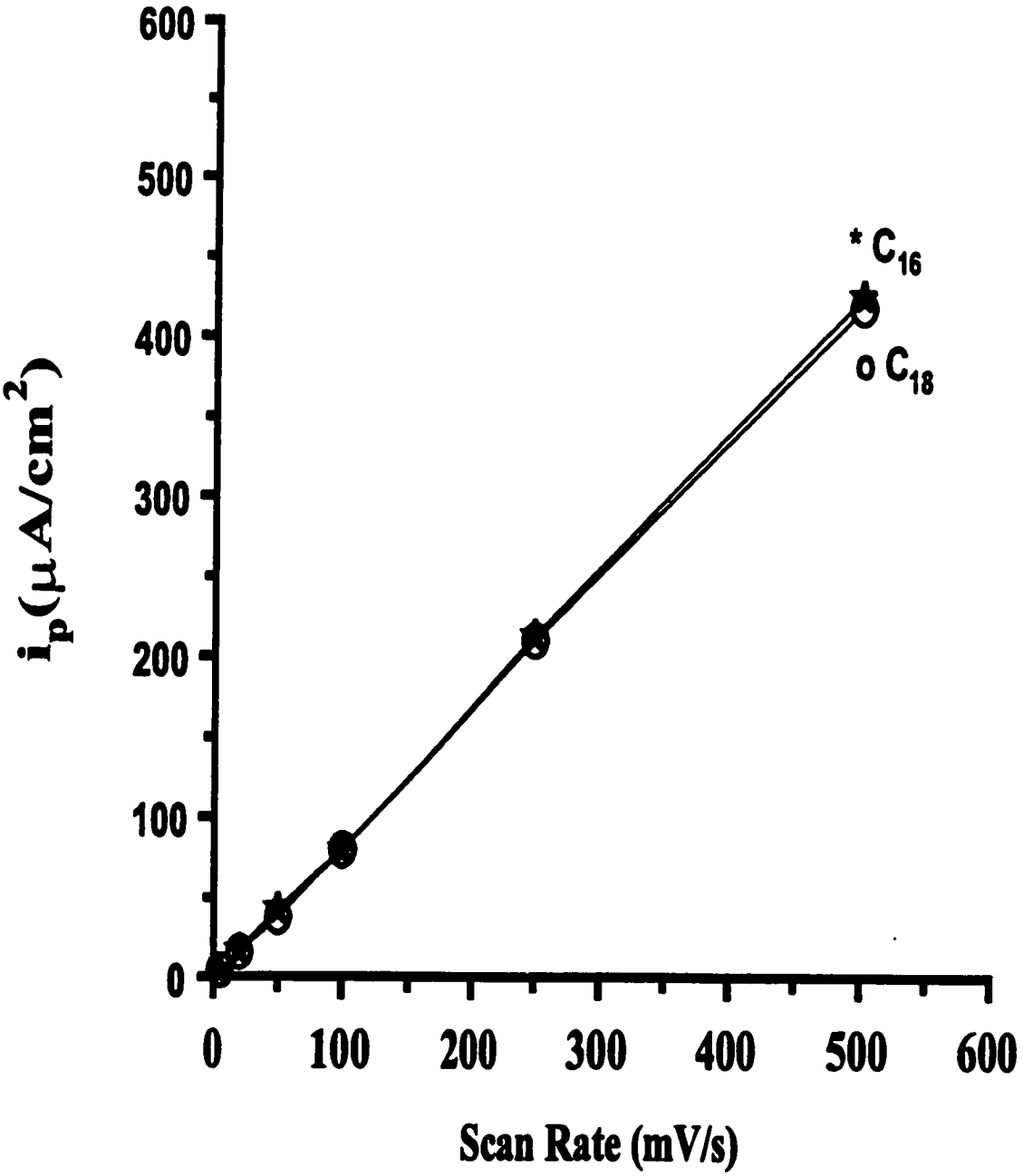

Figure 5.10 : Oxidative peak A' current density of hexadecanethiol and octadecanethiol monolayers as a function of scan rate measured in 0.1 M KOH at 25 ^{o}C.

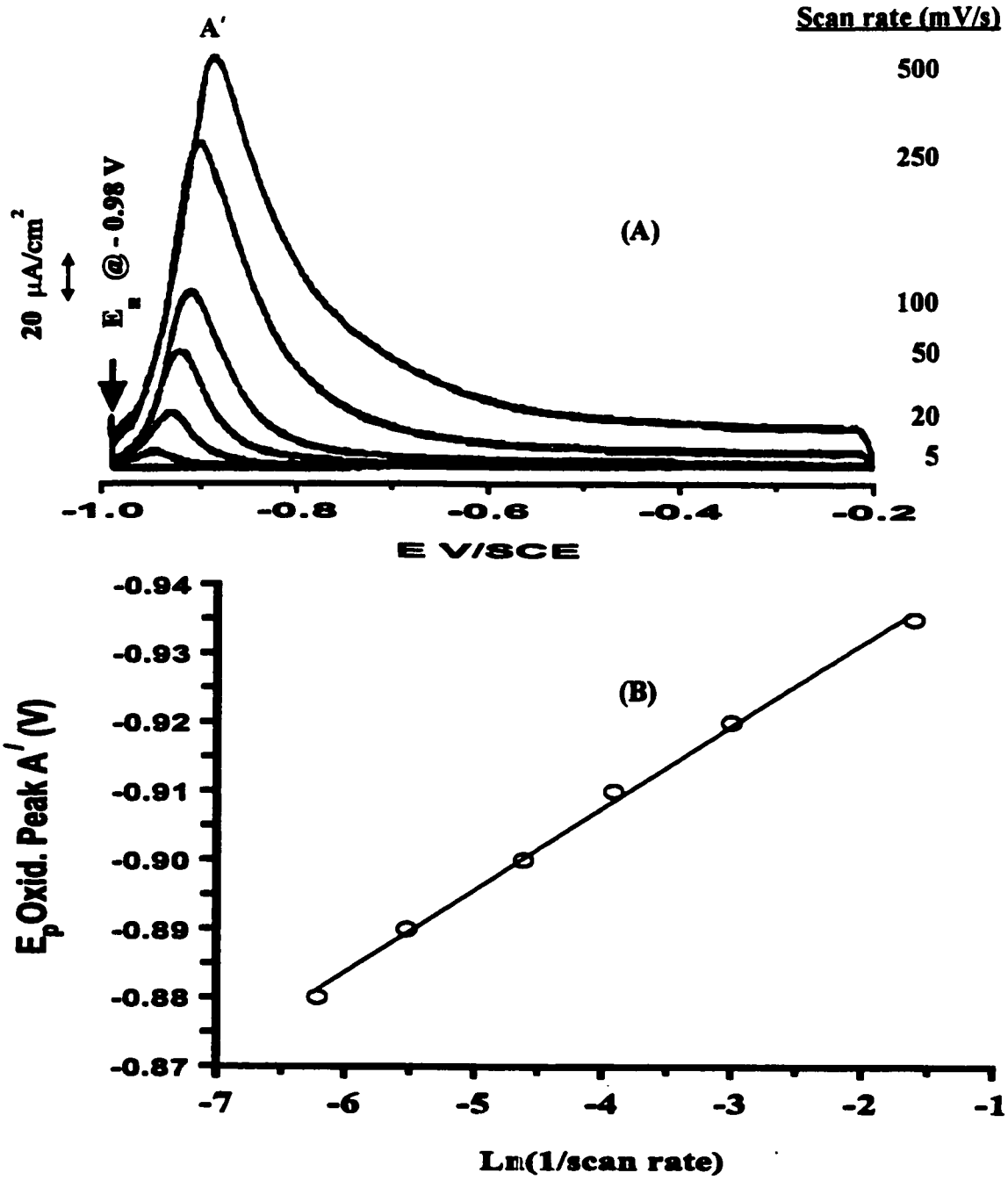

Figure 5.11 : (a) A monolayer of hexadecanethiols is first reduced and then held at a potential of - 0.98 V for 5 seconds and finally the oxidative re-deposition current peak A' was recorded by scanning the potential to - 0.2 V at different potential scan rates. (b) Peak potential, E_p, as a function of ln(1/scan rate). Measurements were done in 0.1 M KOH at 25 $^{\circ}$C. E_H is the holding potential position.

structure. Below 25 °C we could expect that chemisorbed thiols form a crystalline structure.

Going from a crystalline state to a physisorbed state is expected to require a larger activation energy than if the chemisorbed thiolates are initially in a liquid like state. We thus suggest that the observed phase transition between the physisorbed states is related to a change of the structure of the chemisorbed thiols which occur around 25°C.

4. References

1. Lopez, G. P.; Albers, M. W.; Schreiber, S. L.; Carroll, R.; Peralta, E.; Whitesides, G. M. J. Am. Chem. Soc. **1993**, 115, 5877.
2. Singhvi, R.; Kumar, A.; Lopez, G. P.; Stephanopoulos, G. N.; Wang, D. I. C.; Whitesides, G. M.; Ingber, D. E. Science **1994**, 264, 696.
3. Hickman, J. J.; Bhatia, S. K.; Quong, J. N.; Shoen, P.; Stenger, D. A.; Pike, C.; Cotman, C. W. J. Vac. Sci. Technol. A **1994**, 12 607.
4. Mrksich, M.; Whitesides, G. M. Annu. Rev. Biophys. Biomol. Struct. **1996**, 25, 55.
5. Mrksich, M.; Dike, L. E.; Tien, J.; Ingber, D. E.; Whitesides, G. M. Exp. Cell. Res. **1997**, 235, 305.
6. Cooper, E.; Wiggs, R.; Hutt, D. A.; Parker, L.; Leggett, G. J.; Parker, T. L. J. Mater. Chem. **1997**, 7, 435.
7. Tidwell, C. D.; Ertel, S. I.; Ratner, B. D.; Tarasevich, B.; Atre, S.; Allara, D. L. Langmuir **1997**, 13, 3404.
8. Frisbie, C. D.; Martin, J. R.; Duff, R. R.; Wrighton, M. S. J. Am. Chem. Soc. **1992**, 114, 7142.
9. Kumar, A.; Biebuyck, H. A.; Whitesides, G. M. Langmuir **1994**, 10, 1498.
10. Lercel, M. J.; Tiberio, R. C.; Chapman, P. F.; Craighead, H. G.; Sheen, C. W.; Parikh, A. N.; Allara, D. L. J. Vac. Sci. Technol. B **1993**, 11, 2823.
11. Lercel, M. J.; Redinbo, G. F.; Pardo, F. D.; Rooks, M.; Tiberio, R. C.; Simpson, P.;

Craighead, H. G.; Sheen, C. W.; Parikh, A. N.; Allara, D. L. J. Vac. Sci. Technol. B **1994**, 12, 3663.

12. Lercel, M. J.; Redinbo, G. F.; Craighead, H. G.; Sheen, C. W.; Allara. D. L. Appl. Phys. Lett. **1994**, 65, 974.
13. Gardner, T. J.; Frisbie, C. D.; Wrighton, M. S. J. Am. Chem. Soc. **1995**, 117, 6927.
14. Frisbie, C. D.; Rozsnyai, L. F.; Noy, A.; Wrighton, M. S.; Lieber, C. M. Science **1994**, 265, 2071.
15. Green, J. B.; McDermott, M. T.; Porter, M. D.; Siperko, L. M. J. Phys. Chem. **1995**, 99, 10960.
16. Browning-Kelley, M. E.; Hari, V.; Liu, G.-Y. Langmuir **1997**, 13, 343.
17. Chidsey, C. E. D.; Liu, G.-Y.; Rowntree, P.; Scoles, G. J. Chem. Phys. **1989**, 91, 4421.
18. Camillone III, N.; Chidsey, C. E. D.; Liu, G.-y.; Putvinski, T. M.; Scoles, G. J. Chem. Phys. **1991**, 94, 8493.
19. Camilone III, N.; Chidsey, C. E. D.; Liu, G.-y.; Scoles, G. J. Chem. Phys. **1993**, 98 (4), 3503.
20. Badia, A.; Back, R.; Lennox, R. B. Angew. Chem. Int. Ed. Engl. **1994**, 33, 2332.
21. Bensebaa, F.; Ellis, T. H.; Badia, A.; Lennox, R. B. J. Vac. Sci. Technol. A **1995**, 13, 1331.
22. Bensebaa, F.; Ellis, T. H.; Badia, A.; Lennox, R. B. Langmuir **1998**, 14, 2361.
23. Porter, M. D.; Bright, T. B.; Allara, D. L.; Chidsey, C. E. D. J. Am. Chem. Soc. **1987**, 109, 3559.
24. Miller, C.; Cuendet, P.; Gratzel, M. J. Phys. Chem. **1991**, 95, 877.
25. Barbaczy, E.; Dodge, F.; Rabolt, J. F. Applied Spectroscopy **1987**, 41 (2), 176.
26. Riegler, J. E. J. Phys. Chem. **1989**, 93, 6475.
27. LeBihan, Th.; Pézolet, M. Chemistry and Physics of Lipids 1998, 94, 13-33.
28. Marecek, V.; Samec, Z.; Weber, J. J. Electroanal. Chem. **1978**, 94, 169.
29. Marcus, R. A. Ann. Rev. Phys. Chem. **1968**, 13, 955.
30. Bain, C. D.; Troughton, E. B.; Tao, Y.-T.; Evall, J.; Whitesides, G. M. and Nuzzo,

R. G. J. Am. Chem. Soc. **1989**, 111, 321.

31. Tanford, C. in The Hydrophobic Effect : Formation of Micelles and Biological Membranes ; John Wiley & Sons : New York, 1980.

32. Vold, R. D.; Vold, M. J. , Colloid and Interface Chemistry ; Addison-Wesley Publishing Co., INC : London, 1983.

33. Hatchett, D. W.; Uibel, R. H.; Stevenson, K. J.; Harris, J. M.; White, H. S. J. Am. Chem. Soc. **1998**, 120, 1062.

34. Yoshikiyo, M. in Micelles Theoretical and Applied Aspects; Plenum Press : NewYork, 1992.

35. Bard, A. J.; Faulkner, L. R. in Electrochemical Methods : Fundamentals and Applications ; John Wiley & Sons : New York, 1980, pp. 222-223 and 523-525.

Chapter 6

Capacitive Properties of Thiols Adsorbed on Au(111)

1. Introduction

Alkanethiolates SAMs are efficient barriers to electron transfer. They reduce the double layer capacitance, inhibit corrosion, prevent adsorption and allow a control of electron transfer [1,2,3]. The understanding of the effect of holes and defects on the electrochemical properties of electrodes modified by a monolayer of thiols is important in all electrochemical applications of these organic films. In this thesis, we have shown that the adsorption of a monolayer of thiols causes a significant decrease of the current in the double layer region (the range of potentials between the reduction and the oxidation of the chemisorbed thiols) [4]. In the voltammogram shown in the previous chapters, the current in the double layer was found to be independent of the potential but dependent of the chain length: the longer the chain, the lower the current [4]. Numerous studies [5-15] of the capacitance of SAMs have focussed on e-transfer measurements using mainly cyclic voltammetry. However, the double layer capacity obtained from voltammograms are not very precise. They do not allow the detection of a small concentration of holes and defects such as is observed on monolayers of thiols. In this chapter we describe results obtained with AC impedance spectroscopy which gives a more precise measurement of the capacitive properties of thiol monolayers.

Reactions at an electrode can be studied by various methods, for instance cyclic voltammetry (CV), potential step chronoamperometry (CA) or AC impedance spectroscopy (ACIS). Both CV and CA methods are based on large perturbations of the potential. As a result, the electrode is driven far from its initial equilibrium state. This gives rise to a transient current which depends on how the system reaches a new equilibrium. In contrast, AC impedance spectroscopy is based on the superposition of a small (5-10 mV) AC sinusoidal signal on a constant potential. Thus, the system under investigation remains very close to

equilibrium [1,16,17]. This method is described in more detail in Chapter 2. Briefly, impedance spectroscopy offers several advantages: (1) More precise electrochemical measurements; (2) Working very close to equilibrium makes it easier to deal with kinetics and diffusion [1,16] ; (3) The response can often be treated by simple mathematical relationships as the current-potential relationship becomes linear. For example, the current, in the limit of small potential depends linearly on the potential (equation (1)) rather than exponentially (equation (2))

$$I = (nF/RT)\,\eta \qquad (1)$$

$$I = (nF/RT)\exp(\eta) \qquad (2)$$

The modelling of the AC electrochemical impedance is based on the analysis of electrical networks. In this approach, briefly described in Chapter 2, the electrochemical processes are modelled by networks of resistors and capacitors [1,16]. The use of so-called "equivalent circuit" has been shown to be a powerful method to study charge transfer reactions [5]. It also is sensitive to the presence of "pinholes"and defects [18].

Recently Finklea [18] has reviewed the use of electrochemical impedance spectroscopy (EIS) in the characterization of SAMs. This allows for the determination of the capacitance, resistance, impedance from equivalent electrical circuit models. Fokkink et al. [20] performed capacitance measurements of octadecanethiols adsorbed on polycrystalline gold. They reported an electrocapillary maxima at - 0.45 V vs SCE. They interpreted this minima as the potential of zero charge of the thiol coated electrode.

The total capacitance can be divided into two contributions. There is the capacitance C_{SAM}, of a thiolate monolayer and the capacitance of the diffuse layer, C_{GC}. These capacitances are in series and the total capacitance is given by [4]:

$$1/C_{Total} = 1/C_{SAM} + 1/C_{GC} \qquad (3)$$

C_{SAM} depends on the SAM thickness and head group, but it is independent of the electrolyte concentration. C_{GC} is the electrolyte-concentration dependent capacity of the diffuse layer [21]. The total capacitance of the interfacial double layer is dominated by the smaller term in the capacitance sum [21].

Fawcett and co-workers have investigated SAMs of decanethiol, ω-hydroxydecanethiol and 4'-hydroxy-4-mercaptobiphenyl with [5] and without [21] redox species at a Au(111) surface over a wide range of frequencies and electrolyte concentration via AC impedance spectroscopy. They presented a simple model to analyse the impedance results. This model is shown in Figure 6.1. It consists of an R_{uncomp} C_{stray} in parallel that is used to represent stray capacitance and uncompensated resistance. There is a solution resistance, R_s. The thiol monolayer is represented by C_{dl}, the total capacitance, and a resistance, R, associated with the monolayer in a parallel arrangement.

The complex plane plot of decanethiols shows a vertical line at low frequencies typical of a purely capacitive system. The fit confirms that decanethiols can be represented by only C_{dl} in series with the other elements. Hence, the decanethiols form a monolayer which behaves as a perfect capacitor. When the methyl terminal group is replaced by the hydroxyl group, the complex plane (Argand) plot shows a semicircle at high concentrations rather than the capacitive behaviour found for gold modified with decanethiols. It is necessary to add a resistance R to the model in Figure 6.1 to fit the complex plane plots. The addition of the resistance was explained by the diffusion of ions across the hydroxyl-terminated monolayer. The 4'-hydroxy-4-mercaptobiphenyl displays an even more complex behaviour which required the addition of another RC circuit connected in series to the model shown in Figure 6.1. The interpretation of this extra element is unclear.

In this chapter, we present impedance spectroscopy measurements of the double layer properties of hexadecanethiol monolayers on gold (111) single crystal electrodes in acidic, neutral, and alkaline aqueous media. We examined the properties of the oxidatively redeposited monolayer of hexadecanethiols.

An equivalent electrochemical circuit model

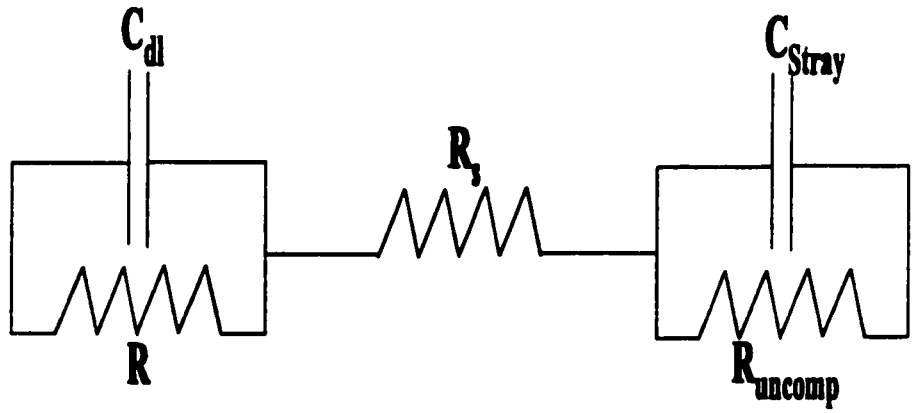

Figure 6.1 : Equivalent electrical circuit model used to fit the impedance of a hexadecanethiol monolayer adsorbed on a Au(111).

2. Results and discussion

We first measured the differential capacitance of a clean Au(111) electrode in 0.01 M $HClO_4$ to characterize the electrode. The differential capacitance measurements were done in a three-electrode electrochemical cell described in Chapter 2. The potential program imposed on the gold (111) working electrode is a dc value, E_{dc}, which is scanned slowly (8 mV/s) with time. A small AC sinusoidal signal, E_{ac}, between 5 to 10 mV, peak-to-peak amplitude oscillating at 20 Hz is superposed on the slowly varying potential. The results in Fig. 6.2 show a clear minimum of 20-25 $\mu F\ cm^{-2}$ and a pzc at 0.2 V. This is similar to the results of Hamelin [3].

Figures 6.2, 6.3 and 6.4 present the differential capacitance of a hexadecanethiol coated Au(111) electrode in 0.01 M $HClO_4$, 0.05 M $KClO_4$, and 0.1 M KOH, respectively. We see that the capacitance change is small (0.05 $\mu F\ cm^{-2}$) and that it does not change significantly over a wide range of potentials. The value of the capacitances are smaller than those we reported in Chapter 3. They are comparable to those reported in the literature. Interestingly, we observe a minimum capacitance between -0.3 and -0.4 V the neutral and alkaline solutions. We do not know if this minimum is related to the pzc of the hexadecanethiol coated electrode or if this indicates a change in the ion permeation at a more negative potential. Nevertheless, this minimum is at the same potential reported in a previous impedance experiment [20].

We performed impedance spectroscopy measurements on clean and modified-Au(111) surfaces with $C_{16}SH$ in the same aqueous electrolyte solutions over a frequency range from 0.01 Hz to 10 kHz. The amplitude of the oscillating potential was 5 mV. The impedance characteristics of the bare gold electrode are compared with those of the same electrode modified.

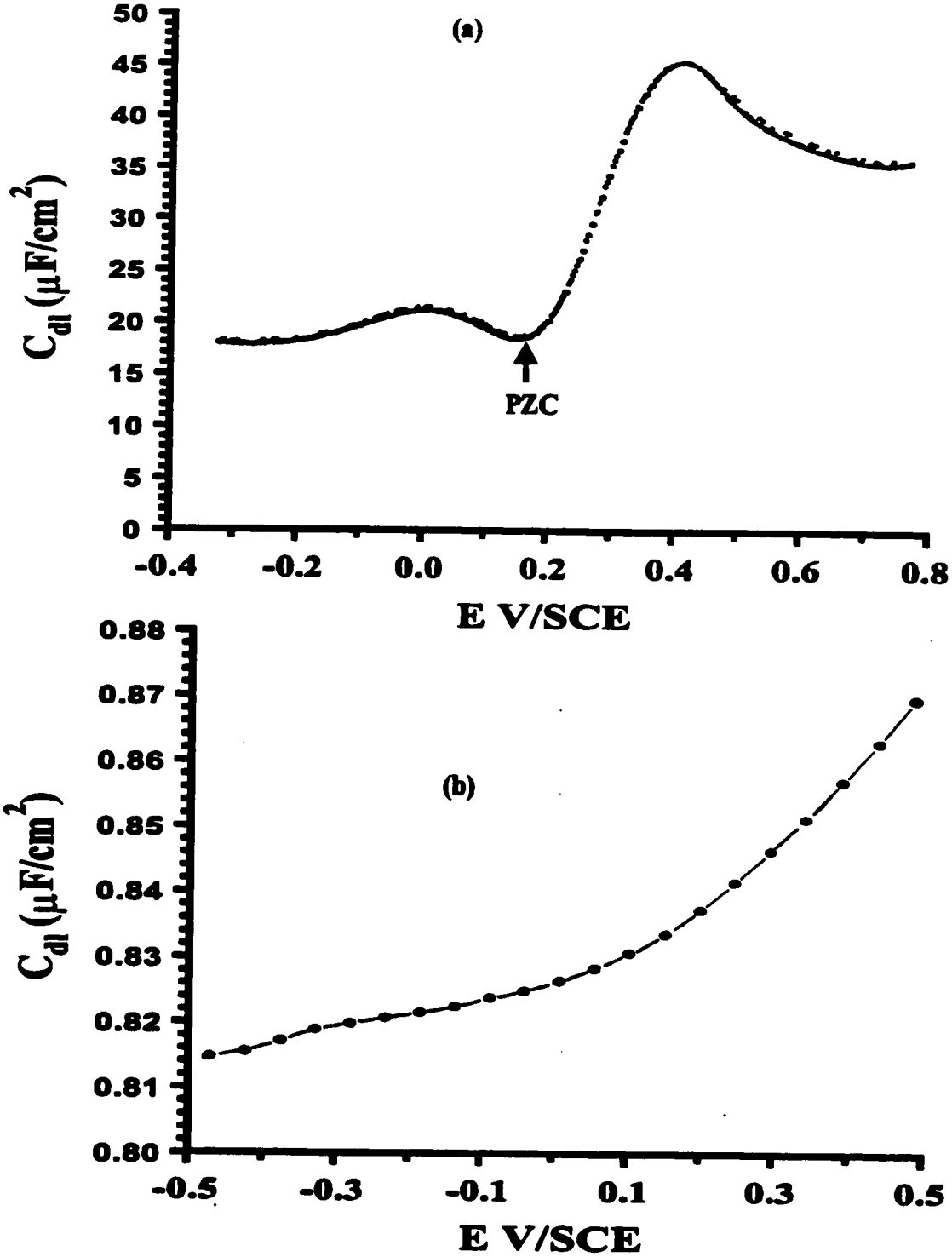

Figure 6.2 : Differential capacitance of (a) a bare and (b) a hexadecanethiol SAM modified Au(111) electrode. Measurements were done in 10 mM $HClO_4$ at a potential scan rate of 8 mV/s and a frequency of 20 Hz and 10 mV amplitude for the AC component.

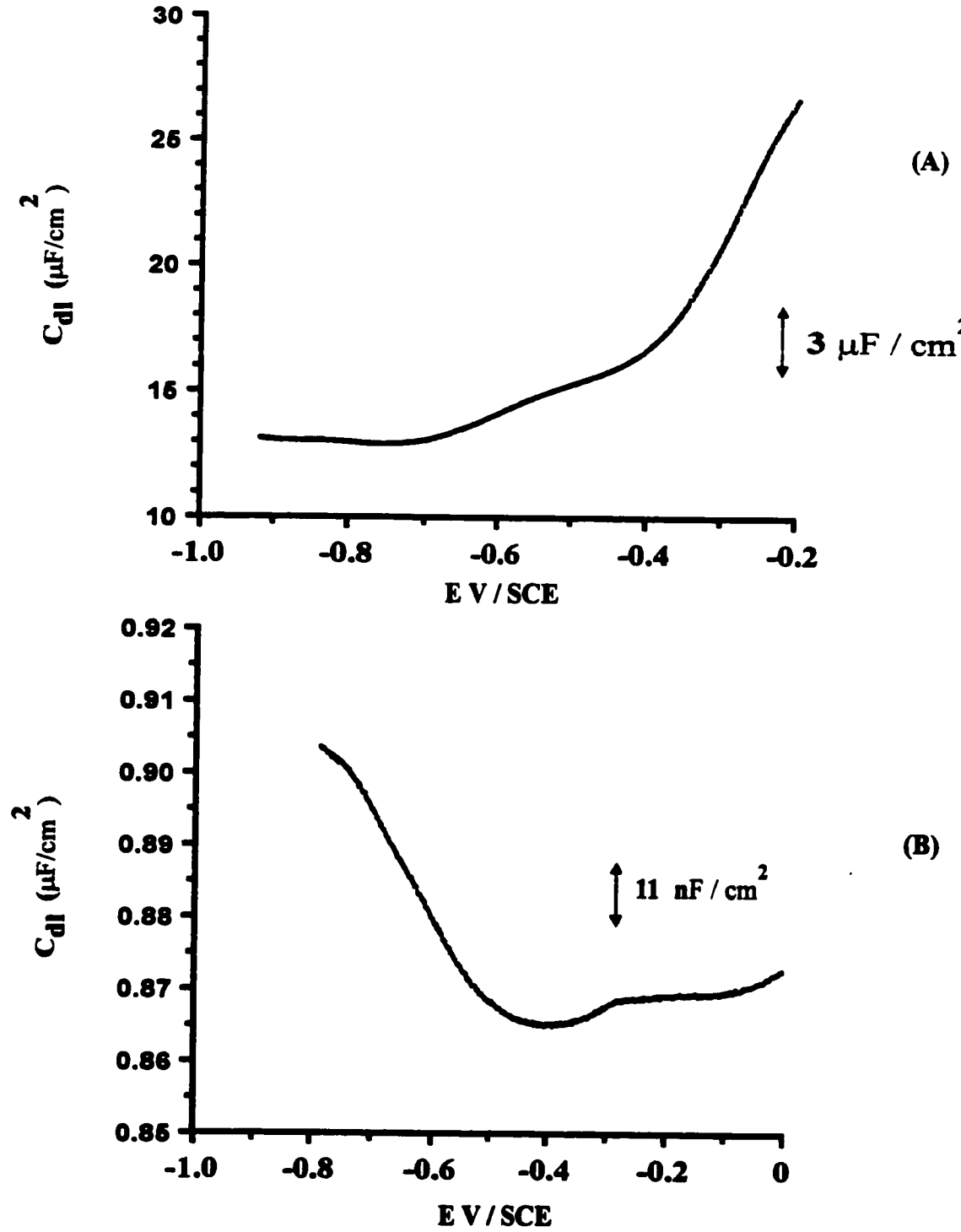

Figure 6.3 : Differential capacitance of (a) a bare and (b) a hexadecanethiol SAM modified Au(111) electrode. Measurements were done in 50 mM $KClO_4$ at a potential scan rate of 8 mV/s and a frequency of 20 Hz and 10 mV amplitude for the AC component.

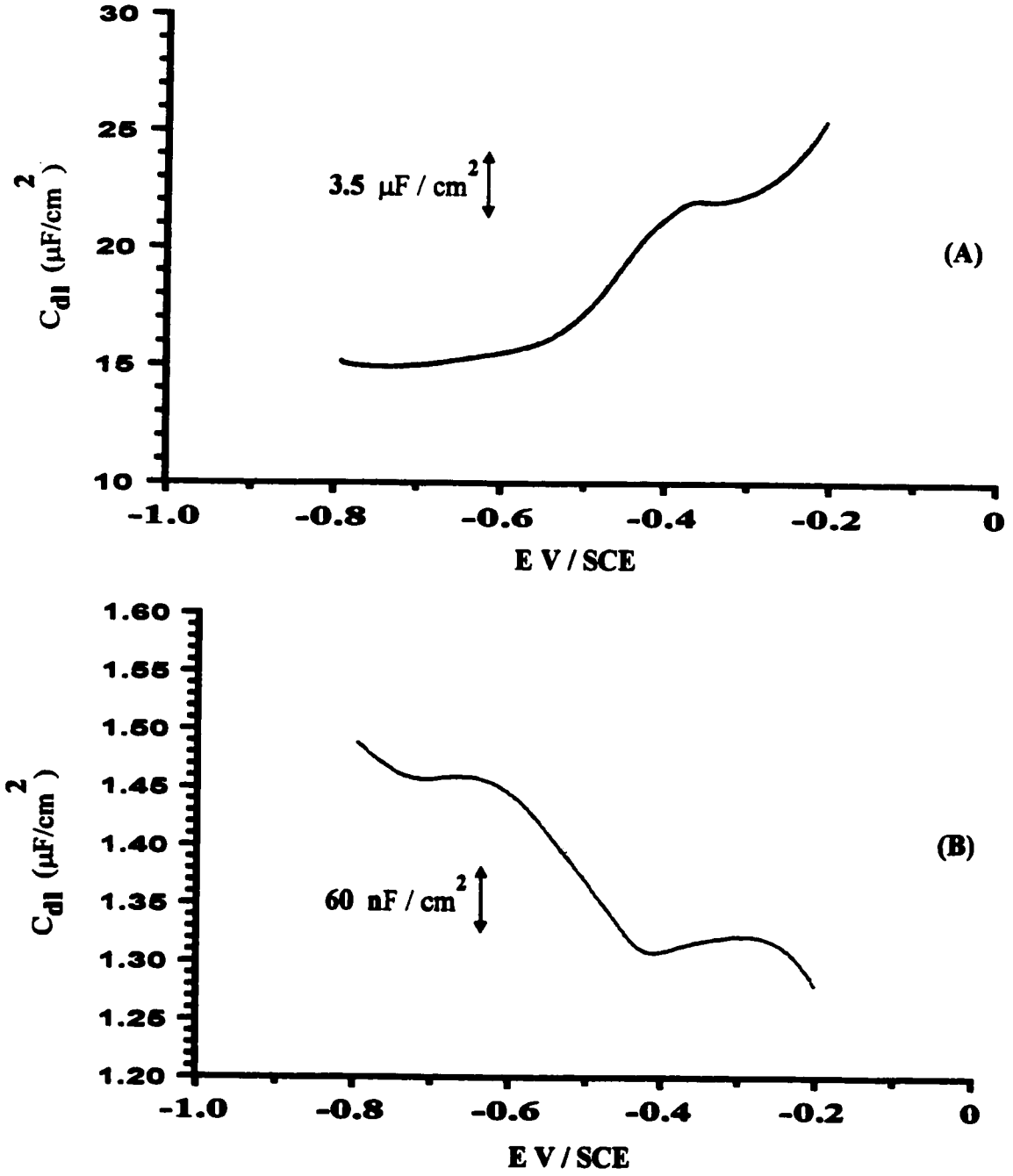

Figure 6.4 : Differential capacitance of (a) a bare and (b) a hexadecanethiol SAM modified Au(111) electrode. Measurements were done in 100 mM KOH at a potential scan rate of 8 mV/s and a frequency of 20 Hz and 10 mV amplitude for the AC component.

In Figure 6.5 the Argand plot shows that at -0.40 V the real component of the impedance is smaller by a factor of 50 at low frequency than the imaginary component for the clean Au(111) in 0.05 M $HClO_4$. Z' does not vary significantly with decreasing frequency. However Z'' decreases significantly (becomes more negative) when the frequency decreases. This behaviour is typical of a capacitor which is expected to show a linear variation of Z'' with the frequency. The solid line is a fit with the model. It consists of an R_{uncomp} C_{stray} in parallel that is used to represent stray capacitance and uncompensated resistance. There is a solution resistance, R_s. R_{uncomp}, C_{stray} and R_s do not change during the experiment. The thiol monolayer is represented by C_{dl}, the total capacitance, and a resistance, R, associated with the monolayer in a parallel arrangement. C_{dl} and R are chain length and potential dependent elements.

The parameters of the fit are shown in Table 1. The fit confirms the capacitive behaviour of the clean electrode in the absence of adsorption since the perchlorate ion does not adsorb strongly on gold. The coated electrode display a similar Argand plot. Z' is independent of the frequency and it has a small value of 30 ohms. Z'' is one order of magnitude larger than for the clean Au(111) electrode. The fit confirms that the thiols behave like a capacitor. The value of C_{dl} is 15 times smaller than the one obtained for the clean surface. This is due to the adsorption of the organic monolayer which has a low dielectric constant which reduces the capacitance of the interface. The value of $0.87 \pm 0.02\ \mu F\ cm^{-2}$ for the capacitance of the coated electrode is in the range of values reported previously. The fits show that the decrease of the double layer capacitance causes the decrease of Z''.

In Figure 6.6, we present measurements of the impedance at various potentials covering the reductive desorption of the hexadecanethiols and its oxidative redeposition in 0.1 M KOH. The clean Au(111) displays an Argand plot as in the other electrolyte. Z' is almost constant at all frequencies and Z'' increases linearly with the frequency. The value of Z'' is larger since the potential is -0.8 V. The fit shows that the capacitance of the double layer is now $14.4\ \mu F\ cm^{-2}$. Three cyclic voltammograms in which the hexadecanethiols were

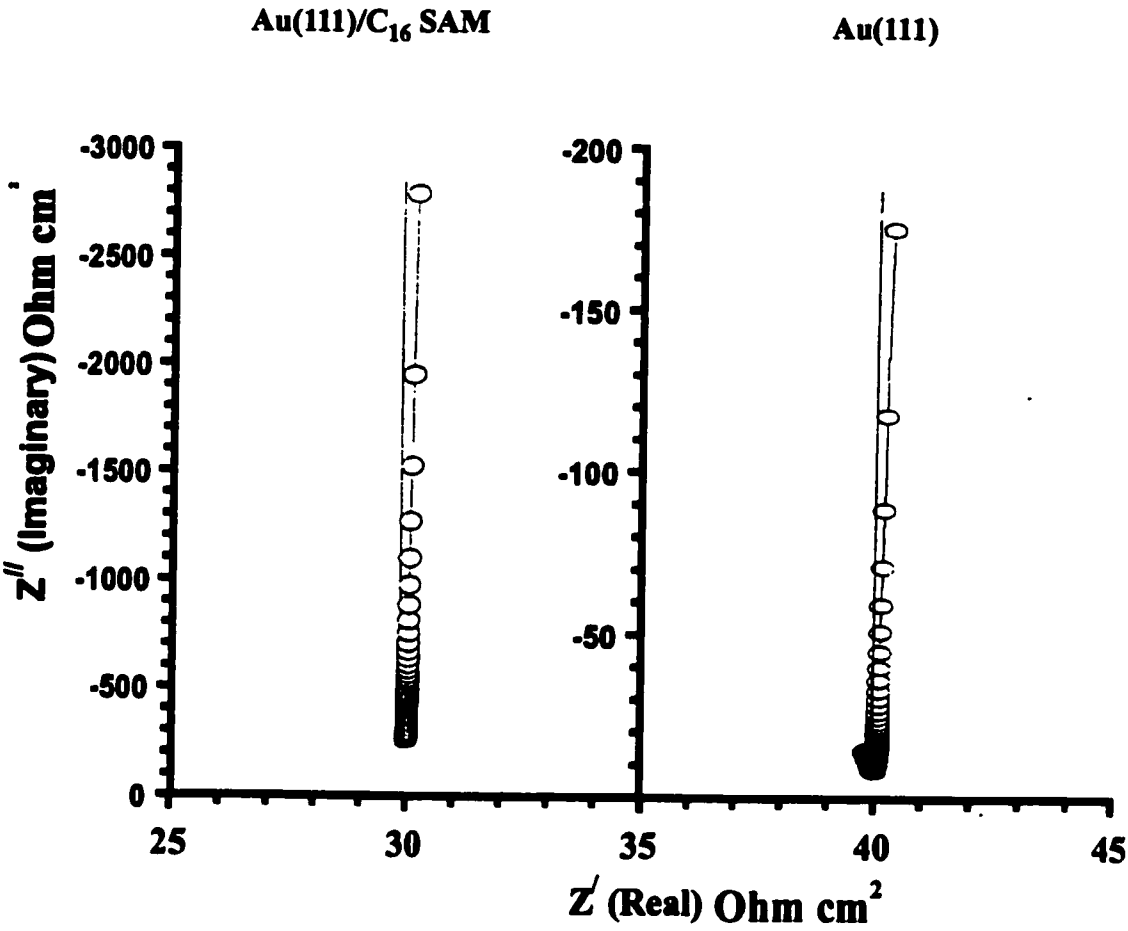

Figure 6.5 : Complex (Argand) plane plot of the impedance of a Au(111) electrode modified with a hexadecanethiol SAM and a bare Au(111) electrode in 50 mM $HClO_4$ electrolyte solution. The frequency range was 66 Hz to 10 kHz and the bias potential was - 400 mV vs SCE. The solid line is the fit with the model shown in Figure 6.1.

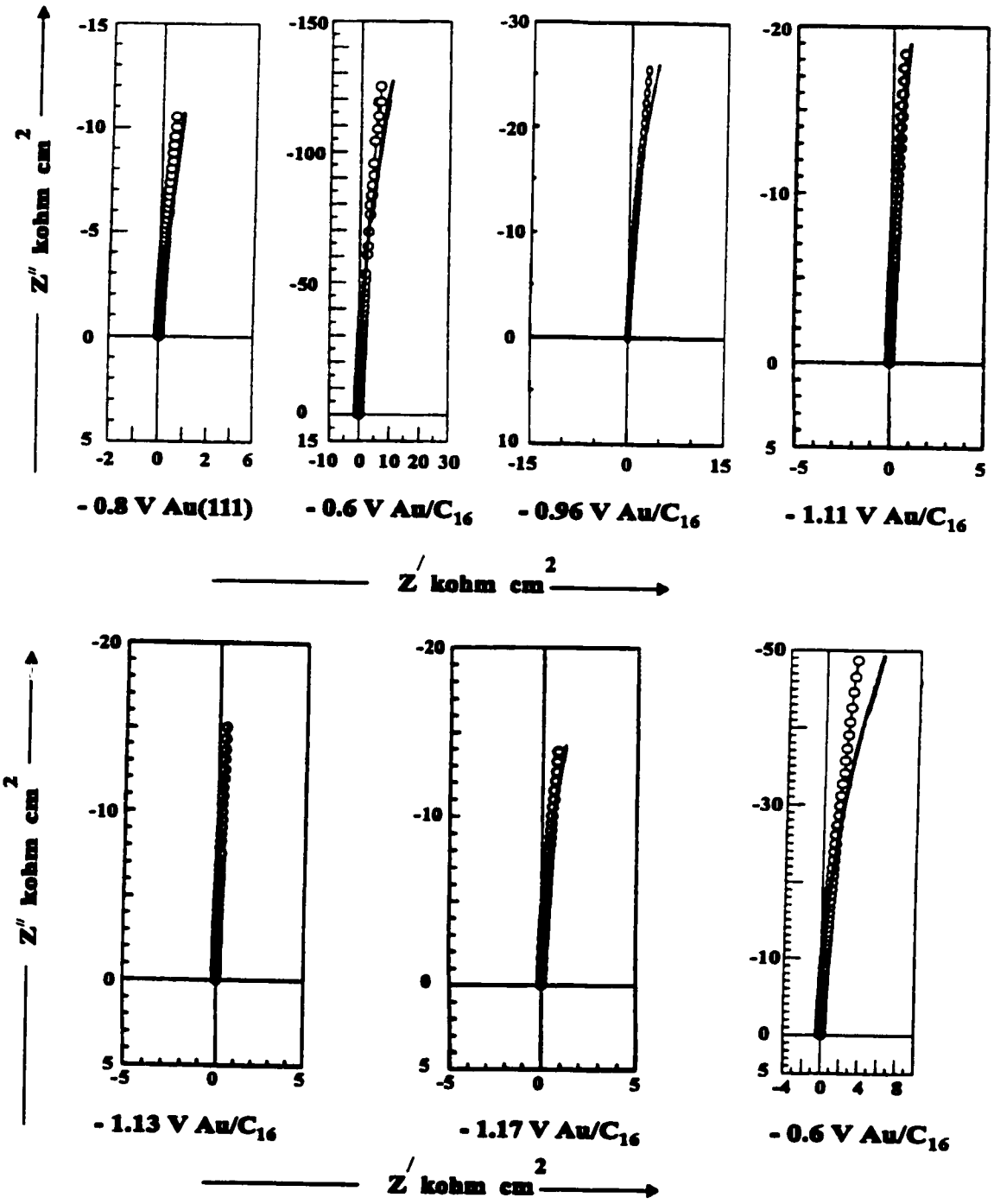

Figure 6.6 : Argand plot at various reductive potentials at a free and hexadecanethiols coated Au(111) electrode in 100 mM KOH. Impedance measurements were done in the frequency range of 1 Hz to 10 kHz and an amplitude of 5 mV. The solid line is the fit with the model in Figure 6.1.

reductively desorbed and oxidatively adsorbed were done prior to recording the impedance at -0.6 V. The impedance of the chemisorbed thiols at -0.6 V reveals a capacitive behaviour. A capacitance of 1.0 $\mu F\ cm^{-2}$ is needed to fit the data. Z'' is about 10 times larger than the one measured for the uncoated electrode. This shows that the oxidatively deposited monolayer does not have a significant number of defects. The impedance measured just before the onset of the reduction of the chemisorbed (thiols chemically adsorbed from solution onto gold surface), -0.96 V, displays a significant curvature and a significant decrease of Z''. Clearly, the monolayer is less capacitive. It is necessary to have a resistance and a capacitor in parallel to adequately fit the Argand plot.

The capacitance has increased to 6.0 $\mu F\ cm^{-2}$, and the resistance is 160 kohms. We interpret the presence of a resistance and the increase of the capacitance as an indication that ions can now permeate the monolayer. This result gives support to our mechanism presented in Chapter 3. We suggested that the reduction of the monolayer is initiated by the diffusion of the ions across the monolayer. We note that the changes in the capacitance are not visible in the voltammogram. At -1.11 V where the peak A occurs, the Z'' component continues to increase. The fit shows an increase of the capacitance to 8.4 $\mu F\ cm^{-2}$. At -1.13 V, a potential located between the peaks A and B, the Argand plot shows a curved line. The fit shows that the capacitance and the resistance have increased. At a potential of -1.17 V the monolayer is completely reduced and a monolayer of physisorbed thiolates is formed. The Argand plot displays a curvature indicating that the system is not purely capacitive. The addition of a resistance is necessary to fit this data. The capacitance is now 11.4 $\mu F\ cm^{-2}$, a value as high as the one of the clean surface at -0.8 V. There is also a resistance of 165 kohms. Thus the monolayer of thiolates is not blocking the surface efficiently. The value of the capacitance suggests that it is possible to form a double layer at the gold surface.

Finally, the impedance measured after the oxidative redeposition of the physisorbed thiolates at -0.6 V differs from the initial one. Z' has not change but Z'' has decrease by a factor of 3. There is also a significant curvature of the Argand plot. The fit shows that the

capacity has increased by a factor of 3 to 3.0 μF cm^{-2}. A resistance of 500 kohms is also needed to fit the data. This indicates a degradation of the ion blocking capacity of the monolayer. This is due to the fact that the potential was maintained at a value where the thiolates are physisorbed for one hour which caused the loss of 10 % of the monolayer. The fits are not describing the behaviour observed at the lowest frequency. This could be due to the change of the capacitance at the lowest frequency. We expect the ion permeation to be a slow process and thus to occur only at the lowest frequency. This will change the capacitance. Hence, the model that we used might not be completely appropriate at these low frequencies. A more sophisticated model, in which the capacitance is allowed to vary with the frequency, should be applied to these results.

Table 1 . Fitting parameters of the model in Figure 6.1 for the data in Figure 6.6 :

Gold	E /V vs SCE	C_d (μF/cm^2)	R_1 (ohm cm^2)	R_u (ohm cm^2)	C_s (μF/cm^2)	R_s (ohm cm^2)
Bare	-0.8	14.4	1.43E+05	19.4	0.02	14.9
Coated	-0.6	1	1.64E+06	19.4	0.02	14.9
	-0.96	5.9	1.64E+05	19.4	0.02	14.9
	-1.11	8.4	3.93E+05	19.4	0.02	14.9
	-1.13	10.6	4.87E+05	19.4	0.02	14.9
	-1.17	11.4	1.65E+05	19.4	0.02	14.9
	-0.6	3	5.04E+05	19.4	0.02	14.9

In summary, our capacitance and impedance spectroscopy results in acidic and neutral solutions are in agreement with previous results [2]. The observation of a small but reproducible capacitance minimum between -0.3 and -0.4 V is compatible with the presence of a pzc for the hexadecanethiol-coated Au(111) electrode. The impedance measurements in 0.1 M KOH show that there is permeation of ions prior to the reduction of the monolayer. We measured differences in the impedance measured for the partial reduction of the monolayer and a complete reduction of a monolayer. The ion permeation is more difficult for a partially reduced monolayer than for a totally reduced monolayer. The loss of thiols was seen as an increase of the capacitance and of the resistance for the oxidatively redeposited hexadecanethiolates. The results are in qualitative agreement with the mechanism of the

reversible reductive desorption/oxidative redeposition.

3. References

1. Bard, A. J.; Faulkner, L. R. in Electrochemical Methods, Fundamentals and Applications, John Wiley and Sons : New York, 1980, Chapter 5.
2. Finklea, H. O.; Snider, D. A.; Fedyk, J.; Sabatani, E.; Gafni, Y.; Rubinstein, I. Langmuir **1993**, 9, 3660.
3. Hamelin, A. J. Electroanal. Chem. **1996**, 407, 1-11.
4. Sondag-Huethorst, J. A. M.; Fokkink, L. G. J. J. Electoanal. Chem. **1994**, 367, 49.
5. Janek, R. P.; Fawcett, W. R. Langmuir **1998**, 14, 3011.
6. Chidsey, C. E. D.; Loiacono, D. N. Langmuir **1990**, 6, 682.
7. Miller, C. J.; Cuendet, P.; Gratzel, M. J. Phys. Chem. **1991**, 95, 877.
8. Miller, C. J.; Gratzel, M. J. Phys. Chem. **1991**, 95, 5225.
9. Sabatani, E.; Cohen-Boulakaia, J.; Bruening, M.; Rubinstein, I. Langmuir **1993**, 9, 2974.
10. Becka, A. M.; Miller, C. J. J. Phys. Chem. **1993**, 97, 6233.
11. Cheng, J.; Saghi-Szabo, G. ; Tossell, J. A.; Miller, C. J. J. Am. Chem. Soc. **1996**, 118, 680.
12. Delahay, P. Double Layer and Electrode Kinetics ; Intersicence Publishers and John Wiley and Sons : New York, 1965.
13. Fawcett, W. R. ; Opallo, M. Angew. Chem., Int. Ed. Engl. **1994**, 33 (21), 2131.
14. Finklea, H. O.; Snider, D. A.; Fedyk, J. Langmuir **1993**, 9, 3660.
15. Chidsey, C. E. D. Science **1991**, 251, 919.
16. Greef, R.; Peat, R.; Peter, L. M.; Pletcher. D.; Robinson, J. Instrumental Methods In Electrochemistry ; John Wiley and Sons : New York, 1985, Chapter 8.
17. Wayne, R. P. "Chemical Instrumentation" ; Oxford University Press : New York, 1994.
18. Finklea, H. O.; Snider, D. A.; Fedyk, J. Langmuir **1993**, 9, 3660.

19. Jennings, G. K.; Munro, J. C.; Yong, T.-H.; Laibinis, P. E. Langmuir **1998**, 14, 6130.

20. Sondag-Huethorst, J. A. M.; Fokkink, L. G. J. Langmuir **1992**, 8, 2560.

21. Janek, R. P.; Fawcett, W. R.; Ulman, A. J. Phys. Chem. B **1997**, 101, 8550.

Chapter 7

Mechanism of the Oxidative Deposition of Insoluble Thiols on Au(111)

1. Introduction

The reduction of alkanethiols has been studied in more detail than the oxidative adsorption of thiolates [1-4]. Recently, we [3] reported FTIR spectroscopy and electrochemical results that suggested that the reductive desorption and the oxidative deposition of insoluble thiols in aqueous media proceed through two steps which have been described in the previous chapters. The first step is the reduction of the chemisorbed thiols which give rise to a faradaic current peak. The orientation of the thiol molecules does not change significantly during this process. The second step is the formation of physisorbed micelles which gives rise to the capacitive current peak and causes the reorientation of the thiolates. The electrooxidative redeposition of the physisorbed thiolates proceeds through the same two mechanisms, but in the reverse order. The kinetics of the reduction of insoluble thiols was measured. It was found to follow a Langmuir process. This differs from the short chains thiols which were reduced via a hole-nuclei process. These results were explained by the fact that long chain thiols are reduced at a large overpotential which causes the reduction to occur randomly at the surface. We notice that the two processes observed in the voltammograms (see Chapter 3) were not resolved in the chronoamperometric measurements.

Fawcett and co-workers [5] have also reported chronoamperometric results on the desorption of 2-mercaptoethanesulfonate (MES) on Au(111) electrodes. They concluded that peak-shaped chronoamperograms arise from two steps. The first one is the nucleation/growth mechanism. The other is the Frumkin isotherm mechanism which takes into account the attractive interactions between adsorbed molecules [6,7].

For short-chain thiols, White and co-workers have studied the oxidative adsorption

of ethanethiolates on Ag(111) [8,9] and on Hg [10] in alkaline aqueous solutions and proposed that the process proceeds via two-steps. The first step is obtained at low coverage phase and is assigned to a Langmuir isotherm and the second step is obtained at high coverage phase due to a nucleation and growth mechanism. On the other hand, Porter et al. [4] reported only a one-step mechanism on Au(111).

The oxidative current peaks are better separated and therefore a study of the kinetics of the different steps involved in the oxidative adsorption of insoluble thiols seems possible. This would provide results to verify the mechanism presented in the previous chapters. We can expect that the kinetics of each step in the oxidative adsorption will display a different dependence on the temperature. We can predict from the model presented in Chapter 3 that the electrospreading of physisorbed micelles should get faster as the temperature is increased. In this chapter, we present chronoamperometric measurements of the oxidative deposition of hexadecanethiolates on a gold (111) electrode between 5° and 40 °C.

2. Results and discussion

Chronoamperometry was used to study the mechanism of the oxidative redeposition of insoluble alkane thiolates on gold (111) in an aqueous alkaline solution. Chronoamperograms of the oxidative redeposition of hexadecanethiolates were recorded at 5°, 25°, 30°, 35° and 40 °C. The temperatures were chosen because important changes were observed in the cyclic voltammograms (see Chapter 5). Before each potential-step experiment, the working electrode is held under potential control at - 0.3 V, followed by stepping the potential to - 1.2 V where it stayed for a maximum of 2-3 seconds, and then to a preselected final oxidative electrodeposition potential. Chronoamperograms from - 1.2 V to oxidative positive potentials between - 1.2 and - 0.7 V were measured.

Fig. 7.1 shows the chronoamperograms of a potential-step from - 1.2 to - 0.7 V at 5 °C. The current transient is decaying exponentially to a very small value in a few msec. The

integrated charge is only 25 (± 2) $\mu C\ cm^{-2}$ over 45 msec. This value is much smaller than the value of 85 (± 5) $\mu C\ cm^{-2}$ obtained for the oxidative redeposition of a monolayer of hexadecanethiolates. This is due to the recording of the current transient over a time shorter than the time required to oxidatively deposit a full monolayer. When the temperature is increased to 25 °C, the current first decreases rapidly for 3 msec and then it decreases exponentially at a much slower rate. We note that the slow component is more important than at 5 °C. The total charge has increased to 55 (± 2) $\mu C\ cm^{-2}$. At 30 °C, the fast decay is still present. However, after 3 msec. the current is almost constant for a few msec and then it decays smoothly. As the temperature is increased to 35° and 40 °C there is no significant change in the initial decay. The magnitude and duration of the plateau increases with the temperature.

These results clearly show that the oxidative deposition of physisorbed alkanethiolates is influenced by the temperature and it occurs in two steps. There is a fast decay which has a weak temperature dependence. This is followed by a slower process which depends more strongly on the temperature. The chronoamperograms of the oxidative deposition are quite different from those measured for the reductive desorption. The reductive desorption of hexadecanethiols yields a smooth exponential decay [11].

Model :

The chronoamperograms show that the oxidative deposition proceeds through two steps. The shape of the current transients suggest that the initial decay of the current could be represented by a Langmuir process. The shape of the slower component is asymmetric. Its decay is slower than its rising edge. The instantaneous nucleation and growth model yields such a current transient. The Langmuir mechanism of the variation of the current at a time t is given by eq. (1) :

$$J\ (\mu A/cm^2) = m\ (1-\exp(-\ k_1 t))\exp(-k_2 t) \qquad (1)$$

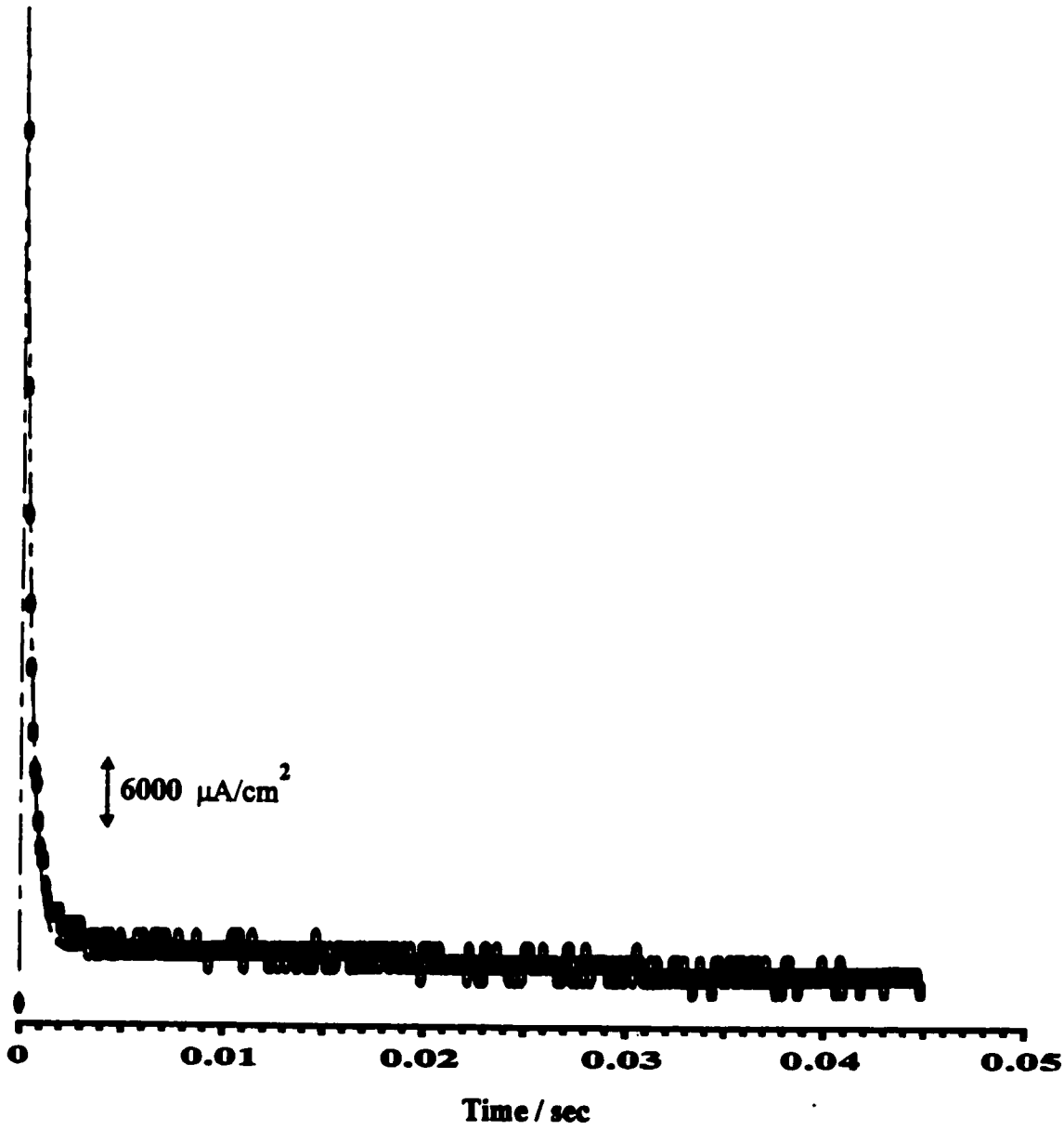

Figure 7.1 : Chronoamperogram of a potential-step from - 1.2 V to - 0.7 V. The circles are the experimental data and the dashed line is the fit with the Langmuir isotherm and nucleation and growth mechanism combination of a hexadecanethiol SAM modified Au(111) electrode in 0.1 M KOH at 5 °C.

The first rate constant, k_1, represents the rising edge and k_2 represents the decaying edge. The Langmuir process assumes that the adsorption occurs at an identical rate on all unoccupied sites.

The nucleation and growth mechanism involves the formation of nuclei of molecules that expands until a full monolayer of thiols is formed. The nucleus formation is expected to be slower than the rate of expansion when the potential is stepped to - 0.7 V. Under these conditions, the nucleation and growth mechanism [12,13] can be expressed as [14]:

$$J\ (\mu A/cm^2) = n\ (t / t_{max})\ \exp\ (t / t_{max})^2 / (2t_{max}^2)) \qquad (2)$$

where t_{max} is the maximum time at which the maximum current density and n is a constant.

The overall current is the sum of the currents generated by each process. We can assume that the two processes are consecutive. The Langmuir process would involve the adsorption of a few thiolates which would act as nucleation centre for the second process. The overall current is given by :

$$J\ (\mu A/cm^2) = m\ (1-\exp(-\ k_1 t))\exp(-k_2 t) + n\ (t / t_{max})\ \exp\ (t / t_{max})^2 / (2t_{max}^2)) + C \qquad (3)$$

where C is a constant used to correct for a small residual current.

The solid lines in Figs. 7.1 to 7.5 are the fits done using eq.(3) . At 5 °C, the initial decay is well fitted by the Langmuir process. The current at longer time is quite small and more difficult to fit with a good confidence level. At 25 °C, eq. (3) provides an adequate fit of the current transient. However, the fit at the end of the initial decay shows a dip.

This discrepancy is probably indicating that the Langmuir and nucleation and growth mechanisms are coupled. At the higher temperatures of 30°, 35° and 40 °C, the fits are better. The initial decay is well fitted by the Langmuir process. The shoulder observed at

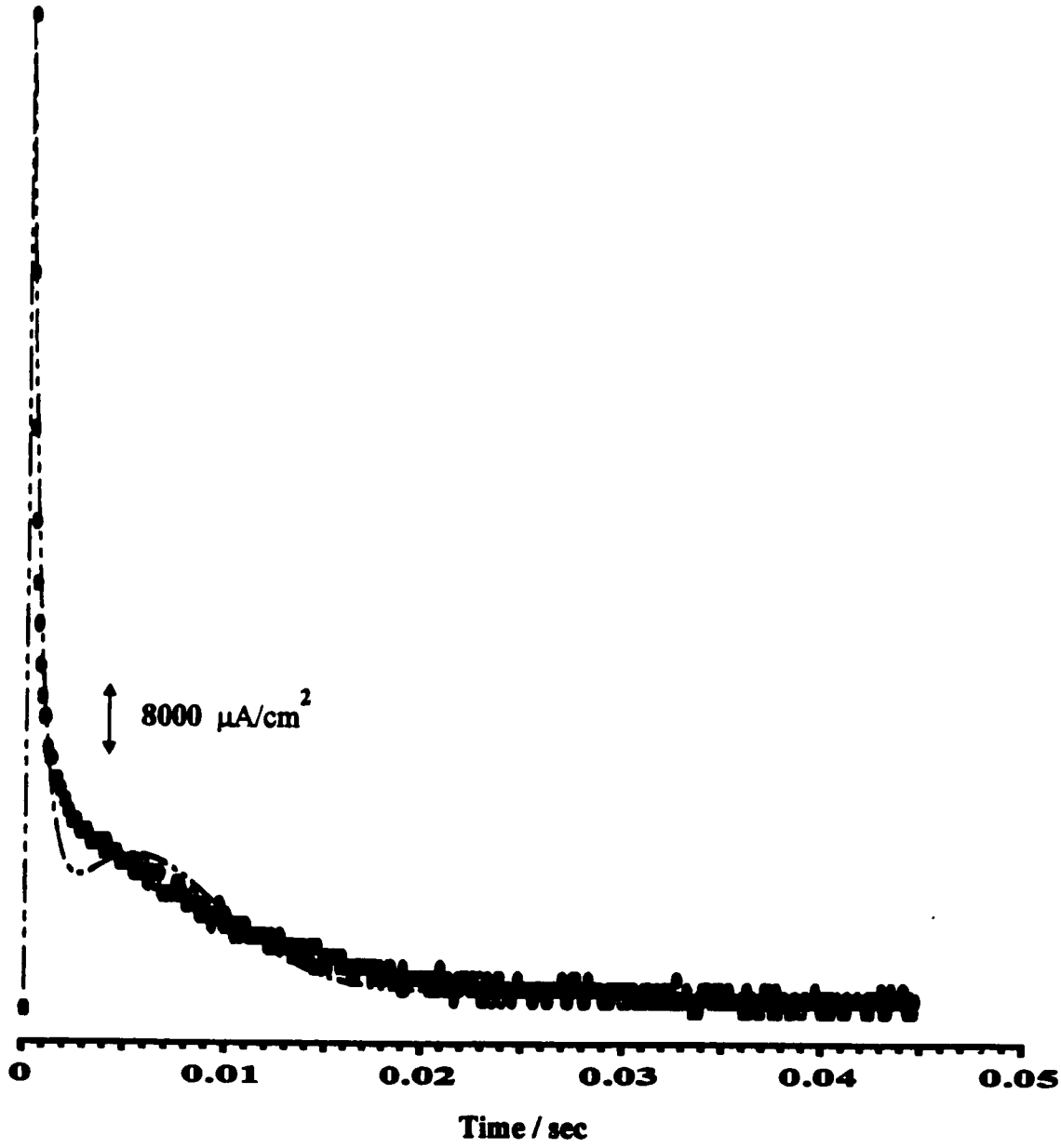

Figure 7.2 : Chronoamperogram of a potential-step from - 1.2 V to - 0.7 V. The circles are the experimental data and the dashed line is the fit with the Langmuir isotherm and nucleation and growth mechanism combination of a hexadecanethiol SAM modified Au(111) electrode in 0.1 M KOH at 25 °C.

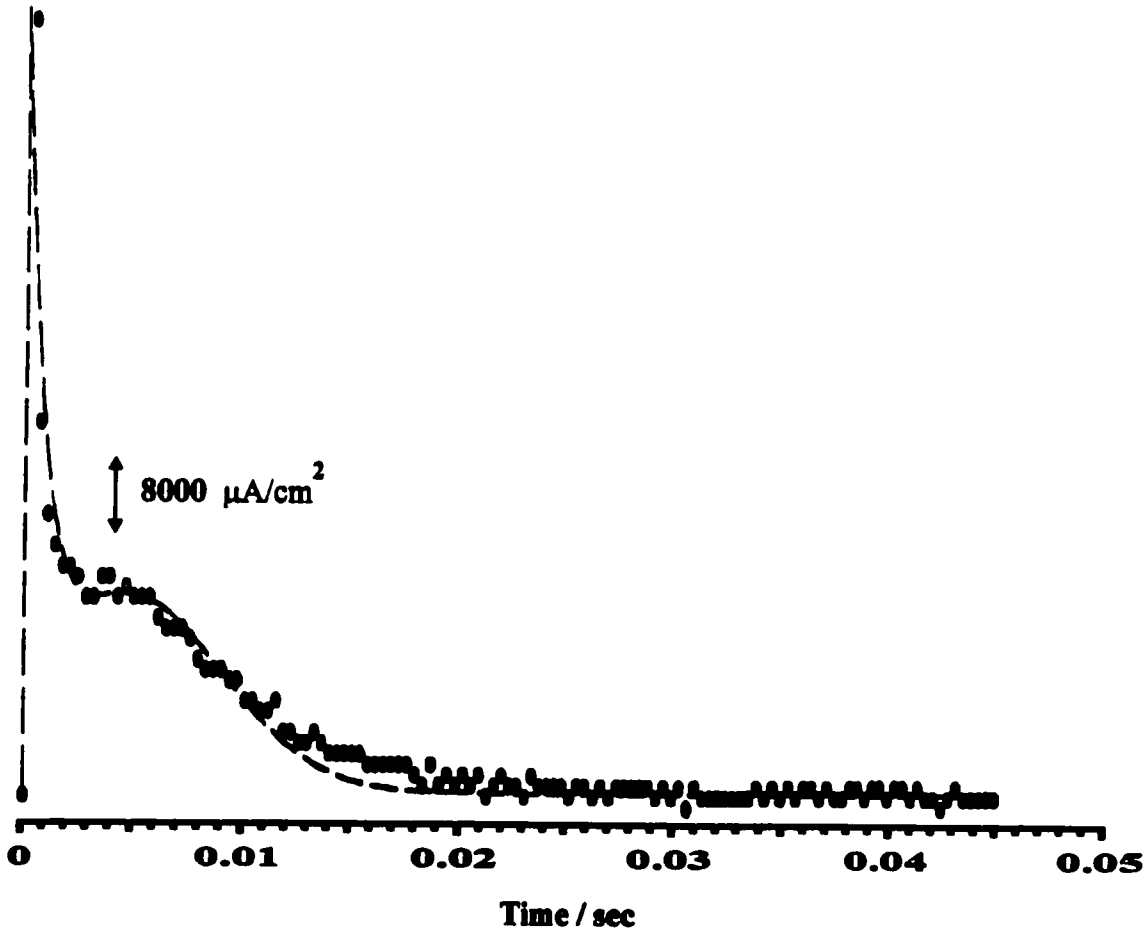

Figure 7.3 : Chronoamperogram of a potential-step from - 1.2 V to - 0.7 V. The circles are the experimental data and the dashed line is the fit with the Langmuir isotherm and nucleation and growth mechanism combination of a hexadecanethiol SAM modified Au(111) electrode in 0.1 M KOH at 30 °C.

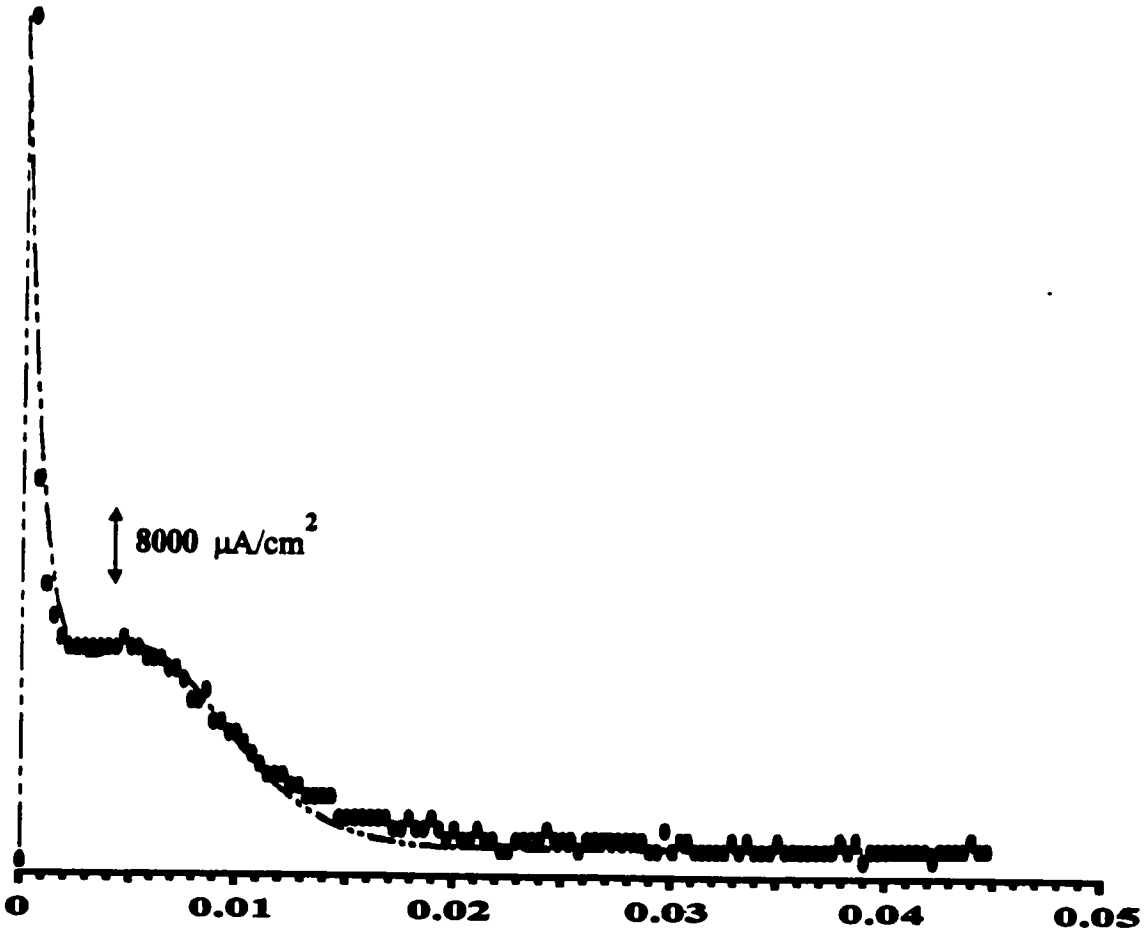

Figure 7.4 : Chronoamperogram of a potential-step from - 1.2 V to - 0.7 V. The circles are the experimental data and the dashed line is the fit with the Langmuir isotherm and nucleation and growth mechanism combination of a hexadecanethiol SAM modified Au(111) electrode in 0.1 M KOH at 35 °C.

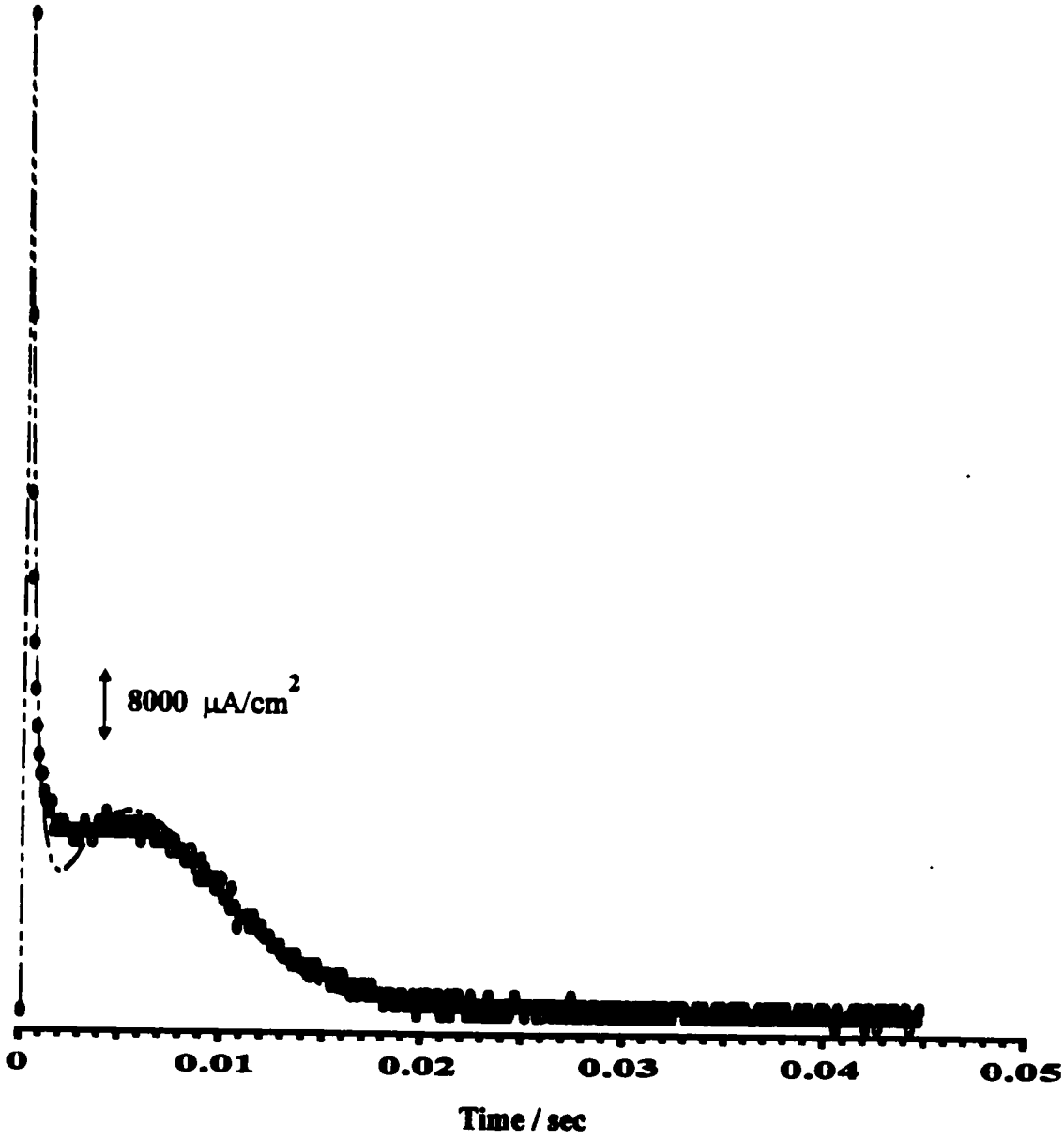

Figure 7.5 : Chronoamperogram of a potential-step from - 1.2 V to - 0.7 V. The circles are the experimental data and the dashed line is the fit with the Langmuir isotherm and nucleation and growth mechanism combination of a hexadecanethiol SAM modified Au(111) electrode in 0.1 M KOH at 40 °C.

longer times is now better fitted by the nucleation and growth process.

Furthermore, the charge density as a function of temperature is shown in Fig. 7.6 for the Langmuir mechanism and the subsequent instantaneous nucleation and growth mechanism proceeds separately. The top plot represents the combination of the two mechanisms . The interesting feature is the sudden increase of the charge density between 25° and 35°C, which then remains approximately constant. This is compatible with the phase transition observed in the same temperature range described in Chap. 5.

The model proposed for the formation of physisorbed micelles and their oxidative electrodeposition in Chapter 3 also has two steps. The first step was the electrospreading of the micelles. The second step was the oxidative adsorption of the thiolates. The analysis of the data with eq.(3) is not compatible with this model. The electrospreading of the micelles should be slow and show a dependence on the temperature. The second step should be faster and weakly dependent on the temperature because it would involve the expulsion of the ions forming a double layer at the gold surface.

This simple interpretation of the results is probably erroneous. The model that we have suggested previously in Chapter 3 and herein ref. 15 is based on slow methods (cyclic voltammetry and FTIR spectroscopy). Voltammograms are acquired at only 20 mV s^{-1}. The oxidative redeposition occurs over 40 seconds. The in-situ vibrational spectra are recorded in 2 minutes. Chronoamperommetry corresponds to applying an instantaneous change of the potential and measuring of the system as it goes back to a new equilibrium state. In the present experiments this event lasts less than 100 msec. It is thus possible that the mechanism observed via these methods show differences. More specifically, a simple interpretation that peak B′ follows a Langmuir process and that peak A′ follows a nucleation and growth process is not correct. First, we note that the magnitude of the Langmuir process does not increase as rapidly as that of peak B′ when the temperature is increased (see Chapter 5). Therefore there is no simple correspondence between the two processes observed in the chronoamperograms and the two current peaks observed in the cyclic voltammograms.

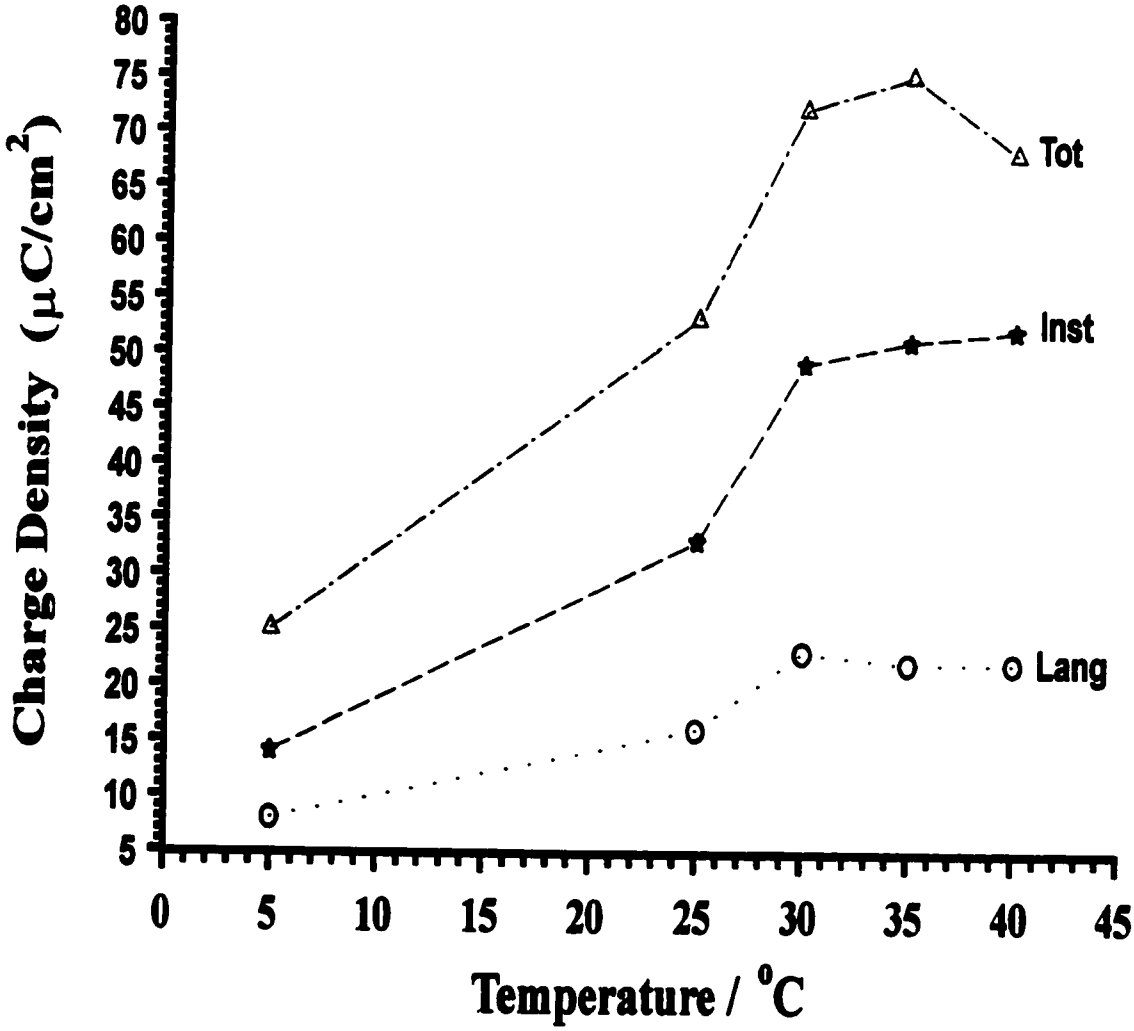

Figure 7.6 : Calculated charge densities of the Langmuir and nucleation and growth processes and the sum of the two processes as a function of temperature obtained from the fit of the oxidative deposition chronoamperograms of hexadecanethiols recorded in 0.1 M KOH.

We thus propose that the oxidative deposition after a potential step proceeds via a mechanism slightly different from the one proposed in Chapter 3. It is shown in Fig. 7.7. In the chronoamperommetric experiments, the temperature independent Langmuir process would correspond to the oxidative adsorption of the thiolates in a micelle that is in direct contact with the surface. The number of thiolates in direct contact with the electrode surface should not vary greatly if the size and shape of the micelles do not vary greatly with the temperature. We can also expect this process to be relatively fast given the proximity of the thiolates and the Au(111) surface. This would explain the temperature independence of the Langmuir process. Once the micelles are adsorbed via a limited number of molecules, the deposition of the remaining thiolates starts. The chemisorbed thiolates act as nucleation centre for the elctrospreading of the micelles. The temperature dependence of this second step is related with the activation energy required for the thiolates to go from a micellar structure to a laminar structure. This mechanism is compatible with the results presented in Chapters 3 and 5.

The significant variations that were observed in the cyclic voltammograms described in Chapter 5 are probably related to the second step that we observed in the chronoamperograms. Below 25 °C the Langmuir and nucleation and growth processes display very different kinetics and the current peaks A′ and B′ are well separated in the voltammogram. At higher temperatures the Langmuir and nucleation and growth processes occur at similar rates and peaks A′ and B′ are much closer. These correlations suggest that the reorientation of the alkanethiolates when the micelles are electrospread has a major influence on the mechanism of electrodeposition of insoluble thiolates.

The presence of two processes is still associated with the fact that the thiolates are physisorbed on the surface in the shape of micelles. The results presented in this Chapter provide an explanation for the difference between the oxidative deposition of insoluble and soluble thiolates or other organic adsorbates. Soluble thiolates will adsorb via a Langmuir process if the interadsorbate interactions are weak or via a nucleation and growth process if

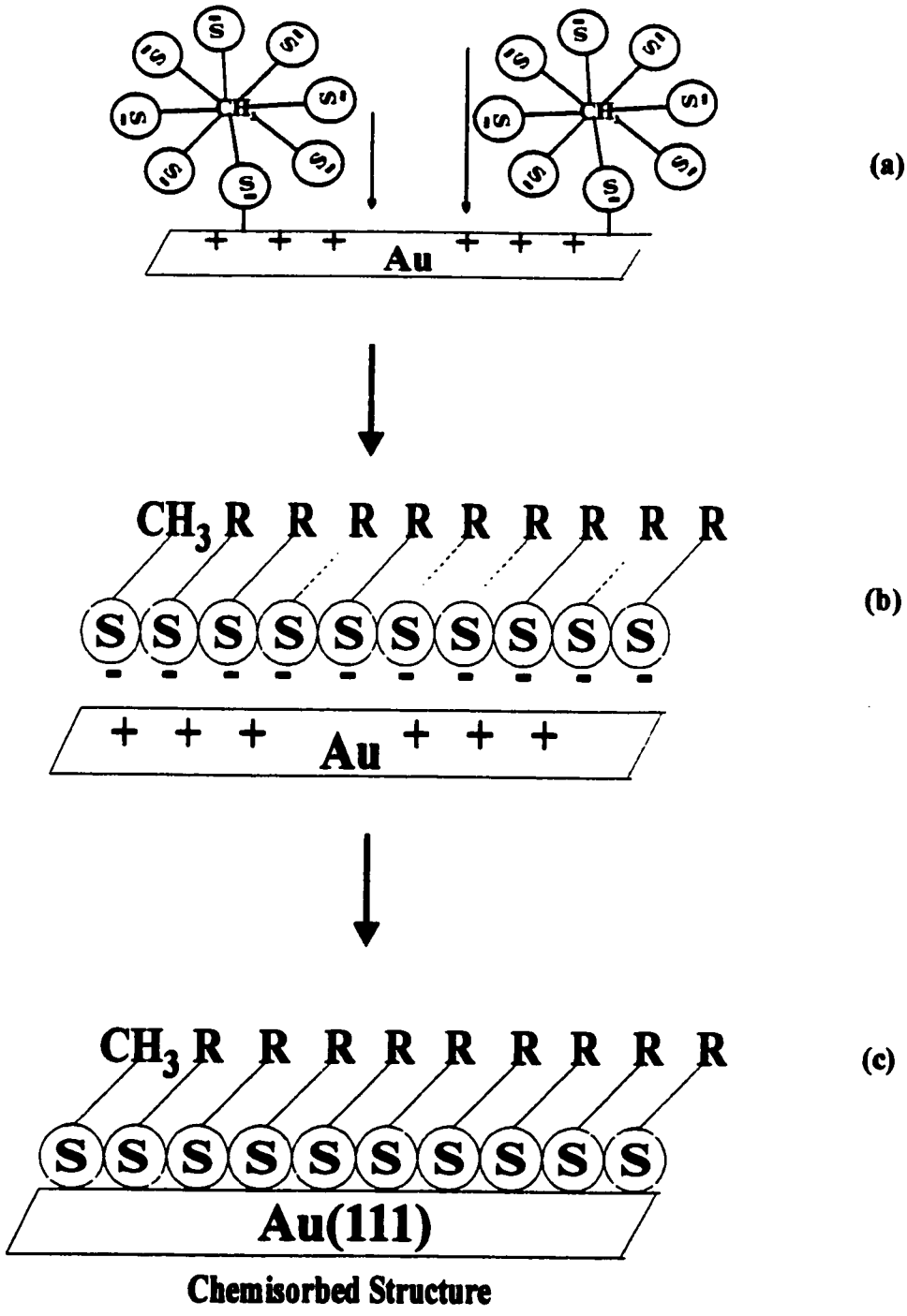

Figure 7.7 : Mechanism of the oxidative redeposition of alkanethiols at a Au(111) electrode. (a) Adsorption of the thiolates in contact with the surface via a Langmuir process; (b) Electrospreading of the micelles via a nucleation and growth process; (c) Electrodeposited monolayer.

the interactions are stronger. In this case, the initial deposition of thiolates will not be separated from the growth of a nucleus since the activation energy is small (the individual thiolates are probably not well solvated). The results obtained in this chapter are consistent with those obtained in chapter 3. The differences between voltammetric and chornoamperommetric results are due to the fact that chronoamperometry measures the transient current of a system after an instantaneous potential perturbation.

These results provide useful insights into the mechanism of electrodeposition of an ordered monolayer of organic molecules. We have shown in the previous chapters that electrodeposition is an efficient, rapid and reliable method to form so called 'self-assembled monolayers'. The temperature dependance of the electrodeposition further shows its robustness. It is possible to deposit a full monolayer of insoluble thiols over a wide range of temperatures.

3. References

1. Zhong, C.-J.; Porter, M. D. J. Electroanal. Chem. **1997**, 425, 147.
2. Widrig, C. A.; Chung, C.; Porter, M. D. J. Electroanal. Chem. **1991**, 310, 335.
3. Yang, D.-F.; Wilde, C. P.; Morin, M. Langmuir **1997**, 13, 243.
4. Weisshaar, D. E.; Lamp, B. D.; Porter, M. D. J. Am. Chem. Soc. **1992**, 114, 5860.
5. Calvente, J. J.; Kovacova, Z.; Sanchez, M. D.; Andreu, R.; Fawcett, W. R. Langmuir **1996**, 12, 5696.
6. Armstrong, R. D. J. Electroanal. Chem. **1969**, 20, 168.
7. Retter, U.; Kent, W. Thin Solid Films 1995, 256, 89.
8. Hatchett, D. W.; Uibel, R. H.; Stevenson, K. J.; Harris, J. M.; White, H. S. J. Am. Chem. Soc. **1998**, 120, 1062.
9. Hatchett, D. W.; Stevenson, K. J.; William, B. L.; Harris, J. M.; White, H. S. J. Am.

Chem. Soc. **1997**, 119, 6596.

10. Stevenson, K. J.; Mitchell, M.; White, H. S. J. Phys. Chem. B **1998**, 102, 1235.
11. Yang, D.-F.; Morin, M. J. Electroanal. Chem. **1998**, 441, 173.
12. Woods, R. In Electroanalytical Chemistry ; Bard, A. J., Ed.; Marcel Dekker : New York, 1976, Vol. 9, 119-125.
13. Ohmori, T.; Enyo, M. Electrochim. Acta **1992**, 37, 2021.
14. Fletcher, S.; Halliday, C. S.; Gates, D.; Westcott, M.; Lwin, T.; Nelson, G. J. Electroanal. Chem. **1983**, 159, 267.
15. Byloos, M.; Al-Maznai, H.; Morin, M. J. Phys. Chem. B in press.

Chapter 8

Oxidation of Thiols Chemisorbed on a Au (111) Single Crystal Electrode

1. Introduction

Sulfur compounds are often used as corrosion inhibitors since they adsorbs strongly on many surfaces. Alkanethiols form a very densely packed monolayer which blocks ions, and they should be efficient corrosion inhibitors. In this Chapter we examine the mechanism of oxidation of chemisorbed thiols in order to determine their efficiency in preventing the formation of an oxide on the surface of gold.

Although gold is not easily oxidized, it is a good electrocatalyst in alkaline medium. The electrocatalytic oxidation of several oxygenated organic compounds have been studied on gold polycrystalline electrodes in acidic and alkaline solutions using cyclic voltammetry [1-3]. The electrocatalytic activity of gold electrodes is far less active than platinum, palladium, or rhodium electrodes, either in an acid [4] or a neutral medium [5]. However, the situation is different if the electro-oxidation is carried out in alkaline electrolyte solutions. Gold is a more active electrocatalyst than platinum [3,6] and it offers a large potential range.

The double layer properties of monolayers of alkanethiols have been well characterized. The resistance to oxidation of these compounds has not been studied in detail. There has been a limited number of studies of the oxidation of chemisorbed alkanethiols. The extent of oxidation of thiols was found to vary greatly. Porter and co-workers [7] reported a three electron mechanism for the oxidation of propanethiols and butanethiols. In this study, we have examined the role of the pH and the scan rate on the oxidation of self-organized chemisorbed butanethiol monolayers on a well-defined gold (111) single crystal substrate.

In this Chapter, the oxidative removal of butanethiol monolayers from a Au (111) electrode in alkaline and neutral aqueous solutions has been studied using cyclic voltammetry and chronoamperometry.

Cyclic voltammetry has shown that the oxidative desorption of a butanethiol SAM depends on the scan rate and the pH of the electrolyte solutions. A slow scan rate of about 1 mV/s is needed to achieve complete removal of a butanethiol SAM from a gold (111) surface. Furthermore, the oxidative removal is found to be a slow multi-electron process in which the Au-S and the C-S bonds can be broken. Up to 11 ± 1 electrons are involved in the oxidation of the thiols. The pH of the electrolyte solution also plays an important role in the oxidative desorption of a butanethiol monolayer. A high pH is required to assure complete removal of a butanethiol monolayer. In a neutral solution there is a partial oxidation.

Chronoamperograms of the electro-oxidation of a butanethiol SAM on Au (111) surfaces have revealed that sulfate and carboxylate species are the most likely products of the electro-oxidation of a butanethiol SAM. Six and four electrons are required to form each species, respectively.

2. Results and Discussion

2.1 Oxidative Desorption of Butanethiol Chemisorbed on Au(111) in 0.1 M KOH :

Figure 8.1a presents the cyclic voltammogram at a Au (111) electrode prior to the adsorption of butanethiol. This voltammogram has been described in Chapter 3. The butanethiol was deposited by incubating the gold electrode in 10 mM solution of butanethiol

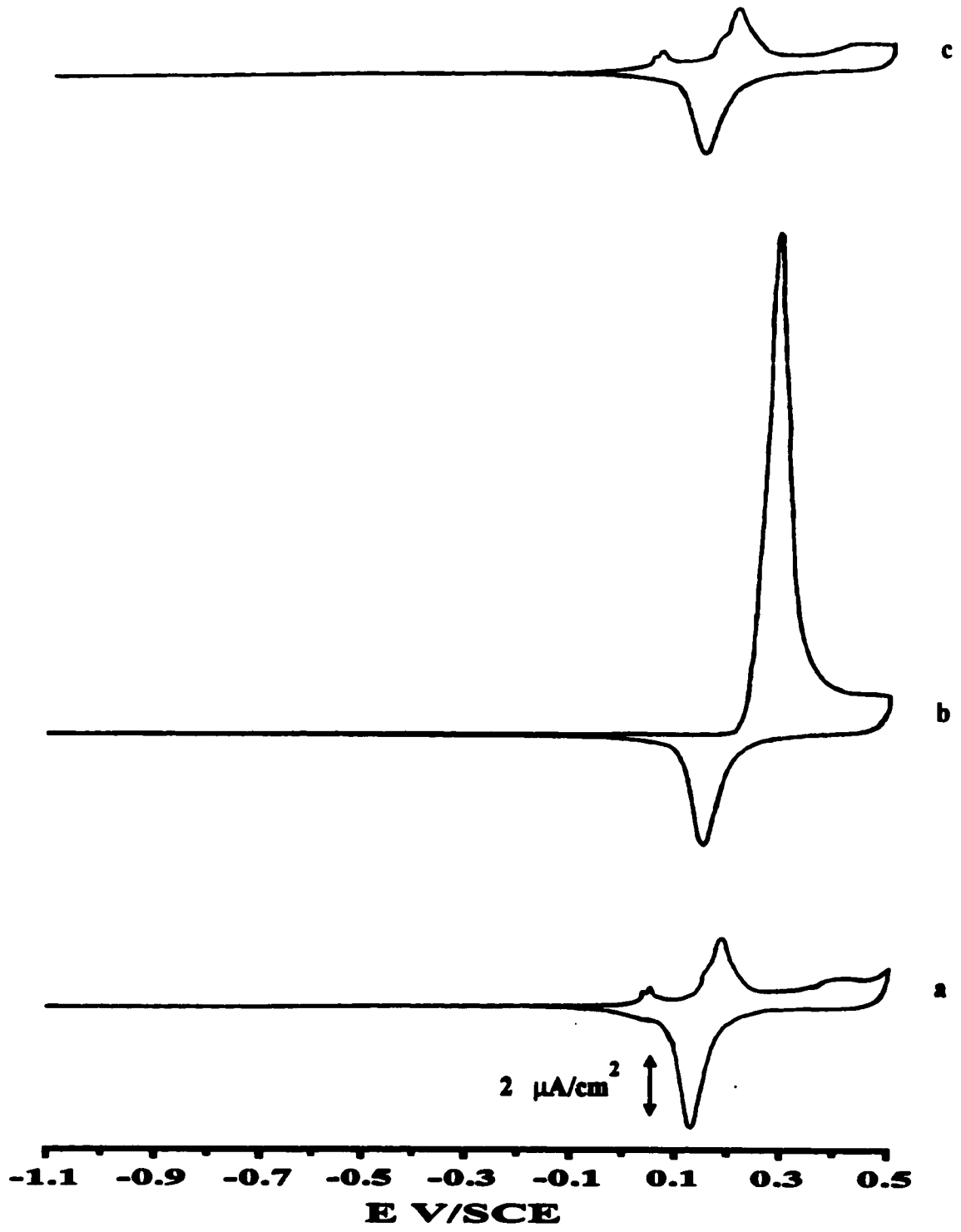

Figure 8.1 : Cyclic voltammograms of (a) a clean Au(111) electrode, (b) the oxidation of a monolayer of butanethiol adsorbed on Au(111) and (c) recorded after (b). Measurements were done in 0.1 M KOH at a scan rate of 1.0 mV/s.

in ethanol for one hour. The electrode was immersed in 0.1 M KOH aqueous solution while maintaining the electrode potential at - 0.3 V. The potential was then scanned at 1 mV s^{-1} from this value to -1.1 V. The slow potential scan rate was chosen to insure that there is sufficient time for the butanethiol to be oxidized . After the potential reached a value of -1.1 V, it was scanned in the reverse direction to 0.5 V (see Fig. 8.1b). We see that the adsorption of butanethiols prevents the formation of the surface oxide up to 0.2 V. Thus the coverage of butanethiols must be high and the uncovered surface must be quite small since no detectable quantity of oxide is formed. A very large oxidative current peak is then observed at 0.295 V. As can be seen from the comparison with Fig. 8.1a, this oxidative current is much larger than the one assigned to the formation of the gold surface oxide. Thus, this peak is assigned to the oxidation of a monolayer of chemisorbed butanethiol. We recorded a complete cyclic voltammogram between 0.5 and -1.1 V after the oxidation of the butanethiols in order to verify if all the butanethiols have been oxidized. The presence of unoxidized thiols would be seen as a reductive current peak around -0.8 V. The resulting voltammogram is shown in Fig. 8.1c. This voltammogram is identical to the one recorded in Fig. 8.1a of a clean Au(111) electrode. This indicated that all the butanethiols have been oxidized since no detectable peak current was observed at -0.8 V. This also shows that a complete oxide layer has been formed during the oxidation of the butanethiols. Thus, the oxidative current peak in Fig. 8.1b corresponds to the oxidation of a complete monolayer of butanethiols and the formation of the gold surface oxide.

The charge corresponding to the oxidative desorption of a butanethiol SAM from a Au (111) electrode is calculated by integrating the current passed during the oxidation (thiol + gold surface oxide) and subtracting the integrated charge due to the oxidation of the gold surface oxide. This latter charge is equal to the charge passed during the reduction of the gold surface oxide [7-9]. Dividing the charge of the oxidation of butanethiol by the geometrical area (geometric area = 0.636 cm^2) of the Au (111) single crystal electrode yields a charge of 955 ($\pm$ 9) $\mu C\ cm^{-2}$.

To obtain the number of electrons required to oxidize one adsorbed butanethiol, we used the charge needed to reduce a complete monolayer of butanethiol (see Chapter 3). 75 (± 5) $\mu C\ cm^{-2}$ are required to reduce a monolayer of thiols via a one electron process [10-12]. The number of electrons per oxidized butanethiol is obtained by dividing the thiol oxidative charge density ($Q_{oxid} = 955\ \mu C\ cm^{-2}$) by the butanethiol reductive desorption charge density ($Q_{red} = 75\ \mu C\ cm^{-2}$). This give a value of 13 (± 1) electrons per butanethiol.

The large number of electrons involved in the oxidation indicates that not only the sulfur is oxidized. There must also be the oxidation of the C-S [13] bond. We suggest a mechanism for the oxidation of thiols which is based on known electrocatalytic properties of gold in an alkaline medium [3,14,15]. A possible mechanism is shown below. The first step corresponds to the oxidation of the gold-sulfur bond to form RSO_2. This requires 4 electrons, a number far from the measured 13 electrons. The complete oxidation of sulfur to a + 6 oxidation state is shown in step 2. This reaction yields a sulfate and an aliphatic alcohol. It requires an additional 3 electrons for a total of 7 electrons. It is well known, as we mentioned in the introduction, that alcohol are easily oxidized on gold in alkaline medium. Steps 4 and 5 were taken from the literature [14] and they show that the alcohol is oxidized to a carboxylate via a 4 electrons process. This gives a total of 11 electrons per thiol. This value is close to the 13 electrons per thiol. It is possible, in alkaline medium, that the carboxylates are oxidized to a CO_2 and a proton by a one electron process. This would explain the larger charge that was measured. We must also remember that only the chemisorbed thiols are oxidized and that they are soluble in the alkaline solution and that they can diffuse away from the surface before being completely oxidized.

2.1.1 Suggested Reaction Mechanism for the Electro-oxidation of a Butanethiol SAM on a Au (111) Single Crystal Electrode in an Alkaline Medium :

1. $RCH_2S\text{-}Au + 4\,OH^- \Rightarrow RCH_2\text{-}SO_2 + 2\,H_2O + Au + 4\,e^-$

2. $RCH_2\text{-}SO_2 + 5\,OH^- \Rightarrow RCH_2\text{-}OH + 2\,H_2O + SO_4^{2-} + 3\,e^-$

3. $RCH_2\text{-}OH + 2\,OH^- \Rightarrow RCOH + 2\,H_2O + 2\,e^-$

4. $RCOH + 3\,OH^- \Rightarrow RCOO^- + 2\,H_2O + 2\,e^-$

$$RCH_2\text{-}Au + 14\,OH^- \Rightarrow RCOO^- + 8\,H_2O + Au + SO_4^{2-} + 11\,e^-$$

The complex oxidative mechanism described above was verified in more detail. The oxidation of the chemisorbed thiols is slow. We can suppose that the rate of oxidation of thiols to sulfate, shown as steps 1 and 2, differs from the rate of oxidation of an alcohol (steps 3 and 4). It should thus be possible, by measuring the oxidative charge as a function of the potential scan rate, to identify some of the steps.

Figs. 8.2 to 8.5 show the voltammograms recorded at 5, 20, 50, and 100 mV/sec. We see that the oxidative current peak moves to more positive potentials and broadens as the scan rate increases. The oxidation of all the butanethiols still occurs. The voltammograms recorded after the oxidation do not show any thiols that are reduced, and a surface oxide typical of a clean Au(111) is formed. Table 1 shows that the charge and the number of electrons required to oxidize a butanethiol decrease.

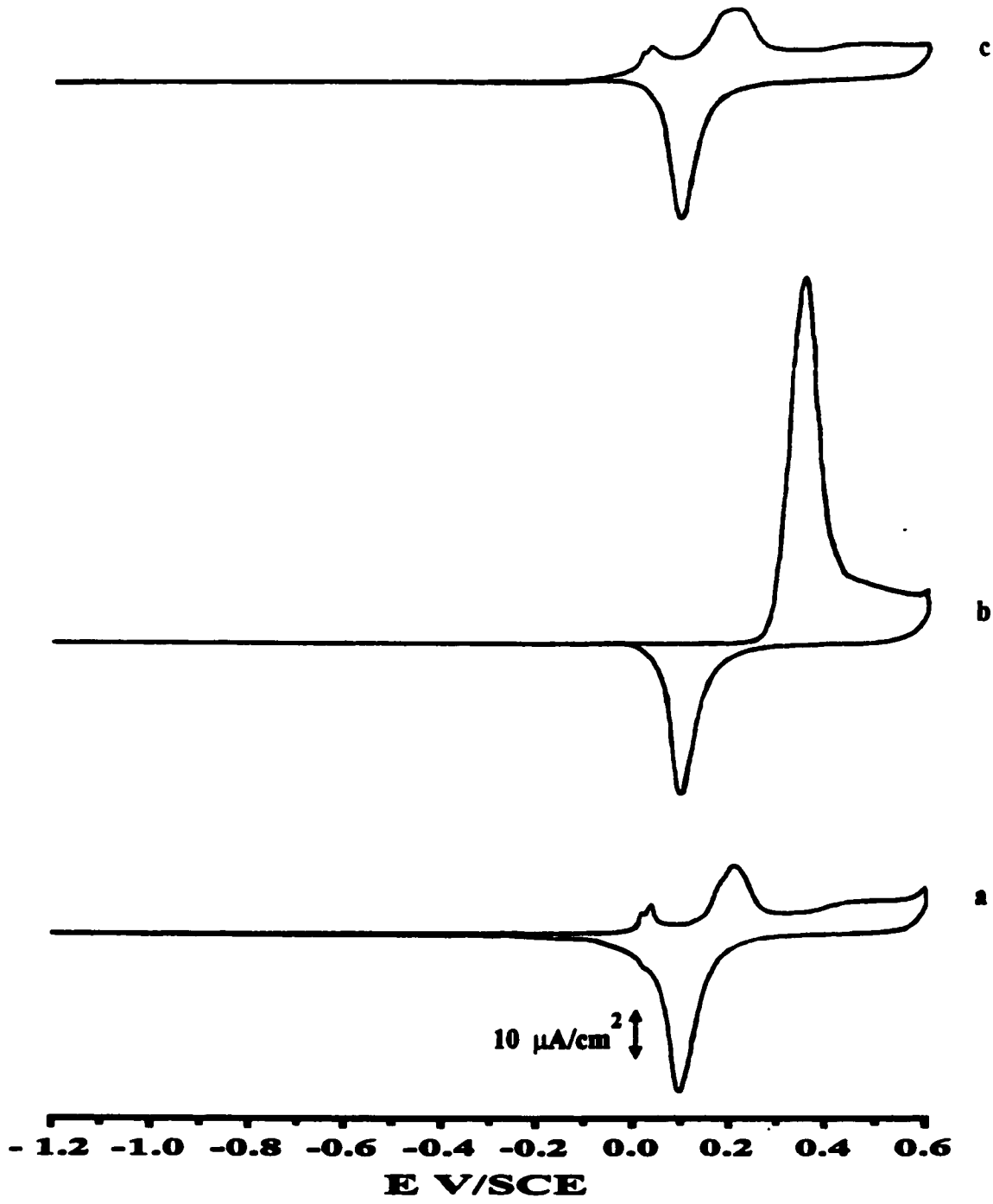

Figure 8.2 : Cyclic voltammograms of (a) a clean Au(111) electrode, (b) the oxidation of a monolayer of butanethiol adsorbed on Au(111) and (c) recorded after (b). Measurements were done in 0.1 M KOH at a scan rate of 5.0 mV/s.

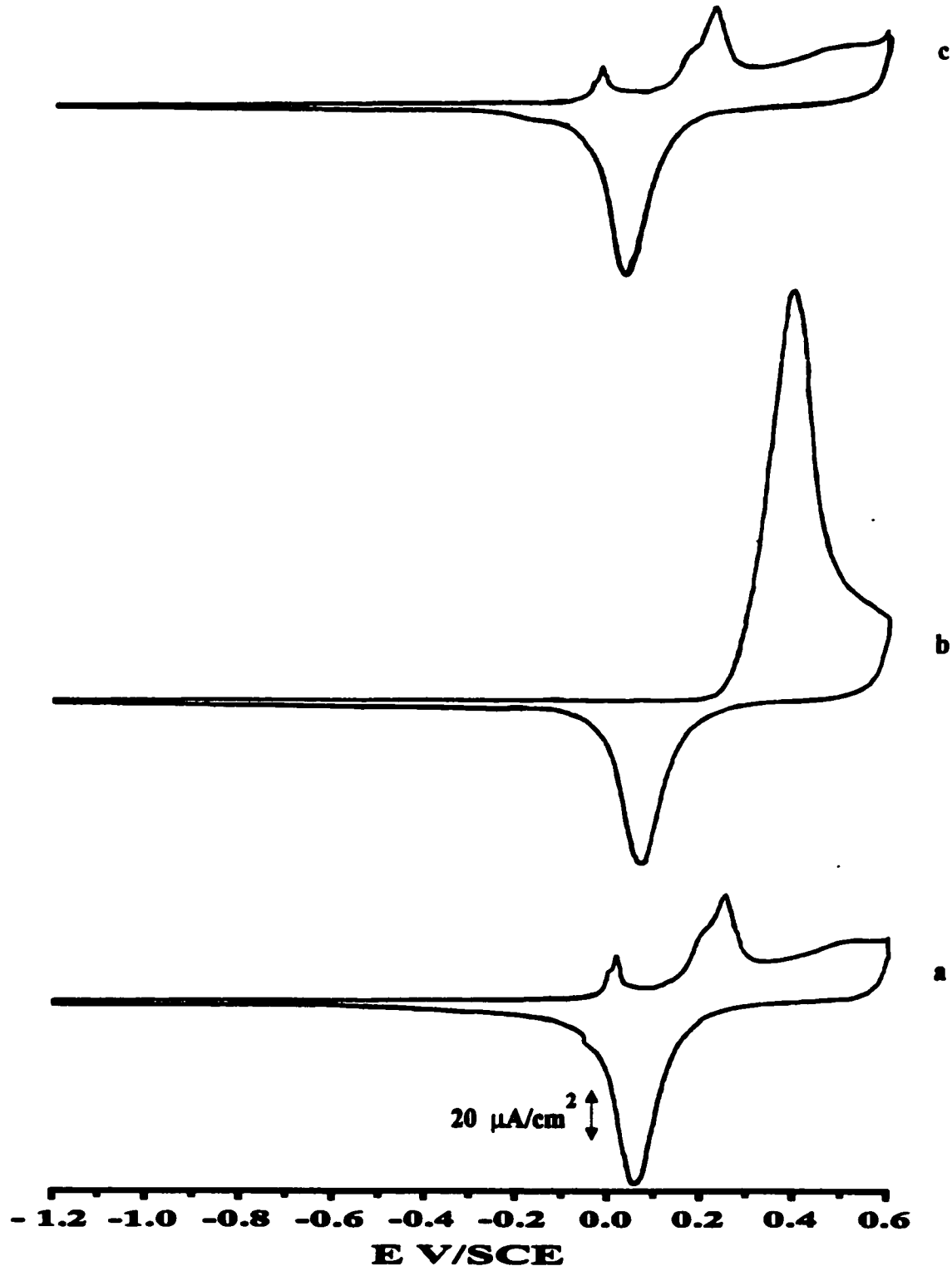

Figure 8.3 : Cyclic voltammograms of (a) a clean Au(111) electrode, (b)the oxidation of a monolayer of butanethiol adsorbed on Au(111) and (c) recorded after (b). Measurements were done in 0.1 M KOH at a scan rate of 20 mV/s.

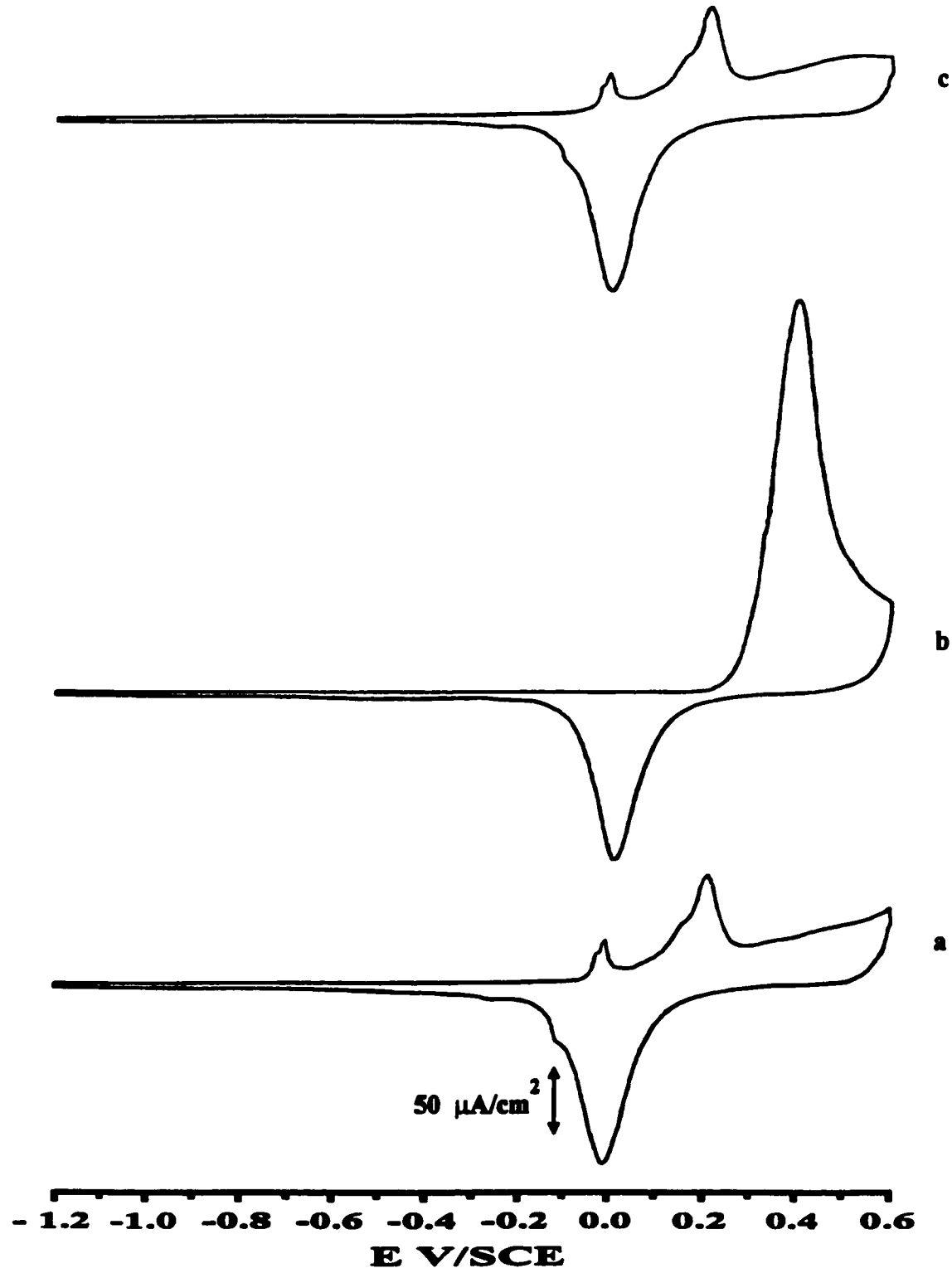

Figure 8.4 : Cyclic voltammograms of (a) a clean Au(111) electrode, (b) the oxidation of a monolayer of butanethiol adsorbed on Au(111) and (c) recorded after (b). Measurements were done in 0.1 M KOH at a scan rate of 50 mV/s.

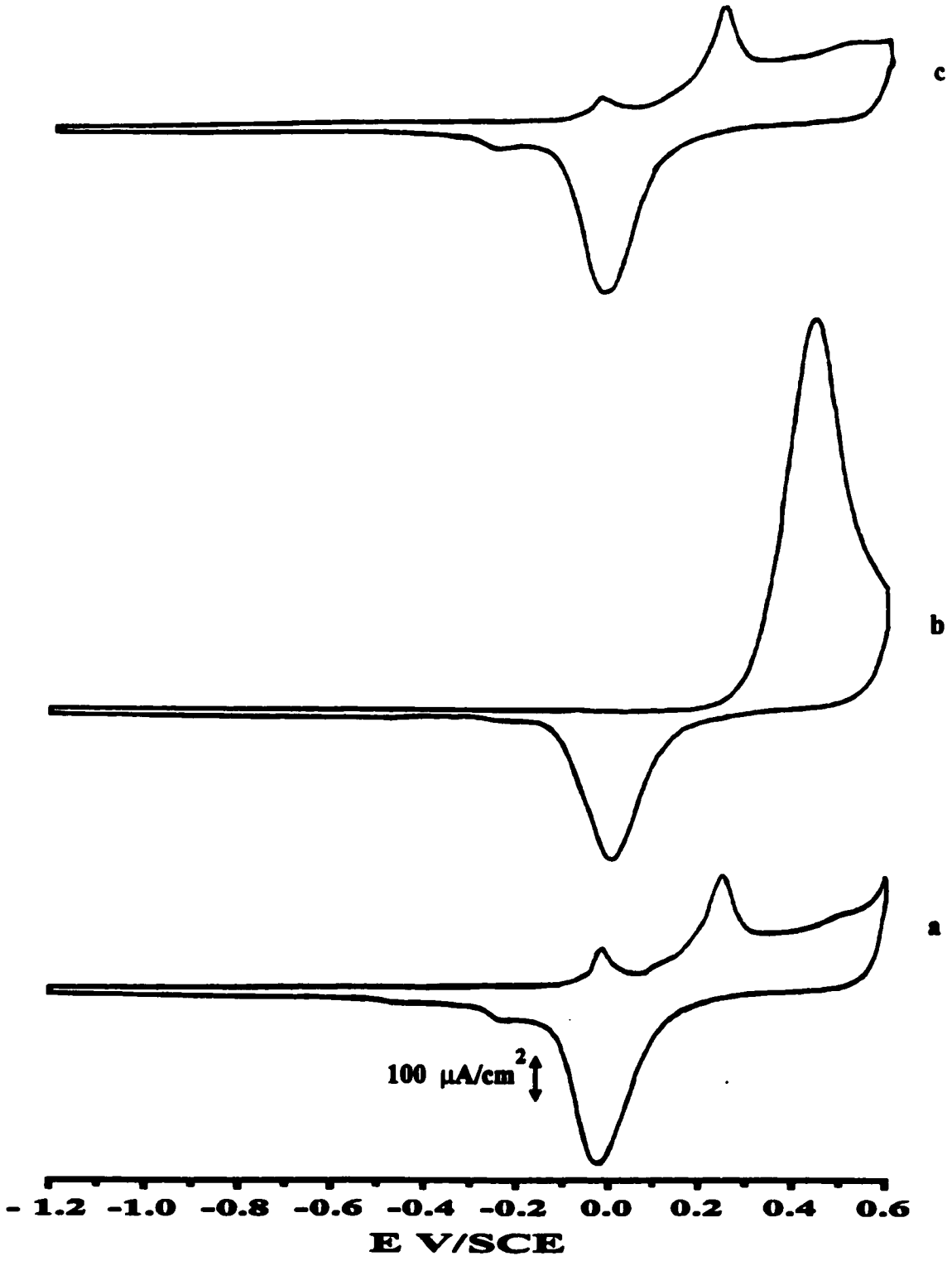

Figure 8.5 : Cyclic voltammograms of (a) a clean Au(111) electrode, (b)the oxidation of a monolayer of butanethiol adsorbed on Au(111) and (c) recorded after (b). Measurements were done in 0.1 M KOH at a scan rate of 100 mV/s.

Table 1. The average oxidative desorption charge densities, Q_d, and the average number of electrons of butanethiol monolayers on a Au (111) single crystal electrode in 0.1 M KOH as a function of the scan rate:

Scan Rate (mV/s)	Average Q_d ($\mu C/cm^2$)	Average Number of Electrons / Thiol
1	955 ± 9	13 ± 1
5	854 ± 3	11 ± 1
20	738 ± 3	10 ± 0.1
50	695 ± 4	9 ± 1
100	626 ± 3	8 ± 1

The decrease confirms that the different steps in the oxidation mechanism are not occurring at similar rates. The oxidation of a butanethiol requires only 8 electrons at a scan rate of 100 mV s^{-1}. This shows that the oxidation of the RCH_2OH to RCO_2^-, steps 3 and 4 in our mechanism, is slow since the number of electrons decreases below 11 electrons at a scan rate of 20 mV s^{-1}. The complete oxidation of the sulfur to sulfate is still occurring even at the highest scan rate.

It is clear from our suggested mechanism that the high concentration of hydroxyls is responsible for the substantial oxidation of the thiols. We do not know if the hydroxyls involved in the oxidation are chemisorbed. It has been suggested that the higher electrocatalytic activity of gold in a higher pH solution is due to the presence of highly reactive adsorbed hydroxyls. The situation here is different since the surface is covered by thiols which prevent the adsorption of the hydroxyls. Also, once they are oxidized they must remain adsorbed at the surface given the extent of their oxidation. This again might prevent or reduce the adsorption of hydroxyls. The adsorption of the oxidized sulfur is reasonable since the species are negatively charged and the potential applied to the electrode is positive. The fact that the oxidation of the alcohol is slow can be interpreted as being due to the low amount of adsorbed hydroxyls prior to the formation of the sulfate (step 2). This would make steps 3 and 4 slow.

Our suggested mechanism was partially confirmed by in-situ FTIR measurements of the oxidation of chemisorbed nonanethiols [10]. A band at 1750 cm^{-1} typical of carboxylates was present in the vibrational spectrum. However, the bands related to the S-O stretching modes which would indicate the formation of sulfates were at frequencies outside the accessible frequency range for this experiment.

The role of the hydroxyls was examined by oxidizing the thiols in 0.1 M $KClO_4$ solution. Lowering the concentration of hydroxyls by a factor of 10^6 causes a decrease of the electrocatalytic activity of gold towards the oxidation of alcohols [16,17] and should decrease the extent of oxidation of the thiols.

Shown in Figure 8.6 are cyclic voltammograms for the electro-oxidation of a butanethiol SAM on a Au (111) single crystal electrode in 0.1 M $KClO_4$ solution recorded at 1 mV s^{-1}. Fig. 8.6a shows the voltammogram of a clean gold (111) electrode surface prior to immersion in 1 mM butanethiol ethanolic solution. The potential is scanned over the region of the formation of a reversible surface oxide. This result is identical to previous reports [11,18,19]. Fig. 8.6b represents the oxidative desorption of butanethiol from Au(111). The adsorption of butanethiol blocks the formation of the surface oxide up to 0.8 V. The large oxidative current peak at + 0.92 V is assigned to the oxidation of the chemisorbed butanethiols. This peak is relatively symmetric. Fig. 8.6c shows that all the thiols have been oxidized since there are no signs of un-oxidized thiols. As we explained above, thiols that have not been oxidized in the positive going positive potential scan should be reduced at - 0.78 V on the subsequent negative going potential scan. We did not measured any reductive current in this region. The complete oxidation of all thiols is further confirmed by the formation of a complete surface oxide. The calculation of the charge and the number of electrons required to oxidize a butanethiol were obtained as described above. The charge required to reduce one monolayer of butanethiols in 0.1 M $KClO_4$ was measured to be 78 (± 5) $\mu C/cm^2$ corrected for the double layer charging current.

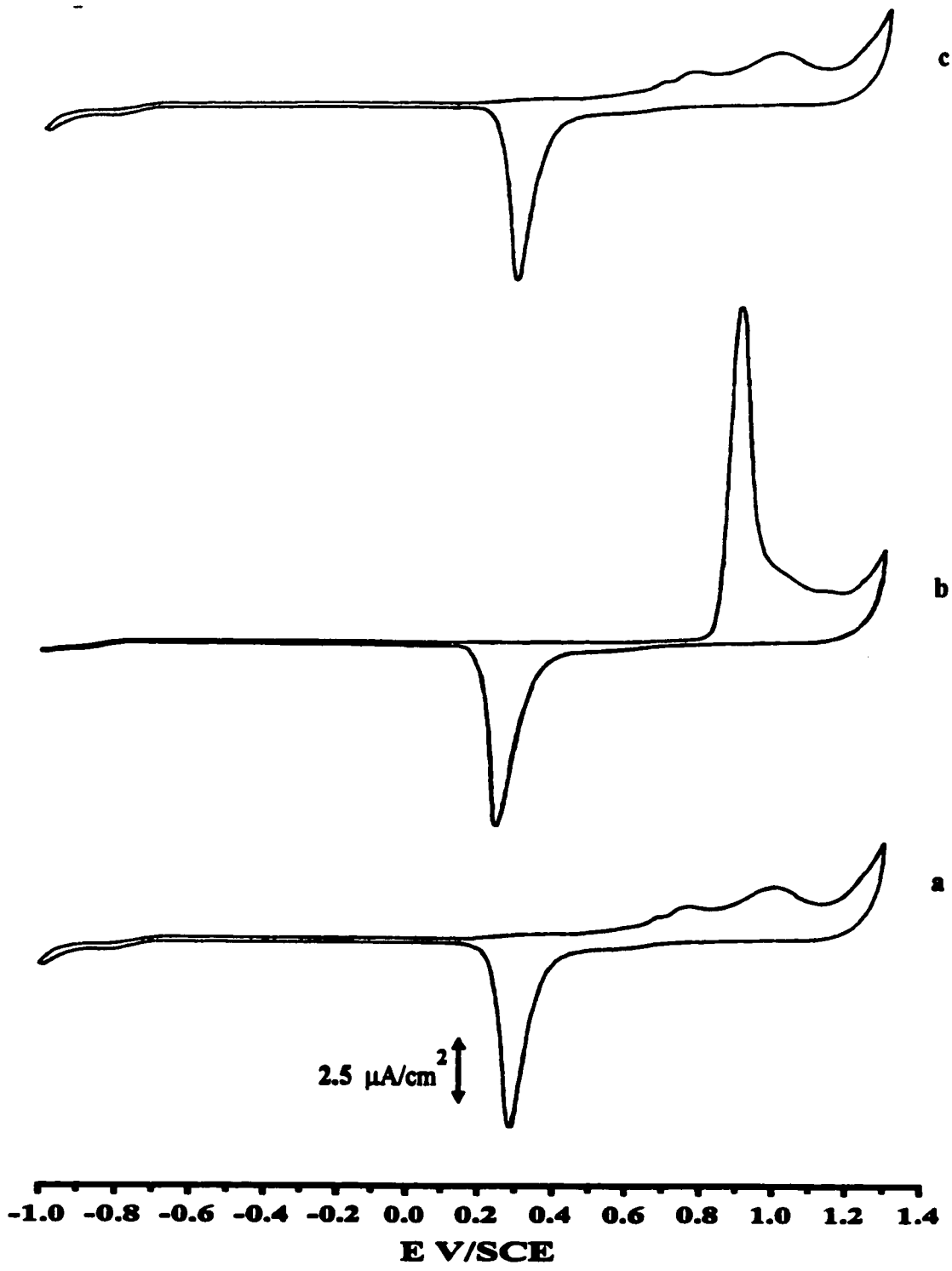

Figure 8.6 : Cyclic voltammograms of (a) a clean Au(111) electrode, (b) the oxidation of a monolayer of butanethiol adsorbed on Au(111) and (c) recorded after (b). Measurements were done in 0.1 M $KClO_4$ at a scan rate of 1.0 mV/s.

We repeated these measurements at different potential scan rates. The results are shown in Figs. 8.7 to 8.10. The oxidation of the thiols is occurring at more positive potentials as the scan rate increases. The oxidative current also broadens. These results show that the oxidation of thiols is still a slow process in a neutral pH solution. At all scan rates, except 100 mV s^{-1}, all the thiols have been oxidized on the positive going scan. Table 2 summarizes the average butanethiol oxidation charge density (Q_d) (for at least 3 experiments each) and the average number of electrons per thiol at different scan rates.

Table 2. The average oxidative desorption charge densities, Q_d, and the average number of electrons of butanethiol monolayers on a Au (111) single crystal electrode in 0.1 M $KClO_4$ as a function of the scan rate:

Scan Rate (mV/s)	Average Q_d ($\mu C/cm^2$)	Average Number of Electrons / Thiol
1	868 ± 15	11 ± 2
5	609 ± 7	8 ± 1
20	573 ± 8	7 ± 1
50	488 ± 11	6 ± 1
100	488 ± 5	6 ± 1

In a neutral medium the oxidation of thiols requires less electrons per molecule. Eleven electrons are needed at the slowest rate compared to 13 electrons in an alkaline medium. The number of electrons rapidly decreases to a value of 6 as the scan rate is increased to 50 mV s^{-1}. Hence, the decrease in the hydroxyl concentration has an influence on the oxidation process. We suggest that the mechanism occurring in alkaline solution is modified as below :

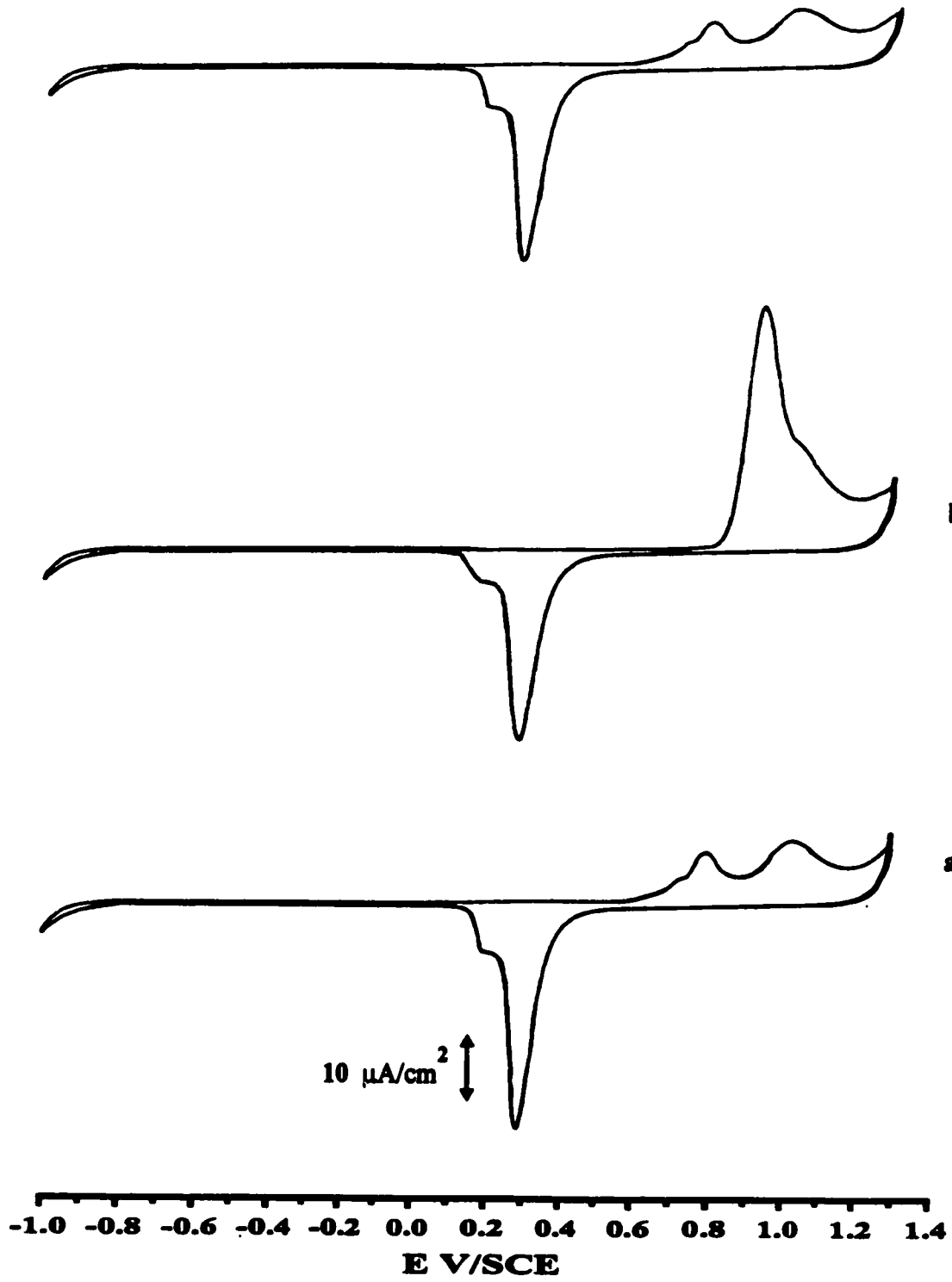

Figure 8.7 : Cyclic voltammograms of (a) a clean Au(111) electrode, (b)the oxidation of a monolayer of butanethiol adsorbed on Au(111) and (c) recorded after (b). Measurements were done in 0.1 M $KClO_4$ at a scan rate of 5.0 mV/s.

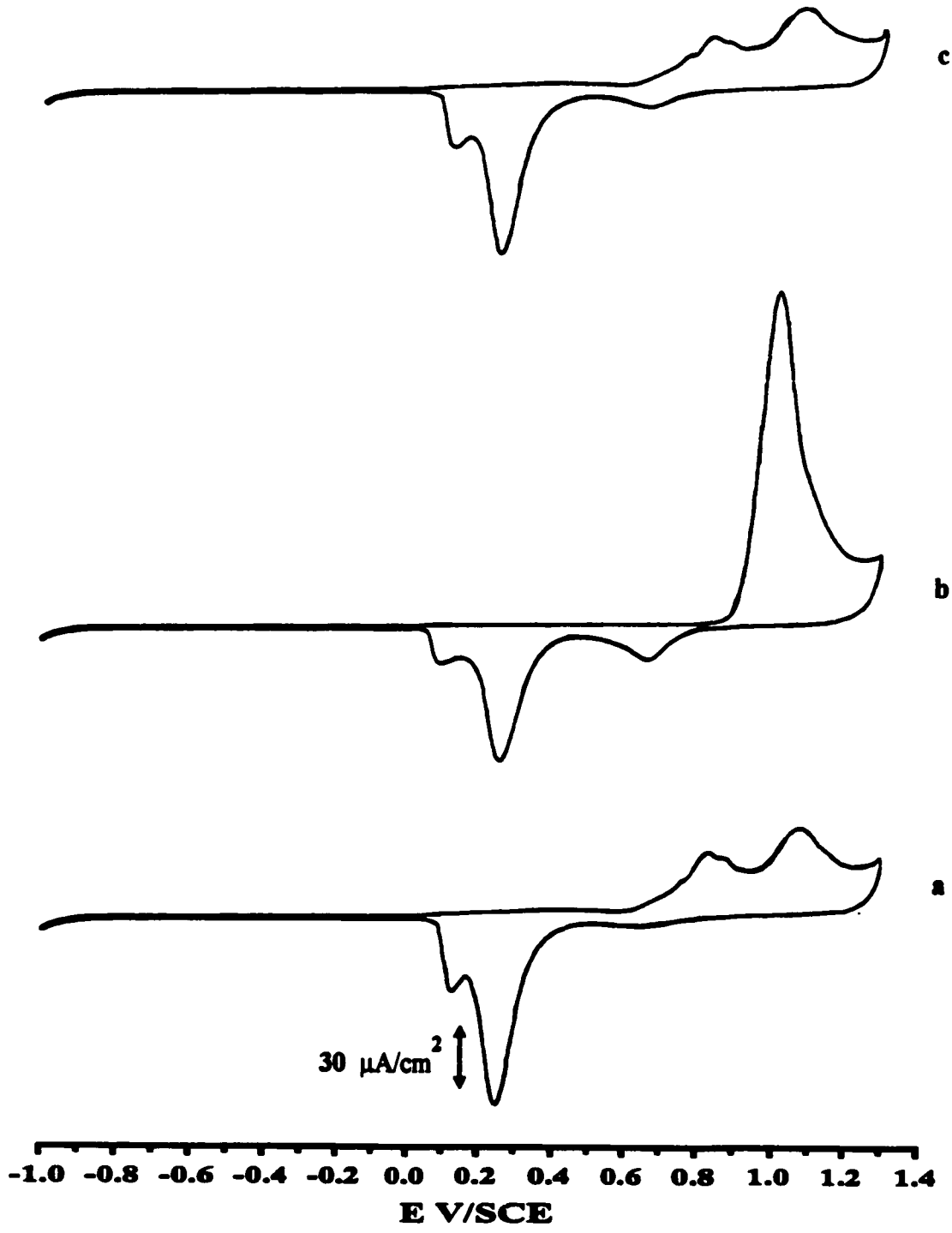

Figure 8.8 : Cyclic voltammograms of (a) a clean Au(111) electrode, (b) the oxidation of a monolayer of butanethiol adsorbed on Au(111) and (c) recorded after (b). Measurements were done in 0.1 M $KClO_4$ at a scan rate of 20 mV/s.

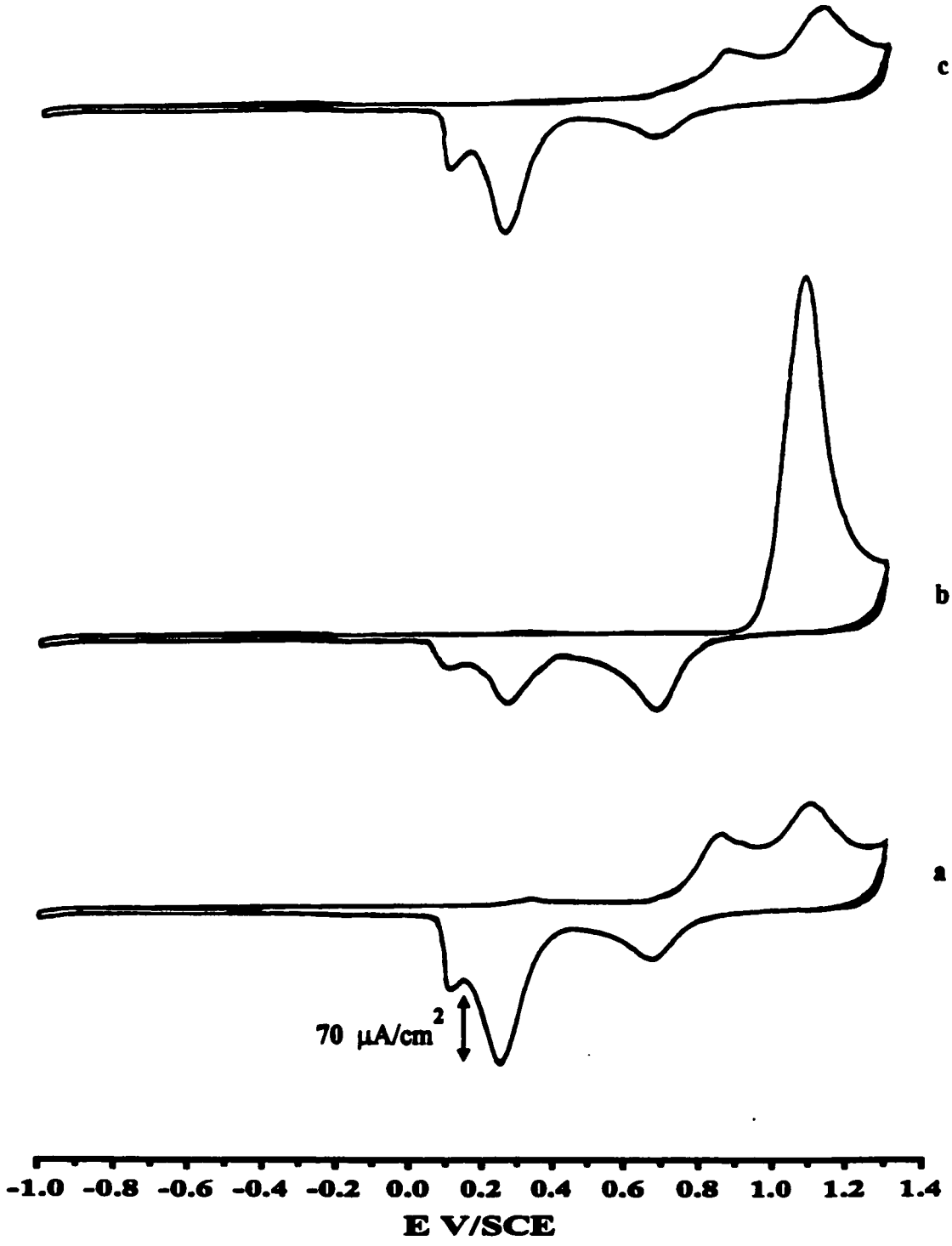

Figure 8.9 : Cyclic voltammograms of (a) a clean Au(111) electrode, (b) the oxidation of a monolayer of butanethiol adsorbed on Au(111) and (c) recorded after (b). Measurements were done in 0.1 M $KClO_4$ at a scan rate of 50 mV/s.

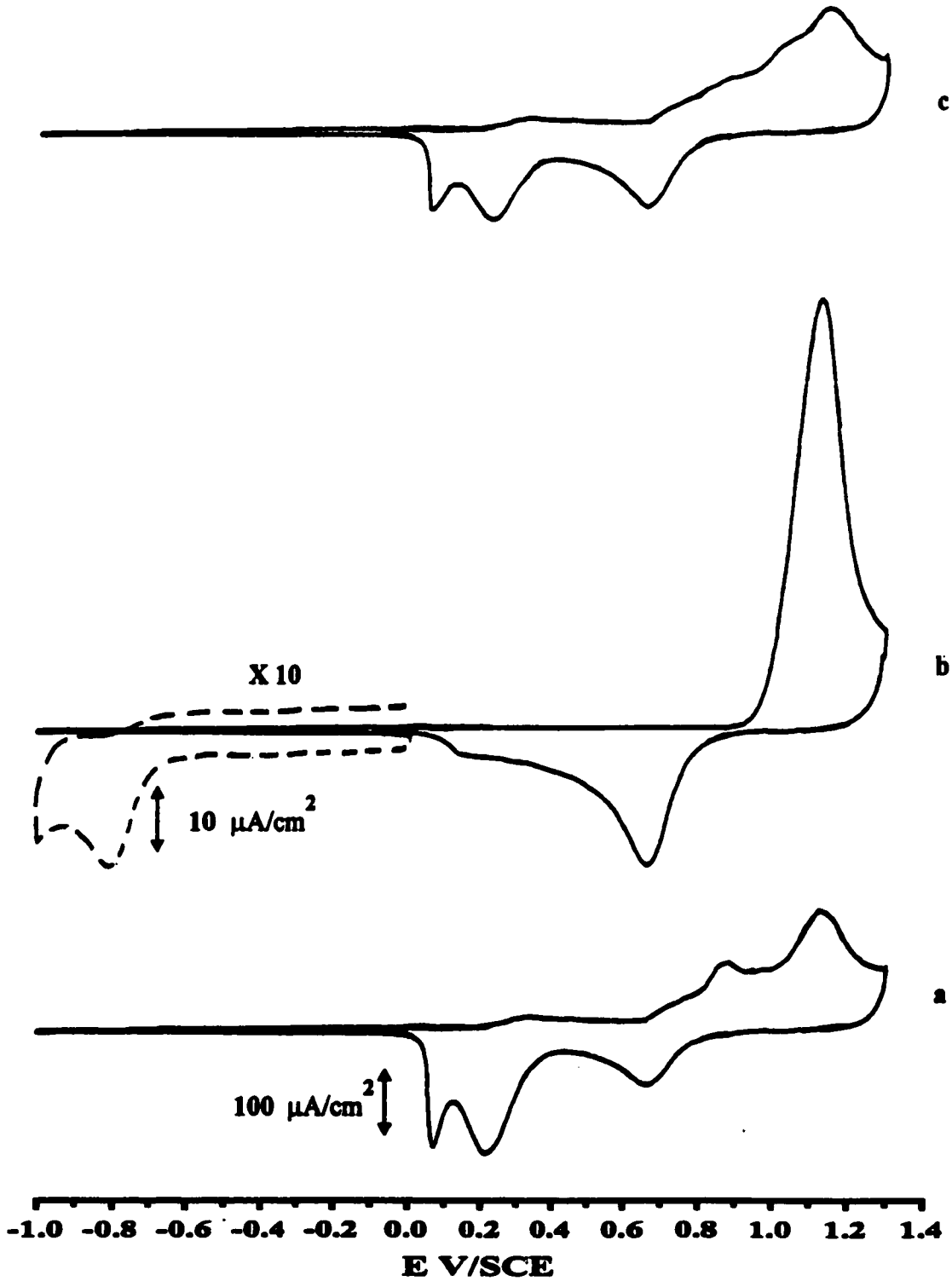

Figure 8.10 : Cyclic voltammograms of (a) a clean Au(111) electrode, (b) the oxidation of a monolayer of butanethiol adsorbed on Au(111) and (c) recorded after (b). Measurements were done in 0.1 M $KClO_4$ at a scan rate of 100 mV/s.

1.	$RCH_2S\text{-}Au$	$+ 2\,H_2O$	$\Rightarrow$	$RCH_2\text{-}SO_2H + 3\,H^+$	$+ Au$	$+ 3e^-$
2.	$RCH_2\text{-}SO_2H$		$\rightleftharpoons$	$RCH_2\text{-}SO_2^- + H^+$		
3.	$RCH_2\text{-}SO_2^-$	$+ 3\,H_2O$	$\Rightarrow$	$RCH_2\text{-}OH + 5\,H^+$	$+ SO_4^{2-}$	$+ 4\,e^-$
4.	$RCH_2\text{-}OH$	$+ H_2O$	$\Rightarrow$	$RCHO + 2\,H^+$		$+ 2\,e^-$
5.	$RCHO$	$+ H_2O$	$\Rightarrow$	$RCOO^- + 3\,H^+$		$+ 2\,e^-$

$$RCH_2S\text{-}Au + 7\,H_2O \Rightarrow RCOO^- + 14\,H^+ + Au + SO_4^{2-} + 11\,e^-$$

In a neutral solution such as $KClO_4$, the concentration of hydroxyls is very low and the oxidation of the thiols proceeds by a reaction with the solvent, water. The water molecules are less reactive than hydroxyls since OH bonds need to be broken to form an S_{ox} species. Steps 1 to 3 represent the complete oxidation of the thiols to a sulfate and an aliphatic alcohol. This requires 7 electrons. We also note that we must take into account the protonation of the (sulfinic acid) RSO_2^- at this pH. Steps 3 and 4 are related to the oxidation of the alcohol. In neutral medium the oxidation of alcohols on gold is slow and incomplete [18,19]. We thus propose that this oxidation proceeds through the formation of an aldehyde via a 2 electrons process. This is followed by a 2 electron oxidation of the aldehyde to a carboxylate.

The overall reaction requires about 11 ± 1 electrons, in agreement with the experimental result obtained at low scan rate. The final products of the oxidation are carboxylates and sulfates. The rapid decrease to 6 electrons indicates that the oxidation of the alcohol is slower in a neutral medium than in an alkaline medium. These measurements provide support for the mechanism in which there is first the complete oxidation of the sulfur and the formation of a sulfate and an aliphatic alcohol. This is followed by the slow oxidation of the alcohol to a carboxylate.

2.1.2 Chronoamperometry Experiments.

The goal of using a potential-step technique was to try to find out if it is possible to separate and to identify any of the proposed product species of the electro-oxidation of a butanethiol monolayer on a Au (111) single crystal electrode.

Potential-step experiments of the electro-oxidation of a butanethiol and the subsequent electro-reduction of the gold surface oxide from a Au (111) electrode were carried out by stepping the potential of the working electrode from an initial potential (- 0.3 V in KOH and 0 V in $KClO_4$) to a potential where oxidation occurs. The potential is then stepped back to the initial potential to measure the amount of surface oxide formed. The results are summarized in Table 3 for a butanethiol coated Au(111) surface in KOH and Table 4 for a butanethiol coated Au(111) surface in $KClO_4$. The current transient following a potential-step is a more direct measure of the kinetics. There is initially a short current transient due to the charging of the electrochemical double layer in the microsecond range, and then the current decays exponentially on the time scale of seconds.

Tables 3 and 4 show the final potential value, the butanethiol integrated oxidative-charge density (transient current vs time) and the number of electrons involved. All the calculations were done as before for the oxidative removal of a butanethiol in an alkaline solution.

Table 3 shows a maximum butanethiol net charge density and a maximum number of electrons at 300 mV where the oxidative desorption peak maximum is located at + 0.295 V in KOH. Beyond this final potential, the number of electrons is decreasing. Hence, at more positive potentials the extent of oxidation of butanethiol decreases.

Table 3. Charge densities and number of electrons per oxidized thiol as a function of potential in 0.1 M KOH :

E (final) mV	Net Q_d (μC/cm2)	No. of Electrons
200	1	0
250	1	0
300	840	11
350	706	9
400	601	8
500	419	6
600	650	9

From Table 3, when the number of electrons involved is equal to 11, both sulfate (7 e^-) and carboxylate (4 e^-) could be formed. As for 9 electrons, the sulfate (7 e^-) and partial oxidation of the alcohol to an aldehyde (2 e^-) occurs. The 6 electrons indicates that only sulfate and alcohol are formed. The complex variation indicates that sulfate is always produced but that the oxidation of the alcohol is only partial.

In a neutral medium, the number of electrons per oxidized thiol are smaller than the ones measured in KOH. This agrees with the oxidation of the alcohol being more difficult in neutral medium. In most of the experiments, only sulfate is formed (7 e^-). The smaller charges observed in potential steps experiments, relative to those measured in the voltammograms, are probably caused by the fact that the oxidized molecules diffuse away from the surface before further oxidation can occur.

Table 4. Charge densities and the calculated number of electrons per oxidized butanethiol in 0.1 M $KClO_4$:

E (final) mV	Net Q_d (μC/cm2)	No. of Electrons
800	1	0
870	625	8
920	377	5
970	484	6
1000	396	5
1100	447	6

3. Summary

Cyclic voltammograms show that the electro-oxidation of a butanethiol is completed in one cycle for potential scan rate of up to 50 mV s^{-1}. A butanethiol self-assembled monolayer oxidizes on a gold (111) single crystal electrode in KOH and $KClO_4$ solutions through an irreversible 11 ± 2 electron reaction at a slow potential scan rate of 1 mV/s and a 6 ± 2 electron reaction at a moderately fast potential scan rate of 100 mV/s. These results have shown that the electro-oxidation of a butanethiol SAM is pH and scan rate dependent. Chronoamperometry results, in 0.1 M KOH, have allowed the identification of sulfate and carboxylate species as the product of the electro-oxidation of butanethiol monolayers on a Au(111) surface. In neutral medium, only sulfate is formed.

4. References

1. Crepy, G.; Lamy, C.; Maximovitch, S. J. Electroanal. Chem. **1974**, 54, 161.
2. Besenhard, J. O.; Parsons, R.; Reeves, R. M. J. Electroanal. Chem. **1979**, 96, 57.
3. Beden, B.; Cetin, I.; Kahyaoglu, A.; Takky, D.; Lamy, C. Journal of Catalysis **1987**, 104, 37.

4. Capon, A.; Parsons, R. J. Electroanal. Chem. **1973**, 44, 239.
5. Beden, B.; Lamy, C.; Leger, J. M. J. Electroanal. Chem. **1979**, 101, 127.
6. Ulman, A., Introduction to Ultrathin Organic Films from Langmuir-Blodgett to Self-assembled, Academic Press: New York, 1991.
7. Widrig, C. A.; Chung, C.; Porter, M. D. J. Electroanal. Chem. **1991**, 310, 335.
8. Fawcett, W. R.; Fedurco, M.; Kovacova, Z.; Borkowska, Z. Langmuir 1994, 10, 912.
9. Calventt, W. R. Langmuir **1996**, 12, 5696.
10. Yang, D. -F.; Al-maznai, H.; Morin, M. J. Phys. Chem. **1997**, 101, 1158.
11. Yang, D. -F.; Wilde, C. P.; Morin, M. Langmuir **1996**, 12, 6570.
12. Yang, D. -F.; Wilde, C. P.; Morin, M. Langmuir **1997**, 13, 243.
13. Weisshaar, D. E.; Walczak, M. M.; Porter, M. D. Langmuir **1993**, 9, 323.
14. Beden, B. ; Leger, Jean-Michel.; Lamy, C. in Modern Aspects of Electrochemistry, Number 22, edited by Bockris et al. Plenum Press: New York, 1992, Chapter 2, pp. 97-264.
15. Enea, O.; Ango, J. P. Electrochimica Acta **1989**, 34, 391 .
16. Pastor, E.; Schmidt, V. M.; Iwasita, T.; Arevalo, M. C.; Gonzalez, S.; Arvia, A. J. Electrochim. Acta **1993**, 38, 1337.
17. Cai, X.; Schell, M. Electrochimica Acta **1992**, 37, 673.
18. Hamelin, A.; Sottomayer, M. J. ; Silva, F. ; Chang, Si-chung.; Weaver, M. J. J. Electroanal. Chem. **1990**, 295, 291.
19. Hamelin, A. J. Electroanal. Chem. **1996**, 407, 1.

Chapter 9

Conclusions

The mechanisms of reduction and oxidative deposition of insoluble alkanehiol self-assembled monolayers at gold (111) have received limited attention during the past 15 years. This thesis provides new knowledge about various factors that influences these processes such as solubility, temperature, pH. The main contributions to original research by the author of this thesis are as follows :

As the chain length of alkanethiols increases, the solubility of thiols decreases while the reductive peak potential shifts to a more negative overpotentials. However, the total charge density of the chemisorbed reductive desorption from cyclic voltammograms for each chain studied is independent of the chain length, within experimental uncertainty. The double layer current was found to be independent of the potential, but dependent of the chain length: The longer the chain, the smaller the current.

The monolayer obtained after a single one-hour incubation has a low number of defects and act as an ensemble of microelectrodes This behavior is compatible with electron transfer occurring via ion permeation. Evidences of a phase transition between 25° and 35 °C of the chemisorbed thiols were found from the variations of the reduction of the thiols. Temperature dependent study of the reduction of ferricyanide also reveals a significant changes in the same temperature range. We assign these changes to an order (crystalline like)/disorder (liquid like) phase transition.

Monolayers obtained after multiple one-hour incubations have a negligible number of defects. Electron transfer measurements for the reduction of ferricyanide are found to be independent of the temperature and potential scan rate This is compatible with electron transfer via tunneling. These experimental results show that methyl terminated thiol

monolayers can block metallic surfaces very efficiently. They also shows that the substrate and the method of deposition of thiols influence the electrochemical properties.

Our differential capacitance and impedance spectroscopy results are in agreement with previously reported results. Impedance spectroscopy reveals that ion permeation occurs before the reduction of the chemisorbed thiols.

In summary, our results have shown that the reductive desorption and the oxidative deposition of insoluble thiols in aqueous media proceed through 2-steps. The first step is the reduction of the chemisorbed thiols. It gives the first reductive current peak. The second step is the formation of physisorbed micelles of thiolates which causes the reorientation of the thiolates. This gives the second reductive current peak. The electrooxidative redeposition of the physisorbed thiolates proceeds through the same 2-step mechanism, but in the reverse order.